Charles University in Prague
Faculty of Mathematics and Physics

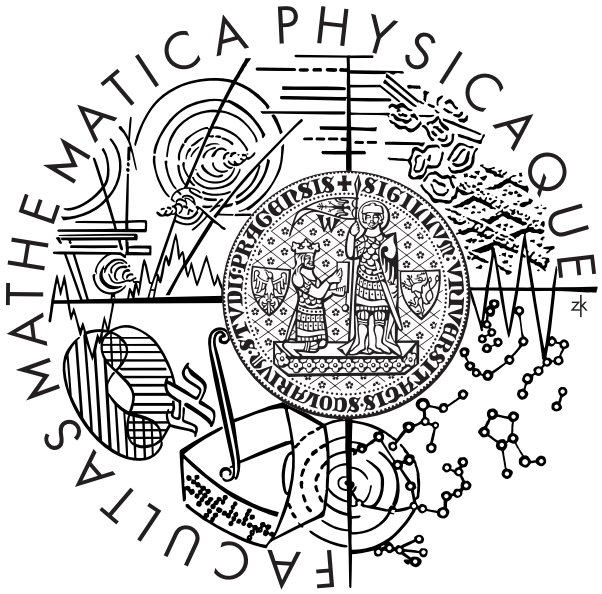

Numerical modeling of ice sheet dynamics

Ondřej Souček

Ph.D. Thesis
Supervisor: Prof. RNDr. Zdeněk Martinec, DrSc.
Prague 2010

Acknowledgements

I would first like to thank to my supervisor, Prof. Zdeněk Martinec, for his inspiring leadership and encouragement, to Dr. Ladislav Hanyk, Dr. Jakub Velímský, and Dr. Marie Běhounková, for their advice and often crucial help with the numerical implementations, and to Doc. Ctirad Matyska, for the fruitful discussions and his neverending patience. I am very thankful to Doc. Ondřej Čadek, and Prof. Jan Kostelecký for their support, to Dr. Oleg Rybak and Prof. Dr. Philippe Huybrechts for providing their model outputs for the Dronning Maude Land simulation, and last but not least to Dr. Kevin Fleming for his help with the English corrections. I would like to thank sincerely all of the teachers, colleagues and students from the Department of Geophysics, for the unique and friendly atmosphere they created.

The work was supported by the Center for Earth Dynamic Research, and also by the Grant Agency of Charles University in Prague through Grant No. UK/252217.

Contents

Title: Numerical modeling of ice sheet dynamics
Author: Ondřej Souček
Department: Department of Geophysics, Faculty of Mathematics and Physics, Charles University in Prague
Supervisor: Prof. RNDr. Zdeněk Martinec, DrSc.
Supervisor's e-mail address: zdenek@cp.dias.ie
Abstract: The main topic of the presented thesis is the numerical modeling of large-scale ice-sheet evolution over several glacial cycles. For this purpose a "Shallow Ice Approximation" (SIA) is traditionally adopted, a scaling approximation utilizing the fact that the vertical-to-horizontal aspect ratio in ice sheets is typically a small parameter allowing for a perturbation expansion of the governing equations with respect to this parameter. We present a formulation of the boundary value problem for a polythermal ice sheet based on the rational thermodynamics of mixtures and derive its "shallow-ice" form. We then provide a novel SIA-I algorithm for iterative improvement of the SIA and thoroughly test its performance in a series of benchmarks including the ISMIP-HOM benchmark and a realistic simulation for the Dronning Maud Land region, Antarctica. The SIA-I algorithm is implemented to an evolutionary thermo-mechanical numerical ice-sheet model and this model is tested in the SIA regime in two EISMINT benchmarks, EISMINT - Effect of thermo-mechanical coupling and EISMINT - Greenland Ice Sheet models.
Keywords: ice sheet, shallow ice approximation, SIA-I algorithm, ISMIP-HOM

Název práce: Numerické modelování dynamiky pevninských ledovců
Autor: Ondřej Souček
Katedra: Katedra geofyziky, MFF UK v Praze
Vedoucí disertační práce: Prof. RNDr. Zdeněk Martinec, DrSc.
e-mail vedoucího: zdenek@cp.dias.ie
Abstrakt: Hlavním tématem předkládané práce je numerické modelování vývoje pevninských ledovců na časové škále několika dob ledových. Pro tyto účely se tradičně používá tzv. "Shallow Ice Approximation" (SIA). Jedná se o škálovací aproximaci, která využívá skutečnosti, že poměr vertikálního a horizontálního rozměru ledovce je malý, což umožňuje provést perturbační rozvoj řídících rovnic vzhledem k tomuto poměru. Prezentujeme formulaci okrajové úlohy pro tzv. polytermální ledovec založenou na racionální termodynamice směsí a odvozujeme její tvar v rámci dané škálovací aproximace. Popisujeme námi vyvinutý SIA-I algoritmus, který iteračně zpřesňuje SIA, a zevrubně testujeme jeho použitelnost v sérii srovnávacích příkladů ISMIP-HOM a dále v realistické simulaci oblasti Dronning Maud Land v Antarktidě. Algoritmus SIA-I je začleněn do termomechanického numerického modelu evoluce pevninských ledovců a tento model je testován v SIA režimu pro dva EISMINT srovnávací příklady, EISMINT - Efekt termomechanické vazby a EISMINT - Modely grónského pevninského ledovce.
Klíčová slova: pevninský ledovec, shallow ice approximation, SIA-I algoritmus, ISMIP-HOM

Preface

Ice sheets are masses of grounded ice that evolve in regions where climatic conditions allow for the long-term deposition of snow cover. Through a complex process of successive compaction inducing internal structure changes, glacier ice is formed, being one of the many known crystalline phases of solid water. At sufficiently long time scales, due to internal creep, glacier ice behaves as a non-Newtonian fluid. This fact enables us to describe and explain the evolution of ice sheets over such time scales by means of continuum thermomechanics, constructing a nonlinear-fluid model with geometry that is controlled by gravitationally driven creep flow, and by the surface processes of accumulation, ablation and basal sliding.

Ice sheets represent a major part of the Earth's cryosphere and play an important role in the global climate system, affecting it both directly, for instance by creating specific local climatic conditions in the glaciated areas, or constraining ocean circulation, or indirectly by varying the total Earth's albedo, being one of the key parameters controlling the total insolation. Last but not least, they are the biggest reservoirs of freshwater on the Earth, holding more than 76% of its total supplies.

From a geophysical point of view, they provide an important source of information about the Earth's lithosphere and mantle rheological properties through the process of glacial-isostatic adjustment (GIA), which deals with the viscoelastic response of the Earth to long-term variations of ice-sheet load distribution caused by glacial cycles. Over the past several million years, the Earth has been subject to approximately periodic changes in global glaciation with a period of about 100 thousand years, considered to be caused by variations in the Earth's orbital parameters (Milankovich cycles). Each period comprises of a longer period of gradual glaciation, during which the ice masses are concentrated in polar regions, and deform the underlying lithosphere and mantle. A relatively short (10 thousand years) period of deglaciation is too fast for the mantle material to relax in time with the change in surface load, thus resulting in ongoing present-day motions (mostly uplift) in the formerly glaciated regions. These surface motions when properly measured by either modern GPS methods, or indirectly by satellite measurements of gravity-field variations, represent valuable data sets for constraining the rheological parameters of the Earth's lithosphere and mantle.

The growth and retreat of ice sheets is the main forcing in the GIA. To model ice-sheet dynamics is thus of key importance, and has motivated us to develop a numerical model for large-scale ice-sheet evolution. Since ice sheets are typically flat, with a vertical-to-horizontal aspect ratio smaller than $1/100$, a scaling approximation utilizing this fact is often adopted in the glaciological community, resulting in the so-called "shallow-ice" approximation. This approximation of ice flow enables us to quickly compute the ice-sheet velocity field, induced by gravity, semi-analytically, which represents an effective computational tool compared to more accurate but more time-expensive approaches. During the last several years, however, the shallow-ice approximation has been slowly abandoned, as the effects of higher-order dynamics or even the exact solution to the ice-flow problem are looked for, typically, by means of advanced numerical techniques such as finite-elements or spectral methods. The increase of computational demands is, however, enormous compared to the SIA, making it problematic to implement these techniques for large-scale evolutionary ice-sheet models.

We have therefore designed an iterative algorithm capable of successive improvements of the SIA solution towards the exact solution, while still possessing the SIA's computational effectiveness. After being intensively tested, the algorithm was incorporated into a large-scale ice-sheet model, providing thus an alternative numerical tool between the two extremes - fast but inaccurate shallow-ice approximation on the one hand and accurate but slow advanced numerical techniques on the other. Our approach provides the SIA solution in regions where it is sufficiently accurate, and enables us to significantly improve the solution in regions where the assumption of "shallowness" becomes violated.

To give some insight into the origin of the algorithm, in Chapter 1 we first outline a brief summary of the ice-sheet continuum thermodynamics, based on the theory of rational thermodynamics of mixtures. For the presented equations we provide their "shallow-ice" counterparts in Chapter 2 by deriving systematically their leading-order (in the scaling flatness parameter) form. A novelty in the derivation is that we consider general curvilinear orthogonal coordinates, obtaining thus a whole class of shallow-ice approximations - its realization for any particular coordinate system is given just by evaluating certain geometrical quantities. This can be useful for large-scale models where the effects of the Earth's surface curvature cannot be neglected. In Chapter 3, we introduce a novel SIA-I iterative algorithm which successively improves the shallow-ice solution. We verify its performance via several benchmarks such as the ISMIP-HOM (Ice-Sheet Model Intercomparison Project - Higher-Order Models) benchmark, which focused on evaluating the "higher-order" (non-shallow) effects in ice-sheet dynamics, and by performing a realistic simulation using the field data from Antarctica. A simplified convergence analysis for the SIA-I algorithm is presented in the Appendix A. In Chapter 4, we provide a detailed description of the ice-sheet numerical model, focusing on the free-surface evolution and the implementation of the heat transport equation in an ice sheet. Both numerical features are validated by the benchmarks - geometry evolution by performing a reference run with an "exact" finite-element model and the heat transport together with the effects of thermomechanical coupling by going through some of the EISMINT (European Ice Sheet Modeling INiTiative) simulations. In Chapter 5, the numerical model is run for a series of three benchmarks for Greenland Ice-Sheet models, including a paleo-climatic simulation over the two last glacial cycles and a prognostic greenhouse warming scenario.

Chapter 1

Glacier Continuum Thermomechanics

1.1 Introduction

In this section, we briefly outline the mathematical apparatus used to describe the essential features of glacier physics within the framework of continuum mechanics and thermodynamics. As usual, when dealing with a real-world physical phenomena, the presented model must be understood as only an idealized simplification with its relevance and validity restricted to certain limits in spatial and time scales.

In terms of macroscopic glaciology, the problem of ice-sheet evolution and flow may be viewed as a gravitationally driven flow of a fluid with a nonlinear viscosity, generally depending on both the strain-rate and temperature. In addition, it is a problem with a free-boundary, that is, the glacier's geometry itself is a part of the solution.

A delicate question arises whether to consider ice as a single-component material, that is dealing with pure ice only, or to take into account the presence and effects of some tracers, for instant percolating liquid water in the so-called temperate-ice zones, or the salinity transport in marine ice-shelves. Both effects require us to adopt a more complex approach of mixture continuum mechanics and thermodynamics. In either case, we may, however, formulate the mass-balance equation, linear and angular momentum balance equations and balance of energy, together with appropriate boundary conditions (both dynamic and kinematic) at the upper free surface, at the glacier's base and at all internal discontinuities.

In the following theoretical summary, we confine ourselves to a model of a polythermal ice sheet, which is defined by the presence of two types of regions: temperate-ice zones are defined by the presence of a certain amount of liquid water, and the cold-ice zones, where only pure ice is considered.

1.2 Cold ice sheet

Consider first a simpler case, where the whole ice sheet is assumed to be composed only of pure glacier ice. The glacier's geometry will be captured by prescribing two intersecting surfaces – the upper free surface and lower glacier bed, given e.g. in Cartesian coordinates (i.e. x_1, x_2, x_3, where x_1, x_2 are the horizontal coordinates and x_3 is the vertical), by

$$x_3 = f_s(x_1, x_2, t) \,, \tag{1.1}$$

$$x_3 = f_b(x_1, x_2, t) \,, \tag{1.2}$$

where f_s and f_b represent the upper free surface and the lower glacier bed, respectively, or, more generally, by implicit functions for the glacier surface and bed, respectively, $F_s(x_1, x_2, x_3, t)$ and $F_b(x_1, x_2, x_3, t)$:

$$F_s(x_1, x_2, x_3, t) = 0 \,, \tag{1.3}$$

$$F_b(x_1, x_2, x_3, t) = 0 \,, \tag{1.4}$$

where: $F_s(x_1, x_2, x_3, t) = x_3 - f_s(x_1, x_2, t)$, $F_b(x_1, x_2, x_3, t) = x_3 - f_b(x_1, x_2, t)$. Taking the total time derivative of (1.3), we obtain

$$\frac{\partial F_s}{\partial t} + \vec{\nu} \cdot \mathrm{grad} F_s = 0 \,, \tag{1.5}$$

where $\vec{\nu}$ is the velocity of surface movement. It is convenient to rewrite this equation by introducing the material (ice) surface velocity $\vec{v}$

$$\frac{\partial F_s}{\partial t} + \vec{v} \cdot \mathrm{grad} F_s = (\vec{v} - \vec{\nu}) \cdot \mathrm{grad} F_s \,, \tag{1.6}$$

or, alternatively, by the (upward-oriented) surface normal vector $\vec{n}_s$,

$$\vec{n}_s := \frac{\mathrm{grad} F_s}{\|\mathrm{grad} F_s\|} \,, \tag{1.7}$$

such that

$$\frac{\partial F_s}{\partial t} + \vec{v} \cdot \mathrm{grad} F_s = (\vec{v} - \vec{\nu}) \cdot \vec{n}_s \|\mathrm{grad} F_s\| \,. \tag{1.8}$$

The term $(\vec{v} - \vec{\nu}) \cdot \vec{n}_s$ is the normal flow of material through the upper free surface, and represents the mass production or loss at the free surface by climatological processes. It is usually prescribed by the accumulation-ablation conditions. We define the accumulation-ablation function (positive for ablation) as

$$a^s := (\vec{v} - \vec{\nu}) \cdot \vec{n}_s \,, \tag{1.9}$$

and finally express the kinematic condition as

$$\frac{\partial F_s}{\partial t} + \vec{v} \cdot \mathrm{grad} F_s = a^s \|\mathrm{grad} F_s\| \,. \tag{1.10}$$

If, for instance, the explicit (Cartesian) description of the free-surface is used, the evolution equation for the free surface reads as:

$$-\frac{\partial f_s}{\partial t} + \vec{v} \cdot \left(-\frac{\partial f_s}{\partial x_1}, -\frac{\partial f_s}{\partial x_2}, 1 \right) = a^s \sqrt{1 + \left(\frac{\partial f_s}{\partial x_1} \right)^2 + \left(\frac{\partial f_s}{\partial x_2} \right)^2} \,. \tag{1.11}$$

We will assume that the glacier bed evolution, i.e. $F_b(x_1, x_2, x_3, t)$ is known, with the glacier bed either being rigid and not moving, hence F_b stands for the prescribed glacier-bed topography, or F_b is given by the solution of the equations for viscoelastic deformational response of the underlying bed to ice-mass load changes.

1.2.1 Field equations

The behavior of a cold ice-sheet may be derived from the single-component conservation laws that read in the Eulerian description as follows (Hutter, 2004).

General balance laws

$$\begin{aligned}
\frac{\partial \rho}{\partial t} + \mathrm{div}(\rho \vec{v}) &= 0 && \ldots && \text{mass balance ,} && (1.12)\\
\rho \dot{\vec{v}} &= \mathrm{div}\boldsymbol{\tau} + \rho \vec{g} && \ldots && \text{linear momentum balance ,} && (1.13)\\
\boldsymbol{\tau} &= \boldsymbol{\tau}^T && \ldots && \text{angular momentum balance ,} && (1.14)\\
\rho \dot{\varepsilon} &= \boldsymbol{\tau} : \boldsymbol{d} - \mathrm{div}\vec{q} + \rho h && \ldots && \text{internal energy balance ,} && (1.15)
\end{aligned}$$

where the quantities used are: ρ - density, $\vec{v}$ - velocity vector, $\boldsymbol{\tau}$ - Cauchy stress tensor, ε - internal energy density, $\boldsymbol{d}$ - strain-rate tensor, $\vec{q}$ - heat flux vector, h - heat supply. The dot operator $\dot{()}$ stands for the material time derivative - $\dot{()} := \frac{\partial()}{\partial t} + \vec{v} \cdot \mathrm{grad}()$.

In order to make the above system of general balance laws solvable, it is necessary to specify the particular material by prescribing appropriate constitutive equations.

The **rheology** is specified as follows. Despite even pure ice is a very complex substance having 13 known phases and several dislocation mechanisms that contribute to the final stress–strain-rate constitutive equation (Hutter, 1983), for glaciological modeling, an idealization by a non-Newtonian incompressible fluid with uniform density is mostly used. To specify this fluid, the stress tensor is split into an isotropic and a deviatoric part:

$$\boldsymbol{\tau} = -p\boldsymbol{I} + \boldsymbol{\sigma} \ , \tag{1.16}$$

where the deviatoric part is described by **Glen's flow law** (e.g. Paterson, 1981):

$$\boldsymbol{\sigma} = 2\eta \boldsymbol{d}, \ \ \eta = \frac{1}{2}\mathcal{A}(T)^{-1/n} d_{II}^{(1-n)/n} \ , \ n = 3 \ , \tag{1.17}$$

or, inversely,

$$\boldsymbol{d} = \mathcal{A}(T)\sigma_{II}^{n-1}\boldsymbol{\sigma} \ , \tag{1.18}$$

where the second invariants d_{II}, σ_{II} are given by[1]

$$d_{II} = \sqrt{\frac{\boldsymbol{d}_{ij}\boldsymbol{d}_{ij}}{2}} \ , \qquad \sigma_{II} = \sqrt{\frac{\boldsymbol{\sigma}_{ij}\boldsymbol{\sigma}_{ij}}{2}} \ , \tag{1.19}$$

and the strain-rate tensor $\boldsymbol{d}$ is defined as

$$\boldsymbol{d} = \frac{1}{2}\left(\mathrm{grad}\vec{v} + \mathrm{grad}^T\vec{v}\right) \ . \tag{1.20}$$

The (absolute) temperature dependence of the rate-factor $\mathcal{A}(T)$ is of the Arrhenius type

$$\mathcal{A}(T) = A\exp\left(-\frac{Q}{k_B T}\right) \ , \tag{1.21}$$

often corrected for the pressure-dependence of the melting temperature (see (1.48)):

$$\mathcal{A}(T,p) = A\exp\left(-\frac{Q}{k_B T^\star}\right) \ , \tag{1.22}$$

with k_B the Boltzmann constant, and $T^\star$ the absolute temperature corrected for the pressure melting point, $T^\star = (T + C_{Cl}p)$, C_{Cl} is the constant from (1.48), and p is the pressure. The activation parameter Q and the constant A may, in general, depend on the considered temperature range.

[1] The Einstein's summation convention is used if not otherwise stated.

Note that, in some applications such as in planetary science, a simple Newtonian rheological model of ice with only temperature-dependent viscosity is considered.

The **constitutive equation for internal energy density** is specified by a simple, only temperature-dependent model of the form

$$\dot{\varepsilon}(T) = c_v(T)\,\dot{T}\,, \tag{1.23}$$

where $c_v(T)$ is the heat capacity at a constant volume. For the **heat flux**, we assume the traditional Fourier law

$$\vec{q} = -k(T)\,\mathrm{grad}T\,, \tag{1.24}$$

with the heat conductivity $k(T)$. For ice sheet flow, we do not consider any internal heat sources, and put $h \equiv 0$ in (1.15).

By these constitutive relations, the general balance laws may be rewritten as follows.

The **mass balance** under the assumption of uniform ice density is expressed as

$$\mathrm{div}\vec{v} = 0\,. \tag{1.25}$$

The **linear momentum balance** is written as

$$\rho\dot{\vec{v}} = -\mathrm{grad}p \;+\; \mathrm{div}\boldsymbol{\sigma} + \rho\vec{g}\,, \qquad \boldsymbol{\sigma} = 2\eta(d_{II}, T)\boldsymbol{d}\,, \tag{1.26}$$

where the inertial term can be neglected due to a very small Froude number (see Section 2.3 on scaling):

$$\vec{0} = -\mathrm{grad}p \;+\; \mathrm{div}\boldsymbol{\sigma} + \rho\vec{g}\,. \tag{1.27}$$

The **energy balance** is given by

$$\rho c_v\dot{T} = \boldsymbol{\sigma} : \boldsymbol{d} + \mathrm{div}(k(T)\mathrm{grad}T)\,. \tag{1.28}$$

1.2.2 Boundary conditions

The boundary conditions closing the system of equations are found for the upper free surface and the glacier bed. The upper **free surface** ($x_3 = f_s(x_1, x_2, t)$ or $F_s(x_1, x_2, x_3, t) = 0$), is assumed traction-free, giving

$$-p_{atm}\vec{n}_s = -p\vec{n}_s + \boldsymbol{\sigma}\cdot\vec{n}_s, \tag{1.29}$$

where $\vec{n}_s := \frac{\mathrm{grad}F_s}{\|\mathrm{grad}F_s\|}$, is by definition positive upwards and p^{atm} is the atmospheric pressure. Typically, the temperature is prescribed at the upper surface as climatological input data together with the accumulation ablation function a^s (defined by (1.9)):

$$T = T^s(x_1, x_2, f_s(x_1, x_2, t), t)\,, \qquad a^s = a^s(x_1, x_2, f_s(x_1, x_2, t), t)\,. \tag{1.30}$$

At the **glacier bed** ($x_3 = f_b(x_1, x_2, t)$ or $F_b(x_1, x_2, x_3, t) = 0$), either **no-slip** is assumed in the case of frozen bed conditions ($T < T_m(p)$), with T_m, the pressure-dependent melting temperature given by (1.48), i.e.:

$$\vec{v} - \vec{\nu}_b = \vec{0}\,, \tag{1.31}$$

or a **sliding law** is specified for the sliding velocity $\vec{v}^{sl}$, defined by

$$\vec{v}^{sl} := (\vec{v} - \vec{\nu}_b) - \vec{n}_b(\vec{v} - \vec{\nu}_b)\cdot\vec{n}_b\,, \tag{1.32}$$

where the surface velocity $\vec{\nu}_b$ equals the bedrock material velocity at the glacier base. Usually the sliding law may be written in the form (Blatter et al., 1998)

$$\beta^2 \vec{t}_b \cdot \vec{v}^{sl} = -\vec{t}_b \cdot \boldsymbol{\sigma} \cdot \vec{n}_b \,, \tag{1.33}$$

where $\vec{t}_b$ is a vector tangent to the glacier bed, $\vec{n}_b$ is the normal to the glacier bed $\vec{n}_b := -\frac{\mathrm{grad} F_b}{\|\mathrm{grad} F_b\|}$ (positive downwards) and $\beta(\vec{n}_b \cdot \boldsymbol{\tau} \cdot \vec{n}_b, T, ...)$ is the sliding coefficient which is, typically, a function of the total normal stress, temperature, and the roughness of the underlying bedrock. In addition, the normal component of the relative velocity is assumed to vanish

$$(\vec{v} - \vec{\nu}_b) \cdot \vec{n}_b = 0 \,, \tag{1.34}$$

which expresses the impermeability of the bedrock to ice.

The **energy equation** is completed by prescribing the geothermal heat flux at the glacier bed

$$\vec{q} = \vec{q}^{geo}(x_1, x_2, f_b(x_1, x_2, t), t) \,. \tag{1.35}$$

It still remains to be discussed possible melting at the glacier's bed (we assume that the rest of the glacier has a temperature below the melting temperature of ice), which requires us to consider the energy balance of a melting surface. This case will be obtained as a limiting case of a polythermal ice sheet with an infinitely thin temperate-ice layer above the glacier bed. This general situation is addressed below.

1.3 Polythermal ice sheet

The presence of liquid water in a glacier cannot, in certain cases, be ignored since its effect on both the rheology of the ice and the subglacial environment (roughness) becomes important. Typical examples are small alpine glaciers at lower altitudes, or fast-flowing ice streams in ice sheets. Although the modeling of glacial drainage systems remains an open challenge due to its enormous complexity and time variability, some basic insights may be gained by treating water content as a diluted component in the ice matrix. This topic has been studied and modelled by e.g. Hutter & Greve (1983), and Souček & Martinec (2005). The approach of the latter is new in terms of the formulation of the governing equations by means of rational thermodynamics. The diffusive water flux is expressed relative to the ice velocity, contrary to the traditional treatment (e.g. Greve, 1997) where barycentric velocity is used instead. Our approach provides a better insight in the generalizations appearing in the constitutive equations for temperate ice, and allows the possibility of further extension. For example, the diffusive water flux is obtained as a limit of the equation of motion for the water component.

We first summarize our treatment of temperate-ice physics. The detailed derivation and explanations of the presented approach can be found in Souček & Martinec (2005). We assume that, in the interior of an ice sheet, there are two types of regions - *cold-ice zones* and *temperate-ice zones*. The former is formed by a pure glacier ice and the latter contains a small amount of liquid water. A sketch of a polythermal ice sheet is presented in Fig. 1.1.

We assume that each zone of temperate ice is separated from the surrounding cold ice by a smooth surface (cts = cold-temperate ice transition surface) given by implicit or explicit equations:

$$F_{cts}(x_1, x_2, x_2, t) = 0 \,, \qquad \text{or} \qquad x_3 = f_{cts}(x_1, x_2, t) \,.$$

The problem of a so-called polythermal (containing both cold and temperate ice zones) ice sheet therefore comprises not only additional temperate ice-physics, but also the evolution problem for the contact surfaces.

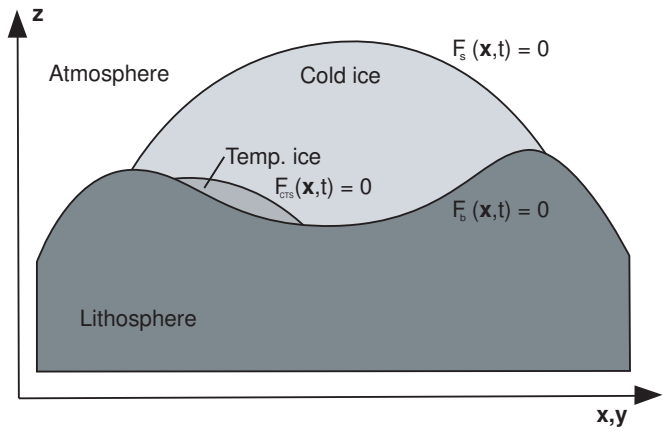

Figure 1.1: A sketch of a polythermal ice sheet.

As in the case of a cold ice sheet, the upper free surface is described by

$$F_s(x_1, x_2, x_3, t) = 0 \,, \qquad \text{or} \qquad x_3 = f_s(x_1, x_2, t) \,,$$

and the glacier base by

$$F_b(x_1, x_2, x_3, t) = 0 \,, \qquad \text{or} \qquad x_3 = f_b(x_1, x_2, t) \,.$$

For all the surfaces, the unique correspondence between the (Cartesian) explicit and implicit forms are assumed

$$F_s(x_1, x_2, x_3, t) = x_3 - f_s(x_1, x_2, t) \,, \tag{1.36}$$
$$F_b(x_1, x_2, x_3, t) = x_3 - f_b(x_1, x_2, t) \,, \tag{1.37}$$
$$F_{cts}(x_1, x_2, x_3, t) = x_3 - f_{cts}(x_1, x_2, t) \,. \tag{1.38}$$

1.3.1 Field equations

For the **cold-ice zone**, the balance laws listed in the previous section for cold ice sheets remain unchanged. However, they must now be accompanied by the boundary conditions at the contact with the temperate ice. Additional details are given below.

In the **temperate-ice zone**, ice is treated as a two-component mixture of ice and water and the continuum mixture approach is adopted to formulate the balance laws for mass, linear and angular momentum and energy. As was pointed out by Hutter (2004), various subclasses of mixture theories exist which differ in their treatment of particular balance laws, where one may prescribe a particular balance law for each mixture component or take one global balance law for the mixture as a whole. Here, we adopt an approach between the two limiting strategies, namely, the balance laws of mass and momenta are considered for each component separately, whilst the energy balance is considered for the ice-water mixture as a whole.

The **mass balance** is derived as follows. Ice-water mixture is considered incompressible, which is justified by the fact that (i) the water content does not exceed few percent and (ii) the relatively small difference between the pure-ice and the pure-water densities. The uniform mixture density is denoted ρ. Ice and water are moving with velocities $\vec{v}$ and $\vec{v}_w$, respectively. Water transport is then described by a relative diffusive water flux $\vec{j}$,

$$\vec{j} := \rho w(\vec{v}_w - \vec{v}) \,, \tag{1.39}$$

where w is the water mass fraction (mass concentration).

Despite the mixture as a whole and the ice specifically remaining incompressible, the mass fraction of ice can be altered due to the process of melting or refreezing. Consequently, the ice-velocity field is no-longer divergence-free and the **mass balance for ice** reads as

$$\mathrm{div}\vec{v} = -\mathrm{div}\left(\frac{\vec{j}}{\rho}\right) . \tag{1.40}$$

The **mass balance for water** can be given in terms of the water mass fraction w,

$$\rho\dot{w} + \mathrm{div}\vec{j} = m_w , \tag{1.41}$$

where $\dot{()} := \frac{\partial()}{\partial t} + \vec{v}\cdot\mathrm{grad}()$ is the material time derivative with respect to ice velocity, and m_w is the water production rate (positive for melting and negative for refreezing), resulting from the balance of energy below.

The **linear momentum balance for ice** can be written in the form

$$\rho(1-w)\rho\dot{\vec{v}} + \rho w\dot{\vec{v}}_w^{(w)} = -\mathrm{grad}p + \mathrm{div}\boldsymbol{\sigma} + \rho\vec{g} , \tag{1.42}$$

where on the left-hand side, $\dot{\vec{v}}_w^{(w)} := \frac{\partial\vec{v}_w}{\partial t} + \vec{v}_w\cdot\mathrm{grad}\vec{v}_w$. The inertial forces will be omitted, as they are very small (which we will justify later by evaluating the corresponding Froude number) and the balance law takes the form

$$\vec{0} = -\mathrm{grad}p + \mathrm{div}\boldsymbol{\sigma} + \rho\vec{g} . \tag{1.43}$$

The **linear momentum balance for the water component** can then be written as

$$\vec{j} = -\alpha_1\mathrm{grad}w + \alpha_2(\rho w\vec{g} - \mathrm{grad}(pw)) , \tag{1.44}$$

which is, in fact, a constitutive equation for the diffusive water flux $\vec{j}$. The term pw can be thought of as one possible realization of the partial water pressure. A reasonable extension might be to replace pw by a more general partial water pressure p_w, defined by the appropriate constitutive equation. Then, (1.44) would read as

$$\vec{j} = -\alpha_1\mathrm{grad}w + \alpha_2(\rho w\vec{g} - \mathrm{grad}p_w) . \tag{1.45}$$

Such a generalization would require modifying the energy balance equation (1.49). Nevertheless, we will not consider this more general case here.

The **angular momentum balance for ice** states the symmetry of the partial Cauchy stress tensor deviator $\boldsymbol{\sigma}$:

$$\boldsymbol{\sigma} = \boldsymbol{\sigma}^T . \tag{1.46}$$

There is no need to consider this equality for the **water** component, because for water the only stress contribution that remains in the equations comes from the partial water pressure, which is symmetric already by definition.

The **energy balance** is considered for the mixture as a whole. Contrary to the cold-ice zone, it does not have a form of an evolution equation for the temperature, as T is no longer an independent field variable in this case. In the temperate-ice zone, ice is, by definition, at the pressure-melting point and the temperature is obtained by solving the Clausius-Clapeyron equation

$$T = T_m(p) , \tag{1.47}$$

where a linear relationship is often assumed (Greve, 1997):

$$T_m(p) = T_{m0} - C_{Cl}p \ , \tag{1.48}$$

with C_{Cl} and T_{m0} constants.

The role of temperature is now replaced by the water content w, as the energy release is associated with melting or refreezing of ice and water, respectively. The energy equation then specifies the rate of water production by

$$Lm_w = \boldsymbol{\sigma} : \boldsymbol{d} - \mathrm{div}\vec{q} - \rho c_v \dot{T}_m + \frac{\vec{j}}{\rho} \cdot (\rho\vec{g} - \mathrm{grad}p) \ , \tag{1.49}$$

where L is the latent heat of melting of ice and $\boldsymbol{d}$ is the strain-rate tensor of ice $\boldsymbol{d} = \frac{1}{2}(\mathrm{grad}\vec{v} + \mathrm{grad}^T\vec{v})$, and the heat flux $\vec{q}$ is given by the Fourier law

$$\vec{q} = -k(T_m(p))\ \mathrm{grad}T_m(p) \ . \tag{1.50}$$

The **rheology** is specified as follows. Glen's flow law as outlined in (1.17) is again considered for ice with the rate factor depending on the water fraction w, since the lubricating effect of water enhances the deformational flow rate

$$\boldsymbol{\sigma} = 2\eta\boldsymbol{d}, \ \ \eta = \frac{1}{2}\mathcal{A}(w)^{-1/n} d_{II}^{(1-n)/n} \ , \ n = 3 \ , \tag{1.51}$$

or, inversely,

$$\boldsymbol{d} = \mathcal{A}(w)\sigma_{II}^{n-1}\boldsymbol{\sigma} \ . \tag{1.52}$$

The water-content dependence of the rate-factor $\mathcal{A}(w)$ is usually assumed to be linear

$$\mathcal{A}(w) = A(1 + \gamma w)\exp\left(-\frac{Q}{k_B T_{0m}}\right) \ , \tag{1.53}$$

where Q is the activation parameter, k_B the Boltzmann constant, A and γ constants, and T_{m0} the constant from (1.48).

1.3.2 Boundary conditions

Apart from the boundary conditions at the upper free surface and the bottom of the glacier, for polythermal ice sheets, we need to also prescribe appropriate interface conditions at the contact between the cold and temperate zones. Souček & Martinec (2005) derived these conditions with the help of the mixture theory, assuming that (i) all mixture components are present at both sides of the interface, and (ii) by limiting the appropriate concentrations to zero.

Free surface

The upper surface is the contact surface of either cold or temperate ice with air. A sketch of the geometry of the free surface is depicted in Fig. 1.2. Describing the free surface by an implicit equation,

$$F_s(x_1, x_2, x_3, t) = 0 \ , \tag{1.54}$$

its evolution is governed by a kinematic equation

$$\frac{\partial F_s}{\partial t} \ + \ \vec{v} \cdot \mathrm{grad}F_s \ = \ (\vec{v} - \vec{\nu}_s) \cdot \vec{n}_s \, \|\mathrm{grad}F_s\| \ , \tag{1.55}$$

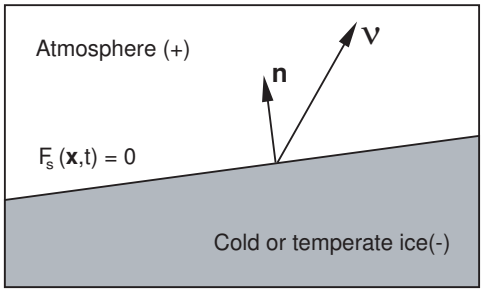

Figure 1.2: The free-surface geometry.

where ν_s is the velocity of the free surface (generally non-material), and $\vec{n}_s := \frac{\mathrm{grad} F_s}{\|\mathrm{grad} F_s\|}$, is the surface normal being positive upwards.

The dynamic boundary conditions following from the general mixture balance laws are as follows:

- *Cold ice - air boundary* (water is not present)
  This case was discussed in the previous section about single-component ice.
- *Temperate ice - air boundary* (water present)
  - *Mass-jump condition*

    The ice component is given by

$$(1-w)(\vec{v}-\vec{\nu}_s)\cdot\vec{n}_s \;=\; -\frac{a^s}{\rho}\;, \tag{1.56}$$

    where a^s is the surface accumulation-ablation function, prescribed by climatological data,

$$a^s = a^s(x_1, x_2, f_s(x_1, x_2, t), t) \tag{1.57}$$

    The water component is given by

$$\vec{j}\cdot\vec{n}_s \;=-\,\mathcal{P}^s\;, \tag{1.58}$$

    where $\mathcal{P}^s$ is the surface-melted water and liquid precipitation that enters the glacier volume, again assumed to be given as an independent input information by climatology,

$$\mathcal{P}^s = \mathcal{P}^s(x_1, x_2, f_s(x_1, x_2, t), t)\;. \tag{1.59}$$

  - *Linear-momentum jump condition*

$$-p_{atm}\vec{n}_s \;=\; -p\vec{n}_s \;+\; \boldsymbol{\sigma}\cdot\vec{n}_s\;, \tag{1.60}$$

    where p_{atm} is the *atmospheric pressure*, p is the sum of partial pressures of ice and water, and $\boldsymbol{\sigma}$ is the ice Cauchy stress deviator.
  - *Energy-jump condition*
    Since the temperature in the temperate part of a glacier is fully determined by the pressure according to the Clausius-Clapeyron equation (1.48), an appropriate boundary condition is (neglecting the surface friction)

$$0 \;=\; m^s_w(\varepsilon_w-\varepsilon_i) \;+\; [\vec{q}]^+_-\cdot\vec{n}_s\;, \tag{1.61}$$

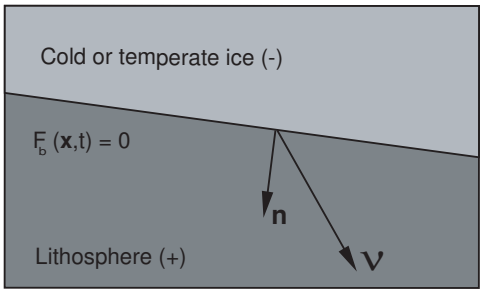

Figure 1.3: The base geometry.

which relates the discontinuity in the heat flux $[\vec{q}]^+_-$ at the surface with the surface melting rate m^s_w, where ε_i and ε_w are internal-energy densities of ice and water, respectively. We will, however, assume the melting rate is given by climatological input data (included already in the ice-accumulation function a^s and water precipitation rate $\mathcal{P}^s$), therefore we do not need to specify any boundary condition, neither for the temperature, nor for the heat flux.

The base

The base geometry is depicted in Fig. 1.3. Similarly, as for the cold-ice glacier, we assume that the base geometry is given a-priori, either it is rigid and does not change in time, or its time evolution is influenced by independent geophysical processes, such as the glacial-isostatic adjustment or tidal loading. We thus assume to know the function

$$F_b(x_1, x_2, x_3, t) = 0\ . \tag{1.62}$$

In the case of the dynamic conditions, we again distinguish between the two cases, cold ice – bedrock boundary and temperate ice – bedrock boundary.

- *Cold ice – bedrock interface* (water is not present)
  This situation has been discussed in the section about single-component ice-bedrock conditions (Section 1.2).

- *Temperate ice – bedrock interface*

  - *Mass-jump condition*
    The ice component is expressed by

$$(1-w)(\vec{v}-\vec{\nu}_b)\cdot\vec{n}_b \;=\; \frac{m^b_w}{\rho}\ , \tag{1.63}$$

    where m^b_w is the rate of surface meltwater production at the glacier base, and the normal $\vec{n}_b := \frac{-\mathrm{grad}F_b}{\|\mathrm{grad}F_b\|}$ is now pointing downwards and $\vec{\nu}_b$ is the velocity of the glacier base.

    The water component is described by

$$\vec{j}\cdot\vec{n}_b \;=\; o^b - \frac{m^b_w}{1-w}\ , \tag{1.64}$$

    where the *water-outflow function* o^b has been introduced to describe the rate of the water-mass flow penetrating into the bedrock, and has to be prescribed independently in the form

$$o^b = o^b(x_1, x_2, f_b(x_1, x_2, t), t)\ . \tag{1.65}$$

- *The linear-momentum jump condition* is expressed as

$$\boldsymbol{\tau}_b \cdot \vec{n}_b = -p\vec{n}_b + \boldsymbol{\sigma} \cdot \vec{n}_b \,, \tag{1.66}$$

where p is the sum of the partial pressures of ice and water, $\boldsymbol{\sigma}$ is the deviator of Cauchy stress of ice, and $\boldsymbol{\tau}_b$ is the Cauchy stress tensor in the underlying bedrock.

- *Sliding law*
Setting naturally the surface velocity $\vec{\nu}_b$ equal to the bedrock velocity at the glacier base, the sliding velocity is defined as

$$\vec{v}^{sl} := (\vec{v} - \vec{\nu}_b) - \vec{n}_b(\vec{v} - \vec{\nu}_b) \cdot \vec{n}_b \,, \tag{1.67}$$

while the sliding law typically has the form

$$\beta^2 \vec{t}_b \cdot \vec{v}^{sl} = -\vec{t}_b \cdot \boldsymbol{\sigma} \cdot \vec{n}_b \,, \tag{1.68}$$

where $\vec{t}_b$ is a vector tangent to the glacier bed, $\vec{n}_b$ is the normal to the glacier bed and $\beta(\vec{n}_b \cdot \boldsymbol{\tau} \cdot \vec{n}_b, w, T_m(p), ...)$ is the sliding coefficient, now also dependent on the water content w. The term $\vec{n}_b \cdot \boldsymbol{\tau} \cdot \vec{n}_b$ stands for the total normal pressure at the glacier base, which is equal to the sum of partial pressures and $\vec{n}_b \cdot \boldsymbol{\sigma} \cdot \vec{n}_b$.

- *The energy-jump condition* as derived by Souček & Martinec (2005), reads as

$$0 = m_w^b (\varepsilon_w - \varepsilon_i) + \vec{v} \cdot \boldsymbol{\tau}_i \cdot \vec{n}_b + \vec{v}_w^- \cdot \boldsymbol{\tau}_w^- \cdot \vec{n}_b - \vec{\nu}_b \cdot \boldsymbol{\tau}_b \cdot \vec{n}_b + [\vec{q}]_-^+ \cdot \vec{n}_b \,, \tag{1.69}$$

where $\boldsymbol{\tau}_i$ and $\boldsymbol{\tau}_w$ are partial stress-tensors of ice and water, respectively. This relation can be further rewritten with the use of the linear momentum jump condition (1.66). If we keep only the partial water pressure contribution to the water partial stress tensor $\boldsymbol{\tau}_w$, that is write $\boldsymbol{\tau}_w \simeq -p_w \mathbf{I}$, and again, by p denote the sum of partial pressures p_i and p_w, and neglect the friction work associated with the diffusion of water in ice, that is, omit the term $(\vec{v}_w^- - \vec{v}) \cdot \boldsymbol{\tau}_w^- \cdot \vec{n}_b$, we arrive at

$$0 = m_w^b(\varepsilon_w - \varepsilon_i) + (\vec{v} - \vec{\nu}^b) \cdot (-p\mathbf{I} + \boldsymbol{\sigma}) \cdot \vec{n}_b + [\vec{q}]_-^+ \cdot \vec{n}_b \,. \tag{1.70}$$

Employing the definition of sliding velocity (1.67), together with (1.63) gives

$$0 = m_w^b \left(\varepsilon_w - \varepsilon_i + \frac{\vec{n}_b \cdot (-p\mathbf{I} + \boldsymbol{\sigma}) \cdot \vec{n}_b}{\rho(1-w)} \right) + \vec{v}^{sl} \cdot \boldsymbol{\sigma} \cdot \vec{n}_b + [\vec{q}]_-^+ \cdot \vec{n}_b \,. \tag{1.71}$$

It is convenient to express the difference of specific internal energies of ice and water by means of latent heat of melting of ice L. Considering simple equilibrium thermodynamics, it holds that (Souček & Martinec, 2005):

$$\varepsilon_w - \varepsilon_i = L - p \left(\frac{1}{\rho_w^{mat}} - \frac{1}{\rho_i^{mat}} \right) \,, \tag{1.72}$$

where the second term corresponds to the work done during the phase change due to different specific volumes of the two phases, and where ρ_i^{mat} and ρ_w^{mat} are material densities of pure ice and pure water. In a large ice sheet, this term is considerably smaller than the latent heat, and so it may be neglected, with the energy jump condition simplified to

$$0 = m_w^b \left(L + \frac{\vec{n}_b \cdot (-p\mathbf{I} + \boldsymbol{\sigma}) \cdot \vec{n}_b}{\rho(1-w)} \right) + \vec{v}^{sl} \cdot \boldsymbol{\sigma} \cdot \vec{n}_b + [\vec{q}]_-^+ \cdot \vec{n}_b \,, \tag{1.73}$$

with the geothermal heat flux prescribed by independent information

$$\vec{q}^+ := \vec{q}^{geo}(x_1, x_2, f_b(x_1, x_2, t), t) \,. \tag{1.74}$$

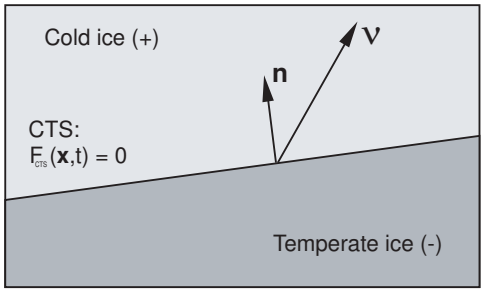

Figure 1.4: The cold-temperate ice transition surface (cts) geometry.

The cold-temperate ice transition surface

The kinematic equation at the cold-temperate ice transition surface cts, (see Fig. 1.4) is

$$\frac{\partial F_{cts}}{\partial t} \; + \; \vec{v}^{-} \cdot \mathrm{grad} F_{cts} \; = \; (\vec{v}^{-} - \vec{\nu}^{cts}) \cdot \vec{n}_{cts} \, \| \mathrm{grad} F_{cts} \| \; , \tag{1.75}$$

where the superscripts $()^+$ and $()^-$ denote the value of a quantity at the corresponding side of the oriented surface (the sign convention is shown in Fig. 1.4).

The dynamic transition conditions are as follows:

- *Mass-jump condition*
  For the ice component the ice velocity is assumed to be continuous across the *cts*, i.e.

  $$\vec{v}^{+} = \vec{v}^{-} = \vec{v} \, , \tag{1.76}$$

  hence the ice-mass jump condition reads

  $$w^{-} (\vec{v} - \vec{\nu}_{cts}) \cdot \vec{n}_{cts} \; = \; - \frac{m_w^{cts}}{\rho} \; , \tag{1.77}$$

  where $\vec{\nu}_{cts}$ is the velocity of the cts surface and the $\vec{n}_{cts} := \frac{\mathrm{grad} F_{cts}}{\| \mathrm{grad} F_{cts} \|}$ is the unit normal, and m_w^{cts} is the rate of meltwater production at the cts.
  The water component is given by

  $$\vec{j}^{-} \cdot \vec{n}_{cts} \; = \; 0 \, . \tag{1.78}$$

- *The linear-momentum jump condition* is expressed as

  $$- p^{+} \vec{n}_{cts} \; + \; \boldsymbol{\sigma}^{+} \cdot \vec{n}_{cts} \; = \; - p^{-} \vec{n}_{cts} \; + \; \boldsymbol{\sigma}^{-} \cdot \vec{n}_{cts} \; , \tag{1.79}$$

  with p^- the sum of partial pressures of ice and water in the temperate region.

- For *the energy-jump condition*, the temperature is continuous,

  $$T^{+} \; = \; T^{-} \; , \tag{1.80}$$

  and the rate of ice surface production is given by

  $$0 \; = \; m_w^{cts} (\varepsilon_w - \varepsilon_i) \; + \; [\vec{q}]_{-}^{+} \cdot \vec{n}_{cts} \, . \tag{1.81}$$

  Performing the same simplification as in the case of (1.72), we may rewrite this condition using the latent heat of melting L as

  $$0 \; = \; m_w^{cts} L \; + \; [\vec{q}]_{-}^{+} \cdot \vec{n}_{cts} \, . \tag{1.82}$$

1.4 Traditional approach

We briefly summarize the main differences between the above presented approach and the traditional approach and comment on advantages and disadvantages of both. In the traditional approach (e.g. Greve, 1997), a barycentric velocity $\vec{v}_b$ is introduced by

$$\rho\vec{v}_b := \rho_i\vec{v}_i + \rho_w\vec{v}_w \ , \tag{1.83}$$

where the ice and water densities ρ_i, ρ_w, express the mass of particular component in a unit-volume of the mixture, and thus do not coincide with the usual material densities of pure water and ice. The mixture density ρ is thus defined by

$$\rho := \rho_i + \rho_w \ . \tag{1.84}$$

The transport of water moving with velocity $\vec{v}_w$ and a concentration $w := \frac{\rho_w}{\rho}$ is then considered and expressed by the water flux relative to the barycenter $\vec{j}^{(b)}$

$$\vec{j}^{(b)} := \rho w(\vec{v}_w - \vec{v}_b) \ . \tag{1.85}$$

Then the balance of mass for the mixture and for water reads as:

$$\begin{aligned} \mathrm{div}\vec{v}_b &= 0 \ , & (1.86)\\ \rho\dot{w} &= -\mathrm{div}\vec{j}^{(b)} + m_w \ , & (1.87) \end{aligned}$$

where $\dot{()} := \frac{\partial()}{\partial t} + \vec{v}_b \cdot \mathrm{grad}()$ is now the material time derivative in the barycentric velocity field, and m_w is the water-production due to melting.

We find it more convenient to consider the ice-velocity rather then the barycentric velocity as the principle variable because water transport in ice generally occurs over much shorter time-scales than deformational ice flow. For certain types of processes, such as water runoff and glacial lake bursts, the barycentric velocity might be greatly affected by the water transport, and then the relevance of barycentric velocity and its relation to the ice-flow speed becomes questionable. Our approach, however, can handle such situations, just by prescribing a proper form of the water flux $\vec{j}$. However, the price paid for choosing the ice velocity as the principle variable is that the ice flow is not divergence-free.

The remaining balance laws are formulated in the classical approach as follows (Greve, 1997). The balance of linear-momentum, or equation of motion, is considered only for the mixture as a whole and reads as

$$\rho\dot{\vec{v}}_b = -\mathrm{grad}p + \mathrm{div}\boldsymbol{\sigma} + \rho\vec{g} \ , \tag{1.88}$$

with the balance of energy given by

$$Lm_w = \boldsymbol{\tau} : \boldsymbol{d}_b - \mathrm{div}\vec{q} - \rho c\dot{T}_m \ , \tag{1.89}$$

and the system is closed by specifying the **rheology** as follows

$$\begin{aligned} \boldsymbol{\tau} &= -p\boldsymbol{I} + \boldsymbol{\sigma} \ , & (1.90)\\ \boldsymbol{d}_b &= \mathcal{A}(w)\sigma_{II}^{n-1}\boldsymbol{\sigma} \ , \qquad n = 3 \ , & (1.91)\\ \vec{j} &= -\alpha\ \mathrm{grad}w \ , & (1.92)\\ \boldsymbol{d}_b &= \frac{1}{2}(\mathrm{grad}\vec{v}_b + \mathrm{grad}^T\vec{v}_b) \ . & (1.93) \end{aligned}$$

This presented set of equations is in good agreement with our formulation from the previous section. It should be noted, however, that the traditional approach, as admitted by Greve (1997), is a result of more physical intuition than consistent and systematic derivations from first principles.

Chapter 2

Shallow Ice Approximation

2.1 Introduction

In this chapter, we will follow the systematic procedure precisely formulated by Baral et al. (2001). The previously derived equations will first be made non-dimensional by introducing appropriate scales and dimensionless numbers. Then a formal polynomial expansion series of field variables in terms of the flatness ratio ϵ will be performed which enables us to carry out a perturbation analysis by successively including higher-order terms in the expansion. In this chapter, we will restrict ourselves merely to the first step of this expansion, that is the $O(\epsilon^0)$ degree terms, and obtain the traditional Shallow Ice Approximation (SIA) (Hutter, 1983).

The SIA is formulated in Cartesian coordinates. However, for large-scale modeling, it is appropriate to use more general coordinates, such as spherical, polar or orthographic. To avoid multiple derivations for each particular case, we derive the SIA in general orthogonal curvilinear coordinates. Performing generalisations of the scaling procedure for Cartesian coordinates, we obtain a whole class of Shallow Ice Approximations, whose particular realization is given only by evaluating geometrical quantities related to the chosen coordinate system. The resultant equations for the basic coordinate systems - Cartesian, spherical and cylindrical - are listed out explicitly.

2.2 Curvilinear orthogonal coordinate system

The equations of motion and evolution of a glacier listed in the previous chapter are expressed in an invariant form by means of invariant differential operators. Hence, they can be expressed in a particular coordinate system. For the purpose of glaciological modeling and also with respect to the scaling analysis, it is convenient to consider only orthogonal curvilinear coordinates, for which the base vectors remain orthogonal in almost all points in the geometrical space R^3. Moreover, for the purpose of scaling, it is convenient to consider only such orthogonal coordinates, in which the first two coordinates, x_1, x_2, refer to "horizontal" dimensions and the third coordinate x_3 stands for the "vertical" dimension. This convention is necessary when introducing the flatness scaling parameter ϵ, essential for the Shallow Ice Approximation.

In particular, three curvilinear orthogonal coordinate systems will be considered as examples (see Fig. 2.1):

- Cartesian coordinates

$$(x_1, x_2, x_3) = (x, y, z) \,, \tag{2.1}$$

where $x, y \in \langle -\mathrm{L_{sc}}, \mathrm{L_{sc}} \rangle$, $z \in \langle -\mathrm{H_{sc}}, \mathrm{H_{sc}} \rangle$,

- Spherical coordinates

$$(x_1, x_2, x_3) = (\vartheta, \varphi, \zeta) \,, \tag{2.2}$$

where $\zeta := r - R$, for r the radial distance and R some mean radius (of the Earth), and $\zeta \in \langle -\mathrm{H_{sc}}, \mathrm{H_{sc}} \rangle$, $\vartheta \in \langle 0, \pi \rangle$, $\varphi \in \langle 0, 2\pi \rangle$. The relation to Cartesian coordinates is

$$x = r \sin\vartheta \cos\varphi, \qquad y = r \sin\vartheta \sin\varphi, \qquad z = r \cos\vartheta \,. \tag{2.3}$$

- Cylindrical coordinates

$$(x_1, x_2, x_3) = (\varrho, \varphi, z) \,, \tag{2.4}$$

where $\varrho \in \langle 0, \mathrm{L_{sc}} \rangle$, $\varphi \in \langle 0, 2\pi \rangle$, $z \in \langle -\mathrm{H_{sc}}, \mathrm{H_{sc}} \rangle$. The relation to Cartesian coordinates is

$$x = \varrho \cos\varphi, \qquad y = \varrho \sin\varphi, \qquad z = z \,. \tag{2.5}$$

2.3 Scaling

We perform the scaling analysis for a general polythermal ice sheet. The simpler case of a purely-cold ice sheet is obtained by letting the cold-ice zone extend throughout the whole volume of the ice sheet.

As the first step of the scaling analysis, we non-dimensionalize the governing equations and the boundary conditions by introducing representative scales for the field quantities. For a field quantity ψ, we define its non-dimensional counterpart $\tilde{\psi}$, by introducing the scale $[\psi]$ (not to be mixed with a jump of quantity at the discontinuity surface, which is denoted $[\psi]^+_-$)

$$\psi = [\psi]\tilde{\psi} \,, \tag{2.6}$$

where the quantity $\tilde{\psi}$, if properly scaled, is without a physical unit and its magnitude is of the order of unity.

We start by scaling the geometry. As already noted, we assume that x_1 and x_2 are "horizontal" coordinates, while x_3 is "vertical". Geometrical scaling is now done by specifying the scales for the Lame coefficients $[h_1]$,$[h_2]$,$[h_3]$, and for the typical scale of change of a particular coordinate, denoted $[\Delta_1]$, $[\Delta_2]$, $[\Delta_3]$. These two requirements follow from the expression for a length of a coordinate line element

$$ds_k = h_k \, dx_k = [h_k][\Delta_k] \, \tilde{h}_k \, d\tilde{x}_k \,, \qquad k = 1, 2, 3 \,. \tag{2.7}$$

Note that, in general, neither $[h_i]$, nor $[\Delta_i]$, but only their product has the dimension of length. We assume that the typical "horizontal" lengths of line elements are equal, i.e.

$$[h_1][\Delta_1] = [h_2][\Delta_2] \,. \tag{2.8}$$

We then introduce the typical vertical-to-horizontal ratio as a first dimensionless number, denoted by ϵ:

$$\epsilon := \frac{[h_3][\Delta_3]}{[h_1][\Delta_1]} = \frac{[h_3][\Delta_3]}{[h_2][\Delta_2]} \,. \tag{2.9}$$

Examples for the scales within the possible coordinate systems are given below:

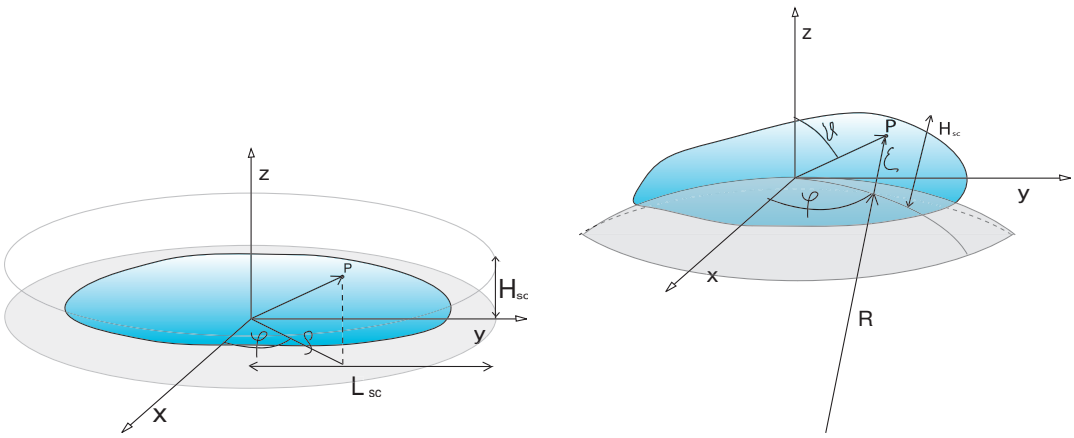

Figure 2.1: Cartesian and cylindrical coordinate system (left) and spherical coordinate system (right).

- Example (1) - for Cartesian coordinates (2.1), we have

$$h_x = [h_x] = \tilde{h}_x = 1, \qquad h_y = [h_y] = \tilde{h}_y = 1, \qquad h_z = [h_z] = \tilde{h}_z = 1\ , \tag{2.10}$$

and

$$[\Delta_x] := \mathrm{L_{sc}}, \qquad [\Delta_y] := \mathrm{L_{sc}}, \qquad [\Delta_z] := \mathrm{H_{sc}}\ . \tag{2.11}$$

- Example (2) - for spherical coordinates (2.2), we define the scales

$$[\Delta_\vartheta] = 1, \qquad [\Delta_\varphi] = 1, \qquad [\Delta_\zeta] = \mathrm{H_{sc}}\ , \tag{2.12}$$

leading to

$$h_\vartheta = r = R + \zeta = R\left(1 + \frac{\mathrm{H_{sc}}}{R}\tilde{\zeta}\right),\ h_\varphi = (R+\zeta)\sin\vartheta = R\left(1 + \frac{\mathrm{H_{sc}}}{R}\tilde{\zeta}\right)\sin\vartheta,\ h_\zeta = 1\ , \tag{2.13}$$

and, therefore, we set

$$[h_\vartheta] = R, \qquad [h_\varphi] = R, \qquad [h_\zeta] = 1\ , \tag{2.14}$$

and

$$\tilde{h}_\vartheta = 1 + \epsilon\tilde{\zeta}, \qquad \tilde{h}_\varphi = (1 + \epsilon\tilde{\zeta})\sin\vartheta, \qquad \tilde{h}_\zeta = 1\ . \tag{2.15}$$

- Example (3) - for cylindrical coordinates (2.4), we define the scales

$$[\Delta_\varrho] = \mathrm{L_{sc}}, \qquad [\Delta_\varphi] = 1, \qquad [\Delta_z] = \mathrm{H_{sc}}\ , \tag{2.16}$$

which gives

$$h_\varrho = 1, \qquad h_\varphi = \varrho = \mathrm{L_{sc}}\tilde{\varrho}, \qquad h_z = 1\ , \tag{2.17}$$

and, therefore, we set

$$[h_\varrho] = 1, \qquad [h_\varphi] = \mathrm{L_{sc}}, \qquad [h_z] = 1\ , \tag{2.18}$$

and

$$\tilde{h}_\varrho = 1, \qquad \tilde{h}_\varphi = \tilde{\varrho}, \qquad \tilde{h}_z = 1\ . \tag{2.19}$$

Introducing the time scale $[t]$ and non-dimensional time $\tilde{t}$ by (2.32), we will always assume that the scaled field quantities are defined in the scaled time-space, i.e. the scaling (2.6) reads as

$$\psi(x_1, x_2, x_3, t) = [\psi]\,\tilde{\psi}(\tilde{x}_1, \tilde{x}_2, \tilde{x}_3, \tilde{t})\ . \tag{2.20}$$

It will be convenient to choose the shape of the implicit surface functions for the free surface, glacier bed and cold-temperate ice transition surface, such that they posses scales

$$(F_s, F_b, F_{cts}) = [h_3][\Delta_3]\,(\tilde{F}_s, \tilde{F}_b, \tilde{F}_{cts})\ , \tag{2.21}$$

or, in the explicit representation,

$$\begin{aligned} f_s &= [f_s]\,\tilde{f}_s = [\Delta_3]\,\tilde{f}_s\ , && (2.22)\\ f_{cts} &= [f_{cts}]\,\tilde{f}_{cts} = [\Delta_3]\,\tilde{f}_{cts}\ , && (2.23)\\ f_b &= [f_b]\,\tilde{f}_b = [\Delta_3]\,\tilde{f}_b\ . && (2.24) \end{aligned}$$

For the horizontal and vertical velocities, we introduce the scales $[v_h]$, and $[v_v]$ as

$$\begin{aligned} (v_1, v_2) &= [v_h]\,(\tilde{v}_1, \tilde{v}_2)\ , && (2.25)\\ v_3 &= [v_v]\,\tilde{v}_v, && (2.26) \end{aligned}$$

asserting the relation

$$\frac{[v_v]}{[v_h]} = \epsilon\ , \tag{2.27}$$

which means that $[v_v]$ and $[v_h]$ are not independent scales. Provided that all the surface non-material velocities are assumed to be small, the relative velocities at the discontinuities will be scaled according to

$$\begin{aligned} (v_1 - \nu_1, v_2 - \nu_2) &= [v_h]\,(\tilde{v}_1 - \tilde{\nu}_1, \tilde{v}_2 - \tilde{\nu}_2)\ , && (2.28)\\ v_3 - \nu_3 &= [v_v]\,(\tilde{v}_3 - \tilde{\nu}_3)\ , && (2.29) \end{aligned}$$

and the sliding basal velocities can be reasonably scaled in the same manner:

$$\begin{aligned} (v_1^{sl}, v_2^{sl}) &= [v_h]\,(\tilde{v}_1^{sl}, \tilde{v}_2^{sl}), && (2.30)\\ v_3^{sl} &= [v_v]\,\tilde{v}_3^{sl}\ . && (2.31) \end{aligned}$$

Having introduced scales for geometry and velocities, it is straightforward to introduce the time scale as

$$t = [t]\,\tilde{t} = \frac{[h_1][\Delta_1]}{[v_h]}\,\tilde{t} = \frac{[h_2][\Delta_2]}{[v_h]}\,\tilde{t} = \frac{[h_3][\Delta_3]}{[v_v]}\,\tilde{t}\ . \tag{2.32}$$

A crucial essence of the Shallow Ice Approximation lies in one particular choice of scaling of the stress-tensor components. Following on from observations and measurements, as well as from theoretically based deductions (Hutter, 1983), the scaling is traditionally chosen to be

$$\begin{aligned} p &= \rho g[h_3][\Delta_3]\,\tilde{p}, && (2.33)\\ (\boldsymbol{\sigma}_{13}, \boldsymbol{\sigma}_{23}) &= \epsilon\rho g[h_3][\Delta_3]\,(\tilde{\boldsymbol{\sigma}}_{13}, \tilde{\boldsymbol{\sigma}}_{23})\ , && (2.34)\\ (\boldsymbol{\sigma}_{11}, \boldsymbol{\sigma}_{22}, \boldsymbol{\sigma}_{12}) &= \epsilon^2\rho g[h_3][\Delta_3]\,(\tilde{\boldsymbol{\sigma}}_{11}, \tilde{\boldsymbol{\sigma}}_{22}, \tilde{\boldsymbol{\sigma}}_{12})\ . && (2.35) \end{aligned}$$

Because the typical aspect ratio ϵ for real ice sheets is a small number (10^{-2}-10^{-3}, Baral et al., 2001), this scaling specifies that the dominant stress component in the ice sheet interior is the overburden pressure. The

vertical shear stresses $\boldsymbol{\sigma}_{13}$, $\boldsymbol{\sigma}_{23}$ are then one order of ϵ smaller, and the longitudinal stresses $\boldsymbol{\sigma}_{11}$, $\boldsymbol{\sigma}_{22}$ (and, of course, $\boldsymbol{\sigma}_{33} = -\boldsymbol{\sigma}_{11} - \boldsymbol{\sigma}_{22}$, by definition), together with the horizontal shear stress $\boldsymbol{\sigma}_{12}$ are even two orders of ϵ smaller. These scaling assumptions are typically valid in large ice sheets with the exception of ice sheet margins or regions of massively undulated bedrock topography, or in highly lubricated regions such as ice streams. That is, in regions where the longitudinal stresses become comparable or even dominant over the shear stresses. This particular scaling thus mainly concerns large-scale behavior of grounded ice masses and completely different stress-scaling assumptions must be introduced when floating ice is investigated. Then, a procedure analogous to the one that follows may be performed, resulting in a "Shallow-Shelf" approximation (Greve, 1997). We will, however, restrict ourselves to grounded ice sheets where the considered scaling (2.33)–(2.35) is the most convenient and appropriate for the perturbation analysis.

It remains to introduce scales also for the following quantities:

$$
\begin{aligned}
w &= [w]\,\tilde{w}\,, && (2.36)\\
(T, T_m) &= [T]\,(\tilde{T}, \tilde{T}_m)\,, && (2.37)\\
k(T) &= [k]\,\tilde{k}(\tilde{T})\,, && (2.38)\\
(\mathcal{A}(T), \mathcal{A}(T,p), \mathcal{A}(w)) &= [\mathcal{A}]\,(\tilde{\mathcal{A}}(\tilde{T}), \mathcal{A}(\tilde{T}, \tilde{p}), \tilde{\mathcal{A}}(\tilde{w}))\,, && (2.39)\\
(a^s, \mathcal{P}^s, o^b) &= \rho[v_v]\,(\tilde{a}^s, \tilde{\mathcal{P}}^s, \tilde{o}^b)\,, && (2.40)\\
(m_w^s, m_w^b, m_w^{cts}) &= \rho[v_v]\,(\tilde{m}_w^s, \tilde{m}_w^b, \tilde{m}_w^{cts})\,, && (2.41)\\
(q_1, q_1^{geo}, q_2, q_2^{geo}) &= \frac{[k][T]}{[h_1][\Delta_1]}\,(\tilde{q}_1, \tilde{q}_1^{geo}, \tilde{q}_2, \tilde{q}_2^{geo})\,, && (2.42)\\
(q_3, q_3^{geo}) &= \frac{[k][T]}{[h_3][\Delta_3]}\,(\tilde{q}_3, \tilde{q}_3^{geo})\,, && (2.43)\\
\beta(\vec{n}_b \cdot \boldsymbol{\tau} \cdot \vec{n}_b, T, w, ...) &= [\beta]\,\tilde{\beta}(\tilde{\vec{n}}_b \cdot \tilde{\boldsymbol{\tau}} \cdot \tilde{\vec{n}}_b, \tilde{T}, \tilde{w}, ...)\,, && (2.44)\\
c_v(T) &= [c_v]\,\tilde{c}_v(\tilde{T})\,, && (2.45)\\
\alpha_1 &= [\alpha_1]\,\tilde{\alpha_1}\,, && (2.46)\\
\alpha_2 &= [\alpha_2]\,\tilde{\alpha_2}\,. && (2.47)
\end{aligned}
$$

To scale the water flux $\vec{j}$, we introduce a scale for the water velocity magnitude $[v_w]$, and assuming that the water flow is governed by relation (1.44), we set the following

$$
\begin{aligned}
(j_1, j_2) &= \epsilon\rho[w][v_w]\,(\tilde{j}_1, \tilde{j}_2)\,, && (2.48)\\
j_3 &= \rho[w][v_w]\,\tilde{j}_3\,, && (2.49)\\
(v_{w1}, v_{w2}) &= \epsilon[v_w]\,(\tilde{v}_{w1}, \tilde{v}_{w2})\,, && (2.50)\\
v_{w3} &= [v_w]\,\tilde{v}_{w3}\,. && (2.51)
\end{aligned}
$$

Now, an elementary scaling analysis can be performed in order to rewrite the equations in a dimensionless form. We have introduced 12 basic independent scales $[v_h]$,$[v_w]$, $[h_1][\Delta_1] = [h_2][\Delta_2]$, $[h_3][\Delta_3]$, $[w]$, $[T]$, $[k]$, $[\mathcal{A}]$, $[c_v]$, $[\beta]$, $[\alpha_1]$, $[\alpha_2]$. Scales $[h_i]$,$[\Delta_i]$ are taken as a couple and count for one quantity only because in all equations they appear only as a product.

Together with 8 physical constants ρ, g, L, γ, C_{Cl}, T_{m0}, $\frac{Q}{k_B}$, p^{atm}, we have in total 20 quantities, whose physical dimensions consist of the basic physical units: meter, kilogram, second and Kelvin. The dimension matrix can be shown to have the rank four, and thus according to Buckingham's Pi Theorem (e.g. Hutter,

2004), $20 - 4 = 16$ independent dimensionless numbers can be introduced. These are

$$\begin{gathered}
\epsilon = \frac{[h_3][\Delta_3]}{[h_1][\Delta_1]}, \qquad \mathcal{C} = \frac{g[h_3][\Delta_3]}{[c_v][T]}, \qquad \mathcal{J} = \frac{[w][v_w][h_1][\Delta_1]}{[v_h][h_3][\Delta_3]}, \qquad \mathcal{E} = \frac{g[h_3][\Delta_3]}{L[w]}, \\
\mathcal{K} = \frac{[\mathcal{A}]\rho^n g^n ([h_3][\Delta_3])^{2n+1}}{([h_1][\Delta_1])^n [v_h]}, \quad \mathcal{B} = \frac{\rho g ([h_3][\Delta_3])^2}{[h_1][\Delta_1][v_h][\beta]^2}, \quad \mathcal{D} = \frac{[k][h_1][\Delta_1]}{\rho[c_v][v_h]([h_3][\Delta_3])^2}, \qquad [w], \\
\mathcal{T}_0 = \frac{T_{m0}}{[T]}, \qquad \mathcal{T} = \frac{C_{Cl}\rho g[h_3][\Delta_3]}{[T]}, \qquad \gamma, \qquad \mathcal{Q} = \frac{Q}{k_B[T]}, \\
\mathcal{N}_1 = \frac{[\alpha_1]}{[h_3][\Delta_3]\rho[v_w]}, \qquad \mathcal{N}_2 = \frac{[\alpha_2]g}{[v_w]}, \qquad \mathcal{F} = \frac{[v_h]^2}{[h_1][\Delta_1]g}, \qquad \mathcal{L} = \frac{p^{atm}}{[h_3][\Delta_3]\rho g}\,.
\end{gathered} \tag{2.52}$$

To gain some insight into the importance of various terms in the following derivations, we find it useful to evaluate the dimensionless numbers in (2.52) for a typical large ice sheet. Assume we are inspecting an ice sheet with a horizontal extent of hundreds of kilometers ($[h_1][\Delta_1] = 100$ km) with typical thickness reaching units of kilometers, we thus set ($[h_3][\Delta_3] = 1$ km). Using previously applied values of the physical properties for ice e.g. in Payne et al. (2000) or Greve (1997), we choose $[T] = T_{m0} = 237.15$ K, $g = 9.81$ m s^{-2}, $\rho = 910$ kg m^{-3}, $[c_v] = 2000$ J kg^{-1} K^{-1}, $[w] = 0.01$, $[v_h] = 1$ m a^{-1}, $L = 3.35 \times 10^5$ J kg^{-1}, $[\mathcal{A}] = 1 \times 10^{-16}$ Pa^{-3} a^{-1}, $[k] = 2$ W m^{-1} K^{-1}, $C_{Cl} = 9.7 \times 10^{-8}$ K Pa^{-1}, $\gamma = 184$, $\frac{Q}{k_B} = 7216$ K, $p^{atm} = 100$ k Pa, $[\beta^2] = 10^{12}$ kg m^{-2} s^{-1}. Unfortunately, we lack reasonable estimates for the values of $[v_w]$, α_1, α_2, therefore the dimensionless numbers $\mathcal{J}, \mathcal{N}_1, \mathcal{N}_2$, remain unevaluated. For the rest, we arrive at:

$$\begin{gathered}
\epsilon \sim 10^{-2}, \qquad \mathcal{C} \sim 0.018, \qquad \mathcal{J} \sim 10^{-4} \times \frac{[v_w]}{[v_h]}, \qquad \mathcal{E} \sim 2.9, \\
\mathcal{K} \sim 71.14, \qquad \mathcal{B} \sim 2.81, \qquad \mathcal{D} \sim 3.44, \qquad [w] \sim 0.01, \\
\mathcal{T}_0 \sim 1, \qquad \mathcal{T} \sim 0.0032, \qquad \gamma \sim 184, \qquad \mathcal{Q} \sim 26.42, \\
\mathcal{N}_1 \sim ?, \qquad \mathcal{N}_2 \sim ?, \qquad \mathcal{F} \sim 1.1 \times 10^{-23}, \quad \mathcal{L} \sim 0.011\,.
\end{gathered} \tag{2.53}$$

2.4 Shallow Ice Approximation

In this section we present the resultant form of the governing equations for a polythermal ice sheet. The procedure is as follows. In the previous section, we introduced appropriate scales for the field quantities. Now, we perform a first step of the perturbation analysis in terms of the scaling parameter ϵ (aspect ratio), reflecting the fact that typically in nature, the value ϵ is small (typically varying between 10^{-3}-10^{-2} for large ice sheets), thus allowing for such a perturbation procedure. Hence for any (already non-dimensional) field quantity $\tilde{\varphi}$, we consider an expansion

$$\tilde{\varphi} = \sum_{n=0}^{\infty} \tilde{\varphi}^{(n)} \epsilon^n\,. \tag{2.54}$$

Inserting this expansion into the non-dimensionalized equations and keeping only the leading terms in ϵ, we obtain in the limit $\epsilon \to 0+$ the zero-order scaling approximation, the so-called Shallow Ice Approximation. To give some insight into this procedure, we will present several more detailed examples of the required derivations, but for the sake of brevity, most of the resultant SIA formulas are presented without detailed derivations, which are nonetheless quite straightforward.

We present only results for a polythermal ice sheet. The special case of a purely-cold ice sheet can be obtained by simply excluding the temperate-ice zone and letting the cold-ice zone extend throughout the whole glacier volume.

2.4.1 Field equations – Cold-ice zone

The **mass balance** for ice (1.25) reads in the general curvilinear coordinates (D.12) as:

$$\begin{aligned}
0 &= \mathrm{div}\vec{v} \\
&= \sum_{k=1}^{3} \frac{1}{h_k}\left(\frac{\partial v_k}{\partial x_k} + \sum_{m,m\neq k}\frac{1}{h_m}\frac{\partial h_k}{\partial x_m}v_m\right) \\
&= \frac{1}{h_1}\frac{\partial v_1}{\partial x_1} + \frac{1}{h_1h_2}\frac{\partial h_1}{\partial x_2}v_2 + \frac{1}{h_1h_3}\frac{\partial h_1}{\partial x_3}v_3 \\
&+ \frac{1}{h_2}\frac{\partial v_2}{\partial x_2} + \frac{1}{h_2h_3}\frac{\partial h_2}{\partial x_3}v_3 + \frac{1}{h_2h_1}\frac{\partial h_2}{\partial x_1}v_1 \\
&+ \frac{1}{h_3}\frac{\partial v_3}{\partial x_3} + \frac{1}{h_3h_1}\frac{\partial h_3}{\partial x_1}v_1 + \frac{1}{h_3h_2}\frac{\partial h_3}{\partial x_2}v_2 \\
&= \frac{[v_h]}{[h_1][\Delta_1]}\frac{1}{\tilde{h}_1}\frac{\partial\tilde{v}_1}{\partial\tilde{x}_1} + \frac{[v_h]}{[h_2][\Delta_2]}\frac{1}{\tilde{h}_1\tilde{h}_2}\frac{\partial\tilde{h}_1}{\partial\tilde{x}_2}\tilde{v}_2 + \frac{[v_v]}{[h_3][\Delta_3]}\frac{1}{\tilde{h}_1\tilde{h}_3}\frac{\partial\tilde{h}_1}{\partial\tilde{x}_3}\tilde{v}_3 \\
&+ \frac{[v_h]}{[h_2][\Delta_2]}\frac{1}{\tilde{h}_2}\frac{\partial\tilde{v}_2}{\partial\tilde{x}_2} + \frac{[v_v]}{[h_3][\Delta_3]}\frac{1}{\tilde{h}_2\tilde{h}_3}\frac{\partial\tilde{h}_2}{\partial\tilde{x}_3}\tilde{v}_3 + \frac{[v_h]}{[h_1][\Delta_1]}\frac{1}{\tilde{h}_2\tilde{h}_1}\frac{\partial\tilde{h}_2}{\partial\tilde{x}_1}\tilde{v}_1 \\
&+ \frac{[v_v]}{[h_3][\Delta_3]}\frac{1}{\tilde{h}_3}\frac{\partial\tilde{v}_3}{\partial\tilde{x}_3} + \frac{[v_h]}{[h_1][\Delta_1]}\frac{1}{\tilde{h}_3\tilde{h}_1}\frac{\partial\tilde{h}_3}{\partial\tilde{x}_1}\tilde{v}_1 + \frac{[v_h]}{[h_2][\Delta_2]}\frac{1}{\tilde{h}_3\tilde{h}_2}\frac{\partial\tilde{h}_3}{\partial\tilde{x}_2}\tilde{v}_2\,,
\end{aligned}$$

which, after dividing by $\frac{[v_h]}{[h_1][\Delta_1]}$ and realizing that $[h_1][\Delta_1] = [h_2][\Delta_2]$ and $\frac{[v_h]}{[h_1][\Delta_1]} = \frac{[v_v]}{[h_3][\Delta_3]}$, leads to

$$\begin{aligned}
0 &= \frac{1}{\tilde{h}_1}\frac{\partial\tilde{v}_1}{\partial\tilde{x}_1} + \frac{1}{\tilde{h}_1\tilde{h}_2}\frac{\partial\tilde{h}_1}{\partial\tilde{x}_2}\tilde{v}_2 + \frac{1}{\tilde{h}_1\tilde{h}_3}\frac{\partial\tilde{h}_1}{\partial\tilde{x}_3}\tilde{v}_3 \\
&+ \frac{1}{\tilde{h}_2}\frac{\partial\tilde{v}_2}{\partial\tilde{x}_2} + \frac{1}{\tilde{h}_2\tilde{h}_3}\frac{\partial\tilde{h}_2}{\partial\tilde{x}_3}\tilde{v}_3 + \frac{1}{\tilde{h}_2\tilde{h}_1}\frac{\partial\tilde{h}_2}{\partial\tilde{x}_1}\tilde{v}_1 \\
&+ \frac{1}{\tilde{h}_3}\frac{\partial\tilde{v}_3}{\partial\tilde{x}_3} + \frac{1}{\tilde{h}_3\tilde{h}_1}\frac{\partial\tilde{h}_3}{\partial\tilde{x}_1}\tilde{v}_1 + \frac{1}{\tilde{h}_3\tilde{h}_2}\frac{\partial\tilde{h}_3}{\partial\tilde{x}_2}\tilde{v}_2\,. \qquad (2.55)
\end{aligned}$$

This is the non-dimensional version of the ice mass balance (1.25). Now, the SIA-limit is obtained by expanding

$$\begin{aligned}
\tilde{v}_i &= \tilde{v}_i^{(0)} + \tilde{v}_i^{(1)}\epsilon + \tilde{v}_i^{(2)}\epsilon^2 + \dots\,, \\
\tilde{h}_i &= \tilde{h}_i^{(0)} + \tilde{h}_i^{(1)}\epsilon + \tilde{h}_i^{(2)}\epsilon^2 + \dots\,, \\
\frac{\partial\tilde{h}_i}{\partial\tilde{x}_j} &= \left(\frac{\partial\tilde{h}_i}{\partial\tilde{x}_j}\right)^{(0)} + \left(\frac{\partial\tilde{h}_i}{\partial\tilde{x}_j}\right)^{(1)}\epsilon + \left(\frac{\partial\tilde{h}_i}{\partial\tilde{x}_j}\right)^{(2)}\epsilon^2 + \dots\,, \\
i,j &= 1,2,3\,,
\end{aligned}$$

Inserting these expansions to (2.55), letting $\epsilon \to 0+$, and keeping only the zero-order $()^{(0)}$ terms, while introducing new symbols

$$H_i := \lim_{\epsilon\to 0+} \tilde{h}_i = \tilde{h}_i^{(0)} , \tag{2.56}$$

$$H_{ij} := \lim_{\epsilon\to 0+} \frac{\partial \tilde{h}_i}{\partial \tilde{x}_j} = \left(\frac{\partial \tilde{h}_i}{\partial \tilde{x}_j}\right)^{(0)} , \tag{2.57}$$

and omitting the $()^{(0)}$ superscript in the resultant form, we arrive at

$$\begin{aligned} 0 &= \frac{1}{H_1}\frac{\partial \tilde{v}_1}{\partial \tilde{x}_1} + \frac{H_{12}}{H_1 H_2}\tilde{v}_2 + \frac{H_{13}}{H_1 H_3}\tilde{v}_3 \\ &+ \frac{1}{H_2}\frac{\partial \tilde{v}_2}{\partial \tilde{x}_2} + \frac{H_{23}}{H_2 H_3}\tilde{v}_3 + \frac{H_{21}}{H_2 H_1}\tilde{v}_1 \\ &+ \frac{1}{H_3}\frac{\partial \tilde{v}_3}{\partial \tilde{x}_3} + \frac{H_{31}}{H_3 H_1}\tilde{v}_1 + \frac{H_{32}}{H_3 H_2}\tilde{v}_2 . \end{aligned} \tag{2.58}$$

- Example (1) - Cartesian coordinates
  For Cartesian coordinates (2.1), according to (2.10), we have

  $$H_i = 1 , \qquad H_{ij} = 0 , \qquad i,j = 1,2,3 , \tag{2.59}$$

  and (2.58) reads

  $$0 = \frac{\partial \tilde{v}_x}{\partial \tilde{x}} + \frac{\partial \tilde{v}_y}{\partial \tilde{y}} + \frac{\partial \tilde{v}_z}{\partial \tilde{z}} . \tag{2.60}$$

- Example (2) - Spherical coordinates
  For spherical coordinates (2.2), following (2.15), we obtain

  $$H_\vartheta = \lim_{\epsilon\to 0+} \tilde{h}_\vartheta = 1 , \; H_\varphi = \lim_{\epsilon\to 0+} \tilde{h}_\varphi = \sin\vartheta , \; H_\zeta = \lim_{\epsilon\to 0+} \tilde{h}_\zeta = 1 , \tag{2.61}$$

  where the only non-zero derivatives $\frac{\partial \tilde{h}_i}{\partial \tilde{x}_j}$ are

  $$\frac{\partial \tilde{h}_\vartheta}{\partial \tilde{\zeta}} = \epsilon , \tag{2.62}$$

  $$\frac{\partial \tilde{h}_\varphi}{\partial \vartheta} = (1+\epsilon\tilde{\zeta})\cos\vartheta , \tag{2.63}$$

  $$\frac{\partial \tilde{h}_\varphi}{\partial \tilde{\zeta}} = \epsilon \sin\vartheta . \tag{2.64}$$

  Taking the limit $\epsilon \to 0+$ results in the only non-zero H_{ij} being

  $$H_{\varphi\vartheta} = \cos\vartheta , \tag{2.65}$$

  thus, (2.58) in spherical coordinates reads as

  $$0 = \frac{\partial \tilde{v}_\vartheta}{\partial \vartheta} + \cot\vartheta\, \tilde{v}_\vartheta + \frac{1}{\sin\vartheta}\frac{\partial \tilde{v}_\varphi}{\partial \varphi} + \frac{\partial \tilde{v}_\zeta}{\partial \tilde{\zeta}} . \tag{2.66}$$

- Example (3) - Cylindrical coordinates
  In view of (2.19),

$$H_\varrho = \lim_{\epsilon\to 0+} \tilde{h}_\varrho = 1 \,,\; H_\varphi = \lim_{\epsilon\to 0+} \tilde{h}_\varphi = \tilde{\varrho} \,,\; H_z = \lim_{\epsilon\to 0+} \tilde{h}_z = 1 \,, \tag{2.67}$$

  hence, the only non-zero derivative $\frac{\partial \tilde{h}_i}{\partial \tilde{x}_j}$ is

$$\frac{\partial \tilde{h}_\varphi}{\partial \tilde{\varrho}} = 1 \,. \tag{2.68}$$

  By taking the limit $\epsilon \to 0+$, the only non-zero H_{ij} is

$$H_{\varphi\varrho} = 1 \,, \tag{2.69}$$

  leading to (2.58) in cylindrical coordinates reading as

$$0 \;=\; \frac{\partial \tilde{v}_\varrho}{\partial \tilde{\varrho}} + \frac{\tilde{v}_\varrho}{\tilde{\varrho}} + \frac{1}{\tilde{\varrho}}\frac{\partial \tilde{v}_\varphi}{\partial \varphi} + \frac{\partial \tilde{v}_z}{\partial \tilde{z}} \,. \tag{2.70}$$

The **linear-momentum balance** equations (1.26) when rewritten in the non-dimensional form with the use of (D.11) and (D.14) read as:

$$\frac{\mathcal{F}}{\epsilon}(\dots) \;=\; -\frac{1}{\tilde{h}_1}\frac{\partial \tilde{p}}{\partial \tilde{x}_1} + \tilde{\boldsymbol{\sigma}}_{13}\left(\frac{2}{\tilde{h}_1\tilde{h}_3}\frac{\partial \tilde{h}_1}{\partial \tilde{x}_3} + \frac{1}{\tilde{h}_2\tilde{h}_3}\frac{\partial \tilde{h}_2}{\partial \tilde{x}_3}\right) + \frac{1}{\tilde{h}_3}\frac{\partial \tilde{\boldsymbol{\sigma}}_{13}}{\partial \tilde{x}_3} + \frac{g_1}{\epsilon g} + O(\epsilon) \,, \tag{2.71}$$

$$\frac{\mathcal{F}}{\epsilon}(\dots) \;=\; -\frac{1}{\tilde{h}_2}\frac{\partial \tilde{p}}{\partial \tilde{x}_2} + \tilde{\boldsymbol{\sigma}}_{23}\left(\frac{1}{\tilde{h}_1\tilde{h}_3}\frac{\partial \tilde{h}_1}{\partial \tilde{x}_3} + \frac{2}{\tilde{h}_2\tilde{h}_3}\frac{\partial \tilde{h}_2}{\partial \tilde{x}_3}\right) + \frac{1}{\tilde{h}_3}\frac{\partial \tilde{\boldsymbol{\sigma}}_{23}}{\partial \tilde{x}_3} + \frac{g_2}{\epsilon g} + O(\epsilon) \,, \tag{2.72}$$

$$\mathcal{F}(\dots) \;=\; -\frac{1}{\tilde{h}_3}\frac{\partial \tilde{p}}{\partial \tilde{x}_3} + \frac{g_3}{g} + O(\epsilon) \,, \tag{2.73}$$

where the left-hand sides are not expressed explicitly, because, as shown in (2.53), the typical magnitude of the Froude number $\mathcal{F}$ and the fraction $\frac{\mathcal{F}}{\epsilon}$ are very small. We may therefore safely assume that, in the SIA limit, together with $\epsilon \to 0+$, both $\mathcal{F}, \frac{\mathcal{F}}{\epsilon} \to 0+$. Thus, the SIA limit of the momentum equations reads as

$$0 \;=\; -\frac{1}{H_1}\frac{\partial \tilde{p}}{\partial \tilde{x}_1} + \tilde{\boldsymbol{\sigma}}_{13}\left(2\frac{H_{13}}{H_1H_3} + \frac{H_{23}}{H_2H_3}\right) + \frac{1}{H_3}\frac{\partial \tilde{\boldsymbol{\sigma}}_{13}}{\partial \tilde{x}_3} + e_{g\,1} \,, \tag{2.74}$$

$$0 \;=\; -\frac{1}{H_2}\frac{\partial \tilde{p}}{\partial \tilde{x}_2} + \tilde{\boldsymbol{\sigma}}_{23}\left(\frac{H_{13}}{H_1H_3} + 2\frac{H_{23}}{H_2H_3}\right) + \frac{1}{H_3}\frac{\partial \tilde{\boldsymbol{\sigma}}_{23}}{\partial \tilde{x}_3} + e_{g\,2} \,, \tag{2.75}$$

$$0 \;=\; -\frac{1}{H_3}\frac{\partial \tilde{p}}{\partial \tilde{x}_3} + e_{g\,3} \,, \tag{2.76}$$

where

$$e_{g\,i} := \lim_{\epsilon\to 0+} \frac{1}{\epsilon}\left(\frac{\vec{g}}{g}\right)_i \,,\; i = 1,2 \,, \qquad e_{g\,3} := \lim_{\epsilon\to 0+} \left(\frac{\vec{g}}{g}\right)_3 \,. \tag{2.77}$$

- Example (1) - Cartesian coordinates
  Taking naturally the z-axis parallel with the vector of the gravitational field, oriented as $\vec{g} = (0, 0, -g)$, with the use of (2.59), gives the SIA form of the linear-momentum equations in Cartesian coordinates as follows (see also e.g. Greve, 1997):

$$0 = -\frac{\partial \tilde{p}}{\partial \tilde{x}} + \frac{\partial \tilde{\boldsymbol{\sigma}}_{xz}}{\partial \tilde{z}} , \tag{2.78}$$

$$0 = -\frac{\partial \tilde{p}}{\partial \tilde{y}} + \frac{\partial \tilde{\boldsymbol{\sigma}}_{yz}}{\partial \tilde{z}} , \tag{2.79}$$

$$0 = -\frac{\partial \tilde{p}}{\partial \tilde{z}} - 1 . \tag{2.80}$$

- Example (2) - Spherical coordinates
  Choosing again the orientation of the coordinate axes such that $\vec{g} = (0, 0, -g)$, and using (2.61) and (2.65), results in

$$0 = -\frac{\partial \tilde{p}}{\partial \vartheta} + \frac{\partial \tilde{\boldsymbol{\sigma}}_{\vartheta\zeta}}{\partial \tilde{\zeta}} , \tag{2.81}$$

$$0 = -\frac{1}{\sin\vartheta}\frac{\partial \tilde{p}}{\partial \varphi} + \frac{\partial \tilde{\boldsymbol{\sigma}}_{\varphi\zeta}}{\partial \tilde{\zeta}} , \tag{2.82}$$

$$0 = -\frac{\partial \tilde{p}}{\partial \tilde{\zeta}} - 1 . \tag{2.83}$$

- Example (3) - Cylindrical coordinates
  Again, provided that $\vec{g} = (0, 0, -g)$, and using (2.67) and (2.69), results in the cylindrical coordinate form

$$0 = -\frac{\partial \tilde{p}}{\partial \tilde{\varrho}} + \frac{\partial \tilde{\boldsymbol{\sigma}}_{\varrho z}}{\partial \tilde{z}} , \tag{2.84}$$

$$0 = -\frac{1}{\tilde{\varrho}}\frac{\partial \tilde{p}}{\partial \varphi} + \frac{\partial \tilde{\boldsymbol{\sigma}}_{\varphi z}}{\partial \tilde{z}} , \tag{2.85}$$

$$0 = -\frac{\partial \tilde{p}}{\partial \tilde{z}} - 1 . \tag{2.86}$$

The **rheology** is specified as follows. We give the SIA form of both (1.17) and (1.18). The five independent equations (1.17) in the SIA approximation read as

$$\tilde{\boldsymbol{\sigma}}_{13} = \tilde{\eta}\left(\frac{1}{H_3}\frac{\partial \tilde{v}_1}{\partial \tilde{x}_3} - \frac{H_{13}}{H_1 H_3}\tilde{v}_1\right) , \tag{2.87}$$

$$\tilde{\boldsymbol{\sigma}}_{23} = \tilde{\eta}\left(\frac{1}{H_3}\frac{\partial \tilde{v}_2}{\partial \tilde{x}_3} - \frac{H_{23}}{H_2 H_3}\tilde{v}_2\right) , \tag{2.88}$$

$$\tilde{\boldsymbol{\sigma}}_{11} = 2\tilde{\eta}\left(\frac{1}{H_1}\frac{\partial \tilde{v}_1}{\partial \tilde{x}_1} + \frac{H_{12}}{H_1 H_2}\tilde{v}_2 + \frac{H_{13}}{H_1 H_3}\tilde{v}_3\right) , \tag{2.89}$$

$$\tilde{\boldsymbol{\sigma}}_{22} = 2\tilde{\eta}\left(\frac{1}{H_2}\frac{\partial \tilde{v}_2}{\partial \tilde{x}_2} + \frac{H_{21}}{H_2 H_1}\tilde{v}_1 + \frac{H_{23}}{H_2 H_3}\tilde{v}_3\right) , \tag{2.90}$$

$$\tilde{\boldsymbol{\sigma}}_{12} = \tilde{\eta}\left(\frac{1}{H_1}\frac{\partial \tilde{v}_2}{\partial \tilde{x}_1} - \frac{H_{12}}{H_1 H_2}\tilde{v}_1 + \frac{1}{H_2}\frac{\partial \tilde{v}_1}{\partial \tilde{x}_2} - \frac{H_{21}}{H_1 H_2}\tilde{v}_2\right) , \tag{2.91}$$

where

$$\tilde{\eta} := \frac{1}{(2\tilde{\mathcal{A}}\mathcal{K})^{\frac{1}{n}}} \left(\left(\frac{1}{H_3} \frac{\partial \tilde{v}_1}{\partial \tilde{x}_3} - \frac{H_{13}}{H_1 H_3} \tilde{v}_1 \right)^2 + \left(\frac{1}{H_3} \frac{\partial \tilde{v}_2}{\partial \tilde{x}_3} - \frac{H_{23}}{H_2 H_3} \tilde{v}_2 \right)^2 \right)^{\frac{1-n}{2n}} , \qquad n = 3 . \tag{2.92}$$

The temperature dependence of $\tilde{\mathcal{A}}(\tilde{T})$ (1.21) is given by

$$\tilde{\mathcal{A}}(\tilde{T}) = \frac{A}{[A]} \exp\left(-\frac{\mathcal{Q}}{\tilde{T}} \right) , \tag{2.93}$$

or, if the pressure-melting point correction is considered as in (1.22):

$$\tilde{\mathcal{A}}(\tilde{T}, \tilde{p}) = \frac{A}{[A]} \exp\left(-\frac{\mathcal{Q}}{(\tilde{T} + \mathcal{T}\tilde{p})} \right) , \tag{2.94}$$

and $\mathcal{Q}$, $\mathcal{T}$ and $\mathcal{K}$ are given in (2.52).

- Example (1) - Cartesian coordinates

$$\tilde{\boldsymbol{\sigma}}_{xz} = \tilde{\eta} \frac{\partial \tilde{v}_x}{\partial \tilde{z}} , \tag{2.95}$$

$$\tilde{\boldsymbol{\sigma}}_{yz} = \tilde{\eta} \frac{\partial \tilde{v}_y}{\partial \tilde{z}} , \tag{2.96}$$

$$\tilde{\boldsymbol{\sigma}}_{xx} = 2\tilde{\eta} \frac{\partial \tilde{v}_x}{\partial \tilde{x}} , \tag{2.97}$$

$$\tilde{\boldsymbol{\sigma}}_{yy} = 2\tilde{\eta} \frac{\partial \tilde{v}_y}{\partial \tilde{y}} , \tag{2.98}$$

$$\tilde{\boldsymbol{\sigma}}_{xy} = \tilde{\eta} \left(\frac{\partial \tilde{v}_y}{\partial \tilde{x}} + \frac{\partial \tilde{v}_x}{\partial \tilde{y}} \right) , \tag{2.99}$$

  where

$$\tilde{\eta} = \frac{1}{(2\tilde{\mathcal{A}}\mathcal{K})^{\frac{1}{n}}} \left(\left(\frac{\partial \tilde{v}_x}{\partial \tilde{z}} \right)^2 + \left(\frac{\partial \tilde{v}_y}{\partial \tilde{z}} \right)^2 \right)^{\frac{1-n}{2n}} , \qquad n = 3 . \tag{2.100}$$

- Example (2) - Spherical coordinates

$$\tilde{\boldsymbol{\sigma}}_{\vartheta\zeta} = \tilde{\eta} \frac{\partial \tilde{v}_\vartheta}{\partial \tilde{\zeta}} , \tag{2.101}$$

$$\tilde{\boldsymbol{\sigma}}_{\varphi\zeta} = \tilde{\eta} \frac{\partial \tilde{v}_\varphi}{\partial \tilde{\zeta}} , \tag{2.102}$$

$$\tilde{\boldsymbol{\sigma}}_{\vartheta\vartheta} = 2\tilde{\eta} \frac{\partial \tilde{v}_\vartheta}{\partial \vartheta} , \tag{2.103}$$

$$\tilde{\boldsymbol{\sigma}}_{\varphi\varphi} = 2\tilde{\eta} \left(\frac{1}{\sin\vartheta} \frac{\partial \tilde{v}_\varphi}{\partial \varphi} + \cot\vartheta \, \tilde{v}_\vartheta \right) , \tag{2.104}$$

$$\tilde{\boldsymbol{\sigma}}_{\vartheta\varphi} = \tilde{\eta} \left(\frac{\partial \tilde{v}_\varphi}{\partial \vartheta} + \frac{1}{\sin\vartheta} \frac{\partial \tilde{v}_\vartheta}{\partial \varphi} - \cot\vartheta \, \tilde{v}_\varphi \right) , \tag{2.105}$$

  where

$$\tilde{\eta} := \frac{1}{(2\tilde{\mathcal{A}}\mathcal{K})^{\frac{1}{n}}} \left(\left(\frac{\partial \tilde{v}_\vartheta}{\partial \tilde{\zeta}} \right)^2 + \left(\frac{\partial \tilde{v}_\varphi}{\partial \tilde{\zeta}} \right)^2 \right)^{\frac{1-n}{2n}} , \qquad n = 3 . \tag{2.106}$$

- Example (3) - Cylindrical coordinates

$$\tilde{\boldsymbol{\sigma}}_{\varrho z} = \tilde{\eta}\frac{\partial \tilde{v}_\varrho}{\partial \tilde{z}}\,, \tag{2.107}$$

$$\tilde{\boldsymbol{\sigma}}_{\varphi z} = \tilde{\eta}\frac{\partial \tilde{v}_\varphi}{\partial \tilde{z}}\,, \tag{2.108}$$

$$\tilde{\boldsymbol{\sigma}}_{\varrho\varrho} = 2\tilde{\eta}\frac{\partial \tilde{v}_\varrho}{\partial \tilde{x}_\varrho}\,, \tag{2.109}$$

$$\tilde{\boldsymbol{\sigma}}_{\varphi\varphi} = 2\tilde{\eta}\left(\frac{1}{\tilde{\varrho}}\frac{\partial \tilde{v}_\varphi}{\partial \varphi} + \frac{\tilde{v}_\varrho}{\tilde{\varrho}}\right)\,, \tag{2.110}$$

$$\tilde{\boldsymbol{\sigma}}_{\varrho\varphi} = \tilde{\eta}\left(\frac{\partial \tilde{v}_\varphi}{\partial \tilde{\varrho}} + \frac{1}{\tilde{\varrho}}\frac{\partial \tilde{v}_\varrho}{\partial \varphi} - \frac{\tilde{v}_\varphi}{\tilde{\varrho}}\right)\,, \tag{2.111}$$

where

$$\tilde{\eta} := \frac{1}{(2\tilde{\mathcal{A}}\mathcal{K})^{\frac{1}{n}}}\left(\left(\frac{\partial \tilde{v}_\varrho}{\partial \tilde{z}}\right)^2 + \left(\frac{\partial \tilde{v}_\varphi}{\partial \tilde{z}}\right)^2\right)^{\frac{1-n}{2n}}\,, \qquad n = 3\,. \tag{2.112}$$

The inverse relation (1.18) in the SIA reads as

$$\frac{1}{H_3}\frac{\partial \tilde{v}_1}{\partial \tilde{x}_3} - \frac{H_{13}}{H_1 H_3}\tilde{v}_1 = 2\mathcal{K}\tilde{\mathcal{A}}\tilde{\boldsymbol{\sigma}}_{II}^{n-1}\tilde{\boldsymbol{\sigma}}_{13}\,, \tag{2.113}$$

$$\frac{1}{H_3}\frac{\partial \tilde{v}_2}{\partial \tilde{x}_3} - \frac{H_{23}}{H_2 H_3}\tilde{v}_2 = 2\mathcal{K}\tilde{\mathcal{A}}\tilde{\boldsymbol{\sigma}}_{II}^{n-1}\tilde{\boldsymbol{\sigma}}_{23}\,, \tag{2.114}$$

$$\frac{1}{H_1}\frac{\partial \tilde{v}_1}{\partial \tilde{x}_1} + \frac{H_{12}}{H_1 H_2}\tilde{v}_2 + \frac{H_{13}}{H_1 H_3}\tilde{v}_3 = \mathcal{K}\tilde{\mathcal{A}}\tilde{\sigma}\tilde{\sigma}_{II}^{n-1}\tilde{\boldsymbol{\sigma}}_{11}\,, \tag{2.115}$$

$$\frac{1}{H_2}\frac{\partial \tilde{v}_2}{\partial \tilde{x}_2} + \frac{H_{21}}{H_1 H_2}\tilde{v}_1 + \frac{H_{23}}{H_2 H_3}\tilde{v}_3 = \mathcal{K}\tilde{\mathcal{A}}\tilde{\boldsymbol{\sigma}}_{II}^{n-1}\tilde{\boldsymbol{\sigma}}_{22}\,, \tag{2.116}$$

$$\frac{1}{H_1}\frac{\partial \tilde{v}_2}{\partial \tilde{x}_1} - \frac{H_{12}}{H_1 H_2}\tilde{v}_1 + \frac{1}{H_2}\frac{\partial \tilde{v}_1}{\partial \tilde{x}_2} - \frac{H_{21}}{H_1 H_2}\tilde{v}_2 = 2\mathcal{K}\tilde{\mathcal{A}}\tilde{\boldsymbol{\sigma}}_{II}^{n-1}\tilde{\boldsymbol{\sigma}}_{12}\,, \tag{2.117}$$

where

$$\tilde{\boldsymbol{\sigma}}_{II} = \sqrt{\tilde{\boldsymbol{\sigma}}_{13}^2 + \tilde{\boldsymbol{\sigma}}_{23}^2}\,. \tag{2.118}$$

- Example (1) - Cartesian coordinates

$$\frac{\partial \tilde{v}_x}{\partial \tilde{z}} = 2\mathcal{K}\tilde{\mathcal{A}}\tilde{\boldsymbol{\sigma}}_{II}^{n-1}\tilde{\boldsymbol{\sigma}}_{xz}\,, \tag{2.119}$$

$$\frac{\partial \tilde{v}_y}{\partial \tilde{z}} = 2\mathcal{K}\tilde{\mathcal{A}}\tilde{\boldsymbol{\sigma}}_{II}^{n-1}\tilde{\boldsymbol{\sigma}}_{yz}\,, \tag{2.120}$$

$$\frac{\partial \tilde{v}_x}{\partial \tilde{x}} = \mathcal{K}\tilde{\mathcal{A}}\tilde{\boldsymbol{\sigma}}_{II}^{n-1}\tilde{\boldsymbol{\sigma}}_{xx}\,, \tag{2.121}$$

$$\frac{\partial \tilde{v}_y}{\partial \tilde{y}} = \mathcal{K}\tilde{\mathcal{A}}\tilde{\boldsymbol{\sigma}}_{II}^{n-1}\tilde{\boldsymbol{\sigma}}_{yy}\,, \tag{2.122}$$

$$\frac{\partial \tilde{v}_y}{\partial \tilde{x}} + \frac{\partial \tilde{v}_x}{\partial \tilde{y}} = 2\mathcal{K}\tilde{\mathcal{A}}\tilde{\boldsymbol{\sigma}}_{II}^{n-1}\tilde{\boldsymbol{\sigma}}_{xy}\,, \tag{2.123}$$

where

$$\tilde{\boldsymbol{\sigma}}_{II} = \sqrt{\tilde{\boldsymbol{\sigma}}_{xz}^2 + \tilde{\boldsymbol{\sigma}}_{yz}^2}\,. \tag{2.124}$$

- Example (2) - Spherical coordinates

$$\frac{\partial \tilde{v}_\vartheta}{\partial \tilde{\zeta}} = 2\mathcal{K}\tilde{\mathcal{A}}\tilde{\boldsymbol{\sigma}}_{II}^{n-1}\tilde{\boldsymbol{\sigma}}_{\vartheta\zeta}\,, \tag{2.125}$$

$$\frac{\partial \tilde{v}_\varphi}{\partial \tilde{\zeta}} = 2\mathcal{K}\tilde{\mathcal{A}}\tilde{\boldsymbol{\sigma}}_{II}^{n-1}\tilde{\boldsymbol{\sigma}}_{\varphi\zeta}\,, \tag{2.126}$$

$$\frac{\partial \tilde{v}_\vartheta}{\partial \vartheta} = \mathcal{K}\tilde{\mathcal{A}}\tilde{\boldsymbol{\sigma}}_{II}^{n-1}\tilde{\boldsymbol{\sigma}}_{\vartheta\vartheta}\,, \tag{2.127}$$

$$\frac{1}{\sin\vartheta}\frac{\partial \tilde{v}_\varphi}{\partial \varphi} + \cot\vartheta\ \tilde{v}_\vartheta = \mathcal{K}\tilde{\mathcal{A}}\tilde{\boldsymbol{\sigma}}_{II}^{n-1}\tilde{\boldsymbol{\sigma}}_{\varphi\varphi}\,, \tag{2.128}$$

$$\frac{\partial \tilde{v}_\varphi}{\partial \vartheta} + \frac{1}{\sin\vartheta}\frac{\partial \tilde{v}_\vartheta}{\partial \varphi} - \cot\vartheta\ \tilde{v}_\varphi = 2\mathcal{K}\tilde{\mathcal{A}}\tilde{\boldsymbol{\sigma}}_{II}^{n-1}\tilde{\boldsymbol{\sigma}}_{\vartheta\varphi}\,, \tag{2.129}$$

where

$$\tilde{\boldsymbol{\sigma}}_{II} = \sqrt{\tilde{\boldsymbol{\sigma}}_{\vartheta\zeta}^2 + \tilde{\boldsymbol{\sigma}}_{\varphi\zeta}^2}\,. \tag{2.130}$$

- Example (3) - Cylindrical coordinates

$$\frac{\partial \tilde{v}_\varrho}{\partial \tilde{z}} = 2\mathcal{K}\tilde{\mathcal{A}}\tilde{\boldsymbol{\sigma}}_{II}^{n-1}\tilde{\boldsymbol{\sigma}}_{\varrho z}\,, \tag{2.131}$$

$$\frac{\partial \tilde{v}_\varphi}{\partial \tilde{z}} = 2\mathcal{K}\tilde{\mathcal{A}}\tilde{\boldsymbol{\sigma}}_{II}^{n-1}\tilde{\boldsymbol{\sigma}}_{\varphi z}\,, \tag{2.132}$$

$$\frac{\partial \tilde{v}_\varrho}{\partial \tilde{\varrho}} = \mathcal{K}\tilde{\mathcal{A}}\tilde{\boldsymbol{\sigma}}_{II}^{n-1}\tilde{\boldsymbol{\sigma}}_{\varrho\varrho}\,, \tag{2.133}$$

$$\frac{1}{\tilde{\varrho}}\frac{\partial \tilde{v}_\varphi}{\partial \varphi} + \frac{\tilde{v}_\varrho}{\tilde{\varrho}} = \mathcal{K}\tilde{\mathcal{A}}\tilde{\boldsymbol{\sigma}}_{II}^{n-1}\tilde{\boldsymbol{\sigma}}_{\varphi\varphi}\,, \tag{2.134}$$

$$\frac{\partial \tilde{v}_\varphi}{\partial \tilde{\varrho}} + \frac{1}{\tilde{\varrho}}\frac{\partial \tilde{v}_\varrho}{\partial \varphi} - \frac{\tilde{v}_\varphi}{\tilde{\varrho}} = 2\mathcal{K}\tilde{\mathcal{A}}\tilde{\boldsymbol{\sigma}}_{II}^{n-1}\tilde{\boldsymbol{\sigma}}_{\varrho\varphi}\,, \tag{2.135}$$

where

$$\tilde{\boldsymbol{\sigma}}_{II} = \sqrt{\tilde{\boldsymbol{\sigma}}_{\varrho z}^2 + \tilde{\boldsymbol{\sigma}}_{\varphi z}^2}\,. \tag{2.136}$$

The **energy balance** (1.28) in the SIA limit reads as

$$\begin{aligned}\tilde{c}_v\left(\frac{\partial \tilde{T}}{\partial \tilde{t}} + \frac{\tilde{v}_1}{H_1}\frac{\partial \tilde{T}}{\partial \tilde{x}_1} + \frac{\tilde{v}_2}{H_2}\frac{\partial \tilde{T}}{\partial \tilde{x}_2} + \frac{\tilde{v}_3}{H_3}\frac{\partial \tilde{T}}{\partial \tilde{x}_3}\right) &= 2\mathcal{C}\left(\tilde{\boldsymbol{\sigma}}_{13}\tilde{\boldsymbol{d}}_{13} + \tilde{\boldsymbol{\sigma}}_{23}\tilde{\boldsymbol{d}}_{23}\right)\\ &+\mathcal{D}\left(\tilde{k}\frac{\partial \tilde{T}}{\partial \tilde{x}_3}\left(\frac{H_{13}}{H_1H_3^2} + \frac{H_{23}}{H_2H_3^2}\right) + \frac{1}{H_3}\frac{\partial}{\partial \tilde{x}_3}\left(\frac{\tilde{k}}{H_3}\frac{\partial \tilde{T}}{\partial \tilde{x}_3}\right)\right)\,,\end{aligned} \tag{2.137}$$

with $\mathcal{C}$, and $\mathcal{D}$ given in (2.52) and

$$\tilde{\boldsymbol{d}}_{13} = \frac{1}{2}\left(\frac{1}{H_3}\frac{\partial \tilde{v}_1}{\partial \tilde{x}_3} - \frac{H_{13}}{H_1H_3}\tilde{v}_1\right)\,, \tag{2.138}$$

$$\tilde{\boldsymbol{d}}_{23} = \frac{1}{2}\left(\frac{1}{H_3}\frac{\partial \tilde{v}_2}{\partial \tilde{x}_3} - \frac{H_{23}}{H_2H_3}\tilde{v}_2\right)\,. \tag{2.139}$$

- Example (1) - Cartesian coordinates

$$\tilde{c}_v \left(\frac{\partial \tilde{T}}{\partial \tilde{t}} + \tilde{v}_x \frac{\partial \tilde{T}}{\partial \tilde{x}} + \tilde{v}_y \frac{\partial \tilde{T}}{\partial \tilde{y}} + \tilde{v}_z \frac{\partial \tilde{T}}{\partial \tilde{z}} \right) = 2\mathcal{C} \left(\tilde{\boldsymbol{\sigma}}_{xz} \tilde{\boldsymbol{d}}_{xz} + \tilde{\boldsymbol{\sigma}}_{yz} \tilde{\boldsymbol{d}}_{yz} \right) + \mathcal{D} \frac{\partial}{\partial \tilde{z}} \left(\tilde{k} \frac{\partial \tilde{T}}{\partial \tilde{z}} \right) , \tag{2.140}$$

and

$$\tilde{\boldsymbol{d}}_{xz} = \frac{1}{2} \frac{\partial \tilde{v}_x}{\partial \tilde{z}} , \tag{2.141}$$

$$\tilde{\boldsymbol{d}}_{yz} = \frac{1}{2} \frac{\partial \tilde{v}_y}{\partial \tilde{z}} . \tag{2.142}$$

- Example (2) - Spherical coordinates

$$\tilde{c}_v \left(\frac{\partial \tilde{T}}{\partial \tilde{t}} + \tilde{v}_\vartheta \frac{\partial \tilde{T}}{\partial \vartheta} + \frac{\tilde{v}_\varphi}{\sin \vartheta} \frac{\partial \tilde{T}}{\partial \varphi} + \tilde{v}_\zeta \frac{\partial \tilde{T}}{\partial \tilde{\zeta}} \right) = 2\mathcal{C} \left(\tilde{\boldsymbol{\sigma}}_{\vartheta\zeta} \tilde{\boldsymbol{d}}_{\vartheta\zeta} + \tilde{\boldsymbol{\sigma}}_{\varphi\zeta} \tilde{\boldsymbol{d}}_{\varphi\zeta} \right) + \mathcal{D} \frac{\partial}{\partial \tilde{\zeta}} \left(\tilde{k} \frac{\partial \tilde{T}}{\partial \tilde{\zeta}} \right) , \tag{2.143}$$

and

$$\tilde{\boldsymbol{d}}_{\vartheta\zeta} = \frac{1}{2} \frac{\partial \tilde{v}_\vartheta}{\partial \tilde{\zeta}} , \tag{2.144}$$

$$\tilde{\boldsymbol{d}}_{\varphi\zeta} = \frac{1}{2} \frac{\partial \tilde{v}_\varphi}{\partial \tilde{\zeta}} . \tag{2.145}$$

- Example (3) - Cylindrical coordinates

$$\tilde{c}_v \left(\frac{\partial \tilde{T}}{\partial \tilde{t}} + \tilde{v}_\varrho \frac{\partial \tilde{T}}{\partial \tilde{\varrho}} + \frac{\tilde{v}_\varphi}{\tilde{\varrho}} \frac{\partial \tilde{T}}{\partial \varphi} + \tilde{v}_z \frac{\partial \tilde{T}}{\partial \tilde{z}} \right) = 2\mathcal{C} \left(\tilde{\boldsymbol{\sigma}}_{\varrho z} \tilde{\boldsymbol{d}}_{\varrho z} + \tilde{\boldsymbol{\sigma}}_{\varphi z} \tilde{\boldsymbol{d}}_{\varphi z} \right) + \mathcal{D} \frac{\partial}{\partial \tilde{z}} \left(\tilde{k} \frac{\partial \tilde{T}}{\partial \tilde{z}} \right) , \tag{2.146}$$

and

$$\tilde{\boldsymbol{d}}_{\varrho z} = \frac{1}{2} \frac{\partial \tilde{v}_\varrho}{\partial \tilde{z}} , \tag{2.147}$$

$$\tilde{\boldsymbol{d}}_{\varphi z} = \frac{1}{2} \frac{\partial \tilde{v}_\varphi}{\partial \tilde{z}} . \tag{2.148}$$

2.4.2 Field equations – Temperate-ice zone

The **mass balance for the ice component** (1.40) in the SIA limit reads as

$$\begin{aligned} &\frac{1}{H_1} \frac{\partial \tilde{v}_1}{\partial \tilde{x}_1} + \frac{H_{12}}{H_1 H_2} \tilde{v}_2 + \frac{H_{13}}{H_1 H_3} \tilde{v}_3 + \frac{1}{H_2} \frac{\partial \tilde{v}_2}{\partial \tilde{x}_2} + \frac{H_{23}}{H_2 H_3} \tilde{v}_3 + \frac{H_{21}}{H_2 H_1} \tilde{v}_1 \\ &+ \frac{1}{H_3} \frac{\partial \tilde{v}_3}{\partial \tilde{x}_3} + \frac{H_{31}}{H_3 H_1} \tilde{v}_1 + \frac{H_{32}}{H_3 H_2} \tilde{v}_2 = -\mathcal{J} \left(\frac{1}{H_3} \frac{\partial \tilde{j}_3}{\partial \tilde{x}_3} + \tilde{j}_3 \left(\frac{H_{13}}{H_1 H_3} + \frac{H_{23}}{H_2 H_3} \right) \right) , \end{aligned} \tag{2.149}$$

where $\mathcal{J}$ is listed among the dimensionless numbers in (2.52).

- Example (1) - Cartesian coordinates

$$\frac{\partial \tilde{v}_x}{\partial \tilde{x}} + \frac{\partial \tilde{v}_y}{\partial \tilde{y}} + \frac{\partial \tilde{v}_z}{\partial \tilde{z}} = -\mathcal{J}\frac{\partial \tilde{j}_z}{\partial \tilde{z}} \ ,$$

- Example (2) - Spherical coordinates

$$\frac{\partial \tilde{v}_\vartheta}{\partial \vartheta} + \frac{1}{\sin\vartheta}\frac{\partial \tilde{v}_\varphi}{\partial \varphi} + \cot\vartheta\ \tilde{v}_\vartheta + \frac{\partial \tilde{v}_\zeta}{\partial \tilde{\zeta}} = -\mathcal{J}\frac{\partial \tilde{j}_\zeta}{\partial \tilde{\zeta}} \ .$$

- Example (3) - Cylindrical coordinates

$$\frac{\partial \tilde{v}_\varrho}{\partial \tilde{\varrho}} + \frac{1}{\tilde{\varrho}}\frac{\partial \tilde{v}_\varphi}{\partial \varphi} + \frac{\tilde{v}_\varrho}{\tilde{\varrho}} + \frac{\partial \tilde{v}_z}{\partial \tilde{z}} = -\mathcal{J}\frac{\partial \tilde{j}_z}{\partial \tilde{z}} \ .$$

The **mass balance for the water component** (1.41) with the water production term m_w derived from the energy balance (1.49) with (1.50), takes the SIA limit in the form

$$\begin{aligned}
&\frac{\partial \tilde{w}}{\partial \tilde{t}} + \frac{\tilde{v}_1}{H_1}\frac{\partial \tilde{w}}{\partial \tilde{x}_1} + \frac{\tilde{v}_2}{H_2}\frac{\partial \tilde{w}}{\partial \tilde{x}_2} + \frac{\tilde{v}_3}{H_3}\frac{\partial \tilde{w}}{\partial \tilde{x}_3} + \frac{\mathcal{J}}{[w]}\left(\frac{1}{H_3}\frac{\partial \tilde{j}_3}{\partial \tilde{x}_3} + \tilde{j}_3\left(\frac{H_{13}}{H_1H_3} + \frac{H_{23}}{H_2H_3}\right)\right) \\
= \ & 2\mathcal{E}(\tilde{\boldsymbol{\sigma}}_{13}\tilde{\boldsymbol{d}}_{13} + \tilde{\boldsymbol{\sigma}}_{23}\tilde{\boldsymbol{d}}_{23}) + \frac{\mathcal{D}\mathcal{E}}{\mathcal{C}}\left(\frac{1}{H_3}\frac{\partial}{\partial \tilde{x}_3}\left(\frac{\tilde{k}}{H_3}\frac{\partial \tilde{T}_m}{\partial \tilde{x}_3}\right) + \tilde{k}\frac{H_{13}}{H_1H_3^2}\frac{\partial \tilde{T}_m}{\partial \tilde{x}_3} + \tilde{k}\frac{H_{23}}{H_2H_3^2}\frac{\partial \tilde{T}_m}{\partial \tilde{x}_3}\right) \\
- \ & \frac{\mathcal{E}}{\mathcal{C}}\tilde{c}_v\left(\frac{\partial \tilde{T}_m}{\partial \tilde{t}} + \frac{\tilde{v}_1}{H_1}\frac{\partial \tilde{T}_m}{\partial \tilde{x}_1} + \frac{\tilde{v}_2}{H_2}\frac{\partial \tilde{T}_m}{\partial \tilde{x}_2} + \frac{\tilde{v}_3}{H_3}\frac{\partial \tilde{T}_m}{\partial \tilde{x}_3}\right) \ .
\end{aligned} \tag{2.150}$$

This form can be further simplified by inserting the Clausius-Clapeyron relation (2.161) and subsequent partial integration of the linear momentum equations, which results in an explicit formula for pressure. We, however, will not perform this simplification here.

- Example (1) - Cartesian coordinates

$$\begin{aligned}
&\frac{\partial \tilde{w}}{\partial \tilde{t}} + \tilde{v}_x\frac{\partial \tilde{w}}{\partial \tilde{x}} + \tilde{v}_y\frac{\partial \tilde{w}}{\partial \tilde{y}} + \tilde{v}_z\frac{\partial \tilde{w}}{\partial \tilde{z}} + \frac{\mathcal{J}}{[w]}\frac{\partial \tilde{j}_z}{\partial \tilde{z}} = 2\mathcal{E}(\tilde{\boldsymbol{\sigma}}_{xz}\tilde{\boldsymbol{d}}_{xz} + \tilde{\boldsymbol{\sigma}}_{yz}\tilde{\boldsymbol{d}}_{yz}) \\
+ \ & \frac{\mathcal{D}\mathcal{E}}{\mathcal{C}}\frac{\partial}{\partial \tilde{z}}\left(\tilde{k}\frac{\partial \tilde{T}_m}{\partial \tilde{z}}\right) - \frac{\mathcal{E}}{\mathcal{C}}\tilde{c}_v\left(\frac{\partial \tilde{T}_m}{\partial \tilde{t}} + \tilde{v}_x\frac{\partial \tilde{T}_m}{\partial \tilde{x}} + \tilde{v}_y\frac{\partial \tilde{T}_m}{\partial \tilde{y}} + \tilde{v}_z\frac{\partial \tilde{T}_m}{\partial \tilde{z}}\right) \ .
\end{aligned} \tag{2.151}$$

- Example (2) - Spherical coordinates

$$\begin{aligned}
&\frac{\partial \tilde{w}}{\partial \tilde{t}} + \tilde{v}_\vartheta\frac{\partial \tilde{w}}{\partial \vartheta} + \frac{\tilde{v}_\varphi}{\sin\vartheta}\frac{\partial \tilde{w}}{\partial \varphi} + \tilde{v}_\zeta\frac{\partial \tilde{w}}{\partial \tilde{\zeta}} + \frac{\mathcal{J}}{[w]}\frac{\partial \tilde{j}_\zeta}{\partial \tilde{\zeta}} = 2\mathcal{E}(\tilde{\boldsymbol{\sigma}}_{\vartheta\zeta}\tilde{\boldsymbol{d}}_{\vartheta\zeta} + \tilde{\boldsymbol{\sigma}}_{\varphi\zeta}\tilde{\boldsymbol{d}}_{\varphi\zeta}) \\
+ \ & \frac{\mathcal{D}\mathcal{E}}{\mathcal{C}}\frac{\partial}{\partial \tilde{\zeta}}\left(\tilde{k}\frac{\partial \tilde{T}_m}{\partial \tilde{\zeta}}\right) - \frac{\mathcal{E}}{\mathcal{C}}\tilde{c}_v\left(\frac{\partial \tilde{T}_m}{\partial \tilde{t}} + \tilde{v}_\vartheta\frac{\partial \tilde{T}_m}{\partial \vartheta} + \frac{\tilde{v}_\varphi}{\sin\vartheta}\frac{\partial \tilde{T}_m}{\partial \varphi} + \tilde{v}_\zeta\frac{\partial \tilde{T}_m}{\partial \tilde{\zeta}}\right) \ .
\end{aligned} \tag{2.152}$$

- Example (3) - Cylindrical coordinates

$$\frac{\partial\tilde{w}}{\partial\tilde{t}}+\tilde{v}_{\varrho}\frac{\partial\tilde{w}}{\partial\tilde{\varrho}}+\frac{\tilde{v}_{\varphi}}{\tilde{\varrho}}\frac{\partial\tilde{w}}{\partial\varphi}+\tilde{v}_{z}\frac{\partial\tilde{w}}{\partial\tilde{z}}+\frac{\mathcal{J}}{[w]}\frac{\partial\tilde{j}_{z}}{\partial\tilde{z}}=2\mathcal{E}(\tilde{\boldsymbol{\sigma}}_{\varrho z}\tilde{\boldsymbol{d}}_{\varrho z}+\tilde{\boldsymbol{\sigma}}_{\varphi z}\tilde{\boldsymbol{d}}_{\varphi z})$$
$$+\quad\frac{\mathcal{D}\mathcal{E}}{\mathcal{C}}\frac{\partial}{\partial\tilde{z}}\left(\tilde{k}\frac{\partial\tilde{T}_{m}}{\partial\tilde{z}}\right)-\frac{\mathcal{E}}{\mathcal{C}}\tilde{c}_{v}\left(\frac{\partial\tilde{T}_{m}}{\partial\tilde{t}}+\tilde{v}_{\varrho}\frac{\partial\tilde{T}_{m}}{\partial\tilde{\varrho}}+\frac{\tilde{v}_{\varphi}}{\tilde{\varrho}}\frac{\partial\tilde{T}_{m}}{\partial\varphi}+\tilde{v}_{z}\frac{\partial\tilde{T}_{m}}{\partial\tilde{z}}\right)\,. \tag{2.153}$$

The **linear momentum balance for the ice component** is given by (1.42). We have seen that, in the SIA-I limit for cold-ice, the linear momentum balance can be simplified such that the inertia terms on the left-hand sides of (2.71)-(2.73) related to the ice component may are omitted due to the very small Froude number $\mathcal{F}$. Now, in (1.42), the same argumentation applies and enables us to neglect the inertia term corresponding to the ice component. The resultant relation in the SIA limit reads as

$$\begin{aligned}
&\lim_{SIA}(\epsilon\mathcal{F}\mathcal{J})\,\tilde{w}\left(\frac{\partial\tilde{v}_{w1}}{\partial\tilde{t}}+\frac{\mathcal{J}}{[w]}\left(\frac{\tilde{v}_{w3}}{H_3}\frac{\partial\tilde{v}_{w1}}{\partial\tilde{x}_3}+\tilde{v}_{w1}\tilde{v}_{w3}\frac{H_{13}}{H_1H_3}-\tilde{v}_{w3}^2\frac{H_{31}}{H_1H_3}\right)\right)\\
=\;&-\frac{1}{H_1}\frac{\partial\tilde{p}}{\partial\tilde{x}_1}+\tilde{\boldsymbol{\sigma}}_{13}\left(2\frac{H_{13}}{H_1H_3}+\frac{H_{23}}{H_2H_3}\right)+\frac{1}{H_3}\frac{\partial\tilde{\boldsymbol{\sigma}}_{13}}{\partial\tilde{x}_3}+e_{g\,1}\,, &(2.154)\\
&\lim_{SIA}(\epsilon\mathcal{F}\mathcal{J})\,\tilde{w}\left(\frac{\partial\tilde{v}_{w2}}{\partial\tilde{t}}+\frac{\mathcal{J}}{[w]}\left(\frac{\tilde{v}_{w3}}{H_3}\frac{\partial\tilde{v}_{w2}}{\partial\tilde{x}_3}+\tilde{v}_{w2}\tilde{v}_{w3}\frac{H_{23}}{H_2H_3}-\tilde{v}_{w3}^2\frac{H_{32}}{H_2H_3}\right)\right)\\
=\;&-\frac{1}{H_2}\frac{\partial\tilde{p}}{\partial\tilde{x}_2}+\tilde{\boldsymbol{\sigma}}_{23}\left(\frac{H_{13}}{H_1H_3}+2\frac{H_{23}}{H_2H_3}\right)+\frac{1}{H_3}\frac{\partial\tilde{\boldsymbol{\sigma}}_{23}}{\partial\tilde{x}_3}+e_{g\,2}\,, &(2.155)\\
&\lim_{SIA}(\epsilon\mathcal{F}\mathcal{J})\,\tilde{w}\left(\frac{\partial\tilde{v}_{w3}}{\partial\tilde{t}}+\frac{\mathcal{J}}{[w]}\frac{\tilde{v}_{w3}}{H_3}\frac{\partial\tilde{v}_{w3}}{\partial\tilde{x}_3}\right)=-\frac{1}{H_3}\frac{\partial\tilde{p}}{\partial\tilde{x}_3}+e_{g\,3}\,. &(2.156)
\end{aligned}$$

The symbol $\lim_{SIA}$ stands for the SIA limit, which is now more difficult to evaluate, because the tilded terms on the left-hand sides of (2.154)-(2.156) are not of the order of unity. Namely, we should, in general assume that the typical spatial and time scales of the water transport processes substantially differ from the scales appropriate for the ice flow. We will, however, still assume that the inertia force of the water component, i.e. the left hand sides of (2.154)-(2.156) can be omitted and the linear momentum equations then take the same form as for a cold ice, i.e. (2.74)-(2.76).

We need not consider all three **linear momentum balance equations for the water component**, because only the vertical component of water flux appears in the SIA limit. The third equation in (1.44) in the SIA limit reads as

$$\tilde{j}_{3}=-\mathcal{N}_{1}\frac{\tilde{\alpha}_{1}}{H_3}\frac{\partial\tilde{w}}{\partial\tilde{x}_3}\;-\mathcal{N}_{2}\tilde{\alpha}_{2}\left(\frac{1}{H_3}\frac{\partial(\tilde{p}\tilde{w})}{\partial\tilde{x}_3}-\tilde{w}e_{g\,3}\right), \tag{2.157}$$

where $\mathcal{N}_1, \mathcal{N}_2$ are listed among the dimensionless numbers in (2.52).

- Example (1) - Cartesian coordinates - (2.157) reads as

$$\tilde{j}_{z}=-\mathcal{N}_{1}\tilde{\alpha}_{1}\frac{\partial\tilde{w}}{\partial\tilde{z}}\;-\mathcal{N}_{2}\tilde{\alpha}_{2}\left(\frac{\partial(\tilde{p}\tilde{w})}{\partial\tilde{z}}+\tilde{w}\right). \tag{2.158}$$

- Example (2) - Spherical coordinates - (2.157) reads as

$$\tilde{j}_{\zeta}=-\mathcal{N}_{1}\tilde{\alpha}_{1}\frac{\partial\tilde{w}}{\partial\tilde{\zeta}}\;-\mathcal{N}_{2}\tilde{\alpha}_{2}\left(\frac{\partial(\tilde{p}\tilde{w})}{\partial\tilde{\zeta}}+\tilde{w}\right). \tag{2.159}$$

- Example (3) - Cylindrical coordinates - (2.157) reads as

$$\tilde{j}_z = -\mathcal{N}_1\tilde{\alpha}_1\frac{\partial\tilde{w}}{\partial\tilde{z}} - \mathcal{N}_2\tilde{\alpha}_2\left(\frac{\partial(\tilde{p}\tilde{w})}{\partial\tilde{z}} + \tilde{w}\right). \tag{2.160}$$

The **energy balance** (1.49) in the SIA limit was already used in the mass balance for water component (2.150) and need not be considered separately. The temperature-pressure relation given by Clausius-Clapeyron equation (1.48) in the SIA limit reads as

$$\tilde{T}_m(\tilde{p}) = \mathcal{T}_0 - \mathcal{T}\tilde{p}\,, \tag{2.161}$$

with the dimensionless numbers $\mathcal{T}_0$, $\mathcal{T}$ defined in (2.52).

The **rheology** for the temperate-ice zone as seen from a comparison of (1.51) and (1.17) is the same as for the cold-ice zone, except that the rate factor $\mathcal{A}(w)$ depends on the water content w. The same applies for the SIA limit. Thus, (2.87)-(2.136) are the correct SIA rheological relations with $\tilde{\mathcal{A}}$ now depending on $\tilde{w}$, e.g. for (1.53) through an expression

$$\tilde{\mathcal{A}} = \frac{A}{[A]}(1+\gamma[w]\tilde{w})\exp\left(-\frac{\mathcal{Q}}{\mathcal{T}_0}\right). \tag{2.162}$$

2.4.3 Boundary conditions - Free surface

The **kinematic condition** (1.55) at the free surface which is a temperate-ice – air interface, with the use of the mass balance for ice component (1.56), takes the SIA limit in the form

$$\frac{\partial\tilde{F}_s}{\partial\tilde{t}} + \frac{\tilde{v}_1}{H_1}\frac{\partial\tilde{F}_s}{\partial\tilde{x}_1} + \frac{\tilde{v}_2}{H_2}\frac{\partial\tilde{F}_s}{\partial\tilde{x}_2} + \frac{\tilde{v}_3}{H_3}\frac{\partial\tilde{F}_s}{\partial\tilde{x}_3} = -\frac{\tilde{a}^s}{1-[w]\tilde{w}}\left|\frac{1}{H_3}\frac{\partial\tilde{F}_s}{\partial\tilde{x}_3}\right|, \tag{2.163}$$

while for the cold-ice – air interface, we only set $\tilde{w}=0$ in (2.163).

- Example (1) - Cartesian coordinates

$$\frac{\partial\tilde{F}_s}{\partial\tilde{t}} + \tilde{v}_x\frac{\partial\tilde{F}_s}{\partial\tilde{x}} + \tilde{v}_y\frac{\partial\tilde{F}_s}{\partial\tilde{y}} + \tilde{v}_z\frac{\partial\tilde{F}_s}{\partial\tilde{z}} = -\frac{\tilde{a}^s}{1-[w]\tilde{w}}\left|\frac{\partial\tilde{F}_s}{\partial\tilde{z}}\right|. \tag{2.164}$$

- Example (2) - Spherical coordinates

$$\frac{\partial\tilde{F}_s}{\partial\tilde{t}} + \tilde{v}_\vartheta\frac{\partial\tilde{F}_s}{\partial\vartheta} + \frac{\tilde{v}_\varphi}{\sin\vartheta}\frac{\partial\tilde{F}_s}{\partial\varphi} + \tilde{v}_\zeta\frac{\partial\tilde{F}_s}{\partial\tilde{\zeta}} = -\frac{\tilde{a}^s}{1-[w]\tilde{w}}\left|\frac{\partial\tilde{F}_s}{\partial\tilde{\zeta}}\right|. \tag{2.165}$$

- Example (3) - Cylindrical coordinates

$$\frac{\partial\tilde{F}_s}{\partial\tilde{t}} + \tilde{v}_\varrho\frac{\partial\tilde{F}_s}{\partial\tilde{\varrho}} + \frac{\tilde{v}_\varphi}{\tilde{\varrho}}\frac{\partial\tilde{F}_s}{\partial\varphi} + \tilde{v}_z\frac{\partial\tilde{F}_s}{\partial\tilde{z}} = -\frac{\tilde{a}^s}{1-[w]\tilde{w}}\left|\frac{\partial\tilde{F}_s}{\partial\tilde{z}}\right|. \tag{2.166}$$

The **water flux** boundary condition for the case of temperate-ice – air interface (1.58) in the SIA limit reads as

$$\tilde{j}_3 = -\frac{\tilde{\mathcal{P}}^s}{\mathcal{J}}\,, \tag{2.167}$$

and, of course, need not be considered for cold-ice – air interface.

- Example (1) - Cartesian and cylindrical coordinates

$$\tilde{j}_z = -\frac{\tilde{\mathcal{P}}^s}{\mathcal{J}} \,. \tag{2.168}$$

- Example (2) - Spherical coordinates

$$\tilde{j}_\zeta = -\frac{\tilde{\mathcal{P}}^s}{\mathcal{J}} \,. \tag{2.169}$$

The linear momentum boundary condition (1.60) takes the SIA form as

$$\tilde{p} = \mathcal{L} \,, \qquad \tilde{\boldsymbol{\sigma}}_{13} = 0 \,, \qquad \tilde{\boldsymbol{\sigma}}_{23} = 0 \,, \tag{2.170}$$

where the dimensionless number $\mathcal{L}$ is listed in (2.52).

- Example (1) - Cartesian coordinates

$$\tilde{p} = \mathcal{L} \,, \qquad \tilde{\boldsymbol{\sigma}}_{xz} = 0 \,, \qquad \tilde{\boldsymbol{\sigma}}_{yz} = 0 \,. \tag{2.171}$$

- Example (2) - Spherical coordinates

$$\tilde{p} = \mathcal{L} \,, \qquad \tilde{\boldsymbol{\sigma}}_{\vartheta\zeta} = 0 \,, \qquad \tilde{\boldsymbol{\sigma}}_{\varphi\zeta} = 0 \,. \tag{2.172}$$

- Example (3) - Cylindrical coordinates

$$\tilde{p} = \mathcal{L} \,, \qquad \tilde{\boldsymbol{\sigma}}_{\varrho z} = 0 \,, \qquad \tilde{\boldsymbol{\sigma}}_{\varphi z} = 0 \,. \tag{2.173}$$

The **energy** boundary condition for the cold-ice free surface takes the form of a Dirichlet boundary condition for surface temperature, c.f. (1.30), i.e.

$$\tilde{T} = \tilde{T}(\tilde{x}_1, \tilde{x}_2, \tilde{f}_s(\tilde{x}_1, \tilde{x}_2, \tilde{t}), \tilde{t}) \,, \tag{2.174}$$

while for the temperate-ice free surface, the energy boundary condition would be a condition constraining the melting-refreezing rate, but since we assume this rate to be a part of the prescribed climatological inputs $\mathcal{P}^s$ and a^s, it need not be explicitly taken into account.

2.4.4 Boundary conditions - Glacier base

The **kinematic condition** is not considered, as the base geometry is assumed to be prescribed c.f. (1.62), i.e. $\tilde{F}_b(\tilde{x}_1, \tilde{x}_2, \tilde{x}_3, \tilde{t})$ is given.

The **ice mass balance** condition (1.63) takes the SIA limit form as

$$\frac{(\tilde{v} - \tilde{\nu}_b)_1}{H_1}\frac{\partial \tilde{F}_b}{\partial \tilde{x}_1} + \frac{(\tilde{v} - \tilde{\nu}_b)_2}{H_2}\frac{\partial \tilde{F}_b}{\partial \tilde{x}_2} + \frac{(\tilde{v} - \tilde{\nu}_b)_3}{H_3}\frac{\partial \tilde{F}_b}{\partial \tilde{x}_3} = -\frac{\tilde{m}_w^b}{1 - [w]\tilde{w}}\left|\frac{1}{H_3}\frac{\partial \tilde{F}_b}{\partial \tilde{x}_3}\right| \,. \tag{2.175}$$

- Example (1) - Cartesian coordinates

$$(\tilde{v} - \tilde{\nu}_b)_x\frac{\partial \tilde{F}_b}{\partial \tilde{x}} + (\tilde{v} - \tilde{\nu}_b)_y\frac{\partial \tilde{F}_b}{\partial \tilde{y}} + (\tilde{v} - \tilde{\nu}_b)_z\frac{\partial \tilde{F}_b}{\partial \tilde{z}} = -\frac{\tilde{m}_w^b}{1 - [w]\tilde{w}}\left|\frac{\partial \tilde{F}_b}{\partial \tilde{z}}\right| \,. \tag{2.176}$$

- Example (2) - Spherical coordinates

$$(\tilde{v}-\tilde{\nu}_b)_\vartheta \frac{\partial \tilde{F}_b}{\partial \vartheta} + \frac{(\tilde{v}-\tilde{\nu}_b)_\varphi}{\sin\vartheta}\frac{\partial \tilde{F}_b}{\partial \varphi} + (\tilde{v}-\tilde{\nu}_b)_\zeta \frac{\partial \tilde{F}_b}{\partial \tilde{\zeta}} = -\frac{\tilde{m}_w^b}{1-[w]\tilde{w}}\left|\frac{\partial \tilde{F}_b}{\partial \tilde{\zeta}}\right| . \tag{2.177}$$

- Example (3) - Cylindrical coordinates

$$(\tilde{v}-\tilde{\nu}_b)_\varrho \frac{\partial \tilde{F}_b}{\partial \tilde{\varrho}} + \frac{(\tilde{v}-\tilde{\nu}_b)_\varphi}{\tilde{\varrho}}\frac{\partial \tilde{F}_b}{\partial \varphi} + (\tilde{v}-\tilde{\nu}_b)_z \frac{\partial \tilde{F}_b}{\partial \tilde{z}} = -\frac{\tilde{m}_w^b}{1-[w]\tilde{w}}\left|\frac{\partial \tilde{F}_b}{\partial \tilde{z}}\right| . \tag{2.178}$$

The **water mass balance** condition (1.64) reads now as

$$\tilde{\dot{j}}_3 = \frac{1}{\mathcal{J}}\left(\frac{\tilde{m}_w^b}{1-[w]\tilde{w}} - \tilde{o}^b\right) . \tag{2.179}$$

- Example (1) - Cartesian and cylindrical coordinates

$$\tilde{\dot{j}}_z = \frac{1}{\mathcal{J}}\left(\frac{\tilde{m}_w^b}{1-[w]\tilde{w}} - \tilde{o}^b\right) . \tag{2.180}$$

- Example (2) - Spherical coordinates

$$\tilde{\dot{j}}_\zeta = \frac{1}{\mathcal{J}}\left(\frac{\tilde{m}_w^b}{1-[w]\tilde{w}} - \tilde{o}^b\right) . \tag{2.181}$$

The **linear momentum** boundary condition (1.66) will not be considered in the SIA limit as, firstly we would have to prescribe a scaling for the stress tensor in the lithosphere $\boldsymbol{\tau}_b$, which is not convenient, and secondly, this condition is necessary only for computing lithosphere deformations, which we do not explicitly discuss here. The proper boundary condition for the ice flow is either a Dirichlet condition for velocity in the case of no-slip frozen-bed conditions at the base or a Newton-type condition when sliding occurs and the sliding law is specified, combined with the normal-flux condition resulting from the ice-mass balance (2.175).

The **no-slip** boundary condition (1.31) is required for the frozen-bed conditions, i.e. at the contact of the cold-ice and bedrock, when the ice temperature is below the pressure melting point, and reads as

$$\vec{\tilde{v}} = \vec{\tilde{\nu}}_b , \qquad \tilde{T} < \tilde{T}_m . \tag{2.182}$$

The **sliding-law** has to be specified for the ice-bedrock interface at the pressure melting point i.e. $\tilde{T} = \tilde{T}_m$. Considering the particular type of sliding law as (1.68), the SIA limit takes the form

$$\tilde{\beta}^2 \tilde{v}_1^{sl} = \mathcal{B}\,\tilde{\boldsymbol{\sigma}}_{13} , \tag{2.183}$$

$$\tilde{\beta}^2 \tilde{v}_2^{sl} = \mathcal{B}\,\tilde{\boldsymbol{\sigma}}_{23} , \tag{2.184}$$

$$\tilde{\beta}^2 \tilde{v}_3^{sl} = \mathcal{B}\left(\tilde{\boldsymbol{\sigma}}_{13}\frac{\frac{1}{H_1}\frac{\partial \tilde{F}_b}{\partial \tilde{x}_1}}{\left|\frac{1}{H_3}\frac{\partial \tilde{F}_b}{\partial \tilde{x}_3}\right|} + \tilde{\boldsymbol{\sigma}}_{23}\frac{\frac{1}{H_2}\frac{\partial \tilde{F}_b}{\partial \tilde{x}_2}}{\left|\frac{1}{H_3}\frac{\partial \tilde{F}_b}{\partial \tilde{x}_3}\right|}\right) , \tag{2.185}$$

where the dimensionless number $\mathcal{B}$ is defined in (2.52).

- Example (1) - Cartesian coordinates

$$\tilde{\beta}^2 \tilde{v}_x^{sl} = \mathcal{B}\,\tilde{\boldsymbol{\sigma}}_{xz}\,, \tag{2.186}$$
$$\tilde{\beta}^2 \tilde{v}_y^{sl} = \mathcal{B}\,\tilde{\boldsymbol{\sigma}}_{yz}\,, \tag{2.187}$$
$$\tilde{\beta}^2 \tilde{v}_z^{sl} = \mathcal{B}\left(\tilde{\boldsymbol{\sigma}}_{xz}\frac{\frac{\partial \tilde{F}_b}{\partial \tilde{x}}}{\left|\frac{\partial \tilde{F}_b}{\partial \tilde{z}}\right|} + \tilde{\boldsymbol{\sigma}}_{yz}\frac{\frac{\partial \tilde{F}_b}{\partial \tilde{y}}}{\left|\frac{\partial \tilde{F}_b}{\partial \tilde{z}}\right|}\right)\,. \tag{2.188}$$

- Example (2) - Spherical coordinates

$$\tilde{\beta}^2 \tilde{v}_\vartheta^{sl} = \mathcal{B}\,\tilde{\boldsymbol{\sigma}}_{\vartheta\zeta}\,, \tag{2.189}$$
$$\tilde{\beta}^2 \tilde{v}_\varphi^{sl} = \mathcal{B}\,\tilde{\boldsymbol{\sigma}}_{\varphi\zeta}\,, \tag{2.190}$$
$$\tilde{\beta}^2 \tilde{v}_\zeta^{sl} = \mathcal{B}\left(\tilde{\boldsymbol{\sigma}}_{\vartheta\zeta}\frac{\frac{\partial \tilde{F}_b}{\partial \vartheta}}{\left|\frac{\partial \tilde{F}_b}{\partial \tilde{\zeta}}\right|} + \tilde{\boldsymbol{\sigma}}_{\varphi\zeta}\frac{\frac{1}{\sin\vartheta}\frac{\partial \tilde{F}_b}{\partial \varphi}}{\left|\frac{\partial \tilde{F}_b}{\partial \tilde{\zeta}}\right|}\right)\,. \tag{2.191}$$

- Example (3) - Cylindrical coordinates

$$\tilde{\beta}^2 \tilde{v}_\varrho^{sl} = \mathcal{B}\,\tilde{\boldsymbol{\sigma}}_{\varrho z}\,, \tag{2.192}$$
$$\tilde{\beta}^2 \tilde{v}_\varphi^{sl} = \mathcal{B}\,\tilde{\boldsymbol{\sigma}}_{\varphi z}\,, \tag{2.193}$$
$$\tilde{\beta}^2 \tilde{v}_z^{sl} = \mathcal{B}\left(\tilde{\boldsymbol{\sigma}}_{\varrho z}\frac{\frac{\partial \tilde{F}_b}{\partial \tilde{\varrho}}}{\left|\frac{\partial \tilde{F}_b}{\partial \tilde{z}}\right|} + \tilde{\boldsymbol{\sigma}}_{\varphi z}\frac{\frac{1}{\tilde{\varrho}}\frac{\partial \tilde{F}_b}{\partial \varphi}}{\left|\frac{\partial \tilde{F}_b}{\partial \tilde{z}}\right|}\right)\,. \tag{2.194}$$

The **sliding velocity** (1.67) in SIA reads

$$\tilde{v}_1^{sl} = \tilde{v}_1 - \tilde{\nu}_{b1}\,, \tag{2.195}$$
$$\tilde{v}_2^{sl} = \tilde{v}_2 - \tilde{\nu}_{b2}\,, \tag{2.196}$$
$$\tilde{v}_3^{sl} = (\tilde{v}_1 - \tilde{\nu}_{b1})\frac{\frac{1}{H_1}\frac{\partial \tilde{F}_b}{\partial \tilde{x}_1}}{\left|\frac{1}{H_3}\frac{\partial \tilde{F}_b}{\partial \tilde{x}_3}\right|} + (\tilde{v}_2 - \tilde{\nu}_{b2})\frac{\frac{1}{H_2}\frac{\partial \tilde{F}_b}{\partial \tilde{x}_2}}{\left|\frac{1}{H_3}\frac{\partial \tilde{F}_b}{\partial \tilde{x}_3}\right|}\,. \tag{2.197}$$

- Example (1) - Cartesian coordinates

$$\tilde{v}_x^{sl} = \tilde{v}_x - \tilde{\nu}_{bx}\,, \tag{2.198}$$
$$\tilde{v}_y^{sl} = \tilde{v}_y - \tilde{\nu}_{by}\,, \tag{2.199}$$
$$\tilde{v}_z^{sl} = (\tilde{v}_x - \tilde{\nu}_{bx})\frac{\frac{\partial \tilde{F}_b}{\partial \tilde{x}}}{\left|\frac{\partial \tilde{F}_b}{\partial \tilde{z}}\right|} + (\tilde{v}_y - \tilde{\nu}_{by})\frac{\frac{\partial \tilde{F}_b}{\partial \tilde{y}}}{\left|\frac{\partial \tilde{F}_b}{\partial \tilde{z}}\right|}\,. \tag{2.200}$$

- Example (2) - Spherical coordinates

$$\tilde{v}_\vartheta^{sl} = \tilde{v}_\vartheta - \tilde{\nu}_{b\vartheta}\,, \tag{2.201}$$
$$\tilde{v}_\varphi^{sl} = \tilde{v}_\varphi - \tilde{\nu}_{b\varphi}\,, \tag{2.202}$$
$$\tilde{v}_\zeta^{sl} = (\tilde{v}_\vartheta - \tilde{\nu}_{b\vartheta})\frac{\frac{\partial \tilde{F}_b}{\partial \vartheta}}{\left|\frac{\partial \tilde{F}_b}{\partial \tilde{\zeta}}\right|} + (\tilde{v}_\varphi - \tilde{\nu}_{b\varphi})\frac{\frac{1}{\sin\vartheta}\frac{\partial \tilde{F}_b}{\partial \varphi}}{\left|\frac{\partial \tilde{F}_b}{\partial \tilde{\zeta}}\right|}\,. \tag{2.203}$$

- Example (3) - Cylindrical coordinates

$$\tilde{v}_\varrho^{sl} = \tilde{v}_\varrho - \tilde{\nu}_{b\varrho} \,, \tag{2.204}$$

$$\tilde{v}_\varphi^{sl} = \tilde{v}_\varphi - \tilde{\nu}_{b\varphi} \,, \tag{2.205}$$

$$\tilde{v}_z^{sl} = (\tilde{v}_\varrho - \tilde{\nu}_{b\varrho}) \frac{\frac{\partial \tilde{F}_b}{\partial \tilde{\varrho}}}{\left| \frac{\partial \tilde{F}_b}{\partial \tilde{z}} \right|} + (\tilde{v}_\varphi - \tilde{\nu}_{b\varphi}) \frac{\frac{1}{\tilde{\varrho}} \frac{\partial \tilde{F}_b}{\partial \varphi}}{\left| \frac{\partial \tilde{F}_b}{\partial \tilde{z}} \right|} \,. \tag{2.206}$$

The **energy jump** condition (1.73) in the SIA limit reads as

$$0 = -\tilde{m}_b^w \left(\frac{1}{\mathcal{E}[w]} - \frac{\tilde{p}}{1 - [w]\tilde{w}} \right) + (\tilde{\boldsymbol{\sigma}}_{13} \tilde{v}_1^{sl} + \tilde{\boldsymbol{\sigma}}_{23} \tilde{v}_2^{sl}) + \frac{\mathcal{D}}{\mathcal{C}} (\tilde{q}_3^{geo} - \tilde{q}_3^-) \,. \tag{2.207}$$

- Example (1) - Cartesian coordinates

$$0 = -\tilde{m}_b^w \left(\frac{1}{\mathcal{E}[w]} - \frac{\tilde{p}}{1 - [w]\tilde{w}} \right) + (\tilde{\boldsymbol{\sigma}}_{xz} \tilde{v}_x^{sl} + \tilde{\boldsymbol{\sigma}}_{yz} \tilde{v}_y^{sl}) + \frac{\mathcal{D}}{\mathcal{C}} (\tilde{q}_z^{geo} - \tilde{q}_z^-) \,. \tag{2.208}$$

- Example (2) - Spherical coordinates

$$0 = -\tilde{m}_b^w \left(\frac{1}{\mathcal{E}[w]} - \frac{\tilde{p}}{1 - [w]\tilde{w}} \right) + (\tilde{\boldsymbol{\sigma}}_{\vartheta\zeta} \tilde{v}_\vartheta^{sl} + \tilde{\boldsymbol{\sigma}}_{\varphi\zeta} \tilde{v}_\varphi^{sl}) + \frac{\mathcal{D}}{\mathcal{C}} (\tilde{q}_\zeta^{geo} - \tilde{q}_\zeta^-) \,. \tag{2.209}$$

- Example (3) - Cylindrical coordinates

$$0 = -\tilde{m}_b^w \left(\frac{1}{\mathcal{E}[w]} - \frac{\tilde{p}}{1 - [w]\tilde{w}} \right) + (\tilde{\boldsymbol{\sigma}}_{\varrho z} \tilde{v}_\varrho^{sl} + \tilde{\boldsymbol{\sigma}}_{\varphi z} \tilde{v}_\varphi^{sl}) + \frac{\mathcal{D}}{\mathcal{C}} (\tilde{q}_z^{geo} - \tilde{q}_z^-) \,. \tag{2.210}$$

2.4.5 Boundary conditions - Cold–temperate ice transition surface (CTS)

The **kinematic condition** (1.75) with the use of the **ice-mass jump** condition (1.77) in the SIA reads as

$$\frac{\partial \tilde{F}_{cts}}{\partial \tilde{t}} + \frac{\tilde{v}_1}{H_1} \frac{\partial \tilde{F}_{cts}}{\partial \tilde{x}_1} + \frac{\tilde{v}_2}{H_2} \frac{\partial \tilde{F}_{cts}}{\partial \tilde{x}_2} + \frac{\tilde{v}_3}{H_3} \frac{\partial \tilde{F}_{cts}}{\partial \tilde{x}_3} = -\frac{1}{[w]} \frac{\tilde{m}_{cts}^w}{\tilde{w}^-} \left| \frac{1}{H_3} \frac{\partial \tilde{F}_{cts}}{\partial \tilde{x}_3} \right| \,. \tag{2.211}$$

- Example (1) - Cartesian coordinates

$$\frac{\partial \tilde{F}_{cts}}{\partial \tilde{t}} + \tilde{v}_x \frac{\partial \tilde{F}_{cts}}{\partial \tilde{x}} + \tilde{v}_y \frac{\partial \tilde{F}_{cts}}{\partial \tilde{y}} + \tilde{v}_z \frac{\partial \tilde{F}_{cts}}{\partial \tilde{z}} = -\frac{1}{[w]} \frac{\tilde{m}_{cts}^w}{\tilde{w}^-} \left| \frac{\partial \tilde{F}_{cts}}{\partial \tilde{z}} \right| \,. \tag{2.212}$$

- Example (2) - Spherical coordinates

$$\frac{\partial \tilde{F}_{cts}}{\partial \tilde{t}} + \tilde{v}_\vartheta \frac{\partial \tilde{F}_{cts}}{\partial \vartheta} + \frac{\tilde{v}_\varphi}{\sin\vartheta} \frac{\partial \tilde{F}_{cts}}{\partial \varphi} + \tilde{v}_\zeta \frac{\partial \tilde{F}_{cts}}{\partial \tilde{\zeta}} = -\frac{1}{[w]} \frac{\tilde{m}_{cts}^w}{\tilde{w}^-} \left| \frac{\partial \tilde{F}_{cts}}{\partial \tilde{\zeta}} \right| \,. \tag{2.213}$$

- Example (3) - Cylindrical coordinates

$$\frac{\partial \tilde{F}_{cts}}{\partial \tilde{t}} + \tilde{v}_\varrho \frac{\partial \tilde{F}_{cts}}{\partial \tilde{\varrho}} + \frac{\tilde{v}_\varphi}{\tilde{\varrho}} \frac{\partial \tilde{F}_{cts}}{\partial \varphi} + \tilde{v}_z \frac{\partial \tilde{F}_{cts}}{\partial \tilde{z}} = -\frac{1}{[w]} \frac{\tilde{m}_{cts}^w}{\tilde{w}^-} \left| \frac{\partial \tilde{F}_{cts}}{\partial \tilde{z}} \right| \,. \tag{2.214}$$

The **ice velocity continuity** condition (1.76) is given by

$$\tilde{\vec{v}}^{+} = \tilde{\vec{v}}^{-} = \tilde{\vec{v}} \,. \tag{2.215}$$

The **water mass jump** condition (1.78) reads now as

$$\tilde{j}_3^{-} = 0 \,. \tag{2.216}$$

- Example (1) - Cartesian and Cylindrical coordinates

$$\tilde{j}_z^{-} = 0 \,. \tag{2.217}$$

- Example (2) - Spherical coordinates

$$\tilde{j}_\zeta^{-} = 0 \,. \tag{2.218}$$

The **linear-momentum jump** condition (1.79) is written as:

$$\tilde{p}^{+} = \tilde{p}^{-} \,, \qquad \tilde{\boldsymbol{\sigma}}_{13}^{+} = \tilde{\boldsymbol{\sigma}}_{13}^{-} \,, \qquad \tilde{\boldsymbol{\sigma}}_{23}^{+} = \tilde{\boldsymbol{\sigma}}_{23}^{-} \,. \tag{2.219}$$

- Example (1) - Cartesian coordinates

$$\tilde{p}^{+} = \tilde{p}^{-} \,, \qquad \tilde{\boldsymbol{\sigma}}_{xz}^{+} = \tilde{\boldsymbol{\sigma}}_{xz}^{-} \,, \qquad \tilde{\boldsymbol{\sigma}}_{yz}^{+} = \tilde{\boldsymbol{\sigma}}_{yz}^{-} \,. \tag{2.220}$$

- Example (2) - Spherical coordinates

$$\tilde{p}^{+} = \tilde{p}^{-} \,, \qquad \tilde{\boldsymbol{\sigma}}_{\vartheta\zeta}^{+} = \tilde{\boldsymbol{\sigma}}_{\vartheta\zeta}^{-} \,, \qquad \tilde{\boldsymbol{\sigma}}_{\varphi r}^{+} = \tilde{\boldsymbol{\sigma}}_{\varphi\zeta}^{-} \,. \tag{2.221}$$

- Example (3) - Cylindrical coordinates

$$\tilde{p}^{+} = \tilde{p}^{-} \,, \qquad \tilde{\boldsymbol{\sigma}}_{\varrho z}^{+} = \tilde{\boldsymbol{\sigma}}_{\varrho z}^{-} \,, \qquad \tilde{\boldsymbol{\sigma}}_{\varphi z}^{+} = \tilde{\boldsymbol{\sigma}}_{\varphi z}^{-} \,. \tag{2.222}$$

The **energy jump** condition (1.82) is expressed as:

$$0 = \tilde{m}_{cts}^{w} + \frac{\mathcal{DE}[w]}{\mathcal{C}} (\tilde{q}_3^{+} - \tilde{q}_3^{-}) \,. \tag{2.223}$$

- Example (1) - Cartesian and Cylindrical coordinates

$$0 = \tilde{m}_{cts}^{w} + \frac{\mathcal{DE}[w]}{\mathcal{C}} (\tilde{q}_z^{+} - \tilde{q}_z^{-}) \,. \tag{2.224}$$

- Example (2) - Spherical coordinates

$$0 = \tilde{m}_{cts}^{w} + \frac{\mathcal{DE}[w]}{\mathcal{C}} (\tilde{q}_\zeta^{+} - \tilde{q}_\zeta^{-}) \,. \tag{2.225}$$

2.5 Summary

We introduced appropriate scales for both the geometric and physical quantities appearing in the equations for ice sheet evolution in Chapter 1. After introducing several dimensionless parameters we arrived at the dimensionless version of these equations. We then derived the Shallow Ice Approximation for the system of equations by rewriting them in general orthogonal curvilinear coordinates, expanding all field quantities into power series in the scaling flatness parameter ϵ, and finally keeping only the leading-order terms of the expansion. The improvement compared to the standard SIA approach comes from the fact that instead of any particular coordinate system, general orthogonal coordinates were used. This resulted to a whole class of Shallow Ice Approximations, its realization for any particular choice of orthogonal coordinate system can be obtained just by evaluating certain geometric quantities. As an example, we explicitly listed out the SIA form for three important coordinate systems, namely the Cartesian, the spherical and the cylindrical.

Chapter 3

Iterative improvement of the Shallow-Ice Approximation - SIA-I algorithm

3.1 Introduction

Increasing demands on the accuracy of the solutions for glacier flow and improving computational possibilities are pushing the glaciological community to leave the traditional Shallow-Ice Approximation (SIA) (Hutter, 1983) and include the computation of longitudinal stresses in their numerical models. This is essential when the scaling assumptions of the SIA approach (Greve, 1997) are violated, such as for small alpine glaciers, ice streams, floating ice shelves, grounding line dynamics and other, usually small-scale, examples of ice dynamics.

A number of theoretical and numerical approaches has been proposed and tested, including several higher-order approximations of the Stokes problem by ”multilayer” methods (Saito et al., 2003; Pattyn, 2003; Blatter, 1995). For their classification and discussion, see Hindmarsh (2004). Also, a number of exact full-Stokes solvers have been developed, based on various numerical techniques such as finite-difference (e.g. Pattyn, 2003), spectral (Hindmarsch, 2004), finite-volume (Price et al., 2007) and finite-element methods (Zwinger, 2007; Gagliardini and Zwinger, 2008; Le Meur et al., 2004).

However, making a step from the SIA approach to more advanced models substantially increases computational demands that subsequently complicates the embedding of these techniques into large-scale models. We have developed a computational algorithm that provides an approximate solution of the Stokes problem that is more accurate than the SIA solution, but still applies the traditional SIA scaling assumption to the aspect ratio of a glacier. The primary criterion for the construction of the new algorithm is its computational efficiency.

The content of this section is a transcription of the author’s article (Souček & Martinec, 2008), with a few minor changes in the text and with the extension of Section 3.4 dealing with the SIA-I algorithm in general orthogonal curvilinear coordinates.

3.2 The Stokes problem for ice flow

Let us recall the physical problem we are dealing with and the assumptions and simplifications we apply. Our aim is to solve the boundary-value problem that allows us to model an incompressible Stokes flow with

non-linear viscous rheology in Cartesian geometry. We are looking for the solution of the Stokes equation with the acceleration term neglected, that is, the linear momentum equation of the form

$$\mathrm{div}\boldsymbol{\tau} + \rho\vec{g} = \vec{0}\,, \tag{3.1}$$

where ρ is the ice density, $\vec{g}$ is the gravity acceleration at the Earth's surface and the stress tensor $\boldsymbol{\tau}$ is given by

$$\boldsymbol{\tau} = -p\mathbf{I} + \boldsymbol{\sigma}\,, \tag{3.2}$$

where p and $\boldsymbol{\sigma}$ are the isotropic and deviatoric parts of $\boldsymbol{\tau}$, respectively, and $\mathbf{I}$ is the identity tensor. Since the ice flow is assumed to be incompressible and ice density homogeneous, the divergence-free constraint on the ice velocity $\vec{v}$ is to be satisfied:

$$\mathrm{div}\vec{v} = 0\,. \tag{3.3}$$

We consider only cold-ice glacier with geometry captured by two continuously differentiable surfaces (i.e. explicit description)

$$z = f_s(x,y)\ \ (\text{free surface})\,, \tag{3.4}$$
$$z = f_b(x,y)\ \ (\text{bed})\,, \tag{3.5}$$

where x, y, z are the Cartesian coordinates, and time is not explicitly considered now.

The scaling analysis corresponding to the Shallow-Ice Approximation, which was performed in the previous chapter, has to be slightly altered to allow the consideration of longitudinal stresses. Considering the typical horizontal ($\mathrm{L_{sc}} = [h_1][\Delta_1] = [h_2][\Delta_2]$) and vertical ($\mathrm{H_{sc}} = [h_3][\Delta_3]$) dimensions of a glacier, and the typical horizontal $[v_h]$ and vertical $[v_v]$ velocities of the glacier flow with the aspect ratio

$$\epsilon = \frac{\mathrm{H_{sc}}}{\mathrm{L_{sc}}} = \frac{[v_v]}{[v_h]}, \tag{3.6}$$

the following scaling is introduced

$$(x,y,z) = (\mathrm{L_{sc}}\tilde{x}, \mathrm{L_{sc}}\tilde{y}, \mathrm{H_{sc}}\tilde{z})\,, \tag{3.7}$$
$$(v_x, v_y, v_z) = ([v_h]\tilde{v}_x, [v_h]\tilde{v}_y, [v_v]\tilde{v}_z)\,, \tag{3.8}$$
$$(f_s(x,y), f_b(x,y)) = \mathrm{H_{sc}}(\tilde{f}_s(\tilde{x},\tilde{y}), \tilde{f}_b(\tilde{x},\tilde{y}))\,, \tag{3.9}$$
$$\mathcal{A} = [A]\tilde{\mathcal{A}}\,. \tag{3.10}$$

The scaling of the stress tensor is chosen as

$$(p, \boldsymbol{\sigma}_{ij}) = \rho g \mathrm{H_{sc}}(\tilde{p}, \tilde{\boldsymbol{\sigma}}_{ij}) \quad i,j \in \{x,y,z\}. \tag{3.11}$$

Such a scaling only non-dimensionalizes the stresses, without requiring the scaled quantities to be of the order of unity, for which case the more appropriate scaling would be that in (2.33)-(2.35).

The Stokes equation (3.1) for the scaled quantities reads as

$$0 = -\frac{\partial\tilde{p}}{\partial\tilde{x}}\epsilon + \frac{\partial\tilde{\boldsymbol{\sigma}}_{xx}}{\partial\tilde{x}}\epsilon + \frac{\partial\tilde{\boldsymbol{\sigma}}_{xy}}{\partial\tilde{y}}\epsilon + \frac{\partial\tilde{\boldsymbol{\sigma}}_{xz}}{\partial\tilde{z}}\,, \tag{3.12}$$
$$0 = -\frac{\partial\tilde{p}}{\partial\tilde{y}}\epsilon + \frac{\partial\tilde{\boldsymbol{\sigma}}_{xy}}{\partial\tilde{x}}\epsilon + \frac{\partial\tilde{\boldsymbol{\sigma}}_{yy}}{\partial\tilde{y}}\epsilon + \frac{\partial\tilde{\boldsymbol{\sigma}}_{yz}}{\partial\tilde{z}}\,, \tag{3.13}$$
$$1 = -\frac{\partial\tilde{p}}{\partial\tilde{z}} + \frac{\partial\tilde{\boldsymbol{\sigma}}_{xz}}{\partial\tilde{x}}\epsilon + \frac{\partial\tilde{\boldsymbol{\sigma}}_{yz}}{\partial\tilde{y}}\epsilon - \frac{\partial(\tilde{\boldsymbol{\sigma}}_{xx} + \tilde{\boldsymbol{\sigma}}_{yy})}{\partial\tilde{z}}\,, \tag{3.14}$$

where the symmetry of the deviatoric stresses $\boldsymbol{\sigma}_{ij}$ was used and $\boldsymbol{\sigma}_{zz}$ was eliminated from the system of equations by making use of the trace-free constraint on the deviatoric stresses in such a way that only six independent stress unknowns remained. The incompressibility condition (3.3) for scaled quantities then reads as

$$\frac{\partial \tilde{v}_x}{\partial \tilde{x}} + \frac{\partial \tilde{v}_y}{\partial \tilde{y}} + \frac{\partial \tilde{v}_z}{\partial \tilde{z}} = 0 \,. \tag{3.15}$$

Boundary conditions.

We assume stress-free conditions at the surface, i.e.

$$\boldsymbol{\tau} \cdot \vec{n} = \vec{0} \,, \qquad \text{at } z = f_s(x,y) \,, \tag{3.16}$$

where $\vec{n}$ is the unit outer normal. In the scaled form, (3.16) reads as

$$0 = \tilde{p}\left(\frac{\partial \tilde{f}_s}{\partial \tilde{x}}\right)\epsilon - \tilde{\boldsymbol{\sigma}}_{xx}\left(\frac{\partial \tilde{f}_s}{\partial \tilde{x}}\right)\epsilon - \tilde{\boldsymbol{\sigma}}_{xy}\left(\frac{\partial \tilde{f}_s}{\partial \tilde{y}}\right)\epsilon + \tilde{\boldsymbol{\sigma}}_{xz}, \tag{3.17}$$

$$0 = \tilde{p}\left(\frac{\partial \tilde{f}_s}{\partial \tilde{y}}\right)\epsilon - \tilde{\boldsymbol{\sigma}}_{xy}\left(\frac{\partial \tilde{f}_s}{\partial \tilde{x}}\right)\epsilon - \tilde{\boldsymbol{\sigma}}_{yy}\left(\frac{\partial \tilde{f}_s}{\partial \tilde{y}}\right)\epsilon + \tilde{\boldsymbol{\sigma}}_{yz}, \tag{3.18}$$

$$0 = \tilde{p} + \tilde{\boldsymbol{\sigma}}_{xx} + \tilde{\boldsymbol{\sigma}}_{yy} + \tilde{\boldsymbol{\sigma}}_{xz}\left(\frac{\partial \tilde{f}_s}{\partial \tilde{x}}\right)\epsilon + \tilde{\boldsymbol{\sigma}}_{yz}\left(\frac{\partial \tilde{f}_s}{\partial \tilde{y}}\right)\epsilon, \tag{3.19}$$

at $\tilde{z} = \tilde{f}_s(\tilde{x},\tilde{y})$.

At the glacier bed, we first for simplicity assume no-slip conditions, i.e.

$$\vec{v} = \vec{0}, \qquad \text{at } z = f_b(x,y) \tag{3.20}$$

or, in the scaled form,

$$\tilde{\vec{v}} = \vec{0}, \qquad \text{at } \tilde{z} = \tilde{f}_b(\tilde{x},\tilde{y}) \,. \tag{3.21}$$

Rheology.

The rheology is expressed by Glen's flow law (1.17) and after applying the scaling forms (3.7)-(3.11), it becomes

$$\tilde{\boldsymbol{\sigma}}_{xz} = \tilde{\eta}\left(\frac{\partial \tilde{v}_x}{\partial \tilde{z}} + \epsilon^2 \frac{\partial \tilde{v}_z}{\partial \tilde{x}}\right), \tag{3.22}$$

$$\tilde{\boldsymbol{\sigma}}_{yz} = \tilde{\eta}\left(\frac{\partial \tilde{v}_y}{\partial \tilde{z}} + \epsilon^2 \frac{\partial \tilde{v}_z}{\partial \tilde{y}}\right), \tag{3.23}$$

$$\tilde{\boldsymbol{\sigma}}_{xy} = \epsilon\tilde{\eta}\left(\frac{\partial \tilde{v}_x}{\partial \tilde{y}} + \frac{\partial \tilde{v}_y}{\partial \tilde{x}}\right), \tag{3.24}$$

$$\tilde{\boldsymbol{\sigma}}_{xx} = 2\epsilon\tilde{\eta}\frac{\partial \tilde{v}_x}{\partial \tilde{x}}, \tag{3.25}$$

$$\tilde{\boldsymbol{\sigma}}_{yy} = 2\epsilon\tilde{\eta}\frac{\partial \tilde{v}_y}{\partial \tilde{y}}, \tag{3.26}$$

$$\tilde{\eta} = \frac{1}{(2\epsilon^{-1}\mathcal{X}\tilde{\mathcal{A}}\tilde{\mathcal{V}})^{\frac{1}{3}}}, \tag{3.27}$$

$$\mathcal{X} = \frac{[\mathcal{A}](\rho g)^3 \mathrm{H}_{\mathrm{sc}}^5}{[v_h]\mathrm{L}_{\mathrm{sc}}} \,, \tag{3.28}$$

$$\begin{aligned}\tilde{\mathcal{V}} &= \left(\frac{\partial \tilde{v}_x}{\partial \tilde{z}} + \epsilon^2 \frac{\partial \tilde{v}_z}{\partial \tilde{x}}\right)^2 + \left(\frac{\partial \tilde{v}_y}{\partial \tilde{z}} + \epsilon^2 \frac{\partial \tilde{v}_z}{\partial \tilde{y}}\right)^2 \\ &+ \epsilon^2 \left(\frac{\partial \tilde{v}_x}{\partial \tilde{y}} + \frac{\partial \tilde{v}_y}{\partial \tilde{x}}\right)^2 + 4\epsilon^2 \left(\frac{\partial \tilde{v}_x}{\partial \tilde{x}}\right)^2 + 4\epsilon^2 \left(\frac{\partial \tilde{v}_y}{\partial \tilde{y}}\right)^2 \\ &+ 4\epsilon^2 \left(\frac{\partial \tilde{v}_x}{\partial \tilde{x}}\right)\left(\frac{\partial \tilde{v}_y}{\partial \tilde{y}}\right) . \end{aligned} \tag{3.29}$$

The inverse relation (1.18) expressed by the scaled quantities therefore reads as

$$\frac{\partial \tilde{v}_x}{\partial \tilde{x}} = \epsilon^{-2} \mathcal{X} \tilde{\mathcal{A}} \tilde{\mathcal{S}} \tilde{\boldsymbol{\sigma}}_{xx} , \tag{3.30}$$

$$\frac{\partial \tilde{v}_y}{\partial \tilde{y}} = \epsilon^{-2} \mathcal{X} \tilde{\mathcal{A}} \tilde{\mathcal{S}} \tilde{\boldsymbol{\sigma}}_{yy} , \tag{3.31}$$

$$\frac{\partial \tilde{v}_x}{\partial \tilde{y}} + \frac{\partial \tilde{v}_y}{\partial \tilde{x}} = 2\epsilon^{-2} \mathcal{X} \tilde{\mathcal{A}} \tilde{\mathcal{S}} \tilde{\boldsymbol{\sigma}}_{xy} , \tag{3.32}$$

$$\frac{\partial \tilde{v}_x}{\partial \tilde{z}} + \epsilon^2 \frac{\partial \tilde{v}_z}{\partial \tilde{x}} = 2\epsilon^{-1} \mathcal{X} \tilde{\mathcal{A}} \tilde{\mathcal{S}} \tilde{\boldsymbol{\sigma}}_{xz} , \tag{3.33}$$

$$\frac{\partial \tilde{v}_y}{\partial \tilde{z}} + \epsilon^2 \frac{\partial \tilde{v}_z}{\partial \tilde{y}} = 2\epsilon^{-1} \mathcal{X} \tilde{\mathcal{A}} \tilde{\mathcal{S}} \tilde{\boldsymbol{\sigma}}_{yz} , \tag{3.34}$$

$$\tilde{\mathcal{S}} = \tilde{\boldsymbol{\sigma}}_{xx}^2 + \tilde{\boldsymbol{\sigma}}_{yy}^2 + \tilde{\boldsymbol{\sigma}}_{xx}\tilde{\boldsymbol{\sigma}}_{yy} + \tilde{\boldsymbol{\sigma}}_{xy}^2 + \tilde{\boldsymbol{\sigma}}_{xz}^2 + \tilde{\boldsymbol{\sigma}}_{yz}^2 . \tag{3.35}$$

3.3 The SIA-I algorithm

In this section, we derive an iterative algorithm for updating the velocity and stress fields. The iterations start with the SIA-derived stress and velocity fields, which are then updated by solving an approximate problem that has more convenient numerical properties compared to the original setting. A crucial issue, convergence of the iterative algorithm, i.e. existence of a fixed point of the solution operator, is ensured if the contractivity of the iterations holds. A detailed theoretical analysis in full detail has yet to be undertaken, although in Appendix A, we present a sketch of the convergence proof for the simplest case - Newtonian rheology with uniform viscosity. The numerical examples presented in the following indicate that the algorithm converges for a wide range of ice-model parameters if the relaxation parameters controlling the iterations are chosen to be sufficiently small.

To derive the algorithm, let us consider the system of equations (3.12)-(3.14) and assume that there is an approximate solution in the kth iterative step, i.e. the field

$$\vec{u}^k \equiv (\tilde{p}^k, \tilde{\boldsymbol{\sigma}}_{xx}^k, \tilde{\boldsymbol{\sigma}}_{xy}^k, \tilde{\boldsymbol{\sigma}}_{yy}^k, \tilde{\boldsymbol{\sigma}}_{xz}^k, \tilde{\boldsymbol{\sigma}}_{yz}^k) . \tag{3.36}$$

The solution in the $(k+1)$th iteration is constructed in a two-step procedure. In the first half-step, we find $\vec{u}^{k+\frac{1}{2}}$ as follows.

Denoting the exact solution of (3.12)-(3.14) by $\vec{u}$ and defining the increment $\delta\vec{u}^{k+\frac{1}{2}}$ as

$$\delta\vec{u}^{k+\frac{1}{2}} = \vec{u} - \vec{u}^k , \tag{3.37}$$

the system of equations (3.12)-(3.14) for $\vec{u}$ may be rewritten as a system of equations for the increment

$\delta u^{k+\frac{1}{2}}$, assuming that $\vec{u}^k$ is known. We therefore obtain

$$
\begin{aligned}
- & \frac{\partial \delta\tilde{p}^{k+\frac{1}{2}}}{\partial \tilde{x}}\epsilon + \frac{\partial \delta\tilde{\boldsymbol{\sigma}}_{xx}^{k+\frac{1}{2}}}{\partial \tilde{x}}\epsilon + \frac{\partial \delta\tilde{\boldsymbol{\sigma}}_{xy}^{k+\frac{1}{2}}}{\partial \tilde{y}}\epsilon + \frac{\partial \delta\tilde{\boldsymbol{\sigma}}_{xz}^{k+\frac{1}{2}}}{\partial \tilde{z}} \\
= & \frac{\partial \tilde{p}^{k}}{\partial \tilde{x}}\epsilon - \frac{\partial \tilde{\boldsymbol{\sigma}}_{xx}^{k}}{\partial \tilde{x}}\epsilon - \frac{\partial \tilde{\boldsymbol{\sigma}}_{xy}^{k}}{\partial \tilde{y}}\epsilon - \frac{\partial \tilde{\boldsymbol{\sigma}}_{xz}^{k}}{\partial \tilde{z}}\,, \qquad (3.38) \\
- & \frac{\partial \delta\tilde{p}^{k+\frac{1}{2}}}{\partial \tilde{y}}\epsilon + \frac{\partial \delta\tilde{\boldsymbol{\sigma}}_{xy}^{k+\frac{1}{2}}}{\partial \tilde{x}}\epsilon + \frac{\partial \delta\tilde{\boldsymbol{\sigma}}_{yy}^{k+\frac{1}{2}}}{\partial \tilde{y}}\epsilon + \frac{\partial \delta\tilde{\boldsymbol{\sigma}}_{yz}^{k+\frac{1}{2}}}{\partial \tilde{z}} \\
= & \frac{\partial \tilde{p}^{k}}{\partial \tilde{y}}\epsilon - \frac{\partial \tilde{\boldsymbol{\sigma}}_{xy}^{k}}{\partial \tilde{x}}\epsilon - \frac{\partial \tilde{\boldsymbol{\sigma}}_{yy}^{k}}{\partial \tilde{y}}\epsilon - \frac{\partial \tilde{\boldsymbol{\sigma}}_{yz}^{k}}{\partial \tilde{z}}\,, \qquad (3.39) \\
& \frac{\partial \delta\tilde{p}^{k+\frac{1}{2}}}{\partial \tilde{z}}\epsilon - \frac{\partial \delta\tilde{\boldsymbol{\sigma}}_{xz}^{k+\frac{1}{2}}}{\partial \tilde{x}}\epsilon - \frac{\partial \delta\tilde{\boldsymbol{\sigma}}_{yz}^{k+\frac{1}{2}}}{\partial \tilde{y}}\epsilon + \frac{\partial (\delta\tilde{\boldsymbol{\sigma}}_{xx}^{k+\frac{1}{2}} + \delta\tilde{\boldsymbol{\sigma}}_{yy}^{k+\frac{1}{2}})}{\partial \tilde{z}} \\
= & -1 - \frac{\partial \tilde{p}^{k}}{\partial \tilde{z}}\epsilon + \frac{\partial \tilde{\boldsymbol{\sigma}}_{xz}^{k}}{\partial \tilde{x}}\epsilon + \frac{\partial \tilde{\boldsymbol{\sigma}}_{yz}^{k}}{\partial \tilde{y}}\epsilon - \frac{\partial (\tilde{\boldsymbol{\sigma}}_{xx}^{k} + \tilde{\boldsymbol{\sigma}}_{yy}^{k})}{\partial \tilde{z}}. \qquad (3.40)
\end{aligned}
$$

We now retain only the stresses $\delta\tilde{p}^{k+\frac{1}{2}}, \delta\tilde{\boldsymbol{\sigma}}_{xz}^{k+\frac{1}{2}}$ and $\delta\tilde{\boldsymbol{\sigma}}_{yz}^{k+\frac{1}{2}}$ in (3.38) and (3.39) and the stress $\delta\tilde{p}^{k+\frac{1}{2}}$ in (3.40), and neglect all other terms on the left-hand sides of the equations. This approximation exactly corresponds to the traditional SIA approach, assuming that only the retaining stress components are dominant. Here, this approach is, however, applied to the stress increments $\delta\vec{u}$ only, instead of the complete stress field as in the SIA (e.g. Greve, 1997). Hence, none of the stress components from the previous kth iterative step are omitted on the right-hand sides of (3.38)-(3.40). The SIA-like approximation results in the equations for the stress increments as follows

$$
\begin{aligned}
-\frac{\partial \delta\tilde{p}^{k+\frac{1}{2}}}{\partial \tilde{x}}\epsilon + \frac{\partial \delta\tilde{\boldsymbol{\sigma}}_{xz}^{k+\frac{1}{2}}}{\partial \tilde{z}} &= \frac{\partial \tilde{p}^{k}}{\partial \tilde{x}}\epsilon - \frac{\partial \tilde{\boldsymbol{\sigma}}_{xx}^{k}}{\partial \tilde{x}}\epsilon - \frac{\partial \tilde{\boldsymbol{\sigma}}_{xy}^{k}}{\partial \tilde{y}}\epsilon - \frac{\partial \tilde{\boldsymbol{\sigma}}_{xz}^{k}}{\partial \tilde{z}}\,, \qquad (3.41) \\
-\frac{\partial \delta\tilde{p}^{k+\frac{1}{2}}}{\partial \tilde{y}}\epsilon + \frac{\partial \delta\tilde{\boldsymbol{\sigma}}_{yz}^{k+\frac{1}{2}}}{\partial \tilde{z}} &= \frac{\partial \tilde{p}^{k}}{\partial \tilde{y}}\epsilon - \frac{\partial \tilde{\boldsymbol{\sigma}}_{xy}^{k}}{\partial \tilde{x}}\epsilon - \frac{\partial \tilde{\boldsymbol{\sigma}}_{yy}^{k}}{\partial \tilde{y}}\epsilon - \frac{\partial \tilde{\boldsymbol{\sigma}}_{yz}^{k}}{\partial \tilde{z}}\,, \qquad (3.42) \\
\frac{\partial \delta\tilde{p}^{k+\frac{1}{2}}}{\partial \tilde{z}} &= -1 - \frac{\partial \tilde{p}^{k}}{\partial \tilde{z}} + \frac{\partial \tilde{\boldsymbol{\sigma}}_{xz}^{k}}{\partial \tilde{x}}\epsilon + \frac{\partial \tilde{\boldsymbol{\sigma}}_{yz}^{k}}{\partial \tilde{y}}\epsilon - \frac{\partial (\tilde{\boldsymbol{\sigma}}_{xx}^{k} + \tilde{\boldsymbol{\sigma}}_{yy}^{k})}{\partial \tilde{z}}\,. \qquad (3.43)
\end{aligned}
$$

Equation (3.43) is now integrated along the vertical coordinate $\tilde{z}$ from the computation point $(\tilde{x}, \tilde{y}, \tilde{z})$ to the boundary point $(\tilde{x}, \tilde{y}, \tilde{f}_s(\tilde{x}, \tilde{y}))$, which yields the pressure increment $\delta\tilde{p}^{k+\frac{1}{2}}$ at the computation point $(\tilde{x}, \tilde{y}, \tilde{z})$. This result is then substituted into (3.41) and (3.42) which, after the integration along the vertical coordinate $\tilde{z}$, gives the increments $\delta\tilde{\boldsymbol{\sigma}}_{xz}^{k+\frac{1}{2}}, \delta\tilde{\boldsymbol{\sigma}}_{yz}^{k+\frac{1}{2}}$ at the computation point $(\tilde{x}, \tilde{y}, \tilde{z})$. The values of the integrands at $(\tilde{x}, \tilde{y}, \tilde{f}_s(\tilde{x}, \tilde{y}))$ are determined from the boundary conditions (3.17)-(3.19). To find them, the same procedure as above is applied. The exact solution is decomposed into the kth iterative-step solution $\vec{u}^k$ and the increment $\delta\vec{u}^{k+\frac{1}{2}}$, and only increments in $\tilde{p}, \tilde{\boldsymbol{\sigma}}_{xz}, \tilde{\boldsymbol{\sigma}}_{yz}$ are retained to compensate for the discrepancy in adjusting the boundary conditions in the kth iterative step. After some algebraic manipulation, we obtain the boundary conditions for the increments in the form

$$
\begin{aligned}
\delta\tilde{p}^{k+\frac{1}{2}}(\cdot, \tilde{f}_s(\cdot)) &= -\tilde{p}^{k}(\cdot, \tilde{f}_s(\cdot)) - \tilde{\boldsymbol{\sigma}}_{xx}^{k}(\cdot, \tilde{f}_s(\cdot)) - \tilde{\boldsymbol{\sigma}}_{yy}^{k}(\cdot, \tilde{f}_s(\cdot)) + \epsilon^2 \ldots \qquad (3.44) \\
\delta\tilde{\boldsymbol{\sigma}}_{xz}^{k+\frac{1}{2}}(\cdot, \tilde{f}_s(\cdot)) &= -\tilde{\boldsymbol{\sigma}}_{xz}^{k}(\cdot, \tilde{f}_s(\cdot)) + 2\tilde{\boldsymbol{\sigma}}_{xx}^{k}(\cdot, \tilde{f}_s(\cdot)) \left(\frac{\partial \tilde{f}_s}{\partial \tilde{x}}\right)\epsilon + \tilde{\boldsymbol{\sigma}}_{xy}^{k}(\cdot, \tilde{f}_s(\cdot)) \left(\frac{\partial \tilde{f}_s}{\partial \tilde{y}}\right)\epsilon \\
&+ \tilde{\boldsymbol{\sigma}}_{yy}^{k}(\cdot, \tilde{f}_s(\cdot)) \left(\frac{\partial \tilde{f}_s}{\partial \tilde{x}}\right)\epsilon + \epsilon^2 \ldots \qquad (3.45)
\end{aligned}
$$

$$\begin{aligned}\delta\tilde{\boldsymbol{\sigma}}_{yz}^{k+\frac{1}{2}}(\cdot,\tilde{f}_s(\cdot)) &= -\tilde{\boldsymbol{\sigma}}_{yz}^{k}(\cdot,\tilde{f}_s(\cdot)) + \tilde{\boldsymbol{\sigma}}_{xx}^{k}(\cdot,\tilde{f}_s(\cdot))\left(\frac{\partial\tilde{f}_s}{\partial\tilde{y}}\right)\epsilon + \tilde{\boldsymbol{\sigma}}_{xy}^{k}(\cdot,\tilde{f}_s(\cdot))\left(\frac{\partial\tilde{f}_s}{\partial\tilde{x}}\right)\epsilon \\ &+ 2\tilde{\boldsymbol{\sigma}}_{yy}^{k}(\cdot,\tilde{f}_s(\cdot))\left(\frac{\partial\tilde{f}_s}{\partial\tilde{y}}\right)\epsilon + \epsilon^2\ldots\,, \end{aligned} \tag{3.46}$$

where $(\cdot,\tilde{f}_s(\cdot))$ stands for $(\tilde{x},\tilde{y},\tilde{f}_s(\tilde{x}_1,\tilde{x}_2))$ for brevity and we do not explicitly write the terms with ϵ^2, because they will be excluded from the computations in the algorithm. Strictly speaking, this cannot be justified by the introduced scaling because we do not assume the scaled quantities and their spatial derivatives to be of the order of unity. What we present may hence be viewed as merely a formal procedure, which will be justified only by the final performance of the algorithm. However, one may recognize that what we are performing is nothing else but the SIA applied only to the incremental stresses rather than the full stress-field solution.

The integration of (3.43), followed by the integration of (3.41) and (3.42) with the use of (3.44)-(3.46), now results in the following formulae for the stress increments $\delta\tilde{p}^{k+\frac{1}{2}}$, $\delta\tilde{\boldsymbol{\sigma}}_{xz}^{k+\frac{1}{2}}$ and $\delta\tilde{\boldsymbol{\sigma}}_{yz}^{k+\frac{1}{2}}$:

$$\begin{aligned}\delta\tilde{p}^{k+\frac{1}{2}}(\cdot,\tilde{z}) &= -\tilde{p}^{k}(\cdot,\tilde{z}) - \tilde{\boldsymbol{\sigma}}_{xx}^{k}(\cdot,\tilde{z}) - \tilde{\boldsymbol{\sigma}}_{yy}^{k}(\cdot,\tilde{z}) + (\tilde{f}_s(\cdot)-\tilde{z}) \\ &- \epsilon\frac{\partial}{\partial\tilde{x}}\int_{\tilde{z}}^{\tilde{f}_s(\cdot)}\tilde{\boldsymbol{\sigma}}_{xz}^{k}(\cdot,\tilde{z}')d\tilde{z}' - \epsilon\frac{\partial}{\partial\tilde{y}}\int_{\tilde{z}}^{\tilde{f}_s(\cdot)}\tilde{\boldsymbol{\sigma}}_{yz}^{k}(\cdot,\tilde{z}')d\tilde{z}' \\ &+ \epsilon\tilde{\boldsymbol{\sigma}}_{xz}^{k}(\cdot,\tilde{f}_s(\cdot))\frac{\partial\tilde{f}_s(\cdot)}{\partial\tilde{x}} + \epsilon\tilde{\boldsymbol{\sigma}}_{yz}^{k}(\cdot,\tilde{f}_s(\cdot))\frac{\partial\tilde{f}_s(\cdot)}{\partial\tilde{y}} + \epsilon^2\ldots\,, \end{aligned} \tag{3.47}$$

$$\begin{aligned}\delta\tilde{\boldsymbol{\sigma}}_{xz}^{k+\frac{1}{2}}(\cdot,\tilde{z}) &= -\tilde{\boldsymbol{\sigma}}_{xz}^{k}(\cdot,\tilde{z}) - \epsilon\frac{\partial\tilde{f}_s(\cdot)}{\partial\tilde{x}}(\tilde{f}_s(\cdot)-\tilde{z}) \\ &+ 2\epsilon\frac{\partial}{\partial\tilde{x}}\int_{\tilde{z}}^{\tilde{f}_s}\tilde{\boldsymbol{\sigma}}_{xx}^{k}(\cdot,\tilde{z}')d\tilde{z}' \\ &+ \epsilon\frac{\partial}{\partial\tilde{y}}\int_{\tilde{z}}^{\tilde{f}_s}\tilde{\boldsymbol{\sigma}}_{xy}^{k}(\cdot,\tilde{z}')d\tilde{z}' \\ &+ \epsilon\frac{\partial}{\partial\tilde{x}}\int_{\tilde{z}}^{\tilde{f}_s}\tilde{\boldsymbol{\sigma}}_{yy}^{k}(\cdot,\tilde{z}')d\tilde{z}' + \epsilon^2\ldots\,, \end{aligned} \tag{3.48}$$

$$\begin{aligned}\delta\tilde{\boldsymbol{\sigma}}_{yz}^{k+\frac{1}{2}}(\cdot,\tilde{z}) &= -\tilde{\boldsymbol{\sigma}}_{yz}^{k}(\cdot,\tilde{z}) - \epsilon\frac{\partial\tilde{f}_s(\cdot)}{\partial\tilde{y}}(\tilde{f}_s(\cdot)-\tilde{z}) \\ &+ \epsilon\frac{\partial}{\partial\tilde{y}}\int_{\tilde{z}}^{\tilde{f}_s}\tilde{\boldsymbol{\sigma}}_{xx}^{k}(\cdot,\tilde{z}')d\tilde{z}' \\ &+ \epsilon\frac{\partial}{\partial\tilde{x}}\int_{\tilde{z}}^{\tilde{f}_s}\tilde{\boldsymbol{\sigma}}_{xy}^{k}(\cdot,\tilde{z}')d\tilde{z}' \\ &+ 2\epsilon\frac{\partial}{\partial\tilde{y}}\int_{\tilde{z}}^{\tilde{f}_s}\tilde{\boldsymbol{\sigma}}_{yy}^{k}(\cdot,\tilde{z}')d\tilde{z}' + \epsilon^2\ldots\,, \end{aligned} \tag{3.49}$$

where the dot in $(\cdot)$ stands for the pair $(\tilde{x},\tilde{y})$ for brevity and again, terms with ϵ^2 are not considered any further and are therefore not explicitly written.

We now define the updated solution in the $k+\frac{1}{2}$ step as

$$\vec{u}^{k+\frac{1}{2}} = \vec{u}^{k} + \theta_1\delta\vec{u}^{k+\frac{1}{2}}\,, \tag{3.50}$$

where $\theta_1 \in \langle 0, 1\rangle$ is the first relaxation parameter of the iterative scheme. Note that, by the previous derivations, we consider

$$\delta\vec{u}^{k+\frac{1}{2}} = (\delta\tilde{p}^{k+\frac{1}{2}}, 0, 0, 0, \delta\tilde{\boldsymbol{\sigma}}_{xz}^{k+\frac{1}{2}}, \delta\tilde{\boldsymbol{\sigma}}_{yz}^{k+\frac{1}{2}}) \,, \tag{3.51}$$

that is, only these three stress components are updated in the first half-step and

$$\delta\tilde{\boldsymbol{\sigma}}_{xx}^{k+\frac{1}{2}} = \delta\tilde{\boldsymbol{\sigma}}_{xy}^{k+\frac{1}{2}} = \delta\tilde{\boldsymbol{\sigma}}_{yy}^{k+\frac{1}{2}} = 0 \,. \tag{3.52}$$

In the second half-step, the consistency of the stress field with the velocity field must be ensured, that is, the rheological equation must be adjusted.

In order to obtain the velocity field from the rheological equations, we first split the equations (3.33) and (3.34) in the following manner:

$$\frac{\partial\tilde{v}_x^{k+\frac{1}{2}}}{\partial\tilde{z}} = 2\epsilon^{-1}\mathcal{X}\tilde{\mathcal{A}}\tilde{\mathcal{S}}^{k+\frac{1}{2}}\tilde{\boldsymbol{\sigma}}_{xz}^{k+\frac{1}{2}} - \epsilon^2\frac{\partial\tilde{v}_z^{k-\frac{1}{2}}}{\partial\tilde{x}} \,, \tag{3.53}$$

$$\frac{\partial\tilde{v}_y^{k+\frac{1}{2}}}{\partial\tilde{z}} = 2\epsilon^{-1}\mathcal{X}\tilde{\mathcal{A}}\tilde{\mathcal{S}}^{k+\frac{1}{2}}\tilde{\boldsymbol{\sigma}}_{yz}^{k+\frac{1}{2}} - \epsilon^2\frac{\partial\tilde{v}_z^{k-\frac{1}{2}}}{\partial\tilde{y}} \,, \tag{3.54}$$

that is, the terms with ϵ^2 on the left-hand sides in (3.33) and (3.34) are taken from the previous time step. The result can now be integrated along the vertical coordinate $\tilde{z}$ from the glacier bed $(\tilde{x}, \tilde{y}, \tilde{f}_b(\tilde{x}, \tilde{y}))$ to the computation point $(\tilde{x}, \tilde{y}, \tilde{z})$. Making use of the no-slip boundary condition (3.21) and considering the updated stress field $\boldsymbol{\sigma}_{ij}^{k+\frac{1}{2}}$, we obtain

$$\tilde{v}_x^{k+\frac{1}{2}}(\cdot,\tilde{z}) = 2\epsilon^{-1}\mathcal{X}\int_{\tilde{f}_b(\cdot)}^{\tilde{z}} \tilde{\mathcal{A}}\tilde{\mathcal{S}}^{k+\frac{1}{2}}\tilde{\boldsymbol{\sigma}}_{xz}^{k+\frac{1}{2}}(\cdot,\tilde{z}')d\tilde{z}' - \epsilon^2\int_{\tilde{f}_b(\cdot)}^{\tilde{z}} \frac{\partial\tilde{v}_z^{k-\frac{1}{2}}}{\partial\tilde{x}}(\cdot,\tilde{z}')\,d\tilde{z}' \,, \tag{3.55}$$

$$\tilde{v}_y^{k+\frac{1}{2}}(\cdot,\tilde{z}) = 2\epsilon^{-1}\mathcal{X}\int_{\tilde{f}_b(\cdot)}^{\tilde{z}} \tilde{\mathcal{A}}\tilde{\mathcal{S}}^{k+\frac{1}{2}}\tilde{\boldsymbol{\sigma}}_{yz}^{k+\frac{1}{2}}(\cdot,\tilde{z}')d\tilde{z}' - \epsilon^2\int_{\tilde{f}_b(\cdot)}^{\tilde{z}} \frac{\partial\tilde{v}_z^{k-\frac{1}{2}}}{\partial\tilde{y}}(\cdot,\tilde{z}')\,d\tilde{z}' \,. \tag{3.56}$$

The velocity $\tilde{v}_z^{k+\frac{1}{2}}$ is then obtained by the integration of the incompressibility condition (3.15) from $(\cdot, \tilde{f}_b(\cdot))$ to $(\cdot, \tilde{z})$. Making use of the no-slip boundary condition (3.21), we obtain

$$\tilde{v}_z^{k+\frac{1}{2}}(\cdot,\tilde{z}) = -\int_{\tilde{f}_b(\cdot)}^{\tilde{z}} \left(\frac{\partial\tilde{v}_x^{k+\frac{1}{2}}}{\partial\tilde{x}} + \frac{\partial\tilde{v}_y^{k+\frac{1}{2}}}{\partial\tilde{y}}\right)(\cdot,\tilde{z}')d\tilde{z}' \,. \tag{3.57}$$

This completes the determination of the velocity field $\vec{v}^{k+\frac{1}{2}}$.

We also propose an alternative to the treatment of the ϵ^2 terms in (3.33) and (3.34) and the $\tilde{v}_z$ component. If rheology equations (3.30) and (3.31) are combined with the incompressibility condition (3.15) and evaluated at the $k+\frac{1}{2}$ step, we obtain

$$\begin{aligned}\frac{\partial\tilde{v}_z^{k+\frac{1}{2}}}{\partial\tilde{z}} &= -\epsilon^{-2}\mathcal{X}\tilde{\mathcal{A}}\tilde{\mathcal{S}}^{k+\frac{1}{2}}(\tilde{\boldsymbol{\sigma}}_{xx}^{k+\frac{1}{2}} + \tilde{\boldsymbol{\sigma}}_{yy}^{k+\frac{1}{2}}) \\ &= -\epsilon^{-2}\mathcal{X}\tilde{\mathcal{A}}\tilde{\mathcal{S}}^{k+\frac{1}{2}}(\tilde{\boldsymbol{\sigma}}_{xx}^{k} + \tilde{\boldsymbol{\sigma}}_{yy}^{k}) \,.\end{aligned} \tag{3.58}$$

This relation can be integrated along the vertical coordinate from the base to the point $(\cdot, \tilde{z})$. Using the no-slip boundary condition at the base, a formula for $\tilde{v}_z^{k+\frac{1}{2}}$ is obtained

$$\tilde{v}_z^{k+\frac{1}{2}}(\cdot,\tilde{z}) = -\epsilon^{-2}\mathcal{X}\int_{\tilde{f}_b(\cdot)}^{\tilde{z}} \tilde{\mathcal{A}}\tilde{\mathcal{S}}^{k+\frac{1}{2}}(\tilde{\boldsymbol{\sigma}}_{xx}^{k} + \tilde{\boldsymbol{\sigma}}_{yy}^{k})(\cdot,\tilde{z}')\,d\tilde{z}' \,. \tag{3.59}$$

Now equations (3.33) and (3.34) may be evaluated at the $k+\frac{1}{2}$ step:

$$\frac{\partial \tilde{v}_x^{k+\frac{1}{2}}}{\partial \tilde{z}} = 2\epsilon^{-1}\mathcal{X}\tilde{\mathcal{A}}\tilde{\mathcal{S}}^{k+\frac{1}{2}}\tilde{\boldsymbol{\sigma}}_{xz}^{k+\frac{1}{2}} - \epsilon^2\frac{\partial \tilde{v}_z^{k+\frac{1}{2}}}{\partial \tilde{x}}\,, \tag{3.60}$$

$$\frac{\partial \tilde{v}_y^{k+\frac{1}{2}}}{\partial \tilde{z}} = 2\epsilon^{-1}\mathcal{X}\tilde{\mathcal{A}}\tilde{\mathcal{S}}^{k+\frac{1}{2}}\tilde{\boldsymbol{\sigma}}_{yz}^{k+\frac{1}{2}} - \epsilon^2\frac{\partial \tilde{v}_z^{k+\frac{1}{2}}}{\partial \tilde{y}}\,, \tag{3.61}$$

leading to alternative formulae to (3.55) and (3.56):

$$\begin{aligned}\tilde{v}_x^{k+\frac{1}{2}}(\cdot,\tilde{z}) &= 2\epsilon^{-1}\mathcal{X}\int_{\tilde{f}_b(\cdot)}^{\tilde{z}}\tilde{\mathcal{A}}\tilde{\mathcal{S}}^{k+\frac{1}{2}}(\cdot,\tilde{z}')\tilde{\boldsymbol{\sigma}}_{xz}^{k+\frac{1}{2}}(\cdot,\tilde{z}')d\tilde{z}' \\ &+ \mathcal{X}\int_{\tilde{f}_b(\cdot)}^{\tilde{z}}\frac{\partial}{\partial\tilde{x}}\int_{\tilde{f}_b(\cdot)}^{\tilde{z}'}\tilde{\mathcal{A}}\tilde{\mathcal{S}}^{k+\frac{1}{2}}(\tilde{\boldsymbol{\sigma}}_{xx}^{k}+\tilde{\boldsymbol{\sigma}}_{yy}^{k})(\cdot,\tilde{z}'')d\tilde{z}''\,d\tilde{z}'\,,\end{aligned} \tag{3.62}$$

$$\begin{aligned}\tilde{v}_y^{k+\frac{1}{2}}(\cdot,\tilde{z}) &= 2\epsilon^{-1}\mathcal{X}\int_{\tilde{f}_b(\cdot)}^{\tilde{z}}\tilde{\mathcal{A}}\tilde{\mathcal{S}}^{k+\frac{1}{2}}(\cdot,\tilde{z}')\tilde{\boldsymbol{\sigma}}_{yz}^{k+\frac{1}{2}}(\cdot,\tilde{z}')d\tilde{z}' \\ &+ \mathcal{X}\int_{\tilde{f}_b(\cdot)}^{\tilde{z}}\frac{\partial}{\partial\tilde{y}}\int_{\tilde{f}_b(\cdot)}^{\tilde{z}'}\tilde{\mathcal{A}}\tilde{\mathcal{S}}^{k+\frac{1}{2}}(\tilde{\boldsymbol{\sigma}}_{xx}^{k}+\tilde{\boldsymbol{\sigma}}_{yy}^{k})(\cdot,\tilde{z}'')d\tilde{z}''\,d\tilde{z}'\,.\end{aligned} \tag{3.63}$$

By either way described above, we obtained the velocity field at the $k+\frac{1}{2}$ time step. This field is now used to update the stress components according to the rheological equations to reduce the inconsistency of the updated velocity field with stresses. The substitution of the velocity $\vec{v}^{k+\frac{1}{2}}$ into the rheological equations (3.22)-(3.29), with all the variables evaluated at the $k+\frac{1}{2}$ step, yields the stress components that forms a stress vector denoted by $\vec{u}^{\star k+\frac{1}{2}}$.

The new $\vec{u}^{k+1}$ is finally defined as a convex combination of the previous estimate given by (3.50) and the rheologically-consistent estimate $\vec{u}^{\star k+\frac{1}{2}}$, i.e. we define

$$\vec{u}^{k+1} = \vec{u}^{k+\frac{1}{2}}(1-\theta_2) + \theta_2\vec{u}^{\star k+\frac{1}{2}}\,, \tag{3.64}$$

where $\theta_2 \in \langle 0,1\rangle$ is the second relaxation parameter of the iterative scheme.

We call the presented approach that iteratively improves the SIA solution the **SIA-I** algorithm. Its computational steps may symbolically be depicted by the following scheme (Table 3.1), starting from u^k:

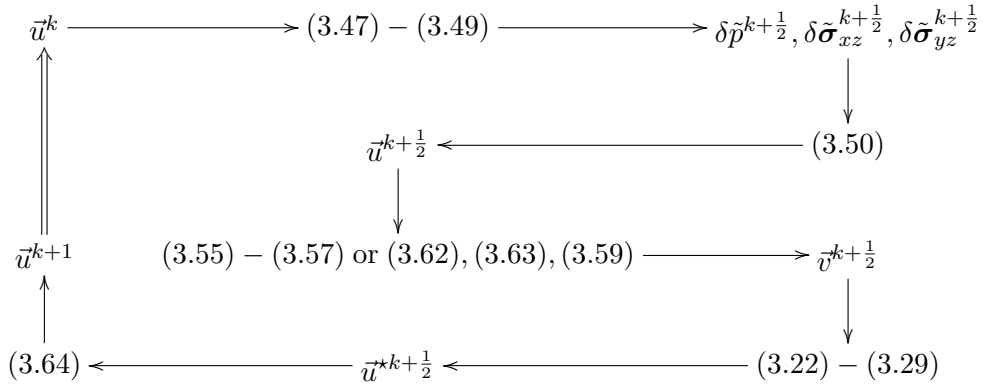

Table 3.1: SIA-I scheme

3.4 SIA-I in general curvilinear orthogonal coordinates

In accordance with our previous approach, we also present the derivation of the SIA-I algorithm in general orthogonal curvilinear coordinates as introduced in Section 2.2.

In the first half-step of the iterative procedure, the balance equation of momentum (equation of motion) (1.27) is updated. With the scaling introduced by (3.7)-(3.11), and with the expressions for gradient of scalar and divergence of tensor operators in general orthogonal curvilinear coordinates (see Appendix D), the linear momentum equations (3.1) may be rewritten in the following manner:

$$\begin{aligned}
0 &= -\frac{\epsilon}{\tilde{h}_1}\frac{\partial\tilde{p}}{\partial\tilde{x}_1} + \frac{\epsilon}{\tilde{h}_1\tilde{h}_2\tilde{h}_3}\frac{\partial}{\partial\tilde{x}_1}(\tilde{h}_2\tilde{h}_3\tilde{\boldsymbol{\sigma}}_{11}) + \frac{\epsilon}{\tilde{h}_1\tilde{h}_2\tilde{h}_3}\frac{\partial}{\partial\tilde{x}_2}(\tilde{h}_1\tilde{h}_3\tilde{\boldsymbol{\sigma}}_{12}) + \frac{1}{\tilde{h}_1\tilde{h}_2\tilde{h}_3}\frac{\partial}{\partial\tilde{x}_3}(\tilde{h}_1\tilde{h}_2\tilde{\boldsymbol{\sigma}}_{13}) \\
&+ \frac{\epsilon}{\tilde{h}_1\tilde{h}_2}\frac{\partial\tilde{h}_1}{\partial\tilde{x}_2}\tilde{\boldsymbol{\sigma}}_{12} - \frac{\epsilon}{\tilde{h}_1\tilde{h}_2}\frac{\partial\tilde{h}_2}{\partial\tilde{x}_1}\tilde{\boldsymbol{\sigma}}_{22} + \frac{1}{\tilde{h}_1\tilde{h}_3}\frac{\partial\tilde{h}_1}{\partial\tilde{x}_3}\tilde{\boldsymbol{\sigma}}_{13} + \frac{\epsilon}{\tilde{h}_1\tilde{h}_3}\frac{\partial\tilde{h}_3}{\partial\tilde{x}_1}(\tilde{\boldsymbol{\sigma}}_{11}+\tilde{\boldsymbol{\sigma}}_{22}) + \tilde{e}_1\,, \qquad (3.65)\\
0 &= -\frac{\epsilon}{\tilde{h}_2}\frac{\partial\tilde{p}}{\partial\tilde{x}_2} + \frac{\epsilon}{\tilde{h}_1\tilde{h}_2\tilde{h}_3}\frac{\partial}{\partial\tilde{x}_1}(\tilde{h}_2\tilde{h}_3\tilde{\boldsymbol{\sigma}}_{12}) + \frac{\epsilon}{\tilde{h}_1\tilde{h}_2\tilde{h}_3}\frac{\partial}{\partial\tilde{x}_2}(\tilde{h}_1\tilde{h}_3\tilde{\boldsymbol{\sigma}}_{22}) + \frac{1}{\tilde{h}_1\tilde{h}_2\tilde{h}_3}\frac{\partial}{\partial\tilde{x}_3}(\tilde{h}_1\tilde{h}_2\tilde{\boldsymbol{\sigma}}_{23}) \\
&+ \frac{\epsilon}{\tilde{h}_1\tilde{h}_2}\frac{\partial\tilde{h}_2}{\partial\tilde{x}_1}\tilde{\boldsymbol{\sigma}}_{12} - \frac{\epsilon}{\tilde{h}_1\tilde{h}_2}\frac{\partial\tilde{h}_1}{\partial\tilde{x}_2}\tilde{\boldsymbol{\sigma}}_{11} + \frac{1}{\tilde{h}_2\tilde{h}_3}\frac{\partial\tilde{h}_2}{\partial\tilde{x}_3}\tilde{\boldsymbol{\sigma}}_{23} + \frac{\epsilon}{\tilde{h}_2\tilde{h}_3}\frac{\partial\tilde{h}_3}{\partial\tilde{x}_2}(\tilde{\boldsymbol{\sigma}}_{11}+\tilde{\boldsymbol{\sigma}}_{22}) + \tilde{e}_2\,, \qquad (3.66)\\
0 &= -\frac{1}{\tilde{h}_3}\frac{\partial\tilde{p}}{\partial\tilde{x}_3} + \frac{\epsilon}{\tilde{h}_1\tilde{h}_2\tilde{h}_3}\frac{\partial}{\partial\tilde{x}_1}(\tilde{h}_2\tilde{h}_3\tilde{\boldsymbol{\sigma}}_{13}) + \frac{\epsilon}{\tilde{h}_1\tilde{h}_2\tilde{h}_3}\frac{\partial}{\partial\tilde{x}_2}(\tilde{h}_1\tilde{h}_3\tilde{\boldsymbol{\sigma}}_{23}) - \frac{1}{\tilde{h}_1\tilde{h}_2\tilde{h}_3}\frac{\partial}{\partial\tilde{x}_3}(\tilde{h}_1\tilde{h}_2(\tilde{\boldsymbol{\sigma}}_{11}+\tilde{\boldsymbol{\sigma}}_{22}) \\
&+ \frac{\epsilon}{\tilde{h}_1\tilde{h}_3}\frac{\partial\tilde{h}_3}{\partial\tilde{x}_1}\tilde{\boldsymbol{\sigma}}_{13} - \frac{1}{\tilde{h}_1\tilde{h}_3}\frac{\partial\tilde{h}_1}{\partial\tilde{x}_3}\tilde{\boldsymbol{\sigma}}_{11} + \frac{\epsilon}{\tilde{h}_2\tilde{h}_3}\frac{\partial\tilde{h}_3}{\partial\tilde{x}_2}\tilde{\boldsymbol{\sigma}}_{23} - \frac{1}{\tilde{h}_2\tilde{h}_3}\frac{\partial\tilde{h}_2}{\partial\tilde{x}_3}\tilde{\boldsymbol{\sigma}}_{22} + \tilde{e}_3\,, \qquad (3.67)
\end{aligned}$$

with $\tilde{e}_i := \frac{g_i}{\|\vec{g}\|}$. As in the Cartesian case, we introduce the stress increments for pressure and dominant shear stresses $\delta\tilde{p}^{k+\frac{1}{2}}$, $\delta\tilde{\boldsymbol{\sigma}}_{13}^{k+\frac{1}{2}}$, $\delta\tilde{\boldsymbol{\sigma}}_{23}^{k+\frac{1}{2}}$, updating in the first half-step of the k-th iteration the stress field. Keeping $\delta\tilde{p}^{k+\frac{1}{2}}$, $\delta\tilde{\boldsymbol{\sigma}}_{xz}^{k+\frac{1}{2}}$, $\delta\tilde{\boldsymbol{\sigma}}_{yz}^{k+\frac{1}{2}}$ in (3.65), (3.66) and only $\delta\tilde{p}^{k+\frac{1}{2}}$ in (3.67), the equations (3.65)-(3.67) are rewritten as explicit equations for the increments, starting with the last one:

$$\begin{aligned}
\frac{\partial\delta\tilde{p}^{k+\frac{1}{2}}}{\partial\tilde{x}_3} &= -\frac{\partial\tilde{p}^k}{\partial\tilde{x}_3} - \frac{\partial\tilde{\boldsymbol{\sigma}}_{11}^k}{\partial\tilde{x}_3} - \frac{\partial\tilde{\boldsymbol{\sigma}}_{22}^k}{\partial\tilde{x}_3} + \epsilon\frac{\tilde{h}_3}{\tilde{h}_1}\frac{\partial\tilde{\boldsymbol{\sigma}}_{13}^k}{\partial\tilde{x}_1} + \epsilon\frac{\tilde{h}_3}{\tilde{h}_2}\frac{\partial\tilde{\boldsymbol{\sigma}}_{23}^k}{\partial\tilde{x}_2} \\
&+ \epsilon\tilde{\boldsymbol{\sigma}}_{13}^k\alpha_{13} + \epsilon\tilde{\boldsymbol{\sigma}}_{23}^k\alpha_{23} - \tilde{\boldsymbol{\sigma}}_{11}^k\alpha_{11} - \tilde{\boldsymbol{\sigma}}_{22}^k\alpha_{22} + \tilde{e}_3\tilde{h}_3\,, \qquad (3.68)
\end{aligned}$$

where

$$\begin{aligned}
\alpha_{13} &:= \frac{1}{\tilde{h}_1\tilde{h}_2}\frac{\partial(\tilde{h}_2\tilde{h}_3)}{\partial\tilde{x}_1} + \frac{1}{\tilde{h}_1}\frac{\partial\tilde{h}_3}{\partial\tilde{x}_1}\,, \qquad & \alpha_{23} &:= \frac{1}{\tilde{h}_1\tilde{h}_2}\frac{\partial(\tilde{h}_1\tilde{h}_3)}{\partial\tilde{x}_2} + \frac{1}{\tilde{h}_2}\frac{\partial\tilde{h}_3}{\partial\tilde{x}_2}\,, \\
\alpha_{11} &:= \frac{1}{\tilde{h}_1\tilde{h}_2}\frac{\partial(\tilde{h}_1\tilde{h}_2)}{\partial\tilde{x}_3} + \frac{1}{\tilde{h}_1}\frac{\partial\tilde{h}_1}{\partial\tilde{x}_3}\,, \qquad & \alpha_{22} &:= \frac{1}{\tilde{h}_1\tilde{h}_2}\frac{\partial(\tilde{h}_1\tilde{h}_2)}{\partial\tilde{x}_3} + \frac{1}{\tilde{h}_2}\frac{\partial\tilde{h}_2}{\partial\tilde{x}_3}\,. \qquad (3.69)
\end{aligned}$$

For $\tilde{\boldsymbol{\sigma}}_{13}$ and $\tilde{\boldsymbol{\sigma}}_{23}$ in (3.65) and (3.66), we first notice that it holds that

$$\begin{aligned}
\frac{1}{\tilde{h}_1\tilde{h}_2\tilde{h}_3}\frac{\partial}{\partial\tilde{x}_3}\left(\tilde{h}_1\tilde{h}_2\tilde{\boldsymbol{\sigma}}_{13}\right) + \frac{1}{\tilde{h}_1\tilde{h}_3}\frac{\partial\tilde{h}_1}{\partial\tilde{x}_3}\tilde{\boldsymbol{\sigma}}_{13} &= \frac{1}{\tilde{h}_1^2\tilde{h}_2\tilde{h}_3}\frac{\partial}{\partial\tilde{x}_3}\left(\tilde{h}_1^2\tilde{h}_2\tilde{\boldsymbol{\sigma}}_{13}\right)\,, \qquad (3.70)\\
\frac{1}{\tilde{h}_1\tilde{h}_2\tilde{h}_3}\frac{\partial}{\partial\tilde{x}_3}\left(\tilde{h}_1\tilde{h}_2\tilde{\boldsymbol{\sigma}}_{23}\right) + \frac{1}{\tilde{h}_2\tilde{h}_3}\frac{\partial\tilde{h}_2}{\partial\tilde{x}_3}\tilde{\boldsymbol{\sigma}}_{23} &= \frac{1}{\tilde{h}_1\tilde{h}_2^2\tilde{h}_3}\frac{\partial}{\partial\tilde{x}_3}\left(\tilde{h}_1\tilde{h}_2^2\tilde{\boldsymbol{\sigma}}_{23}\right)\,, \qquad (3.71)
\end{aligned}$$

which allows us to postulate the equation for increments in the following manner:

$$\begin{aligned} -\frac{\partial}{\partial\tilde{x}_3}(\tilde{h}_1^2\tilde{h}_2\delta\tilde{\boldsymbol{\sigma}}_{13}^{k+\frac{1}{2}}) + \epsilon\tilde{h}_1\tilde{h}_2\tilde{h}_3\frac{\partial\delta\tilde{p}^{k+\frac{1}{2}}}{\partial\tilde{x}_1} &= \frac{\partial}{\partial\tilde{x}_3}(\tilde{h}_1^2\tilde{h}_2\tilde{\boldsymbol{\sigma}}_{13}^k) - \epsilon\tilde{h}_1\tilde{h}_2\tilde{h}_3\frac{\partial\tilde{p}^k}{\partial\tilde{x}_1} + \epsilon\tilde{h}_1\tilde{h}_2\tilde{h}_3\frac{\partial\tilde{\boldsymbol{\sigma}}_{11}^k}{\partial\tilde{x}_1} \\ &+ \epsilon\tilde{h}_1^2\tilde{h}_3\frac{\partial\tilde{\boldsymbol{\sigma}}_{12}^k}{\partial\tilde{x}_2} + \epsilon(\tilde{\boldsymbol{\sigma}}_{11}^k\beta_{11} + \tilde{\boldsymbol{\sigma}}_{12}^k\beta_{12} + \tilde{\boldsymbol{\sigma}}_{22}^k\beta_{22}) \\ &+ \tilde{e}_1\tilde{h}_1^2\tilde{h}_2\tilde{h}_3\,, \end{aligned} \tag{3.72}$$

and

$$\begin{aligned} -\frac{\partial}{\partial\tilde{x}_3}(\tilde{h}_1\tilde{h}_2^2\delta\tilde{\boldsymbol{\sigma}}_{23}^{k+\frac{1}{2}}) + \epsilon\tilde{h}_1\tilde{h}_2\tilde{h}_3\frac{\partial\delta\tilde{p}^{k+\frac{1}{2}}}{\partial\tilde{x}_2} &= \frac{\partial}{\partial\tilde{x}_3}(\tilde{h}_1\tilde{h}_2^2\tilde{\boldsymbol{\sigma}}_{23}^k) - \epsilon\tilde{h}_1\tilde{h}_2\tilde{h}_3\frac{\partial\tilde{p}^k}{\partial\tilde{x}_2} + \epsilon\tilde{h}_2^2\tilde{h}_3\frac{\partial\tilde{\boldsymbol{\sigma}}_{12}^k}{\partial\tilde{x}_1} \\ &+ \epsilon\tilde{h}_1\tilde{h}_2\tilde{h}_3\frac{\partial\tilde{\boldsymbol{\sigma}}_{22}^k}{\partial\tilde{x}_2} + \epsilon(\tilde{\boldsymbol{\sigma}}_{11}^k\gamma_{11} + \tilde{\boldsymbol{\sigma}}_{12}^k\gamma_{12} + \tilde{\boldsymbol{\sigma}}_{22}^k\gamma_{22}) \\ &+ \tilde{e}_2\tilde{h}_1\tilde{h}_2^2\tilde{h}_3\,, \end{aligned} \tag{3.73}$$

where

$$\begin{aligned} \beta_{11} &:= \tilde{h}_1\frac{\partial(\tilde{h}_2\tilde{h}_3)}{\partial\tilde{x}_1} + \tilde{h}_1\tilde{h}_2\frac{\partial\tilde{h}_3}{\partial\tilde{x}_1}\,, & \gamma_{11} &:= -\tilde{h}_2\tilde{h}_3\frac{\partial\tilde{h}_1}{\partial\tilde{x}_2} + \tilde{h}_1\tilde{h}_2\frac{\partial\tilde{h}_3}{\partial\tilde{x}_2} \\ \beta_{22} &:= -\tilde{h}_1\tilde{h}_3\frac{\partial\tilde{h}_2}{\partial\tilde{x}_1} + \tilde{h}_1\tilde{h}_2\frac{\partial\tilde{h}_3}{\partial\tilde{x}_1}\,, & \gamma_{22} &:= \tilde{h}_2\frac{\partial(\tilde{h}_1\tilde{h}_3)}{\partial\tilde{x}_2} + \tilde{h}_1\tilde{h}_2\frac{\partial\tilde{h}_3}{\partial\tilde{x}_2}\,, \\ \beta_{12} &:= \tilde{h}_1\frac{\partial(\tilde{h}_1\tilde{h}_3)}{\partial\tilde{x}_2} + \tilde{h}_1\tilde{h}_3\frac{\partial\tilde{h}_1}{\partial\tilde{x}_2}\,, & \gamma_{12} &:= \tilde{h}_2\frac{\partial(\tilde{h}_2\tilde{h}_3)}{\partial\tilde{x}_1} + \tilde{h}_2\tilde{h}_3\frac{\partial\tilde{h}_2}{\partial\tilde{x}_1}\,. \end{aligned}$$

Before we solve the approximate system for stress increments, we first evaluate the stress condition at the upper surface (1.29). Neglecting the atmospheric pressure p_{atm}, which is small compared to typical hydrostatic pressures in ice sheets, and expressing (1.29) in the curvilinear coordinates by using the explicit description of the free surface, this condition reads as:

$$0 = \epsilon\frac{\tilde{h}_3}{\tilde{h}_1}\frac{\partial\tilde{f}_s}{\partial\tilde{x}_1}\tilde{p} - \epsilon\frac{\tilde{h}_3}{\tilde{h}_1}\frac{\partial\tilde{f}_s}{\partial\tilde{x}_1}\tilde{\boldsymbol{\sigma}}_{11} - \epsilon\frac{\tilde{h}_3}{\tilde{h}_2}\frac{\partial\tilde{f}_s}{\partial\tilde{x}_2}\tilde{\boldsymbol{\sigma}}_{12} + \tilde{\boldsymbol{\sigma}}_{13}\,, \tag{3.74}$$

$$0 = \epsilon\frac{\tilde{h}_3}{\tilde{h}_2}\frac{\partial\tilde{f}_s}{\partial\tilde{x}_2}\tilde{p} - \epsilon\frac{\tilde{h}_3}{\tilde{h}_1}\frac{\partial\tilde{f}_s}{\partial\tilde{x}_1}\tilde{\boldsymbol{\sigma}}_{12} - \epsilon\frac{\tilde{h}_3}{\tilde{h}_2}\frac{\partial\tilde{f}_s}{\partial\tilde{x}_2}\tilde{\boldsymbol{\sigma}}_{22} + \tilde{\boldsymbol{\sigma}}_{23}\,, \tag{3.75}$$

$$0 = -\tilde{p} - \epsilon\frac{\tilde{h}_3}{\tilde{h}_1}\frac{\partial\tilde{f}_s}{\partial\tilde{x}_1}\tilde{\boldsymbol{\sigma}}_{13} - \epsilon\frac{\tilde{h}_3}{\tilde{h}_2}\frac{\partial\tilde{f}_s}{\partial\tilde{x}_2}\tilde{\boldsymbol{\sigma}}_{23} - \tilde{\boldsymbol{\sigma}}_{11} - \tilde{\boldsymbol{\sigma}}_{22}\,, \tag{3.76}$$

at $\tilde{x}_3 = \tilde{f}_s(\tilde{x}_1, \tilde{x}_2)$. We again expect that for each iteration step of the SIA-I procedure, this set of boundary conditions need not be fulfilled exactly and we again compensate the possible discrepancy by the stress increments $\delta\tilde{p}$, $\delta\tilde{\boldsymbol{\sigma}}_{13}$, $\delta\tilde{\boldsymbol{\sigma}}_{23}$. We may explicitly express the increments by solving the algebraic system (3.74)-(3.76), which, after omitting the terms multiplied by the small factor ϵ^2, leads to

$$\delta\tilde{p}^{k+\frac{1}{2}}(\cdot,\tilde{f}_s) = -(\tilde{p}^k + \tilde{\boldsymbol{\sigma}}_{11}^k + \tilde{\boldsymbol{\sigma}}_{22}^k)(\cdot,\tilde{f}_s)\,, \tag{3.77}$$

$$\delta\tilde{\boldsymbol{\sigma}}_{13}^{k+\frac{1}{2}}(\cdot,\tilde{f}_s) = \left(-\tilde{\boldsymbol{\sigma}}_{13}^k + 2\epsilon\frac{\tilde{h}_3}{\tilde{h}_1}\frac{\partial\tilde{f}_s}{\partial\tilde{x}_1}\tilde{\boldsymbol{\sigma}}_{11}^k + \epsilon\frac{\tilde{h}_3}{\tilde{h}_1}\frac{\partial\tilde{f}_s}{\partial\tilde{x}_1}\tilde{\boldsymbol{\sigma}}_{22}^k + \epsilon\frac{\tilde{h}_3}{\tilde{h}_2}\frac{\partial\tilde{f}_s}{\partial\tilde{x}_2}\tilde{\boldsymbol{\sigma}}_{12}^k\right)(\cdot,\tilde{f}_s)\,, \tag{3.78}$$

$$\delta\tilde{\boldsymbol{\sigma}}_{23}^{k+\frac{1}{2}}(\cdot,\tilde{f}_s) = \left(-\tilde{\boldsymbol{\sigma}}_{23}^k + \epsilon\frac{\tilde{h}_3}{\tilde{h}_2}\frac{\partial\tilde{f}_s}{\partial\tilde{x}_2}\tilde{\boldsymbol{\sigma}}_{11}^k + 2\epsilon\frac{\tilde{h}_3}{\tilde{h}_2}\frac{\partial\tilde{f}_s}{\partial\tilde{x}_2}\tilde{\boldsymbol{\sigma}}_{22}^k + \epsilon\frac{\tilde{h}_3}{\tilde{h}_1}\frac{\partial\tilde{f}_s}{\partial\tilde{x}_1}\tilde{\boldsymbol{\sigma}}_{12}^k\right)(\cdot,\tilde{f}_s)\,. \tag{3.79}$$

Equation (3.68) can now be integrated along the "vertical" coordinate $\tilde{x}_3$ from $(\cdot,\tilde{x}_3)$ to $(\cdot,\tilde{f}_s(\cdot))$. With the use of (3.76), we obtain:

$$\begin{aligned}\delta\tilde{p}^{k+\frac{1}{2}}(\cdot,\tilde{x}_3) &= -(\tilde{p}^k+\tilde{\boldsymbol{\sigma}}^k_{11}+\tilde{\boldsymbol{\sigma}}^k_{22})(\cdot,\tilde{x}_3)+\int_{\tilde{x}_3}^{\tilde{f}_s}(\tilde{\boldsymbol{\sigma}}^k_{11}\alpha_{11}+\tilde{\boldsymbol{\sigma}}^k_{22}\alpha_{22})\,d\tilde{x}_3'-\int_{\tilde{x}_3}^{\tilde{f}_s}\tilde{e}_3\tilde{h}_3\,d\tilde{x}_3'\\ &- \epsilon\int_{\tilde{x}_3}^{\tilde{f}_s}\left(\frac{\tilde{h}_3}{\tilde{h}_1}\frac{\partial\tilde{\boldsymbol{\sigma}}^k_{13}}{\partial\tilde{x}_1}+\frac{\tilde{h}_3}{\tilde{h}_2}\frac{\partial\tilde{\boldsymbol{\sigma}}^k_{23}}{\partial\tilde{x}_2}+\tilde{\boldsymbol{\sigma}}^k_{13}\alpha_{13}+\tilde{\boldsymbol{\sigma}}^k_{23}\alpha_{23}\right)d\tilde{x}_3'. \qquad (3.80)\end{aligned}$$

This expression can be inserted into (3.72) and (3.73), which again after integration along the "vertical" coordinate $\tilde{x}_3$ from $(\cdot,\tilde{x}_3)$ to $(\cdot,\tilde{f}_s(\cdot))$, with the use of (3.78), (3.79) and after neglecting the terms multiplied by the factor ϵ^2, finally gives

$$\begin{aligned}\tilde{h}_1^2\tilde{h}_2\delta\tilde{\boldsymbol{\sigma}}_{13}^{k+\frac{1}{2}}(\cdot,\tilde{x}_3) &= -\tilde{h}_1^2\tilde{h}_2\tilde{\boldsymbol{\sigma}}^k_{13}(\cdot,\tilde{x}_3)+\epsilon\int_{\tilde{x}_3}^{\tilde{f}_s}\tilde{h}_1\tilde{h}_2\tilde{h}_3\frac{\partial}{\partial\tilde{x}_1}\int_{\tilde{x}_3'}^{\tilde{f}_s}\tilde{e}_3\tilde{h}_3\,d\tilde{x}_3''\,d\tilde{x}_3'+\int_{\tilde{x}_3}^{\tilde{f}_s}\tilde{e}_1\tilde{h}_1^2\tilde{h}_2\tilde{h}_3\,d\tilde{x}_3'\\ &+ \epsilon\left(2\int_{\tilde{x}_3}^{\tilde{f}_s}\tilde{h}_1\tilde{h}_2\tilde{h}_3\frac{\partial\tilde{\boldsymbol{\sigma}}^k_{11}}{\partial\tilde{x}_1}\,d\tilde{x}_3'+\int_{\tilde{x}_3}^{\tilde{f}_s}\tilde{h}_1\tilde{h}_2\tilde{h}_3\frac{\partial\tilde{\boldsymbol{\sigma}}^k_{22}}{\partial\tilde{x}_1}\,d\tilde{x}_3'+\int_{\tilde{x}_3}^{\tilde{f}_s}\tilde{h}_1^2\tilde{h}_3\frac{\partial\tilde{\boldsymbol{\sigma}}^k_{12}}{\partial\tilde{x}_2}\,d\tilde{x}_3'\right)\\ &+ \epsilon\left(2\tilde{\boldsymbol{\sigma}}^k_{11}\tilde{h}_1\tilde{h}_2\tilde{h}_3\frac{\partial\tilde{f}_s}{\partial\tilde{x}_1}+\tilde{\boldsymbol{\sigma}}^k_{22}\tilde{h}_1\tilde{h}_2\tilde{h}_3\frac{\partial\tilde{f}_s}{\partial\tilde{x}_1}+\tilde{\boldsymbol{\sigma}}^k_{12}\tilde{h}_1^2\tilde{h}_3\frac{\partial\tilde{f}_s}{\partial\tilde{x}_2}\right)(\cdot,\tilde{f}_s)\\ &+ \epsilon\int_{\tilde{x}_3}^{\tilde{f}_s}\tilde{\boldsymbol{\sigma}}^k_{11}\beta_{11}+\tilde{\boldsymbol{\sigma}}^k_{22}\beta_{22}+\tilde{\boldsymbol{\sigma}}^k_{12}\beta_{12})\,d\tilde{x}_3'\\ &- \epsilon\int_{\tilde{x}_3}^{\tilde{f}_s}\tilde{h}_1\tilde{h}_2\tilde{h}_3\frac{\partial}{\partial\tilde{x}_1}\int_{\tilde{x}_3'}^{\tilde{f}_s}(\tilde{\boldsymbol{\sigma}}^k_{11}\alpha_{11}+\tilde{\boldsymbol{\sigma}}^k_{22}\alpha_{22})\,d\tilde{x}_3''\,d\tilde{x}_3'\,, \qquad (3.81)\end{aligned}$$

and

$$\begin{aligned}\tilde{h}_1\tilde{h}_2^2\delta\tilde{\boldsymbol{\sigma}}_{23}^{k+\frac{1}{2}}(\cdot,\tilde{x}_3) &= -\tilde{h}_1\tilde{h}_2^2\tilde{\boldsymbol{\sigma}}^k_{23}(\cdot,\tilde{x}_3)+\epsilon\int_{\tilde{x}_3}^{\tilde{f}_s}\tilde{h}_1\tilde{h}_2\tilde{h}_3\frac{\partial}{\partial\tilde{x}_2}\int_{\tilde{x}_3'}^{\tilde{f}_s}\tilde{e}_3\tilde{h}_3\,d\tilde{x}_3''\,d\tilde{x}_3'+\int_{\tilde{x}_3}^{\tilde{f}_s}\tilde{e}_2\tilde{h}_1\tilde{h}_2^2\tilde{h}_3\,d\tilde{x}_3'\\ &+ \epsilon\left(\int_{\tilde{x}_3}^{\tilde{f}_s}\tilde{h}_1\tilde{h}_2\tilde{h}_3\frac{\partial\tilde{\boldsymbol{\sigma}}^k_{11}}{\partial\tilde{x}_2}\,d\tilde{x}_3'+2\int_{\tilde{x}_3}^{\tilde{f}_s}\tilde{h}_1\tilde{h}_2\tilde{h}_3\frac{\partial\tilde{\boldsymbol{\sigma}}^k_{22}}{\partial\tilde{x}_2}\,d\tilde{x}_3'+\int_{\tilde{x}_3}^{\tilde{f}_s}\tilde{h}_2^2\tilde{h}_3\frac{\partial\tilde{\boldsymbol{\sigma}}^k_{12}}{\partial\tilde{x}_1}\,d\tilde{x}_3'\right)\\ &+ \epsilon\left(\tilde{\boldsymbol{\sigma}}^k_{11}\tilde{h}_1\tilde{h}_2\tilde{h}_3\frac{\partial\tilde{f}_s}{\partial\tilde{x}_2}+\tilde{\boldsymbol{\sigma}}^k_{22}\tilde{h}_1\tilde{h}_2\tilde{h}_3\frac{\partial\tilde{f}_s}{\partial\tilde{x}_2}+\tilde{\boldsymbol{\sigma}}^k_{12}\tilde{h}_2^2\tilde{h}_3\frac{\partial\tilde{f}_s}{\partial\tilde{x}_1}\right)(\cdot,\tilde{f}_s)\\ &+ \epsilon\int_{\tilde{x}_3}^{\tilde{f}_s}\tilde{\boldsymbol{\sigma}}^k_{11}\gamma_{11}+\tilde{\boldsymbol{\sigma}}^k_{22}\gamma_{22}+\tilde{\boldsymbol{\sigma}}^k_{12}\gamma_{12})\,d\tilde{x}_3'\\ &- \epsilon\int_{\tilde{x}_3}^{\tilde{f}_s}\tilde{h}_1\tilde{h}_2\tilde{h}_3\frac{\partial}{\partial\tilde{x}_2}\int_{\tilde{x}_3'}^{\tilde{f}_s}(\tilde{\boldsymbol{\sigma}}^k_{11}\alpha_{11}+\tilde{\boldsymbol{\sigma}}^k_{22}\alpha_{22})\,d\tilde{x}_3''\,d\tilde{x}_3'\,. \qquad (3.82)\end{aligned}$$

For the standard choice of Cartesian coordinates with the vertical x_3 axis, we have, according to (2.10), $\tilde{h}_1=\tilde{h}_2=\tilde{h}_3=1$, and $\tilde{e}_3=-1$, $\tilde{e}_1=\tilde{e}_2=0$. Formulae (3.80)-(3.82) then reduce to the form (3.47)-(3.49) from the previous section. As another example, let us consider the spherical coordinates as introduced in (2.2). Then, according to (2.15), we have

$$\begin{aligned}\tilde{h}_1 &= (1+\epsilon\tilde{\zeta})\,, &(3.83)\\ \tilde{h}_2 &= (1+\epsilon\tilde{\zeta})\sin\vartheta\,, &(3.84)\\ \tilde{h}_3 &= 1\,, &(3.85)\end{aligned}$$

$$
\begin{aligned}
&\alpha_{13} = \tfrac{\cot\vartheta}{1+\epsilon\tilde{\zeta}}\,, && \alpha_{23} = 0\,,\\
&\alpha_{11} = \tfrac{3\epsilon}{1+\epsilon\tilde{\zeta}}\,, && \alpha_{22} = \tfrac{3\epsilon}{1+\epsilon\tilde{\zeta}}\,,\\
&\beta_{11} = (1+\epsilon\tilde{\zeta})^2\cos\vartheta\,, && \gamma_{11} = 0\,,\\
&\beta_{22} = -(1+\epsilon\tilde{\zeta})^2\cos\vartheta\,, && \gamma_{22} = 0\,,\\
&\beta_{12} = 0\,, && \gamma_{12} = 2(1+\epsilon\tilde{\zeta})^2\sin\vartheta\cos\vartheta\,.
\end{aligned}
$$

and $\vec{\tilde{e}} = (0,0,-1)$.

Now, we insert these expressions to (3.80)-(3.82), neglect terms multiplied by ϵ^2 and arrive at the following:

$$
\begin{aligned}
\delta\tilde{p}^{k+\frac{1}{2}} &= -\tilde{p}^k - \tilde{\boldsymbol{\sigma}}^k_{\vartheta\vartheta} - \tilde{\boldsymbol{\sigma}}^k_{\varphi\varphi} + 3\epsilon\int_{\tilde{\zeta}}^{\tilde{f}_s}(\tilde{\boldsymbol{\sigma}}^k_{\vartheta\vartheta} + \tilde{\boldsymbol{\sigma}}^k_{\varphi\varphi})\,d\tilde{\zeta}' + (\tilde{f}_s - \tilde{\zeta})\\
&- \epsilon\int_{\tilde{\zeta}}^{\tilde{f}_s}\frac{\partial\tilde{\boldsymbol{\sigma}}_{\vartheta\zeta}}{\partial\vartheta}\,d\tilde{\zeta}' - \frac{\epsilon}{\sin\vartheta}\int_{\tilde{\zeta}}^{\tilde{f}_s}\frac{\partial\tilde{\boldsymbol{\sigma}}_{\varphi\zeta}}{\partial\varphi}\,d\tilde{\zeta}' - \epsilon\cot\vartheta\int_{\tilde{\zeta}}^{\tilde{f}_s}\tilde{\boldsymbol{\sigma}}_{\vartheta\zeta}\,d\tilde{\zeta}'\,, \qquad (3.86)\\
\delta\tilde{\boldsymbol{\sigma}}^{k+\frac{1}{2}}_{\vartheta\zeta} &= -\tilde{\boldsymbol{\sigma}}^k_{\vartheta\zeta} - \epsilon\frac{\partial\tilde{f}_s}{\partial\vartheta}(\tilde{f}_s - \tilde{\zeta})\\
&+ \epsilon\left(2\int_{\tilde{\zeta}}^{\tilde{f}_s}\frac{\partial\tilde{\boldsymbol{\sigma}}^k_{\vartheta\vartheta}}{\partial\vartheta}\,d\tilde{\zeta}' + \int_{\tilde{\zeta}}^{\tilde{f}_s}\frac{\partial\tilde{\boldsymbol{\sigma}}^k_{\varphi\varphi}}{\partial\vartheta}\,d\tilde{\zeta}' + \frac{1}{\sin\vartheta}\int_{\tilde{\zeta}}^{\tilde{f}_s}\frac{\partial\tilde{\boldsymbol{\sigma}}^k_{\vartheta\varphi}}{\partial\varphi}\,d\tilde{\zeta}'\right)\\
&+ \epsilon\left(2\tilde{\boldsymbol{\sigma}}^k_{\vartheta\vartheta}\frac{\partial\tilde{f}_s}{\partial\vartheta} + \tilde{\boldsymbol{\sigma}}^k_{\varphi\varphi}\frac{\partial\tilde{f}_s}{\partial\vartheta} + \frac{\tilde{\boldsymbol{\sigma}}^k_{\vartheta\varphi}}{\sin\vartheta}\frac{\partial\tilde{f}_s}{\partial\varphi}\right)(\cdot,\tilde{f}_s) + \epsilon\cot\vartheta\int_{\tilde{\zeta}}^{\tilde{f}_s}(\tilde{\boldsymbol{\sigma}}^k_{\vartheta\vartheta} - \tilde{\boldsymbol{\sigma}}^k_{\varphi\varphi})\,d\tilde{\zeta}'\,,\\
\delta\tilde{\boldsymbol{\sigma}}^{k+\frac{1}{2}}_{\varphi\zeta} &= -\tilde{\boldsymbol{\sigma}}_{\varphi r} - \frac{\epsilon}{\sin\vartheta}\frac{\partial\tilde{f}_s}{\partial\varphi}(\tilde{f}_s - \tilde{\zeta})\\
&+ \epsilon\left(\frac{1}{\sin\vartheta}\int_{\tilde{\zeta}}^{\tilde{f}_s}\frac{\partial\tilde{\boldsymbol{\sigma}}^k_{\vartheta\vartheta}}{\partial\varphi}\,d\tilde{\zeta}' + \frac{2}{\sin\vartheta}\int_{\tilde{\zeta}}^{\tilde{f}_s}\frac{\partial\tilde{\boldsymbol{\sigma}}^k_{\varphi\varphi}}{\partial\varphi}\,d\tilde{\zeta}' + \int_{\tilde{\zeta}}^{\tilde{f}_s}\frac{\partial\tilde{\boldsymbol{\sigma}}^k_{\vartheta\varphi}}{\partial\vartheta}\,d\tilde{\zeta}'\right)\\
&+ \epsilon\left(\frac{\tilde{\boldsymbol{\sigma}}^k_{\vartheta\vartheta}}{\sin\vartheta}\frac{\partial\tilde{f}_s}{\partial\varphi} + 2\frac{\tilde{\boldsymbol{\sigma}}^k_{\varphi\varphi}}{\sin\vartheta}\frac{\partial\tilde{f}_s}{\partial\varphi} + \tilde{\boldsymbol{\sigma}}^k_{\vartheta\varphi}\frac{\partial\tilde{f}_s}{\partial\vartheta}\right)(\cdot,\tilde{f}_s) + 2\epsilon\cot\vartheta\int_{\tilde{\zeta}}^{\tilde{f}_s}\tilde{\boldsymbol{\sigma}}^k_{\vartheta\varphi}\,d\tilde{\zeta}'\,.
\end{aligned}
$$

The computed stress updates are added to the stress field according to (3.50).

In the second half-step, the stress field is updated in order to be consistent with the rheology. Taking the Glen's flow law (1.18) and inspecting the "13" and "23" components of this tensorial relation, using the general orthogonal coordinates (Appendix D), and applying the scaling (3.7)-(3.11) from the previous section, we obtain

$$
\begin{aligned}
\frac{\partial}{\partial\tilde{x}_3}\left(\frac{\tilde{v}_1}{\tilde{h}_1}\right) + \epsilon^2\left(\frac{\tilde{h}_3}{\tilde{h}_1}\right)^2\frac{\partial}{\partial\tilde{x}_1}\left(\frac{\tilde{v}_3}{\tilde{h}_3}\right) &= 2\epsilon^{-1}\mathcal{X}\tilde{\mathcal{A}}\frac{\tilde{h}_3}{\tilde{h}_1}\tilde{\mathcal{S}}\tilde{\boldsymbol{\sigma}}_{13}\,, \qquad (3.87)\\
\frac{\partial}{\partial\tilde{x}_3}\left(\frac{\tilde{v}_2}{\tilde{h}_2}\right) + \epsilon^2\left(\frac{\tilde{h}_3}{\tilde{h}_2}\right)^2\frac{\partial}{\partial\tilde{x}_2}\left(\frac{\tilde{v}_3}{\tilde{h}_3}\right) &= 2\epsilon^{-1}\mathcal{X}\tilde{\mathcal{A}}\frac{\tilde{h}_3}{\tilde{h}_2}\tilde{\mathcal{S}}\tilde{\boldsymbol{\sigma}}_{23}\,, \qquad (3.88)
\end{aligned}
$$

where

$$
\tilde{\mathcal{S}} = \tilde{\boldsymbol{\sigma}}^2_{11} + \tilde{\boldsymbol{\sigma}}^2_{22} + \tilde{\boldsymbol{\sigma}}_{11}\tilde{\boldsymbol{\sigma}}_{22} + \tilde{\boldsymbol{\sigma}}^2_{12} + \tilde{\boldsymbol{\sigma}}^2_{13} + \tilde{\boldsymbol{\sigma}}^2_{23}\,. \qquad (3.89)
$$

Now, as in the previous section, we have two possibilities of treating the "ϵ^2" terms in (3.87) and (3.88). In the first case, we take these terms from $(k-\frac{1}{2})$-th iteration and integrate both equations along the "vertical" coordinate $\tilde{x}_3$ from the base $(\cdot,\tilde{f}_b)$ to the computational point $(\cdot,\tilde{x}_3)$. Assuming the basal velocity

$\vec{\tilde{v}}^{k+\frac{1}{2}}(\cdot,\tilde{f}_b)$ is either prescribed independently or given by the sliding law as a function of $\tilde{\boldsymbol{\sigma}}^{k+\frac{1}{2}}$, (see Section 3.5.7), we arrive at the updated velocity field:

$$\begin{aligned}
\tilde{v}_1^{k+\frac{1}{2}}(\cdot,\tilde{x}_3) &= \frac{\tilde{h}_1(\cdot,\tilde{x}_3)}{\tilde{h}_1(\cdot,\tilde{f}_b)}\tilde{v}_1^{k+\frac{1}{2}}(\cdot,\tilde{f}_b) + 2\epsilon^{-1}\mathcal{X}\tilde{h}_1(\cdot,\tilde{x}_3)\int_{\tilde{f}_b}^{\tilde{x}_3}\frac{\tilde{h}_3}{\tilde{h}_1}\tilde{\mathcal{A}}\tilde{\mathcal{S}}^{k+\frac{1}{2}}\tilde{\boldsymbol{\sigma}}_{13}^{k+\frac{1}{2}}(\cdot,\tilde{x}_3')\,d\tilde{x}_3' \\
&- \epsilon^2\tilde{h}_1(\cdot,\tilde{x}_3)\int_{\tilde{f}_b}^{\tilde{x}_3}\left(\frac{\tilde{h}_3}{\tilde{h}_1}\right)^2\frac{\partial}{\partial\tilde{x}_1}\left(\frac{\tilde{v}_3^{k-\frac{1}{2}}}{\tilde{h}_3}\right)(\cdot,\tilde{x}_3')\,d\tilde{x}_3'\,, \qquad (3.90)\\
\tilde{v}_2^{k+\frac{1}{2}}(\cdot,\tilde{x}_3) &= \frac{\tilde{h}_2(\cdot,\tilde{x}_3)}{\tilde{h}_2(\cdot,\tilde{f}_b)}\tilde{v}_2^{k+\frac{1}{2}}(\cdot,\tilde{f}_b) + 2\epsilon^{-1}\mathcal{X}\tilde{h}_2(\cdot,\tilde{x}_3)\int_{\tilde{f}_b}^{\tilde{x}_3}\frac{\tilde{h}_3}{\tilde{h}_2}\tilde{\mathcal{A}}\tilde{\mathcal{S}}^{k+\frac{1}{2}}\tilde{\boldsymbol{\sigma}}_{23}^{k+\frac{1}{2}}(\cdot,\tilde{x}_3')\,d\tilde{x}_3' \\
&- \epsilon^2\tilde{h}_2(\cdot,\tilde{x}_3)\int_{\tilde{f}_b}^{\tilde{x}_3}\left(\frac{\tilde{h}_3}{\tilde{h}_2}\right)^2\frac{\partial}{\partial\tilde{x}_2}\left(\frac{\tilde{v}_3^{k-\frac{1}{2}}}{\tilde{h}_3}\right)(\cdot,\tilde{x}_3')\,d\tilde{x}_3'\,. \qquad (3.91)
\end{aligned}$$

The "vertical" velocity component $\tilde{v}_3^{k+\frac{1}{2}}$ can be obtained from the mass balance (continuity) equation (1.25), which, with the use of (D.12) and the scaling (3.7)-(3.11) reads as

$$0 = \frac{\partial}{\partial\tilde{x}_3}(\tilde{h}_1\tilde{h}_2\tilde{v}_3) + \frac{\partial}{\partial\tilde{x}_1}(\tilde{h}_2\tilde{h}_3\tilde{v}_1) + \frac{\partial}{\partial\tilde{x}_2}(\tilde{h}_1\tilde{h}_3\tilde{v}_2)\,. \qquad (3.92)$$

After integration along the vertical coordinate as in the case of $\tilde{v}_1$, $\tilde{v}_2$, we arrive at the final expression:

$$\begin{aligned}
\tilde{v}_3^{k+\frac{1}{2}}(\cdot,\tilde{x}_3) &= \frac{\tilde{h}_1(\cdot,\tilde{f}_b)\tilde{h}_2(\cdot,\tilde{f}_b)}{\tilde{h}_1(\cdot,\tilde{x}_3)\tilde{h}_2(\cdot,\tilde{x}_3)}\tilde{v}_3^{k+\frac{1}{2}}(\cdot,\tilde{f}_b) \\
&- \frac{1}{\tilde{h}_1(\cdot,\tilde{x}_3)\tilde{h}_2(\cdot,\tilde{x}_3)}\int_{\tilde{f}_b}^{\tilde{x}_3}\left(\frac{\partial}{\partial\tilde{x}_1}(\tilde{h}_2\tilde{h}_3\tilde{v}_1^{k+\frac{1}{2}}) + \frac{\partial}{\partial\tilde{x}_2}(\tilde{h}_1\tilde{h}_3\tilde{v}_2^{k+\frac{1}{2}})\right)(\cdot,\tilde{x}_3')\,d\tilde{x}_3'\,. \qquad (3.93)
\end{aligned}$$

In the previous sections, we have discussed only the case of no-slip conditions at the base. The case presented here is slightly more general, as non-zero basal velocities can also be taken into account. This is crucial for the implementation of either non-homogeneous Dirichlet boundary conditions for velocity or even a sliding law, as will be presented in Section 3.5.7.

However, for no-slip conditions and Cartesian geometry, we obtain the formulae (3.55)-(3.57). For spherical coordinates, introduced in (2.2), we have

$$\begin{aligned}
\tilde{v}_\vartheta^{k+\frac{1}{2}}(\cdot,\tilde{\zeta}) &= \frac{1+\epsilon\tilde{\zeta}}{1+\epsilon\tilde{f}_b}\tilde{v}_\vartheta^{k+\frac{1}{2}}(\cdot,\tilde{f}_b) + 2\epsilon^{-1}\mathcal{X}(1+\epsilon\tilde{\zeta})\int_{\tilde{f}_b}^{\tilde{\zeta}}\frac{1}{1+\epsilon\tilde{\zeta}'}\tilde{\mathcal{A}}\tilde{\mathcal{S}}^{k+\frac{1}{2}}\tilde{\boldsymbol{\sigma}}_{\vartheta\zeta}^{k+\frac{1}{2}}(\cdot,\tilde{\zeta}')\,d\tilde{\zeta}' \\
&- \epsilon^2(1+\epsilon\tilde{\zeta})\int_{\tilde{f}_b}^{\tilde{\zeta}}\left(\frac{1}{1+\epsilon\tilde{\zeta}'}\right)^2\frac{\partial\tilde{v}_\zeta^{k-\frac{1}{2}}}{\partial\vartheta}(\cdot,\tilde{\zeta}')\,d\tilde{\zeta}'\,, \qquad (3.94)\\
\tilde{v}_\varphi^{k+\frac{1}{2}}(\cdot,\tilde{\zeta}) &= \frac{1+\epsilon\tilde{\zeta}}{1+\epsilon\tilde{f}_b}\tilde{v}_\varphi^{k+\frac{1}{2}}(\cdot,\tilde{f}_b) + 2\epsilon^{-1}\mathcal{X}(1+\epsilon\tilde{\zeta})\int_{\tilde{f}_b}^{\tilde{\zeta}}\frac{1}{1+\epsilon\tilde{\zeta}'}\tilde{\mathcal{A}}\tilde{\mathcal{S}}^{k+\frac{1}{2}}\tilde{\boldsymbol{\sigma}}_{\varphi\zeta}^{k+\frac{1}{2}}(\cdot,\tilde{\zeta}')\,d\tilde{\zeta}' \\
&- \epsilon^2(1+\epsilon\tilde{\zeta})\int_{\tilde{f}_b}^{\tilde{\zeta}}\left(\frac{1}{1+\epsilon\tilde{\zeta}'}\right)^2\frac{1}{\sin\vartheta}\frac{\partial\tilde{v}_\zeta^{k-\frac{1}{2}}}{\partial\varphi}(\cdot,\tilde{\zeta}')\,d\tilde{\zeta}'\,, \qquad (3.95)\\
\tilde{v}_\zeta^{k+\frac{1}{2}}(\cdot,\tilde{\zeta}) &= \frac{(1+\epsilon\tilde{f}_b)^2}{(1+\epsilon\tilde{\zeta})^2}\tilde{v}_\zeta^{k+\frac{1}{2}}(\cdot,\tilde{f}_b) - \frac{1}{(1+\epsilon\tilde{\zeta})^2\sin\vartheta}\int_{\tilde{f}_b}^{\tilde{\zeta}}(1+\epsilon\tilde{\zeta}')\left(\frac{\partial}{\partial\vartheta}(\sin\vartheta\tilde{v}_\vartheta^{k+\frac{1}{2}}) + \frac{\partial\tilde{v}_\varphi^{k+\frac{1}{2}}}{\partial\varphi}\right)(\cdot,\tilde{\zeta}')\,d\tilde{\zeta}'\,. \qquad (3.96)
\end{aligned}$$

The second possibility of treating the "ϵ^2" terms in (3.87) and (3.88), lies in first computing the vertical velocity $\tilde{v}_3$, which is then inserted into (3.87) and (3.88) and again these equations are integrated along the vertical coordinate in order to obtain the velocity components $\tilde{v}_1$, $\tilde{v}_2$. The procedure starts from expressing "33" component of the rheological equation (1.18). When scaled, and with $\boldsymbol{\sigma}_{33}$ expressed by $\boldsymbol{\sigma}_{33} = -\boldsymbol{\sigma}_{11} - \boldsymbol{\sigma}_{22}$ (since $\boldsymbol{\sigma}$ is traceless), it reads as

$$\tilde{\boldsymbol{d}}_{33} = -\epsilon^{-2}\mathcal{X}\tilde{\mathcal{A}}\tilde{S}(\tilde{\boldsymbol{\sigma}}_{11} + \tilde{\boldsymbol{\sigma}}_{22}) \,, \tag{3.97}$$

which, with the use of the definition of $\boldsymbol{d}_{33}$ in curvilinear coordinates (3.118), can be taken at the $(k+\frac{1}{2})$-th iteration as follows

$$\frac{\partial \tilde{v}_3^{k+\frac{1}{2}}}{\partial \tilde{x}_3} = -\left(\frac{\tilde{v}_1^{k-\frac{1}{2}}}{\tilde{h}_1}\frac{\partial \tilde{h}_3}{\partial \tilde{x}_1} + \frac{\tilde{v}_2^{k-\frac{1}{2}}}{\tilde{h}_2}\frac{\partial \tilde{h}_3}{\partial \tilde{x}_2}\right) - \epsilon^{-2}\mathcal{X}\tilde{h}_3\tilde{\mathcal{A}}\tilde{S}^{k+\frac{1}{2}}(\tilde{\boldsymbol{\sigma}}_{11}^{k+\frac{1}{2}} + \tilde{\boldsymbol{\sigma}}_{22}^{k+\frac{1}{2}}) \,. \tag{3.98}$$

Now this form allows us to obtain $\tilde{v}_3^{k+\frac{1}{2}}$ by vertical integration, considering again the value at the base from the k-th iteration as

$$\begin{aligned}
\tilde{v}_3^{k+\frac{1}{2}}(\cdot,\tilde{x}_3) &= \tilde{v}_3^{k+\frac{1}{2}}(\cdot,\tilde{f}_b) - \int_{\tilde{f}_b}^{\tilde{x}_3}\left(\frac{\tilde{v}_1^{k-\frac{1}{2}}}{\tilde{h}_1}\frac{\partial \tilde{h}_3}{\partial \tilde{x}_1} + \frac{\tilde{v}_2^{k-\frac{1}{2}}}{\tilde{h}_2}\frac{\partial \tilde{h}_3}{\partial \tilde{x}_2}\right)(\cdot,\tilde{x}_3')\,d\tilde{x}_3' \\
&- \epsilon^{-2}\mathcal{X}\int_{\tilde{f}_b}^{\tilde{x}_3}\tilde{h}_3\tilde{\mathcal{A}}\tilde{S}^{k+\frac{1}{2}}(\tilde{\boldsymbol{\sigma}}_{11}^{k+\frac{1}{2}} + \tilde{\boldsymbol{\sigma}}_{22}^{k+\frac{1}{2}})(\cdot,\tilde{x}_3')\,d\tilde{x}_3' \,.
\end{aligned} \tag{3.99}$$

Substituting now $\tilde{v}_3^{k+\frac{1}{2}}$ into (3.87) and (3.88) for $\tilde{v}_3$, and integrating along the vertical coordinate from the base $(\cdot,\tilde{f}_b(\cdot))$ to the computational point $(\cdot,\tilde{x}_3)$, we arrive at

$$\begin{aligned}
\tilde{v}_1^{k+\frac{1}{2}}(\cdot,\tilde{x}_3) &= \frac{\tilde{h}_1(\cdot,\tilde{x}_3)}{\tilde{h}_1(\cdot,\tilde{f}_b)}\tilde{v}_1^{k+\frac{1}{2}}(\cdot,\tilde{f}_b) + 2\epsilon^{-1}\mathcal{X}\tilde{h}_1(\cdot,\tilde{x}_3)\int_{\tilde{f}_b}^{\tilde{x}_3}\frac{\tilde{h}_3}{\tilde{h}_1}\tilde{\mathcal{A}}\tilde{\mathcal{S}}^{k+\frac{1}{2}}\tilde{\boldsymbol{\sigma}}_{13}^{k+\frac{1}{2}}(\cdot,\tilde{x}_3')\,d\tilde{x}_3' \\
&- \epsilon^2\tilde{h}_1(\cdot,\tilde{x}_3)\int_{\tilde{f}_b}^{\tilde{x}_3}\left(\frac{\tilde{h}_3}{\tilde{h}_1}\right)^2\frac{\partial}{\partial \tilde{x}_1}\left(\frac{\tilde{v}_3^{k+\frac{1}{2}}}{\tilde{h}_3}\right)(\cdot,\tilde{x}_3')\,d\tilde{x}_3' \,,
\end{aligned} \tag{3.100}$$

$$\begin{aligned}
\tilde{v}_2^{k+\frac{1}{2}}(\cdot,\tilde{x}_3) &= \frac{\tilde{h}_2(\cdot,\tilde{x}_3)}{\tilde{h}_2(\cdot,\tilde{f}_b)}\tilde{v}_2^{k+\frac{1}{2}}(\cdot,\tilde{f}_b) + 2\epsilon^{-1}\mathcal{X}\tilde{h}_2(\cdot,\tilde{x}_3)\int_{\tilde{f}_b}^{\tilde{x}_3}\frac{\tilde{h}_3}{\tilde{h}_2}\tilde{\mathcal{A}}\tilde{\mathcal{S}}^{k+\frac{1}{2}}\tilde{\boldsymbol{\sigma}}_{23}^{k+\frac{1}{2}}(\cdot,\tilde{x}_3')\,d\tilde{x}_3' \\
&- \epsilon^2\tilde{h}_2(\cdot,\tilde{x}_3)\int_{\tilde{f}_b}^{\tilde{x}_3}\left(\frac{\tilde{h}_3}{\tilde{h}_2}\right)^2\frac{\partial}{\partial \tilde{x}_2}\left(\frac{\tilde{v}_3^{k+\frac{1}{2}}}{\tilde{h}_3}\right)(\cdot,\tilde{x}_3')\,d\tilde{x}_3' \,.
\end{aligned} \tag{3.101}$$

In particular, for Cartesian coordinates (2.1) due to (2.10), and no-slip at the base, we obtain (3.62), (3.63) and (3.59). For spherical coordinates (2.2), due to (2.15), we obtain

$$\tilde{v}_\zeta^{k+\frac{1}{2}}(\cdot,\tilde{\zeta}) = \tilde{v}_\zeta^{k+\frac{1}{2}}(\cdot,\tilde{f}_b) - \epsilon^{-2}\mathcal{X}\int_{\tilde{f}_b}^{\tilde{\zeta}}\tilde{\mathcal{A}}\tilde{S}^{k+\frac{1}{2}}(\tilde{\boldsymbol{\sigma}}_{\vartheta\vartheta}^{k+\frac{1}{2}} + \tilde{\boldsymbol{\sigma}}_{\varphi\varphi}^{k+\frac{1}{2}})(\cdot,\tilde{\zeta}')\,d\tilde{\zeta}' \,, \tag{3.102}$$

$$\tilde{v}_{\vartheta}^{k+\frac{1}{2}}(\cdot,\tilde{\zeta}) = \frac{1+\epsilon\tilde{\zeta}}{1+\epsilon\tilde{f}_b}\tilde{v}_{\vartheta}^{k+\frac{1}{2}}(\cdot,\tilde{f}_b) + 2\epsilon^{-1}\mathcal{X}(1+\epsilon\tilde{\zeta})\int_{\tilde{f}_b}^{\tilde{\zeta}}\frac{1}{1+\epsilon\tilde{\zeta}'}\tilde{\mathcal{A}}\tilde{\mathcal{S}}^{k+\frac{1}{2}}\tilde{\boldsymbol{\sigma}}_{\vartheta r}^{k+\frac{1}{2}}(\cdot,\tilde{\zeta}')\,d\tilde{\zeta}'$$
$$- \epsilon^2(1+\epsilon\tilde{\zeta})\int_{\tilde{f}_b}^{\tilde{\zeta}}\left(\frac{1}{1+\epsilon\tilde{\zeta}'}\right)^2\frac{\partial\tilde{v}_{\zeta}^{k+\frac{1}{2}}}{\partial\vartheta}(\cdot,\tilde{\zeta}')\,d\tilde{\zeta}'\,, \tag{3.103}$$

$$\tilde{v}_{\varphi}^{k+\frac{1}{2}}(\cdot,\tilde{\zeta}) = \frac{1+\epsilon\tilde{\zeta}}{1+\epsilon\tilde{f}_b}\tilde{v}_{\varphi}^{k+\frac{1}{2}}(\cdot,\tilde{f}_b) + 2\epsilon^{-1}\mathcal{X}(1+\epsilon\tilde{\zeta})\int_{\tilde{f}_b}^{\tilde{\zeta}}\frac{1}{1+\epsilon\tilde{\zeta}'}\tilde{\mathcal{A}}\tilde{\mathcal{S}}^{k+\frac{1}{2}}\tilde{\boldsymbol{\sigma}}_{\varphi r}^{k+\frac{1}{2}}(\cdot,\tilde{\zeta}')\,d\tilde{\zeta}'$$
$$- \epsilon^2(1+\epsilon\tilde{\zeta})\int_{\tilde{f}_b}^{\tilde{\zeta}}\left(\frac{1}{1+\epsilon\tilde{\zeta}'}\right)^2\frac{1}{\sin\vartheta}\frac{\partial\tilde{v}_{\zeta}^{k+\frac{1}{2}}}{\partial\varphi}(\cdot,\tilde{\zeta}')\,d\tilde{\zeta}'\,. \tag{3.104}$$

$$\tag{3.105}$$

The computed velocity fields (3.90), (3.91), and (3.93) are used to evaluate the auxiliary stress field $\vec{u}^{\star} = (\tilde{\boldsymbol{\sigma}}_{11}^{\star}, \tilde{\boldsymbol{\sigma}}_{22}^{\star}, \tilde{\boldsymbol{\sigma}}_{12}^{\star}, \tilde{\boldsymbol{\sigma}}_{13}^{\star}, \tilde{\boldsymbol{\sigma}}_{23}^{\star})$ using the rheology (1.17). In orthogonal coordinates with the scaling (3.7)-(3.11) and with the help of (D), we obtain:

$$\tilde{\boldsymbol{\sigma}}_{13} = 2\tilde{\eta}\tilde{\boldsymbol{d}}_{13}\,, \tag{3.106}$$
$$\tilde{\boldsymbol{\sigma}}_{23} = 2\tilde{\eta}\tilde{\boldsymbol{d}}_{23}\,, \tag{3.107}$$
$$\tilde{\boldsymbol{\sigma}}_{11} = 2\epsilon\tilde{\eta}\tilde{\boldsymbol{d}}_{11}\,, \tag{3.108}$$
$$\tilde{\boldsymbol{\sigma}}_{22} = 2\epsilon\tilde{\eta}\tilde{\boldsymbol{d}}_{22}\,, \tag{3.109}$$
$$\tilde{\boldsymbol{\sigma}}_{12} = 2\epsilon\tilde{\eta}\tilde{\boldsymbol{d}}_{12}\,, \tag{3.110}$$

where

$$\tilde{\eta} = \frac{1}{(2\epsilon^{-1}\mathcal{X}\tilde{\mathcal{A}}\tilde{\mathcal{V}})^{\frac{1}{3}}}\,, \tag{3.111}$$

$$\tilde{\mathcal{V}} = 4(\tilde{\boldsymbol{d}}_{13}^2 + \tilde{\boldsymbol{d}}_{23}^2 + \epsilon^2(\tilde{\boldsymbol{d}}_{11}^2 + \tilde{\boldsymbol{d}}_{22}^2 + \tilde{\boldsymbol{d}}_{11}\tilde{\boldsymbol{d}}_{22} + \tilde{\boldsymbol{d}}_{12}^2))\,, \tag{3.112}$$

$$\mathcal{X} = \frac{[\mathcal{A}](\rho g)^3([h_3][\Delta_3])^5}{[v_h][h_1][\Delta_1]}\,, \tag{3.113}$$

and

$$\tilde{\boldsymbol{d}}_{13} = \frac{1}{2}\left(\frac{1}{\tilde{h}_3}\frac{\partial\tilde{v}_1}{\partial\tilde{x}_3} - \frac{1}{\tilde{h}_1\tilde{h}_3}\frac{\partial\tilde{h}_1}{\partial\tilde{x}_3}\tilde{v}_1 + \epsilon^2\left(\frac{1}{\tilde{h}_1}\frac{\partial\tilde{v}_3}{\partial\tilde{x}_1} - \frac{1}{\tilde{h}_1\tilde{h}_3}\frac{\partial\tilde{h}_3}{\partial\tilde{x}_1}\tilde{v}_3\right)\right)\,, \tag{3.114}$$

$$\tilde{\boldsymbol{d}}_{23} = \frac{1}{2}\left(\frac{1}{\tilde{h}_3}\frac{\partial\tilde{v}_2}{\partial\tilde{x}_3} - \frac{1}{\tilde{h}_2\tilde{h}_3}\frac{\partial\tilde{h}_2}{\partial\tilde{x}_3}\tilde{v}_2 + \epsilon^2\left(\frac{1}{\tilde{h}_2}\frac{\partial\tilde{v}_3}{\partial\tilde{x}_2} - \frac{1}{\tilde{h}_2\tilde{h}_3}\frac{\partial\tilde{h}_3}{\partial\tilde{x}_2}\tilde{v}_3\right)\right)\,, \tag{3.115}$$

$$\tilde{\boldsymbol{d}}_{11} = \left(\frac{1}{\tilde{h}_1}\frac{\partial\tilde{v}_1}{\partial\tilde{x}_1} + \frac{1}{\tilde{h}_1\tilde{h}_2}\frac{\partial\tilde{h}_1}{\partial\tilde{x}_2}\tilde{v}_2 + \frac{1}{\tilde{h}_1\tilde{h}_3}\frac{\partial\tilde{h}_1}{\partial\tilde{x}_3}\tilde{v}_3\right)\,, \tag{3.116}$$

$$\tilde{\boldsymbol{d}}_{22} = \left(\frac{1}{\tilde{h}_2}\frac{\partial\tilde{v}_2}{\partial\tilde{x}_2} + \frac{1}{\tilde{h}_1\tilde{h}_2}\frac{\partial\tilde{h}_2}{\partial\tilde{x}_1}\tilde{v}_1 + \frac{1}{\tilde{h}_2\tilde{h}_3}\frac{\partial\tilde{h}_2}{\partial\tilde{x}_3}\tilde{v}_3\right)\,, \tag{3.117}$$

$$\tilde{\boldsymbol{d}}_{33} = \left(\frac{1}{\tilde{h}_3}\frac{\partial\tilde{v}_3}{\partial\tilde{x}_3} + \frac{1}{\tilde{h}_1\tilde{h}_3}\frac{\partial\tilde{h}_3}{\partial\tilde{x}_1}\tilde{v}_1 + \frac{1}{\tilde{h}_2\tilde{h}_3}\frac{\partial\tilde{h}_3}{\partial\tilde{x}_2}\tilde{v}_2\right)\,, \tag{3.118}$$

$$\tilde{\boldsymbol{d}}_{12} = \frac{1}{2}\left(\frac{1}{\tilde{h}_2}\frac{\partial\tilde{v}_1}{\partial\tilde{x}_2} - \frac{1}{\tilde{h}_1\tilde{h}_2}\frac{\partial\tilde{h}_1}{\partial\tilde{x}_2}\tilde{v}_1 + \frac{1}{\tilde{h}_1}\frac{\partial\tilde{v}_2}{\partial\tilde{x}_1} - \frac{1}{\tilde{h}_1\tilde{h}_2}\frac{\partial\tilde{h}_2}{\partial\tilde{x}_1}\tilde{v}_2\right)\,. \tag{3.119}$$

For Cartesian coordinates, these formulae reduce to (3.22)-(3.29), while for spherical coordinates we arrive at:

$$\tilde{\boldsymbol{\sigma}}_{\vartheta\zeta} = 2\tilde{\eta}\tilde{\boldsymbol{d}}_{\vartheta\zeta} , \tag{3.120}$$
$$\tilde{\boldsymbol{\sigma}}_{\varphi\zeta} = 2\tilde{\eta}\tilde{\boldsymbol{d}}_{\varphi\zeta} , \tag{3.121}$$
$$\tilde{\boldsymbol{\sigma}}_{\vartheta\vartheta} = 2\epsilon\tilde{\eta}\tilde{\boldsymbol{d}}_{\vartheta\vartheta} , \tag{3.122}$$
$$\tilde{\boldsymbol{\sigma}}_{\varphi\varphi} = 2\epsilon\tilde{\eta}\tilde{\boldsymbol{d}}_{\varphi\varphi} , \tag{3.123}$$
$$\tilde{\boldsymbol{\sigma}}_{\vartheta\varphi} = 2\epsilon\tilde{\eta}\tilde{\boldsymbol{d}}_{\vartheta\varphi} , \tag{3.124}$$

and

$$\tilde{\mathcal{V}} = 4(\tilde{\boldsymbol{d}}^2_{\vartheta\zeta} + \tilde{\boldsymbol{d}}^2_{\varphi\zeta} + \epsilon^2(\tilde{\boldsymbol{d}}^2_{\vartheta\vartheta} + \tilde{\boldsymbol{d}}^2_{\varphi\varphi} + \tilde{\boldsymbol{d}}_{\vartheta\vartheta}\tilde{\boldsymbol{d}}_{\varphi\varphi} + \tilde{\boldsymbol{d}}^2_{\vartheta\varphi})) , \tag{3.125}$$

where

$$\tilde{\boldsymbol{d}}_{\vartheta\zeta} = \frac{1}{2}\left(\frac{\partial\tilde{v}_\vartheta}{\partial\tilde{\zeta}} - \frac{\epsilon}{1+\epsilon\tilde{\zeta}}\tilde{v}_\vartheta + \frac{\epsilon^2}{1+\epsilon\tilde{\zeta}}\frac{\partial\tilde{v}_\zeta}{\partial\vartheta}\right) , \tag{3.126}$$
$$\tilde{\boldsymbol{d}}_{\varphi\zeta} = \frac{1}{2}\left(\frac{\partial\tilde{v}_\varphi}{\partial\tilde{\zeta}} - \frac{\epsilon}{(1+\epsilon\tilde{\zeta})}\tilde{v}_\varphi + \frac{\epsilon^2}{(1+\epsilon\tilde{\zeta})\sin\vartheta}\frac{\partial\tilde{v}_\zeta}{\partial\varphi}\right) , \tag{3.127}$$
$$\tilde{\boldsymbol{d}}_{\vartheta\vartheta} = \left(\frac{1}{1+\epsilon\tilde{\zeta}}\frac{\partial\tilde{v}_\vartheta}{\partial\vartheta} + \frac{\epsilon}{1+\epsilon\tilde{\zeta}}\tilde{v}_\zeta\right) , \tag{3.128}$$
$$\tilde{\boldsymbol{d}}_{\varphi\varphi} = \left(\frac{1}{(1+\epsilon\tilde{\zeta})\sin\vartheta}\frac{\partial\tilde{v}_\varphi}{\partial\varphi} + \frac{\cot\vartheta}{1+\epsilon\tilde{\zeta}}\tilde{v}_\vartheta + \frac{\epsilon}{1+\epsilon\tilde{\zeta}}\tilde{v}_\zeta\right) , \tag{3.129}$$
$$\tilde{\boldsymbol{d}}_{\vartheta\varphi} = \frac{1}{2}\left(\frac{1}{(1+\epsilon\tilde{\zeta})\sin\vartheta}\frac{\partial\tilde{v}_\vartheta}{\partial\varphi} + \frac{1}{1+\epsilon\tilde{\zeta}}\frac{\partial\tilde{v}_\varphi}{\partial\vartheta} - \frac{\cot\vartheta}{1+\epsilon\tilde{\zeta}}\tilde{v}_\varphi\right) . \tag{3.130}$$

The SIA-I scheme itself may then again be depicted a scheme analogous to that from Table 3.1:

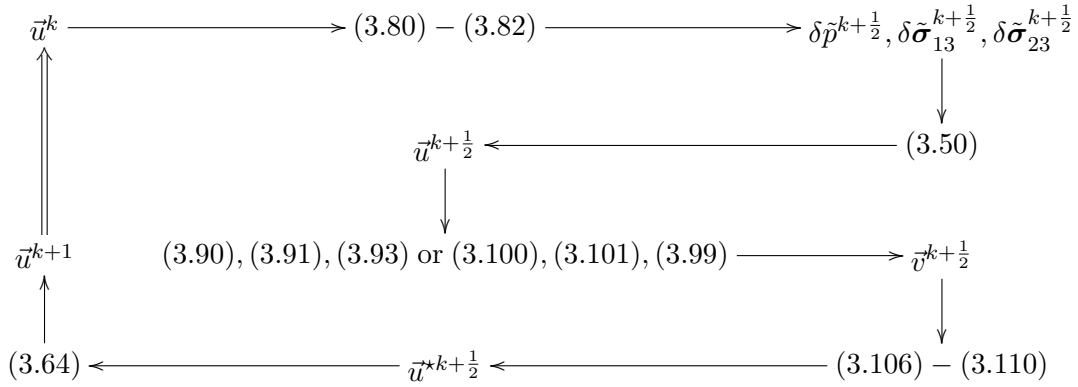

Table 3.2: SIA-I scheme in general orthogonal curvilinear coordinates.

3.5 Numerical simulations

In this section, we present numerical results obtained by the SIA-I approach for the **Ice-Sheet Model Intercomparison Project – Higher Order Models (ISMIP-HOM)** (Pattyn, 2007, http://homepages.ulb.ac.be/

∼fpattyn/ismip/). This benchmark experiment aimed to demonstrate the effects of higher-order solutions of various ice-flow model problems compared to the solution by the Shallow Ice Approximation, where by "higher-order" all such solutions are meant that take into account the longitudinal stresses.

Our approach has been incorporated into experiments A and B (model *oso1*, see Pattyn et al. (2008), for a discussion of the results and model outputs). Since experiment B is only a 2-D (flowline) version of experiment A, we present here only the results for the more challenging 3-D experiment A.

Although we did not participate in experiment C, we now discuss the performance of the SIA-I algorithm for this case, where basal sliding with a prescribed sliding law is considered in contrast to A and B where no-slip was considered at the glacier base.

3.5.1 Numerical implementation of the SIA-I algorithm

For the examples shown below, a rather elementary approach was adopted for the numerical implementation of the SIA-I algorithm. After inspecting the particular steps of the iterative scheme shown in Table 3.1, one realizes that the whole algorithm is relatively simple from the numerical point of view, as the only operations to be applied are

- **Data storage**
  We have chosen a staggered grid with two types of alternating nodes, where one type of node contains the velocity vector components $\tilde{v}_x, \tilde{v}_y, \tilde{v}_z$, while the other nodes contain the stress-tensor components $\tilde{\boldsymbol{\sigma}}_{xx}, \tilde{\boldsymbol{\sigma}}_{yy}, \tilde{\boldsymbol{\sigma}}_{xy}, \tilde{\boldsymbol{\sigma}}_{xz}, \tilde{\boldsymbol{\sigma}}_{yz}$, and pressure $\tilde{p}$. Such a choice provides better stability of the iterative scheme.

- **Numerical differentiation**
  This is performed by a two-sided symmetrical finite difference scheme, i.e. we approximate

$$\left(\frac{\partial\varphi}{\partial x}\right)(x_i, y_j, z_k) \approx \frac{\varphi(x_{i+1}, y_j, z_k) - \varphi(x_{i-1}, y_j, z_k)}{x_{i+1} - x_{i-1}}\,, \tag{3.131}$$

$$\left(\frac{\partial\varphi}{\partial y}\right)(x_i, y_j, z_k) \approx \frac{\varphi(x_i, y_{j+1}, z_k) - \varphi(x_i, y_{j-1}, z_k)}{y_{j+1} - y_{j-1}}\,, \tag{3.132}$$

$$\left(\frac{\partial\varphi}{\partial z}\right)(x_i, y_j, z_k) \approx \frac{\varphi(x_i, y_j, z_{k+1}) - \varphi(x_i, y_j, z_{k-1})}{z_{k+1} - z_{k-1}}\,. \tag{3.133}$$

- **One-dimensional numerical integration** is performed by the simple extended trapezoidal rule (e.g. Press, 1992):

$$\int_a^b \varphi(z)dz \approx \frac{b-a}{n}\left(\varphi(z_0) + 2\varphi(z_1) + 2\varphi(z_2) + \cdots + 2\varphi(z_{n-1}) + \varphi(z_n)\right)\,. \tag{3.134}$$

The application of more sophisticated methods such as a higher-order differentiation scheme or higher-order integration approach is possible, but the overall effect was found to be negligible. Moreover, the relative simplicity of the numerical realization of the SIA-I algorithm in the following demonstrations results in its efficiency in terms of computational speed and lower computer memory demands.

3.5.2 ISMIP-HOM experiment A

This experiment is set up as follows. It involves a Stokes flow problem, no slip at the bed, stress-free conditions at the surface and the ice is considered isothermal. The values of the physical parameters used

Symbol	Constant	Value	Units
$\mathcal{A}$	Ice-flow parameter	10^{-16}	$\mathrm{Pa}^{-3}\mathrm{a}^{-1}$
ρ	Ice density	910	$\mathrm{kg\,m}^{-3}$
g	Gravitational acceleration	9.81	$\mathrm{m\,s}^{-2}$

Table 3.3: Values of the physical parameters used in experiment A.

are given in Table 3.3.

The glacier has a square base of size $\mathrm{L_{sc}} \times \mathrm{L_{sc}}$. The upper and lower surfaces are given (in m) by

$$f_s(x,y) = -x\tan\alpha\,, \qquad \alpha = 0.5^\circ, \tag{3.135}$$

$$f_b(x,y) = f_s(x,y) - 1000 + 500\sin(\omega x)\sin(\omega y)\,, \tag{3.136}$$

with

$$\omega = \frac{2\pi}{\mathrm{L_{sc}}}\,.$$

At the sides, the periodic boundary conditions are prescribed:

$$\forall x \in \langle 0, \mathrm{L_{sc}}\rangle, \forall z \in \langle f_b(\cdot), f_s(\cdot)\rangle : \ \vec{v}(x,0,z) = \vec{v}(x,\mathrm{L_{sc}},z)\,, \tag{3.137}$$

$$\forall y \in \langle 0, \mathrm{L_{sc}}\rangle, \forall z \in \langle f_b(\cdot), f_s(\cdot)\rangle : \ \vec{v}(0,y,z) = \vec{v}(\mathrm{L_{sc}},y,z)\,. \tag{3.138}$$

The plotted quantities are the velocities v_x, v_y, v_z at the upper surface (in $\mathrm{m\,a}^{-1}$) and the stress components $\boldsymbol{\sigma}_{xz}$, $\boldsymbol{\sigma}_{yz}$, $\Delta p = p - \mathcal{H}\rho g$ at the bottom (in kPa), $\mathcal{H} = f_s - f_b$. All quantities are mapped onto the scaled domain $\langle 0,1\rangle \times \langle 0,1\rangle$.

The numerical implementation includes the transformation of the problem into stretched coordinates, as usual in glaciology (e.g. Pattyn, 2003). The SIA-I algorithm in stretched Cartesian coordinates is outlined in Appendix C.

The glacier flow computed by the SIA-I approach is first checked against a finite-difference full-Stokes solver that we developed and that is briefly described in the next section. We also present comparisons with other ISMIP-HOM participants, based on the published ISMIP-HOM results in Pattyn et al. (2008), where a detailed description of the benchmark and the comparisons between our SIA-I-based results and other solvers can be found.

3.5.3 The finite-difference full-Stokes solver

To carry out the benchmarks against which the SIA-I solution can be checked, we developed a simple full-Stokes solver. The governing equations (3.12)-(3.14), (3.15) and (3.22)-(3.29) are rewritten in the stretched coordinates (see e.g. Pattyn, 2003) or Appendix C.

The spatial derivatives are approximated by two-point symmetric differences and the resulting system of non-linear algebraic equations is solved on the staggered grid with two types of alternating nodes, first for the rheology equations and the equation of continuity, the others for the momentum balance equations. For a fixed viscosity, the linear system of equations is solved by a PARDISO (Parallel Sparse Direct Linear Solver) routine (http://www.intel.com), and the viscosity is iteratively updated by the convex combination of the previous and updated velocity fields. The convergence is checked by inspecting the evolution of the maximal difference between two successively computed velocity fields.

3.5.4 Results I - Comparison with a finite-difference full-Stokes solver

The ISMIP-HOM benchmark was performed for aspect ratios $\epsilon = \frac{1}{5}, \frac{1}{10}, \frac{1}{20}, \frac{1}{40}, \frac{1}{80}$, and $\frac{1}{160}$. As one might expect, the higher the aspect ratio, the worse the performance of the SIA-I algorithm. Bellow, we display the comparison of the SIA-I solution and the full-Stokes solution by a finite-difference solver, described in the previous section, for the most interesting cases of $\epsilon = \frac{1}{20}$ and $\frac{1}{10}$. For $\epsilon = \frac{1}{5}$ the SIA-I algorithm already fails to converge for this particular problem.

Results for $\epsilon = \frac{1}{20}$. The SIA-I solution is computed with the relaxation parameters $\theta_1 = 0.2$ and $\theta_2 = 0.05$. The results are stored in a staggered grid of dimensions $41 \times 41 \times 41$. The SIA-I solution, obtained after 60 iterations, is shown in Fig. 3.1 (full lines). The computation was performed on an Intel Pentium 4, 3.2GHz computer and took approximately 52s. The full-Stokes solution (dotted lines in Fig. 3.1) was obtained by the finite-difference code from Section 3.5.3 by an iterative updating of the nonlinear viscosity until the convergence criterion was fulfilled. The computation was started from the SIA-I solution interpolated to a staggered $20 \times 20 \times 20$ grid.

Fig. 3.1 shows almost perfect agreement between the SIA-I and the full-Stokes surface velocities and a minor quantitative mismatch for the bottom stress components $\boldsymbol{\sigma}_{xz}, \boldsymbol{\sigma}_{yz}$. The main difference appears, however, in the bottom pressure difference Δp.

Results for $\epsilon = \frac{1}{10}$. The SIA-I solution is computed with the relaxation parameters $\theta_1 = 0.2$ and $\theta_2 = 0.02$. The resolution of the computational domain for both solutions was the same as in the previous case. The SIA-I solution, obtained now after 100 iterations to achieve the required tolerance (Fig. 3.2, full lines), is again compared with the full-Stokes solution (dotted lines) which was obtained by the finite-difference approach.

Inspecting Fig. 3.2, we can see a rather good agreement between both the solutions, in particular for the velocities. Again, the largest difference appears in the pressure difference Δp. It is noted that the SIA-I solution is smoother than the finite-difference solution, indicating possibly some numerical instabilities in the finite-difference solver.

To estimate the order of improvement of the SIA-I solution compared to the SIA solution, Fig. 3.3 plots the SIA solution for v_x, v_z at the surface (v_y is identically zero) and $\boldsymbol{\sigma}_{xz}$ at the bottom ($\boldsymbol{\sigma}_{yz}$ and Δp identically zero). Comparing Fig. 3.2 with Fig. 3.3, we can see that the SIA-I solution differs significantly from the SIA solution, demonstrating that the SIA-I approach is capable of providing a significantly improved solution to the problem.

As demonstrated in the following section, the convergence of the SIA-I algorithm worsens with increasing aspect ratio ϵ. This can be to some extent overcome by choosing sufficiently small relaxation parameters θ_1, θ_2, but a threshold aspect ratio value appears to exist for the practical usage of our method. For the current geometry setting from the ISMIP-HOM experiment A, this value is $\frac{1}{10}$. For an aspect ratio larger than $\epsilon = \frac{1}{10}$, and for the current geometry setting, the SIA-I algorithm fails to converge no matter how small relaxation parameters θ_1 and θ_2 are chosen. We may thus say that there is a threshold of the aspect ratio ϵ above which the SIA-I algorithm does not converge. Below this threshold, our numerical experiments have demonstrated that the smaller the aspect ratio, the faster the convergence of the SIA-I algorithm for a prescribed accuracy. This behavior resembles that of the SIA approach.

3.5.5 Results II - Comparison with the ISMIP-HOM benchmark

In Figs. 3.5-3.7, we display a comparison of the SIA-I output and a representative set of ISMIP-HOM experiment A solutions published in the benchmark (our model participated as well - is denoted as *oso1*).

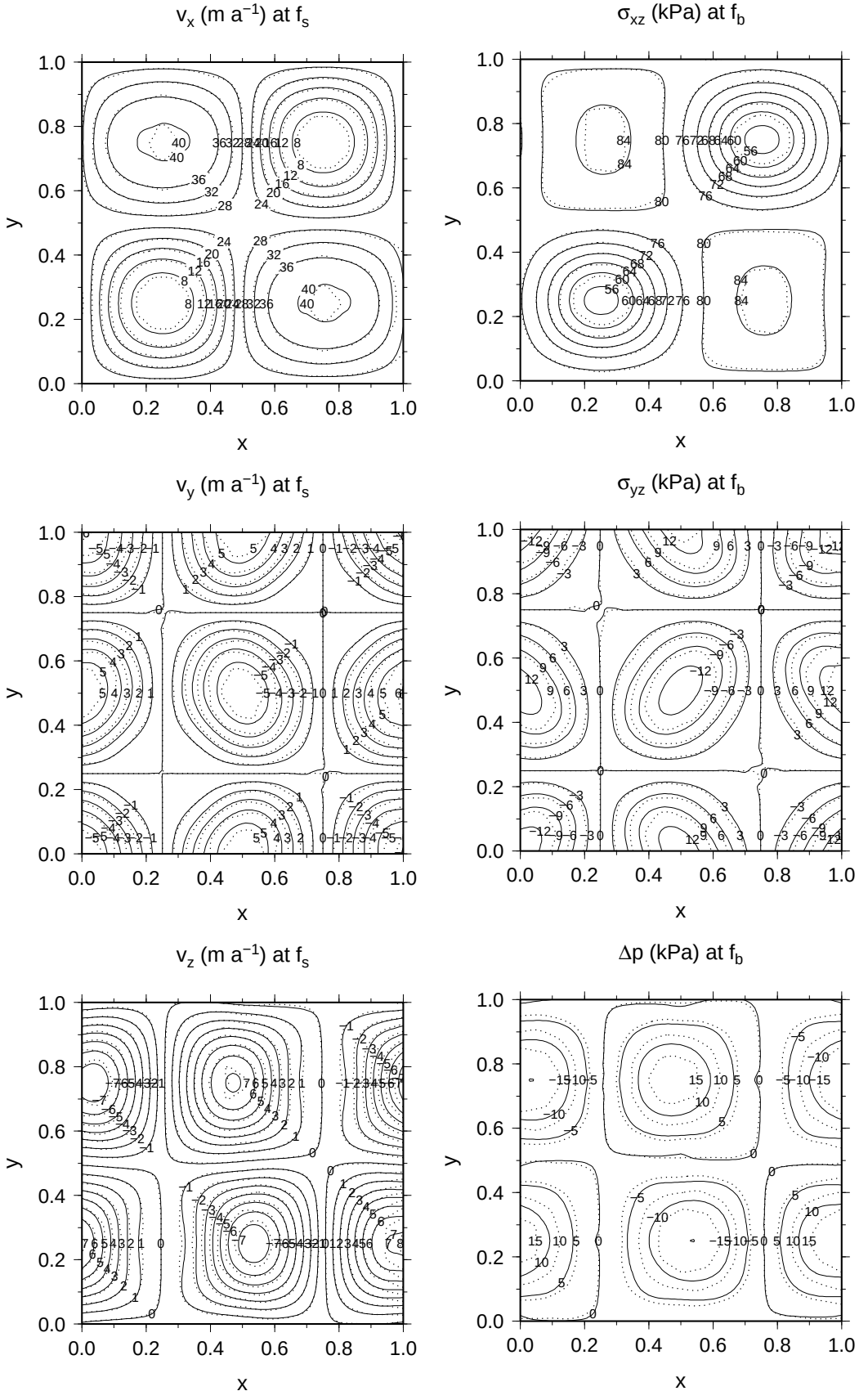

Figure 3.1: Comparison of the surface velocity fields (in $m\,a^{-1}$), the stress components $\boldsymbol{\sigma}_{xz}$, $\boldsymbol{\sigma}_{yz}$ and the pressure difference $\Delta p = p - \mathcal{H}\rho g$ at the bottom (in kPa), obtained by the SIA-I solver (full line labelled diagonally) and the full-Stokes solver (dotted line labelled horizontally), respectively, for the aspect ratio $\epsilon = \frac{1}{20}$.

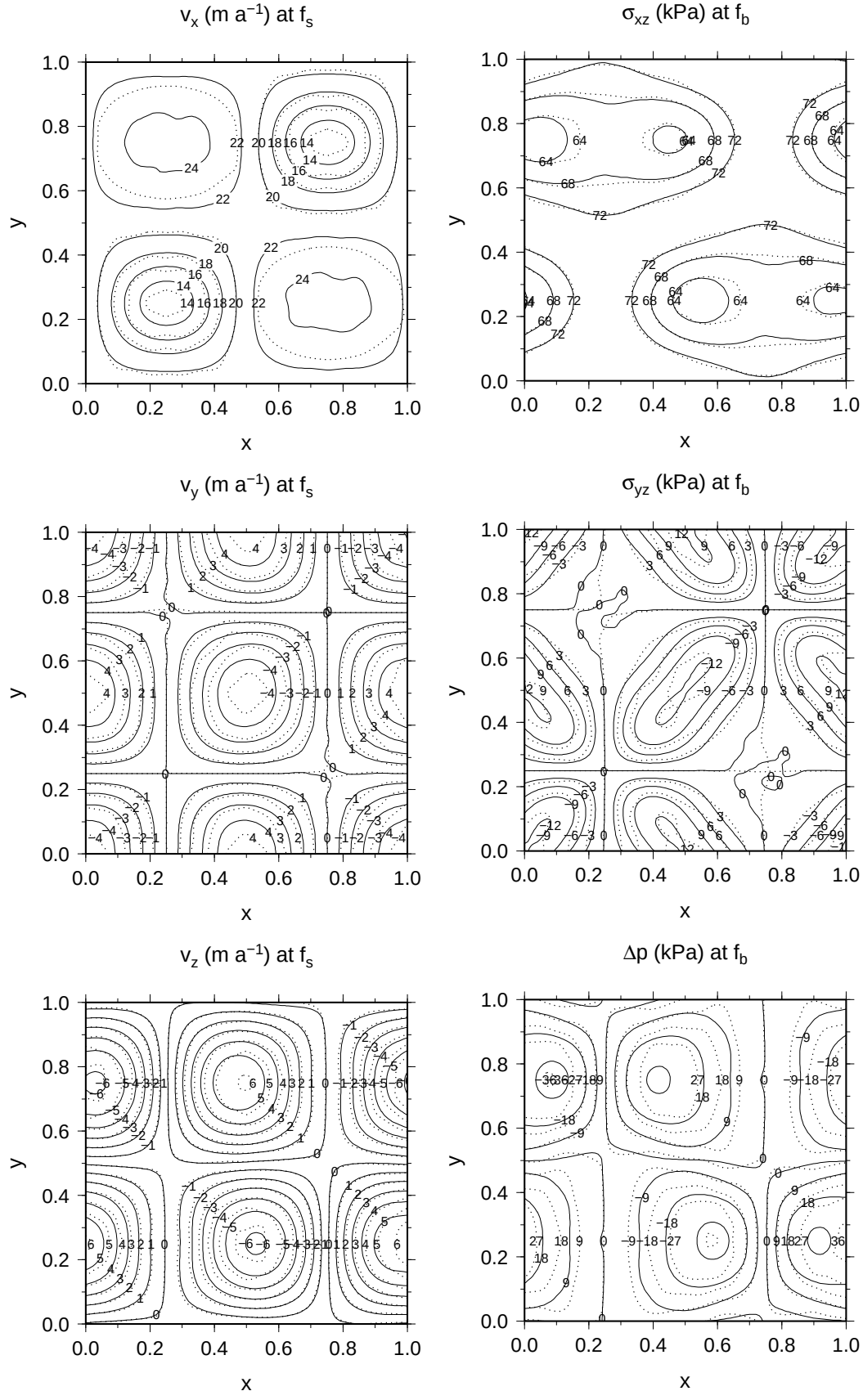

Figure 3.2: As for Fig. 3.1 but for $\epsilon = \frac{1}{10}$.

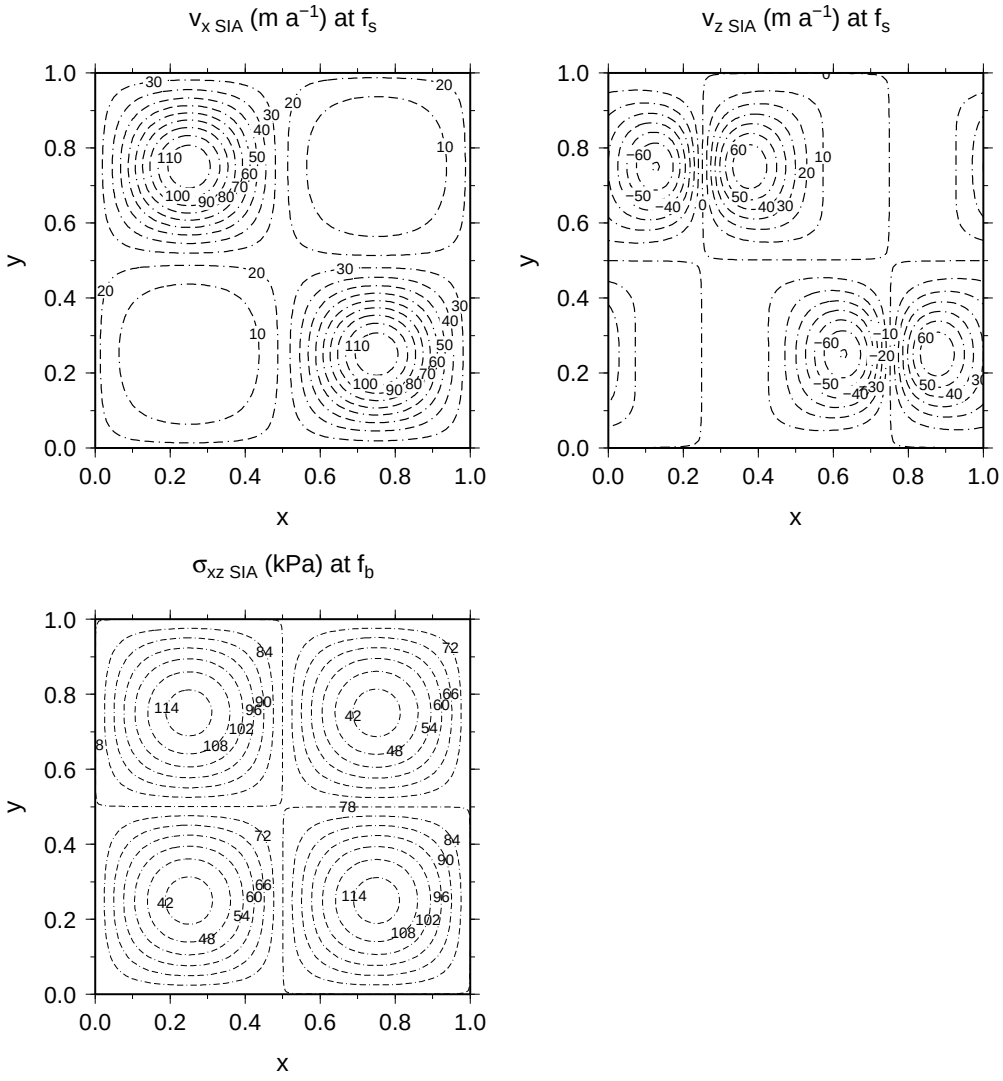

Figure 3.3: The SIA solution for aspect ratio $\epsilon = \frac{1}{10}$. Note that the field quantities not shown here, that is v_y at f_s and Δp, $\boldsymbol{\sigma}_{yz}$ at f_b, are identically equal to zero in this case.

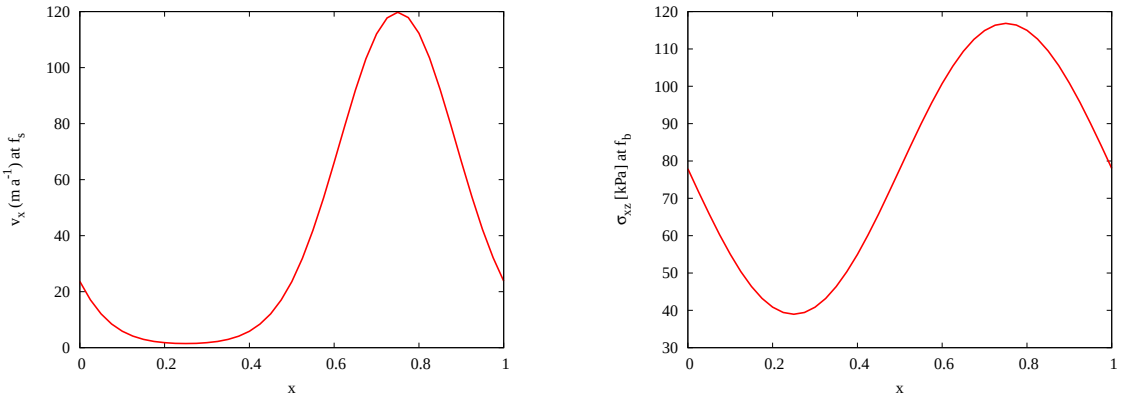

Figure 3.4: The SIA solution for surface velocity v_x at f_s and the bottom stress component $\boldsymbol{\sigma}_{xz}$ at f_b, at the cross-section with the plane $y = 0.25$. These two quantities are independent of the aspect ratio ϵ.

We plot values of six control quantities: surface velocity vector (v_x, v_y, v_z), the stress components $\boldsymbol{\sigma}_{xz}$, $\boldsymbol{\sigma}_{yz}$ and the pressure difference $\Delta p = p - \mathcal{H}\rho g$ at the glacier base. The data are displayed at the cross section with a plane $y = 0.25$. Results are shown for aspect ratios $\epsilon = \frac{1}{10}, \frac{1}{40}, \frac{1}{160}$. We may observe that our solution (light blue dots) for all the displayed cases lies in the region of highest "solution density" representing, hopefully, the exact solution as the considered problem does not possess any known analytical solution. The full-Stokes solutions are plotted with lines, and the other higher-order models with dots. The discrepancy between the various full-Stokes solutions for the pressure difference Δp (bottom-right panel) is possibly only due to an erroneous sign convention of some of the solutions, as indicated by the symmetry of the pattern with respect to the x-axis. In Fig. 3.4 we plot, for comparison, the surface velocity v_x and the bottom-stress component $\boldsymbol{\sigma}_{xz}$, as they would be obtained by the Shallow-Ice Approximation. These two quantities are independent of the aspect ratio for the considered problem and may thus serve as a good measure of the difference between the higher-order and full-Stokes solutions. Note that for high aspect ratios, such as $\epsilon = \frac{1}{10}$, the difference in surface velocity is rather substantial.

3.5.6 Convergence of the SIA-I algorithm

In this section, we demonstrate how the convergence of the solutions is affected by varying the aspect ratio ϵ, and the magnitudes of the relaxation parameters θ_1, θ_2. We perform all runs with the ISMIP-HOM experiment A settings.

The convergence rate is inspected by checking the evolution of the errors of the linear momentum balances, rheology equations and equation of continuity, respectively. These errors are defined as follows. All equations are evaluated at the nodes using the discretisation of spatial derivatives by two-point symmetric finite differences. If we had an analytical solution, that is a solution satisfying the equations exactly in the limit of an infinitesimally small discretisation, such a procedure would provide the so-called discretisation error. In the case of the SIA-I solution, there is an additional error, resulting from the fact that only an approximate problem to the full-Stokes problem is solved at each SIA-I iteration. We divide the error by the magnitude of the largest term in each particular equation and obtain the relative error at each node. For conciseness, we first average these errors over the nodes and than compute one average value from the three linear-momentum balance errors, one from the five rheology equations errors, and finally one continuity equation error.

In Fig. 3.8 we plot the total (discretisation plus approximation) errors of the SIA-I solution for various combinations of the relaxation parameters $\theta_1 = 0.2, 0.5, 0.8$, $\theta_2 = 0.2, 0.1, 0.05$, and a fixed aspect ratio $\epsilon = \frac{1}{80}$ and a spatial resolution $31 \times 31 \times 31$. For all cases, the overall error decreases and eventually reaches a limit (except for the uppermost curves in the second and third panel where more iterations would be needed to reach the limit). As documented for $\theta_1 = 0.8$ and $\theta_2 = 0.2$ (black triangles), when the relaxation parameters are chosen to be too large, the solution is scattered by a persistent high-frequency noise preventing the error from dropping below a certain value.

Observe that e.g. for $\theta_1 = 0.5$ and $\theta_2 = 0.2$, the error decreases relatively quickly and a sufficiently accurate solution is obtained after 20 iterations. We also see that below a certain critical value of the relaxation parameters, the convergence speeds up as the relaxation parameters grow, while above the critical threshold the too-large relaxation parameters induce high-frequency scattering of the output. This may be connected to the spatial resolution since the sequence of successive iterative solutions may formally be viewed as a time-discretised evolution, and as the spatial dependency of field variables is also discretised by finite differences, one may expect a criterion, analogous to the Courant criterion (Press et al., 1992), to be fulfilled to ensure stability of the algorithm. For a given spatial resolution, this criterion would constrain the maximum values of the relaxation parameters θ_1 and θ_2 that control the evolution in 'time'.

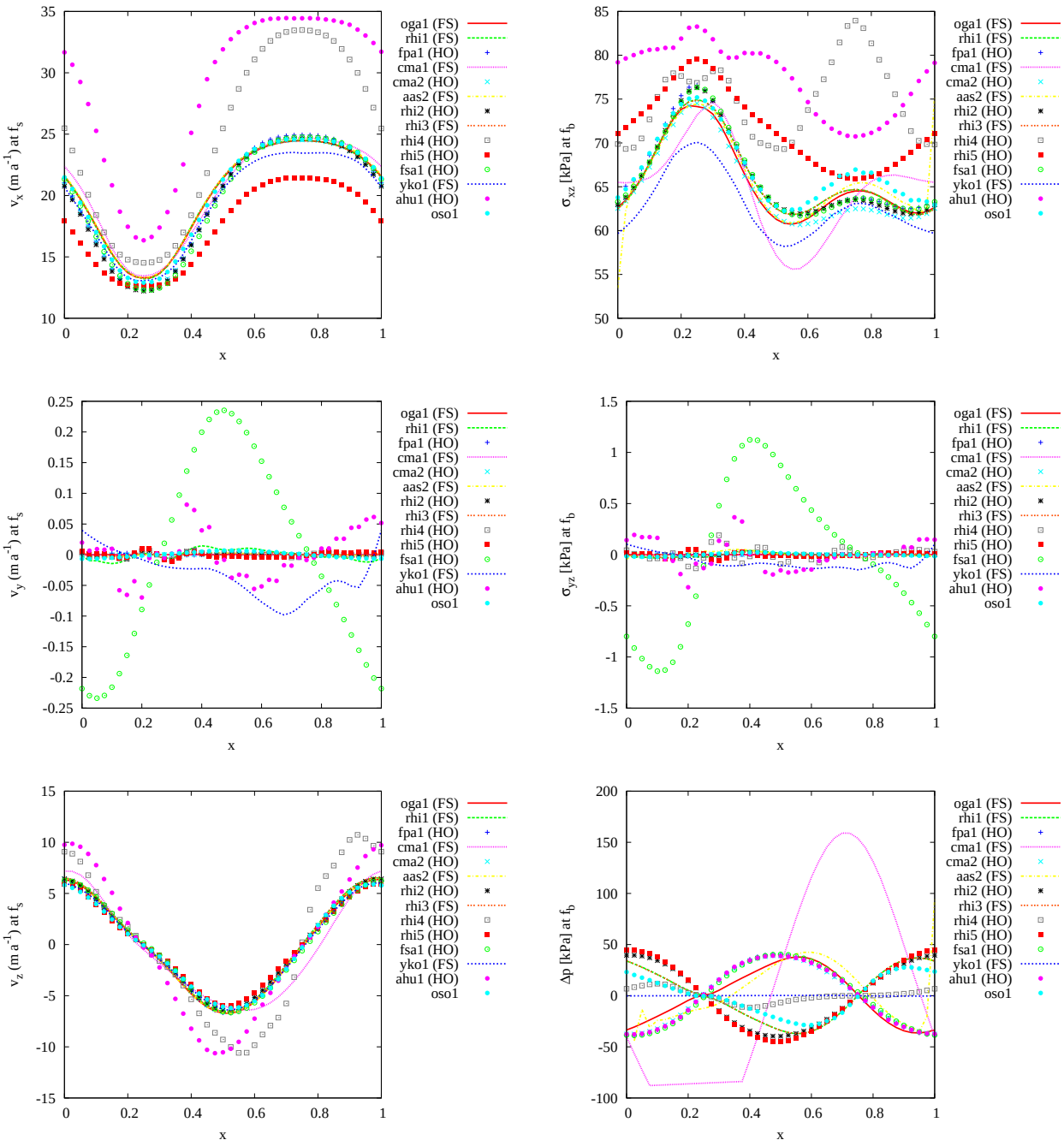

Figure 3.5: Comparison of the surface velocity fields v_x, v_y and v_z (in $\mathrm{m\,a^{-1}}$), and stress components $\boldsymbol{\sigma}_{xz}$, $\boldsymbol{\sigma}_{yz}$ and pressure difference $\Delta p = p - \mathcal{H}\rho g$ at the base f_b (in k Pa), obtained by the SIA-I solver (light blue dots - model *oso1*) and several full-Stokes solvers (lines) and higher-order models (dots) from the ISMIP-HOM A experiment, for the aspect ratio $\epsilon = \frac{1}{10}$. The displayed results are taken at an intersection of the scaled domain with the plane $y = 0.25$.

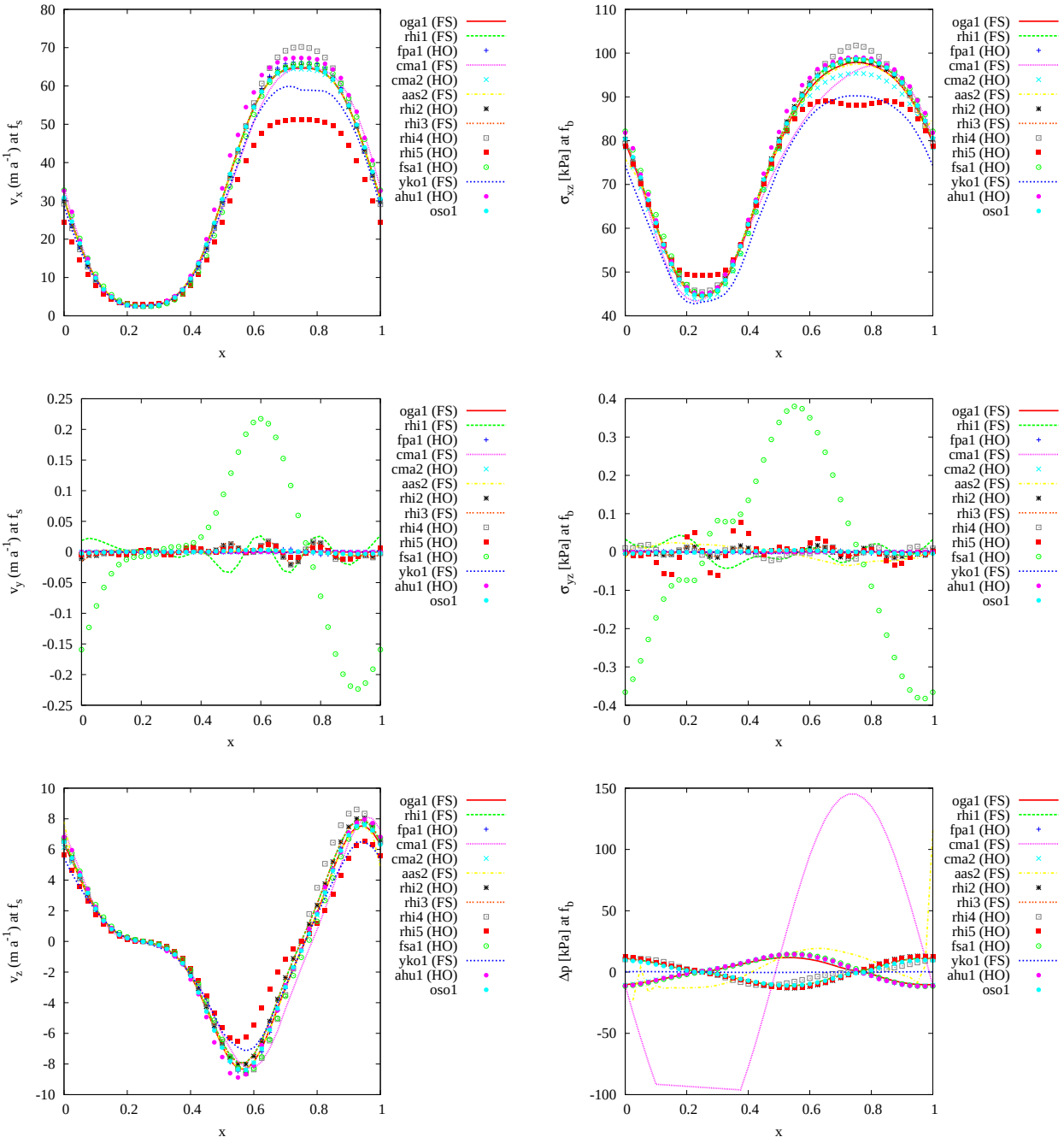

Figure 3.6: As for Fig. 3.5 but with $\epsilon = \frac{1}{40}$.

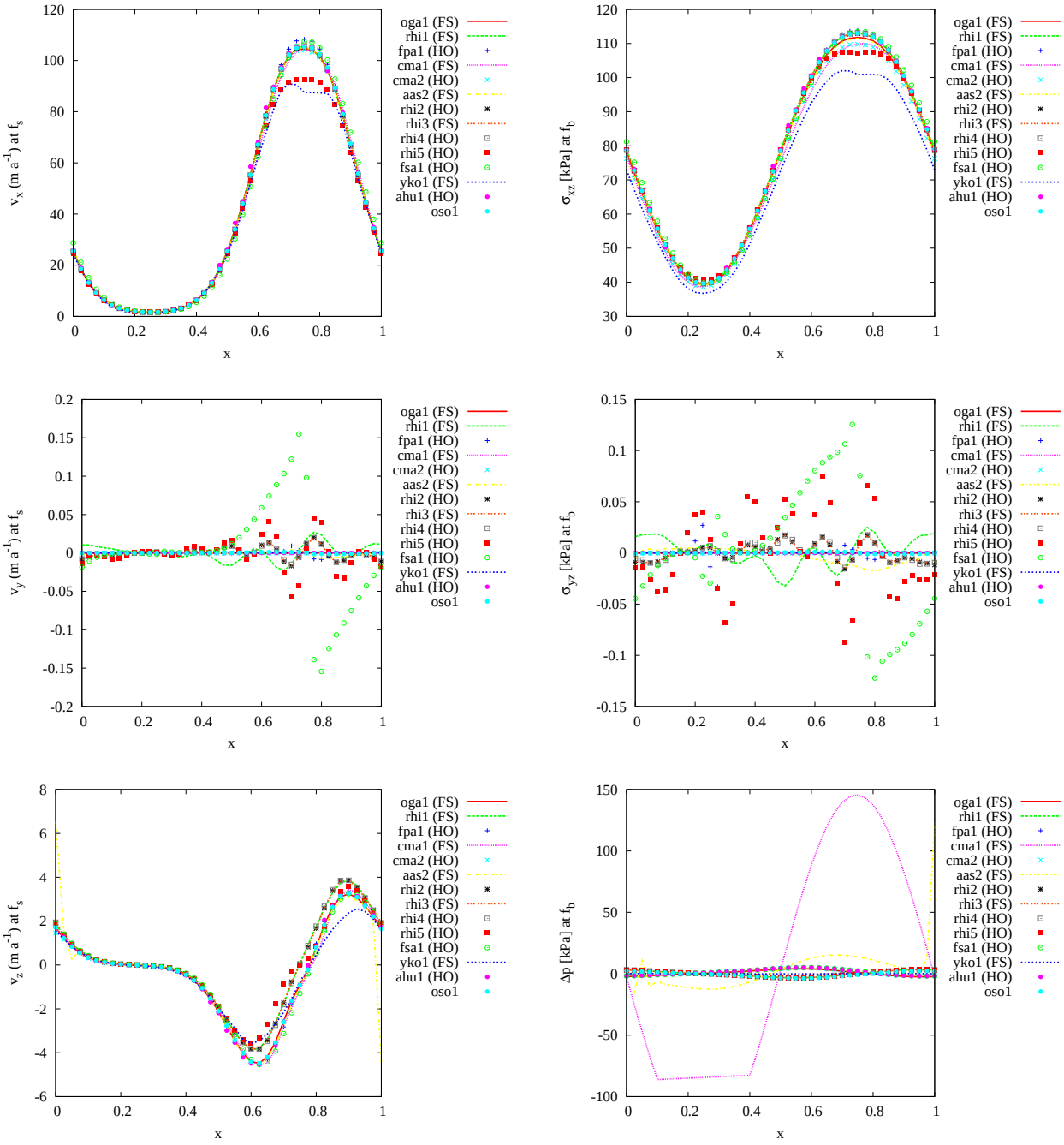

Figure 3.7: As for Fig. 3.5 but with $\epsilon = \frac{1}{160}$.

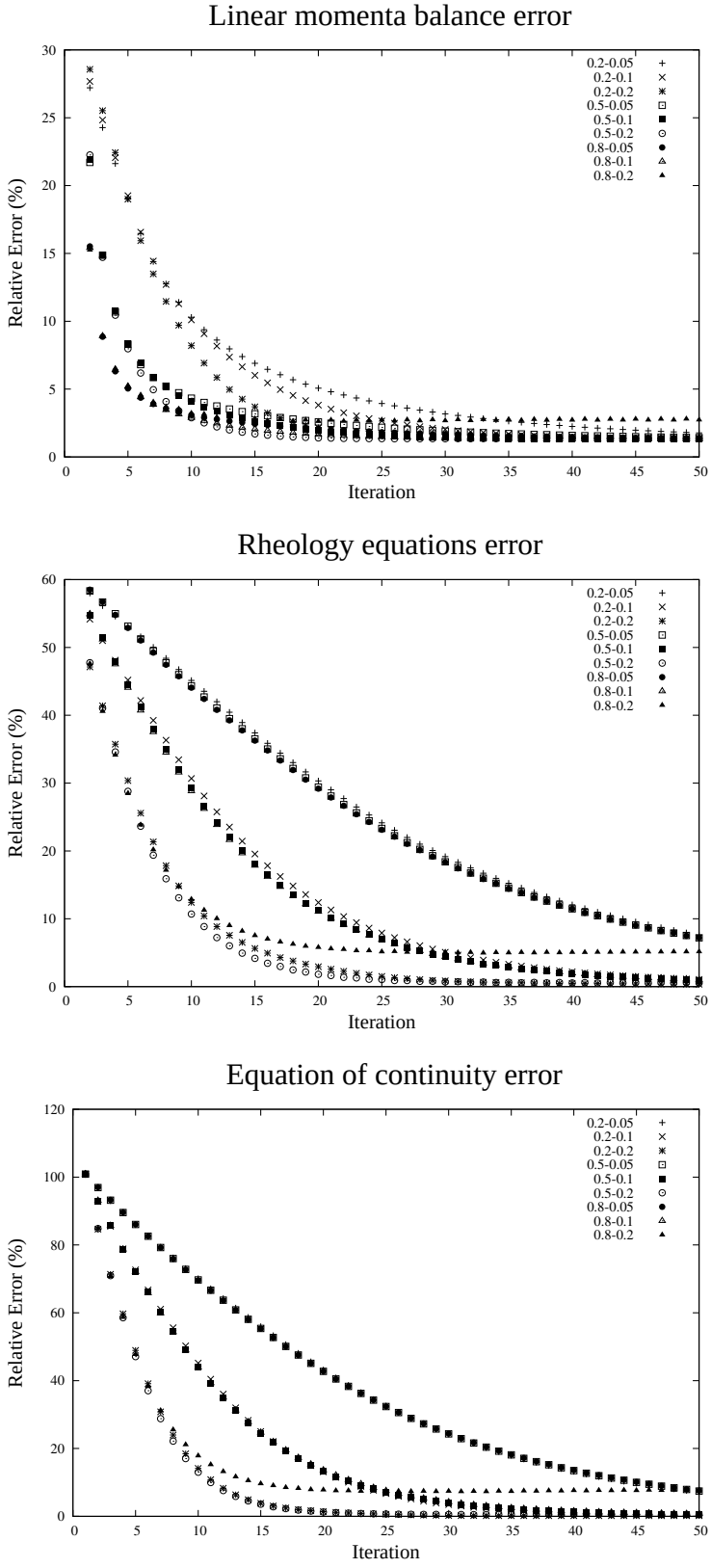

Figure 3.8: The evolution of the averaged relative error of the linear momentum balances, rheology equations and equation of continuity, for various combinations of the relaxation parameters θ_1 and θ_2. The labels read as, for example "0.2-0.05": $\theta_1 = 0.2$, $\theta_2 = 0.05$. The results apply to the case of a spatial resolution $31 \times 31 \times 31$ and aspect ratio $\frac{1}{80}$.

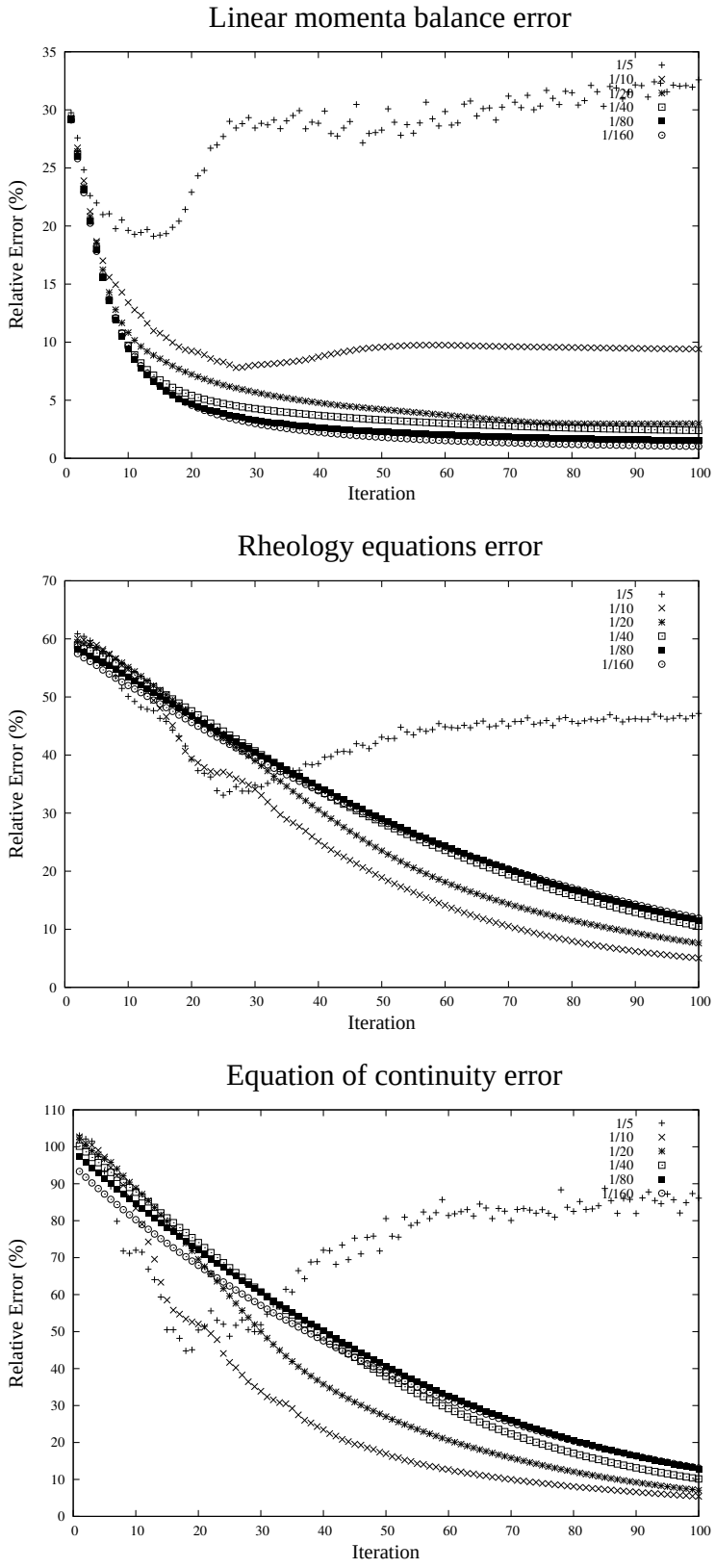

Figure 3.9: The evolution of the averaged relative error of the linear momentum balances, rheology equations and equation of continuity, for various aspect ratios $\epsilon = \frac{1}{5}, \frac{1}{10}, \frac{1}{20}, \frac{1}{40}, \frac{1}{80}, \frac{1}{160}$ and for a fixed spatial resolution $31 \times 31 \times 31$. The results apply to $\theta_1 = 0.2$ and $\theta_2 = 0.02$.

Next, in Fig. 3.9, we inspect the role of the aspect ratio ϵ. Since the derivation of the SIA-I approach requires ϵ be sufficiently small, there is a threshold value of ϵ above which the SIA-I algorithm will not converge. Figure 3.9 plots the errors for aspect ratios $\epsilon = \frac{1}{5}, \frac{1}{10}, \frac{1}{20}, \frac{1}{40}, \frac{1}{80}, \frac{1}{160}$ for a fixed spatial resolution $31 \times 31 \times 31$. The relaxation parameters are $\theta_1 = 0.2$ and $\theta_2 = 0.02$ for all computations. Figure 3.9 demonstrates well the key role of the aspect ratio ϵ for convergence of the SIA-I algorithm. For the chosen relaxation parameters θ_1,θ_2, the value $\epsilon = \frac{1}{10}$ is the threshold and for larger aspect ratios the algorithm fails to converge.

In summary, whether the SIA-I algorithm converges and how fast is a matter of several coupled factors. For a sufficiently small aspect ratio ϵ, (less than $\frac{1}{10}$ for the ISMIP-HOM A experiment), the algorithm converges by choosing relaxation parameters θ_1, θ_2 that are below certain threshold values, dependent on both the aspect ratio and the spatial resolution, and the convergence of the algorithm improves by approaching these critical values from below. Moreover, the critical values decrease with increasing aspect ratio ϵ, as a result, for $\epsilon > \frac{1}{10}$, it is impossible to reach convergence within the ISMIP-HOM A experimental setting.

3.5.7 Performance of the SIA-I for other than no-slip boundary condition, ISMIP-HOM experiment C

The SIA-I algorithm as described above may easily be modified to allow a Dirichlet boundary condition for velocity at the glacier bed, that is the condition $\vec{v}(\cdot, f_b(\cdot)) = \vec{v}^0(\cdot)$. We only modify (3.55)-(3.57) as follows:

$$\tilde{v}_x^{k+\frac{1}{2}}(\cdot,\tilde{z}) = \tilde{v}_x^0(\cdot) + 2\epsilon^{-1}\mathcal{X}\int_{\tilde{f}_b(\cdot)}^{\tilde{z}} \tilde{\mathcal{A}}\tilde{\mathcal{S}}^{k+\frac{1}{2}}(\cdot,\tilde{z}')\tilde{\boldsymbol{\sigma}}_{xz}^{k+\frac{1}{2}}(\cdot,\tilde{z}')d\tilde{z}' \,, \tag{3.139}$$

$$\tilde{v}_y^{k+\frac{1}{2}}(\cdot,\tilde{z}) = \tilde{v}_y^0(\cdot) + 2\epsilon^{-1}\mathcal{X}\int_{\tilde{f}_b(\cdot)}^{\tilde{z}} \tilde{\mathcal{A}}\tilde{\mathcal{S}}^{k+\frac{1}{2}}(\cdot,\tilde{z}')\tilde{\boldsymbol{\sigma}}_{yz}^{k+\frac{1}{2}}(\cdot,\tilde{z}')d\tilde{z}' \,, \tag{3.140}$$

$$\tilde{v}_z^{k+\frac{1}{2}}(\cdot,\tilde{z}) = \tilde{v}_z^0(\cdot) - \int_{\tilde{f}_b(\cdot)}^{\tilde{z}} \left(\frac{\partial \tilde{v}_x^{k+\frac{1}{2}}}{\partial \tilde{x}} + \frac{\partial \tilde{v}_y^{k+\frac{1}{2}}}{\partial \tilde{y}} \right)(\cdot,\tilde{z}')d\tilde{z}' \,. \tag{3.141}$$

With this modification, the SIA-I algorithm was tested on real data from the Antarctic region, considering in addition temperature-dependent viscosity (see Section 3.5.9), remembering that so far we have been restricted to the isothermal case in the numerical examples, i.e. we had systematically set $\tilde{\mathcal{A}} = 1$. It may be stated that, for a reasonably smooth non-homogeneous Dirichlet condition on velocity at the glacier bed, the performance of the SIA-I approach is comparable to the no-slip case.

To involve the sliding at the glacier bed, it is, however, necessary to switch from the Dirichlet boundary condition to a Newton-type of boundary condition such as (1.68). Although we did not participate in the ISMIP-HOM C experiment which applies to this case, we may, however, compare our SIA-I solution with the published results from the benchmark.

The problem is set up very similarly to experiment A, the difference being that the driving effect is, instead of bed-geometry undulations, the spatial inhomogeneity in the basal-friction coefficient. The upper

and lower surfaces are both inclined planes given (in m) by

$$\begin{aligned} f_s(x_1, x_2) &= -x_1 \tan\alpha \,, \qquad \alpha = 0.1^\circ, \\ f_b(x_1, x_2) &= f_s(x_1, x_2) - 1000 \,. \end{aligned} \tag{3.142}$$

At the sides, periodic boundary conditions (3.137) and (3.138) are again prescribed for the velocity field. At the glacier bed, the sliding law (1.68) is prescribed, i.e.

$$\beta^2 \vec{t}_b \cdot \vec{v} = -\vec{t}_b \cdot \boldsymbol{\sigma} \cdot \vec{n}_b \,, \tag{3.143}$$

where $\vec{t}_b$ and $\vec{n}_b$ are the tangent and downward normal vectors to the glacier base f_b, respectively. The sliding coefficient is given by

$$\beta^2(x, y) = 1000 + 1000 \sin(\omega x) \sin(\omega y) \,, \tag{3.144}$$

with

$$\omega = \frac{2\pi}{\mathrm{L_{sc}}} \,.$$

The Dirichlet condition on basal velocity, either homogeneous or non-homogeneous, is crucial in the SIA-I algorithm, since it allows a straightforward computation of the velocities by integration along the vertical coordinate, c.f. (3.139)-(3.141). That is why the sliding law (3.143), despite being a Newton-type boundary condition, has to be transformed to a Dirichlet-type condition. This can be done quite naturally thanks to the iterative character of the problem. For $\beta(\cdot) \neq 0$, the stress field from the previous half-step is used to provide

$$\vec{t}_b \cdot \vec{v}^{0\ k+\frac{1}{2}} = -\frac{\vec{t}_b \cdot \boldsymbol{\sigma}^{k+\frac{1}{2}} \cdot \vec{n}_b}{\beta^2} \,. \tag{3.145}$$

The sliding velocity $\vec{v}^{0\ k+\frac{1}{2}}$ is then substituted into (3.139)-(3.141) for $\vec{v}^0$. Obviously, this approach can be applied only to the region with $\beta \neq 0$ and fails in the case of free-slip conditions, where $\beta = 0$. Such a singularity, however, occurs in the experiment C, since $\beta = 0$ at two points, $(\frac{3\mathrm{L_{sc}}}{4}, \frac{\mathrm{L_{sc}}}{4})$ and $(\frac{\mathrm{L_{sc}}}{4}, \frac{3\mathrm{L_{sc}}}{4})$. To avoid the failure of the SIA-I approach, we add a small positive constant to β and successively decrease it during the iterations.

The results are shown in Figs. 3.10 and 3.11. The plotted quantities are velocities v_x, v_y, v_z, at the upper surface (in $\mathrm{m\,a^{-1}}$) and the stress components $\boldsymbol{\sigma}_{xz}$, $\boldsymbol{\sigma}_{yz}$ and pressure difference $\Delta p = p - \mathcal{H}\rho g$ at the bottom (in kPa). As in the previous experiment, all quantities are mapped onto the scaled domain $\langle 0, 1\rangle \times \langle 0, 1\rangle$ and the solutions are plotted at the cross-section with the plane $y = 0.25$. For the comparison, we also plot some of the solutions from the ISMIP-HOM experiment C. Results are shown for two aspect ratios, $\frac{1}{80}$ in Fig. 3.10, and $\frac{1}{20}$ in Fig. 3.11. All solutions are computed with a resolution of $31 \times 31 \times 31$, and are stopped after 200 iterations. The relaxation parameters are $\theta_1 = 0.2$, $\theta_2 = 0.02$ for aspect ratio $\epsilon = \frac{1}{80}$, and $\theta_1 = 0.1$, $\theta_2 = 0.01$ for aspect ratio $\epsilon = \frac{1}{20}$. To compute each example takes approximately 50 seconds of CPU time on a Intel Pentium 4 with 3.2GHz.

Figures 3.10 and 3.11 show that, in accordance with our assumption, the SIA-I algorithm fails to compute the horizontal velocities correctly in the neighborhood of the point where the sliding friction coefficient goes to zero ($\beta = 0$), that is at the point $(0.75, 0.25)$ in our case. Moreover, also intuitively, the error increases with the increasing aspect ratio. However, the error is localized in a small region surrounding the point with $\beta = 0$, and the stresses are well computed everywhere else, even for a relatively large aspect ratio ($\frac{1}{20}$). In general, we may conclude that the Newton boundary condition at the glacier base, i.e. the sliding law of the form (3.143), represents a restriction for the applicability of the SIA-I only in the case where a region with a very small basal friction coefficient β is present. To demonstrate the difference, the Shallow-Ice Approximation solution is plotted in Fig. 3.11 (model SIA). Note that the surface velocity v_x for the SIA solution diverges at the point where $\beta = 0$.

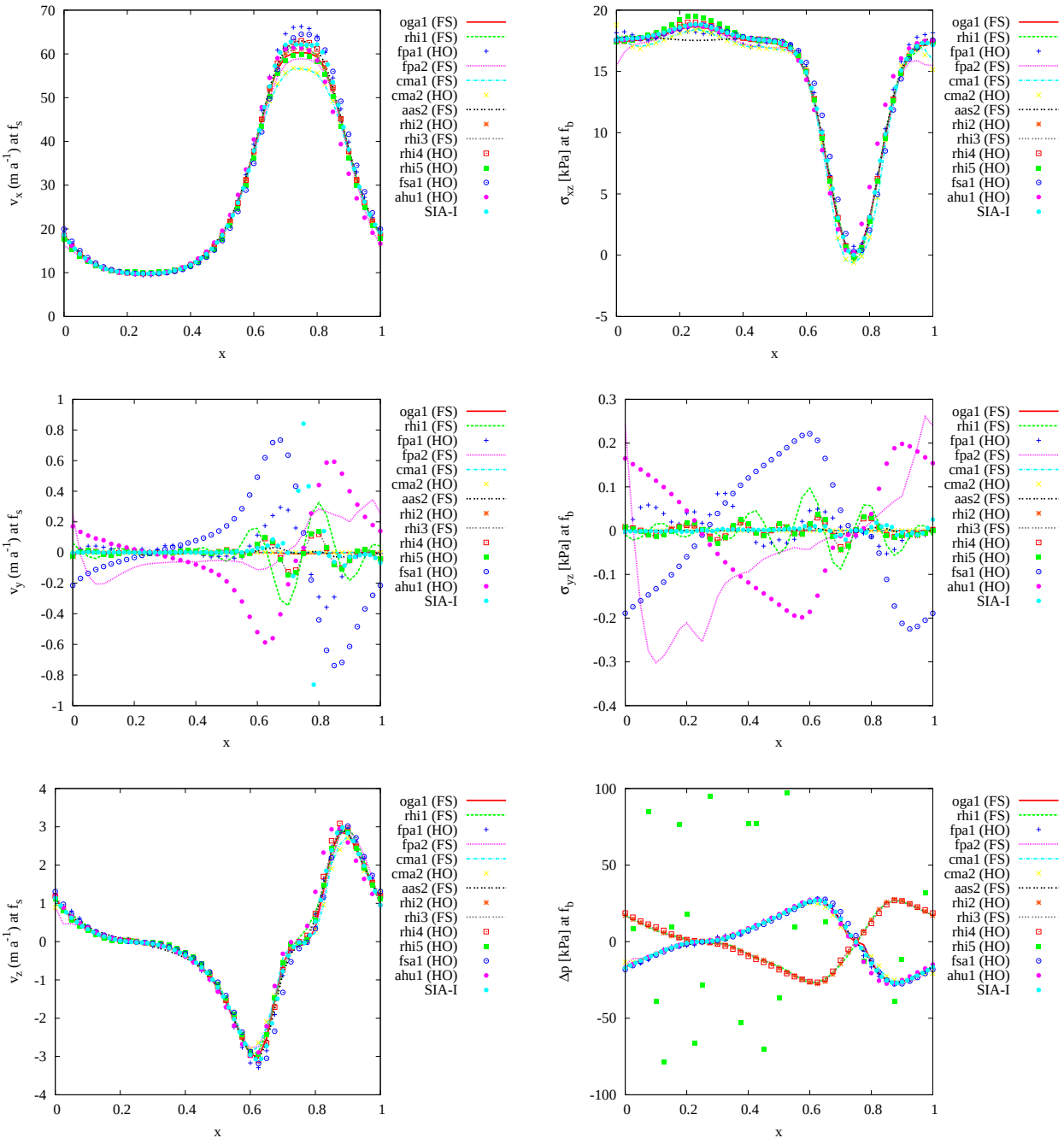

Figure 3.10: Comparison of the surface velocity fields v_x, v_y and v_z (in $\mathrm{m\,a^{-1}}$), and the stress components $\boldsymbol{\sigma}_{xz}$, $\boldsymbol{\sigma}_{yz}$ and the pressure difference $\Delta p = p - \mathcal{H}\rho g$ (in kPa) at the base f_b, obtained by the SIA-I solver (model "SIA-I" light blue points), compared with several full-Stokes (lines) and higher-order (dots) solutions from the ISMIP-HOM C experiment, for the aspect ratio $\epsilon = \frac{1}{80}$. The displayed results are taken at an intersection of the scaled domain with the plane $y = 0.25$.

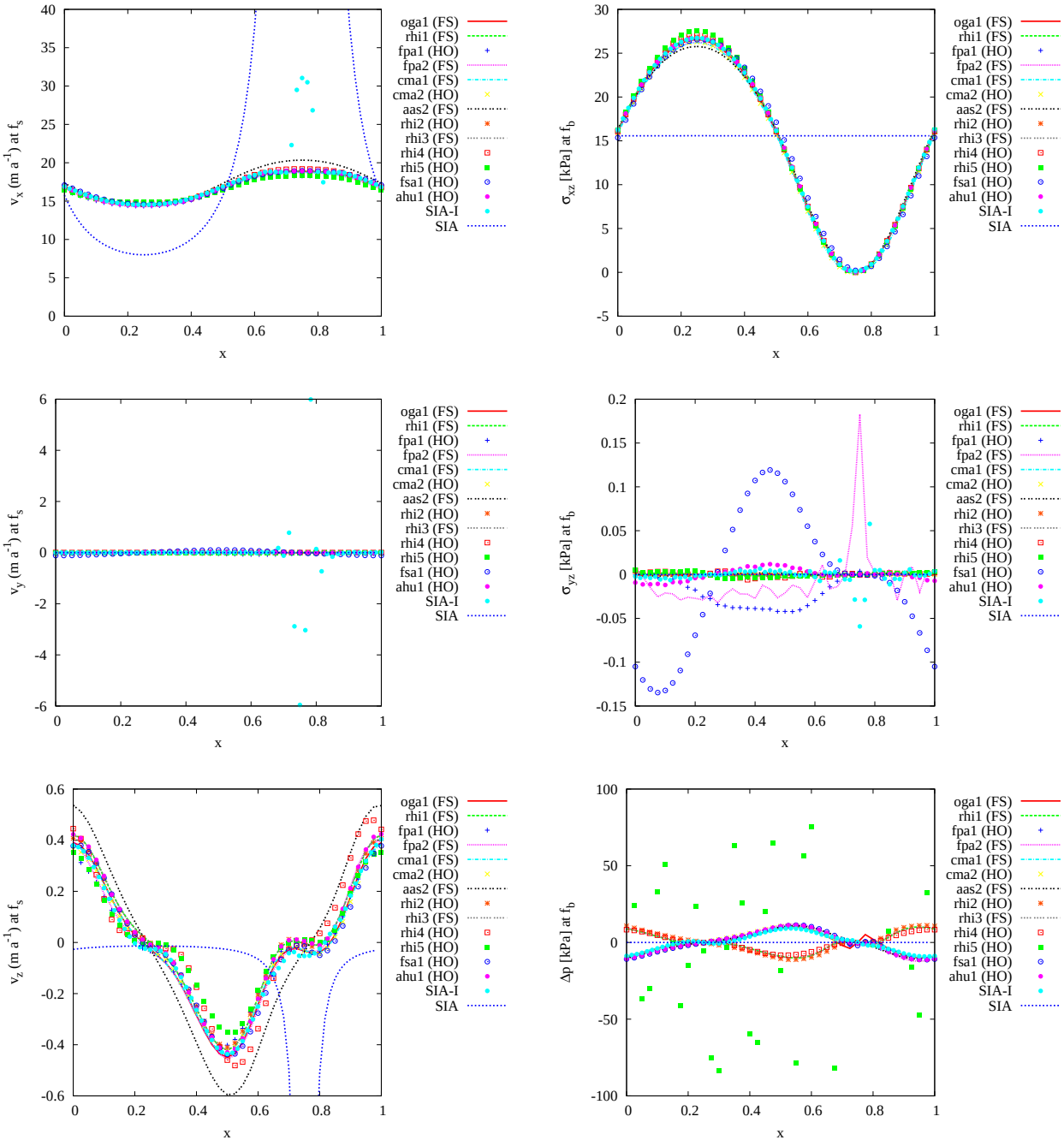

Figure 3.11: As for Fig. 3.10, but for $\epsilon = \frac{1}{20}$.

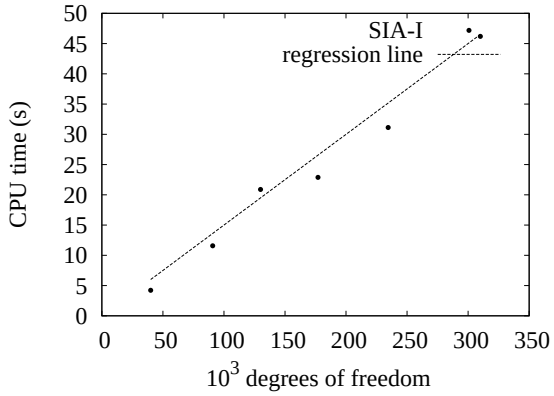

Figure 3.12: CPU-time demands of the SIA-I algorithm as a function of degrees of freedom for the ISMIP-HOM A setting with $\epsilon = \frac{1}{80}$ and for 50 iterations, computed on a Intel Pentium 4, 3.2GHz computer.

3.5.8 Numerical performance

The essential feature of the presented SIA-I approach is its computational effectiveness. The algorithm is designed such that the time cost spent at each iterative step is similar to that required for the SIA approach. Using an Intel Pentium 4, 3.2GHz computer, we have performed 50 iterations for the ISMIP-HOM A setting with $\epsilon = \frac{1}{80}$, which is a sufficient number of iterations so that the SIA-I solution converges to the full-Stokes solution. In Fig. 3.12, we plot the total CPU time for SIA-I as a function of the degrees of freedom, that is the number of the computed velocity and stress variables stored in the computational grid. We can see that the computational time increases linearly with the increasing number of degrees of freedom.

Since our full-Stokes solver is not optimized for numerical performance, we consider the CPU-time demands for the professionally optimized finite-element solver Elmer (Gagliardini and Zwinger, 2008). For the current ISMIP-HOM A setting the authors provide an analytical formula for CPU-time costs in (s) as a function of the number of degrees of freedom: $y = 0.013x^{1.11}$. If we make a similar estimate for the SIA-I solver, we obtain $y = 0.00015x$ (see Fig. 3.12).

3.5.9 Performance of the SIA-I algorithm on real data

Thanks to Dr. Oleg Rybak (AWI) and Prof. Dr. Philippe Huybrechts (Vrije Universiteit Brussel), we could perform a test of the SIA-I algorithm on more realistic data. We obtained surface velocities resulting from a higher-order model (Pattyn, 2003) of a 600×400 km region in Dronning Maud Land, Antarctica.

The domain resolution was 241×161 grid points in horizontal (corresponding to 2.5 km resolution) and 101 in the vertical direction. The model input for the simulation is the bedrock topography, the free surface elevation (Fig. 3.13), and basal velocities (Fig. 3.14). They appear strongly non-homogeneous due to the presence of temperate-ice regions where a rapid sliding occurs opposed to cold-ice frozen-bed conditions in the rest of domain.

We were also provided with the 3-D temperature field for the whole computational domain. Hence, we can also incorporate the temperature dependence of ice viscosity. In particular, the rheology (1.17) was used with

$$\mathcal{A}(T) = mA \exp\left(-\frac{Q}{RT^*}\right) \tag{3.146}$$

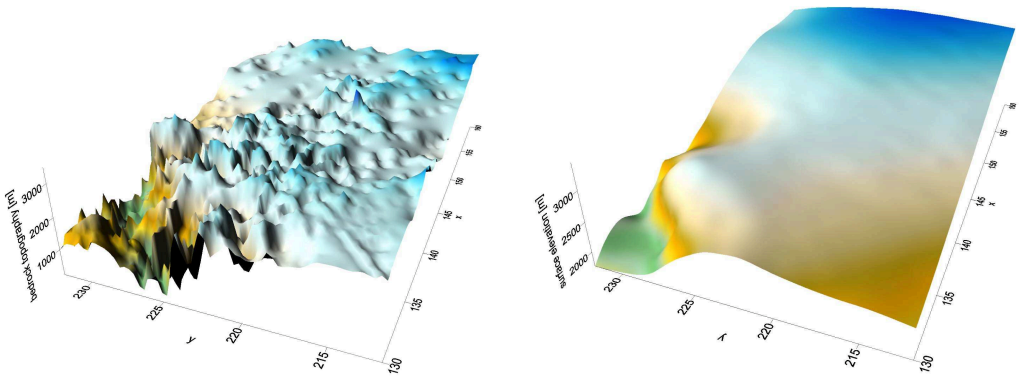

Figure 3.13: Bedrock topography (left) and surface elevation (right) in the Dronning Maud Land simulation.

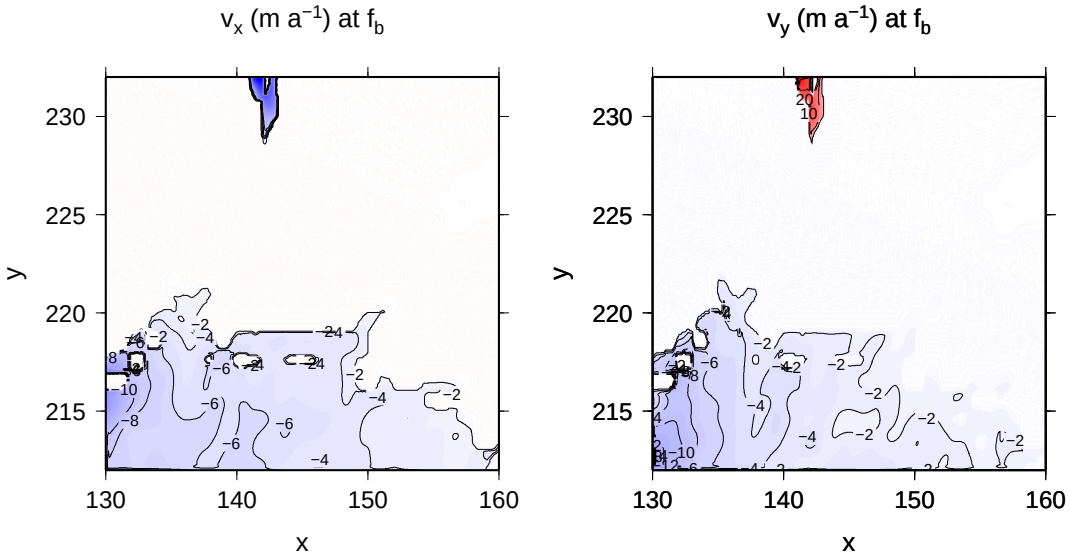

Figure 3.14: Input basal velocities, v_x (left) and v_y (right) used in the Dronning Maud Land simulation.

$$T^* < 263.15\,\mathrm{K} \quad : \qquad A = 1.14 \times 10^{-5}\,\mathrm{Pa}^{-3}\,a^{-1}\,, Q = 60\,\mathrm{kJ\,mol}^{-1}\,, \tag{3.147}$$

$$T^* \geq 263.15\,\mathrm{K} \quad : \qquad A = 5.47 \times 10^{10}\,\mathrm{Pa}^{-3}\,a^{-1}\,, Q = 139\,\mathrm{kJ\,mol}^{-1}\,, \tag{3.148}$$

where R is the universal gas constant ($R = 8.314\,\mathrm{J\,mol}^{-1}\,\mathrm{K}^{-1}$), Q is the activation energy of creep and T^* is the absolute temperature corrected for the pressure melting-point $T^\star = T + C_{Cl}\,p$ and m is the enhancement factor (in the comparison set as $m = 1.061$). The values of the prescribed physical parameters are taken from Huybrechts (1992), and are the same for both compared models.

The temperature and temperature rate factor $\tilde{\mathcal{A}}$ are plotted in Fig. 3.15. We may observe a relatively strong temperature variability of viscosity both in the lateral and vertical directions. In total, the temperature contribution to the viscosity variation reaches 3 orders of magnitude.

We solve a Stokes-flow problem looking for a steady-state solution with non-homogeneous boundary conditions on velocity at the base, and free-surface conditions at the upper surface. At the sides of the domain, we replace symmetric differences by one-sided differences, which enables us to avoid specifying the boundary conditions there.

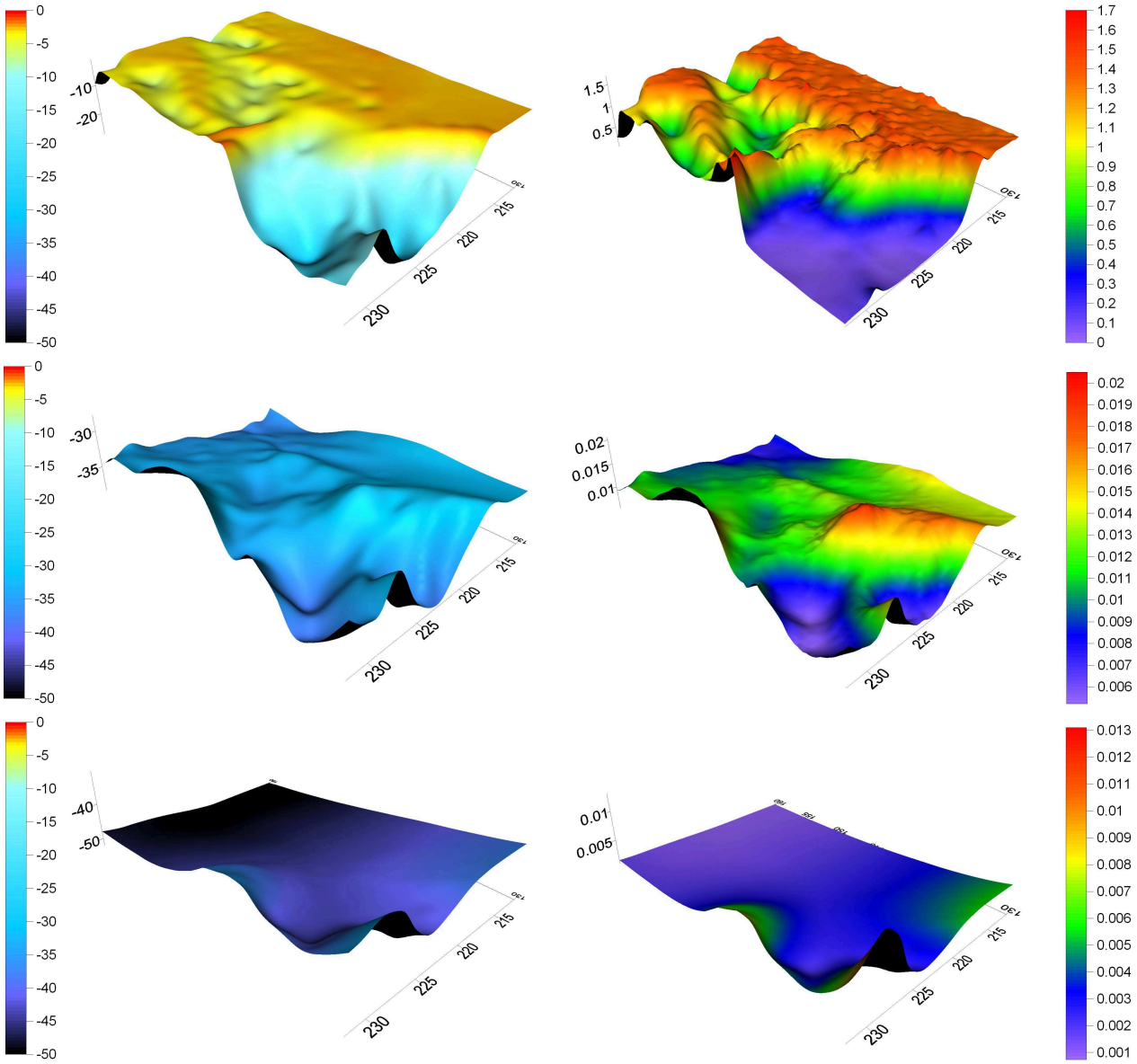

Figure 3.15: Temperature (in $^\circ$ C) (left column) and the rate factor $\tilde{\mathcal{A}}(\tilde{T})$ (right column) at the base (upper row), a middle-depth layer (middle row), and at the surface (bottom row), for the Dronning Maud Land simulation.

As an output to be compared, we choose the surface deformational velocities, i.e. the difference between the velocity at the surface and the basal velocity at the underlying basal point. This choice is motivated by the fact that such a quantity is not affected by the rapid changes in basal conditions and better reflects the deformational contribution to glacier flow. In Fig. 3.16, we plot the SIA-I solution, which is compared with the higher-order model, the so-called incomplete 2nd-order model in Pattyn (2003), which was used as the fine-scale part of a two-component nested model described in Huybrechts (2007). We denote this Higher-Order Model by the label "HOM". Finally, we also show the deformational velocities corresponding to the Shallow Ice Approximation (SIA) to provide better insight into the contribution of the higher-order dynamics.

In Fig. 3.16, we may observe a relatively good agreement between the higher-order model (HOM) and our solution (SIA-I), and a distinct difference between these solutions and the much less smooth result coming from the Shallow-Ice Approximation (SIA) solution. A detailed quantitative analysis of the differences is not performed since it may be misleading to some extent as none of the models provides a truly full-Stokes solution. Thus, the differences in the solutions may be merely artifacts of the different approaches in handling the longitudinal stresses. We have already deduced from the ISMIP-HOM benchmarks A and C that some of the higher-order (non-full Stokes) models may differ quite substantially among themselves and from the full-Stokes solution.

Despite all the differences, this example serves as a demonstration that the SIA-I algorithm may be successfully applied to real-nature conditions and provide reasonably accurate output. Concerning the numerical performance, the displayed SIA-I output was obtained after 60 iterations with approximately 3.8 s of CPU time per iteration (performed on an Intel Pentium Core 2 Quad 2.4 x 4, 8GB RAM, 800 MHz, in non-parallel version), while the HOM model took approximately 5000 CPU seconds (on a NEC SX8 in parallel mode using OMP and 8 CPUs, Rybak, pers. comm.).

3.6 Summary

The new iterative SIA-I algorithm is derived on the basis of the traditional scaling "shallow-ice" property by assuming that the aspect ratio of the vertical/horizontal dimensions of a glacier is sufficiently small. The algorithm represents an iterative extension of the SIA approach, and, in general, may provide an improved solution of the Stokes-flow problem. The key parameters controlling the performance of the algorithm are the aspect ratio ϵ and relaxation parameters θ_1, θ_2. For the model example taken from the ISMIP-HOM A experiment with $\epsilon \leq \frac{1}{10}$, the SIA-I algorithm converges if sufficiently small relaxation parameters are chosen, for example, $\theta_1 = 0.2$, $\theta_2 = 0.05$. The case with $\epsilon = \frac{1}{10}$ is a threshold above which the SIA-I algorithm fails to converge and thus gives inaccurate and noisy results.

Relative theoretical simplicity leads to faster computational speeds, since the numerical computations consist of only numerical integration over the vertical coordinate and the differentiation of field quantities, which are similar numerical operations as performed in the SIA approach. Moreover, the computational demand grows only linearly with the number of degrees of freedom.

The performance of the SIA-I algorithm was also tested for the ISMIP-HOM experiment C, where a Newton-type sliding law is applied at the glacier base. The SIA-I approach requires the reformulation of the sliding law as a Dirichlet boundary condition for velocity. This disables us to resolve the velocities correctly in the regions with a small sliding friction coefficient β and fails completely for free-slip conditions (β = 0). However, the errors in the velocities are localized in the vicinity of the singular region where $\beta = 0$. The erroneous behavior of the SIA-I algorithm disappears with decreasing aspect ratio. For instance, in the case where $\epsilon = \frac{1}{80}$, the SIA-I converges everywhere in the solution domain and shows good agreement with the

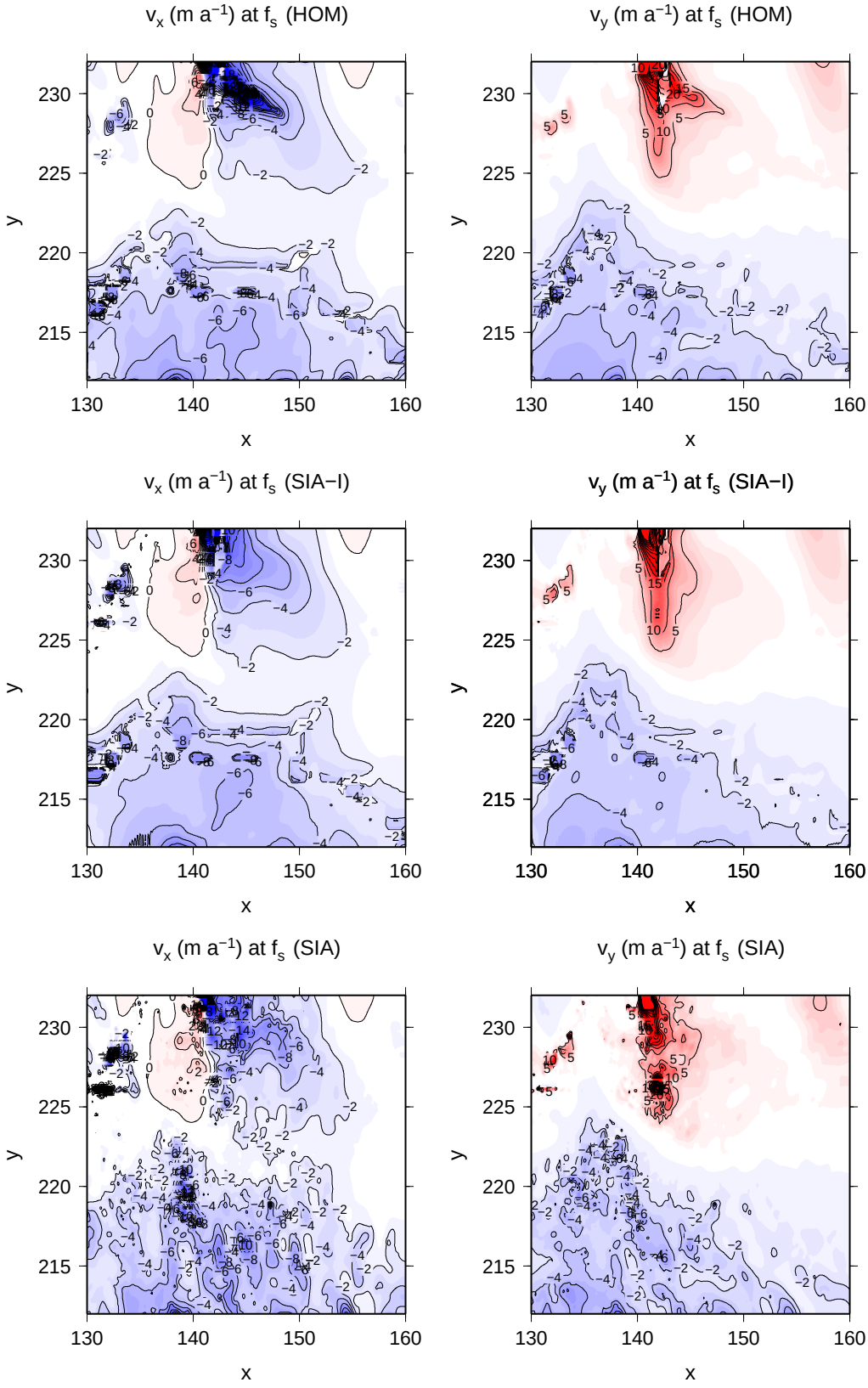

Figure 3.16: Comparison of the horizontal deformational surface velocities - v_x (left column), v_y (right column) for the higher-order model HOM (first row), our SIA-I output (middle row) and the Shallow-Ice Approximation (bottom row), for the Dronning Maud Land simulation.

numerical full-Stokes solution.

We also performed a test of the SIA-I approach on more realistic data from Dronning Maud Land, Antarctica, which is a Stokes-flow problem characterized by strongly inhomogeneous Dirichlet boundary conditions for velocity and the temperature dependence of ice viscosity. The comparison with output from a higher-order model again shows a satisfactory performance of the SIA-I algorithm, both in accuracy and computational effectiveness.

Chapter 4

Evolutionary numerical ice-sheet model based on the SIA-I algorithm

4.1 Introduction

So far we have been dealing with the steady-state Stokes problem for ice flow. Its solution was found by a novel computational algorithm (SIA-I) and we ran several tests inspecting its performance in comparison to various higher-order or full-Stokes methods.

For more realistic modeling, the steady-state scenario will now be abandoned and a transient case allowing temporal changes in the glacier geometry that captures the evolution of the glacier will be considered in this section. The processes changing the glacier geometry are both the surface accumulation and ablation and the deformational flow. As we have already seen in the scaling analysis, the Froude number in the ice equation of motion (the balance of linear momentum) has a negligible value. This allows us to represent the time evolution of ice-flow as a sequence of steady-state Stokes problems. The evolution is driven by updating the surface ice geometry, temperature and possibly also the water-content distribution. This means solving the corresponding kinematic equations for the boundary surfaces together with the heat and mass transport equations.

We will start with an isothermal case, i.e. when the thermal equation is not considered. We assume purely cold-ice conditions, however, with possible basal sliding. Under the assumption that the glacier base does not evolve, this setting requires us to solve the kinematic condition for the free surface evolution and, in general, also to track the glacier margin. At a later stage, we will include the heat-transport equation and inspect the role of the thermo-mechanical coupling.

We start with a brief summary of the most essential components of our numerical code developed for ice sheet evolution modeling. However, particular parts will be discussed in more detail in the following sections.

The fundamental part of the model is the SIA-I algorithm, which, for a given ice sheet geometry, computes the induced stress field together with the deformational and basal sliding velocities. The solution of this problem is strongly coupled with the temperature conditions inside the glacier due to the relatively strong temperature-dependence of ice viscosity. The computed velocity field, together with the independent surface climatological inputs, that is the accumulation and ablation rates, allows for updating the free surface geometry at each time by solving the kinematic equation for the surface function. In turn, the updated geometry serves then as input data for a new steady-state Stokes problem, which is solved by the SIA-I

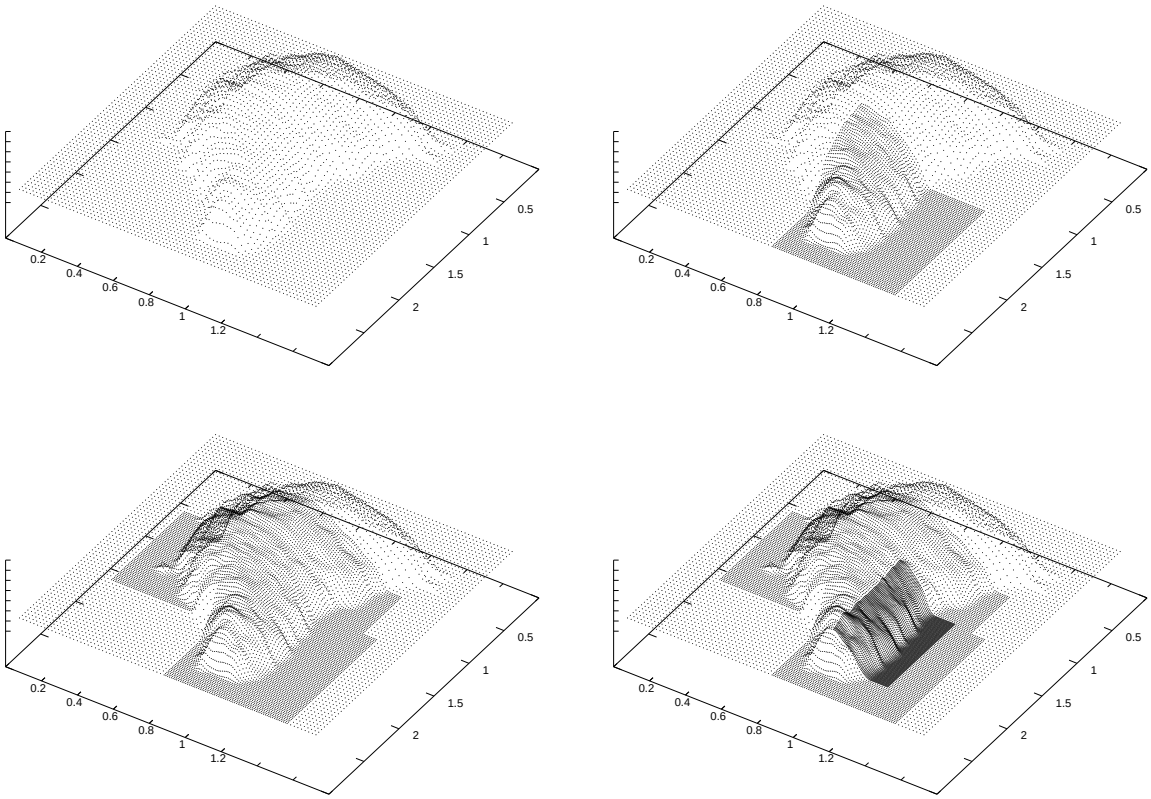

Figure 4.1: Example of a computational grid with successive increased grid-point densification by a factor of 2.

algorithm, and, in addition, for the heat-transport equation.

Now, we will discuss the numerical implementation of the whole method. This consists of time and spatial discretisations, the numerical solution of the kinematic equation, tracking the ice sheet margin and solving the heat transport equation.

4.2 Spatial discretisation by finite difference grid

The SIA-I algorithm requires that, for spatially discretised velocity, temperature and stress fields, partial spatial derivatives of these fields and a definite integral along the vertical coordinate are numerically computed. For this reason, we apply the finite-difference discretisation for which partial spatial derivatives are approximated by finite differences of a chosen accuracy and integration is approximated by a weighted summation of the nodal values of integrated field variable.

In order to achieve a better resolution in areas of a particular interest, we implement a non-regular grid which can be locally densified in the following way. In the horizontal directions, we start with a regular grid with a chosen Δx_1 and Δx_2 spacing and with $N_1 \times N_2$ nodes. This grid can then be locally densified by a factor of 2 (see Fig. 4.1) in order to obtain a better resolution in areas of a particular interest. This densification can be performed always only in such a way that the neighboring regions have either the same grid-point densities or their grid-point densities differ by a factor of 2. This rule helps to avoid the problems with data projection and interpolation between the grids of different grid-point densities.

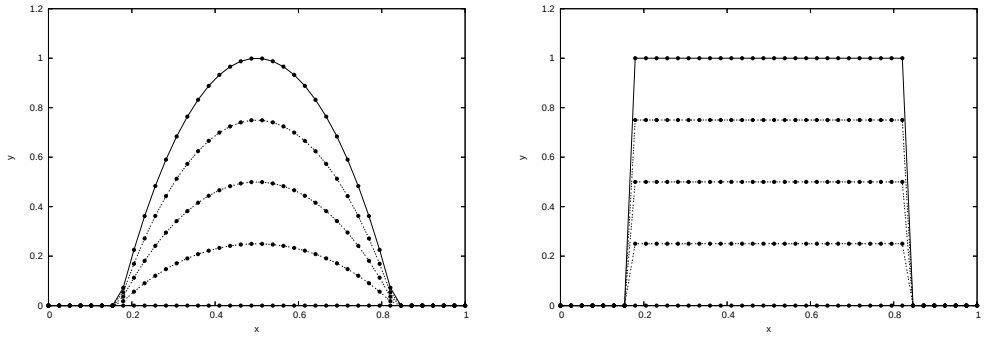

Figure 4.2: Example of the "stretch" transformation of the computation domain - left: the original shape, right - the stretched shape with uniform vertical node spacing.

In the vertical direction, a traditional approach in glaciology uses stretched coordinates (see Appendix C), which is a non-orthogonal mapping that "stretches" the vertical dimensions of the glacier to a layer of uniform height (Fig. 4.2). This simplification results, however, in more complicated expressions for partial spatial derivatives of field variables. The resulting shape with a uniform thickness is divided equidistantly in the stretched coordinates into N_3 layers. We do not perform a local grid densification in the vertical direction. Each node of the computational grid contains all the field variables. Hence, no staggered grid is implemented a-priori, as we have done, for instance, in the case of a simple model for the ISMIP-HOM experiment A. However, a staggered-grid approach can be implemented by interpolating appropriate nodal values during the computation. It turns out that the computational performance and stability of the model without applying the staggered-grid approach is satisfactory for all the model runs.

4.3 Updating geometry by solving kinematic equation

The kinematic equation (1.10) for free surface movement is an example of a transport equation, which, in general, is of the form

$$\frac{\partial \varphi(\vec{x},t)}{\partial t} + \vec{v} \cdot \mathrm{grad}\varphi(\vec{x},t) = f \ , \tag{4.1}$$

$$\varphi(\vec{x},t_0) = \varphi_0(\vec{x}) \ , \tag{4.2}$$

where a required quantity φ moves with velocity $\vec{v}$ and f is a source term. A numerical solution of this equation is known to be a difficult problem, because most numerical schemes have a tendency to induce undesired numerical oscillations. In the case of the SIA or the SIA-I approaches, where $\varphi = F_s$ is the free-surface function, such numerical oscillations induce destructive oscillations in the velocity field as the surface-topography gradient is the main driving force for velocities. A positive feedback from velocities as a result of surface topography speeds up the failure of computations.

To avoid this, we adopted two approaches that handle the problem of instability in a manner satisfactory for our purposes. The first one is a time-explicit method using special numerical schemes to evaluate the gradient operator in a way that no oscillations are produced by it, as long as the Courant-Friedrichs-Lewy (CFL) condition is satisfied. The second is an implicit method possessing a self-smoothing property similar to the traditional shallow ice approach with respect to free-surface evolution.

4.3.1 Time-explicit approach

The equation (4.1) may be expressed even more generally as

$$\begin{aligned} \frac{\partial\varphi(\vec{x},t)}{\partial t} &= L(\varphi(\vec{x},t)) \,, \\ \varphi(\vec{x},t_0) &= \varphi_0(\vec{x}) \,, \end{aligned} \tag{4.3}$$

where L is a spatial-differential operator, which may be already discretised. For an explicit time scheme, we approximate the time derivative by a 3rd order Runge-Kutta scheme. Equation (4.3) at the $(n+1)$th time level reads as

$$\begin{aligned} \hat{\varphi}^{n+1} &= \varphi^n + \Delta t\, L(\varphi^n) \\ \hat{\varphi}^{n+\frac{1}{2}} &= \varphi^n + \frac{\Delta t}{4}\left(L(\varphi^n) + L(\hat{\varphi}^{n+1})\right) \\ \varphi^{n+1} &= \varphi^n + \frac{\Delta t}{6}\left(L(\varphi^n) + 4L(\hat{\varphi}^{n+\frac{1}{2}}) + L(\hat{\varphi}^{n+1})\right) \,, \end{aligned} \tag{4.4}$$

where $\varphi^n := \varphi(t_0+(n-1)\Delta t)$, and Δt is the time step. Keeping in mind that $L = f - \vec{v}\cdot\mathrm{grad}\varphi$ in our case, assuming that the source term f is given and remembering that velocity $\vec{v}$ at the nth time instant is obtained by the SIA-I algorithm, we only need to discretise $\mathrm{grad}\varphi$ in a convenient way. Note that equation (4.1) is a hyperbolic partial differential equation, which is known to be problematic when numerically implementing it as most of the standard discretisation schemes (e.g. Quarteroni & Valli (1994)) suffer from undesired phenomena such as oscillations, geometrical spreading, and so on. In order to avoid such a behavior, we choose a discretisation of $\mathrm{grad}\varphi$ by the so-called Essentially Non-Oscillatory (ENO) schemes.

- **Essentially Non-Oscillatory (ENO) schemes**
  Here we briefly summarize the basic properties and construction of the ENO schemes following the comprehensive paper by Shu (1998).

  The ENO schemes are polynomial interpolation schemes, for which the interpolation stencil is not prescribed a-priori, but it is chosen adaptively for each grid point according to the data values in the neighborhood of this point and choosing automatically the locally smoothest variant. This avoids crossing a discontinuity in the interpolation procedure, as its crossing leads to an oscillatory behavior of the interpolated function in the vicinity of the discontinuity. The ENO schemes are widely used in applications such as aero-acustics, or turbulence simulations, in general in applications where discontinuities (shocks) of the field variables appear and propagate.

  For a 1D function, the ENO interpolation procedure may be described as follows. Consider N equally spaced data points $x_1, \ldots x_N$, $x_i = x_1 + (i-1)\Delta x$, holding values $y_1, \ldots, y_N$, where $y_i = y(x_i)$ for a smooth function $y(x)$. By I_i we denote the interval $I_i = (x_{i-\frac{1}{2}}, x_{i+\frac{1}{2}})$, where $x_{i+\frac{1}{2}} := \frac{x_i+x_{i+1}}{2}$. The aim is to find the so-called numerical fluxes, that is functions

$$\hat{y}^-_{i+\frac{1}{2}} = \hat{y}^-_{i+\frac{1}{2}}(y_{i-r}, \ldots, y_{i+s}) \,, \tag{4.5}$$

$$\hat{y}^+_{i-\frac{1}{2}} = \hat{y}^+_{i-\frac{1}{2}}(y_{i-r}, \ldots, y_{i+s}) \,, \tag{4.6}$$

  such that the flux difference approximates the derivative $y'(x)$ to k-th order accuracy:

$$\frac{\hat{y}^-_{i+\frac{1}{2}} - \hat{y}^+_{i-\frac{1}{2}}}{\Delta x_i} = y'(x_i) + O(\Delta x^k) \,, \tag{4.7}$$

where $\Delta x_i := x_{i+\frac{1}{2}} - x_{i-\frac{1}{2}}$. Consider an auxiliary function $h(x)$ such that

$$y(x) = \frac{1}{\Delta x} \int_{x-\frac{\Delta x}{2}}^{x+\frac{\Delta x}{2}} h(\xi)\, d\xi \,. \tag{4.8}$$

Then

$$y'(x_i) = \frac{h(x_{i+\frac{1}{2}}) - h(x_{i-\frac{1}{2}})}{\Delta x_i} \,, \qquad i = 1, \ldots, N \,, \tag{4.9}$$

and the sought after numerical fluxes may be obtained by a sufficiently high-order approximation of the function $h(x)$. Since it is difficult to obtain the function $h(x)$ from the integral equation (4.8), the following trick based on a primitive function is applied. Let $H(x)$ be a primitive function of $h(x)$

$$H(x) := \int_{-\infty}^{x} h(\xi) d\xi \,, \tag{4.10}$$

and let $H(x)$ be evaluated at point $x_{i+\frac{1}{2}}$:

$$H(x_{i+\frac{1}{2}}) = \int_{-\infty}^{x_{i+\frac{1}{2}}} h(\xi)\, d\xi = \sum_{j=-\infty}^{i} \int_{x_{j-\frac{1}{2}}}^{j+\frac{1}{2}} h(\xi)\, d\xi = \sum_{j=1}^{i} \Delta x_j\, y_j \,, \tag{4.11}$$

where y_i is defined equal to 0, $y_i = 0$, outside the interval $\{1, \ldots, N\}$. Having the point values $H(x_{i+\frac{1}{2}})$ of $H(x)$, the numerical fluxes are obtained by constructing a polynomial approximation of an appropriate order of $H(x)$ using values $H(x_{i+\frac{1}{2}})$ and differentiating this approximation with respect to x. Note that for a chosen order of approximation, there is a freedom in the choice of the stencil, i.e. the set of points used for the polynomial reconstruction.

When the procedure is completed, the flux for a stencil $\{I_{i-r}, \ldots, I_{i+s}\}$ where $r + s + 1 = k$, is expressed as

$$\hat{y}^{-}_{i+\frac{1}{2}} = \sum_{j=0}^{k-1} c_{rj} y_{i-r+j} \,, \tag{4.12}$$

$$\hat{y}^{+}_{i-\frac{1}{2}} = \sum_{j=0}^{k-1} \tilde{c}_{rj} y_{i-r+j} \,, \tag{4.13}$$

where the constants c_{rj}, $\tilde{c}_{rj}$ can be computed explicitly. Their table is given in Shu (1998).

When a polynomial interpolation scheme is constructed, the stencil is usually taken fixed, which means that the r coefficient is fixed for all points, i.e. the shape of the stencil is the same. An example is a central fourth-order reconstruction of the flux taken as $\hat{y}^{-}_{i+\frac{1}{2}}$

$$\hat{y}^{-}_{i+\frac{1}{2}} = -\frac{1}{12} y_{i-1} + \frac{7}{12} y_i + \frac{7}{12} y_{i+1} - \frac{1}{12} y_{i+2} \,. \tag{4.14}$$

Now if the function $y(x)$ is only piecewise smooth, such as a step function, the approximation property in the vicinity of the jump is no longer valid. For fixed stencil schemes, we then obtain oscillations of the interpolated function in the vicinity of the jump. A way to avoid this so-called Gibbs' Phenomena is to choose the stencil adaptively according to the data character. For ENO schemes, the choice of the stencil is governed by a certain smoothness request.

First, the Newton divided differences are defined recursively by

$$y_i[x_i] = y_i \,, \tag{4.15}$$

$$y_i[x_i, \ldots, x_{i+j}] = \frac{y_i[x_{i+1}, \ldots, x_{i+j}] - y_i[x_i, \ldots, x_{i+j-1}]}{x_{i+j} - x_i} \,. \tag{4.16}$$

The ENO piecewise polynomial reconstruction of at most degree $k-1$ for the interval I_i will be constructed by the following algorithm.

- Compute the divided differences for degrees 1 to k using (4.15).
- Start with a one-point stencil
$$S_1(i) = \{I_i\} \tag{4.17}$$
- For $l = 2, \ldots, k-1$ the stencil
$$S_l(i) = \{I_j, \ldots, I_{j+l-1}\} \,, \tag{4.18}$$
is modified such that one of the two neighboring cells I_{j-1}, I_{j+l} is added to the stencil. If
$$|y[x_{j-1}, \ldots, x_{j+l-1}]| < |y[x_j, \ldots, x_{j+l}]| \,, \tag{4.19}$$
add the cell I_{j-1} to the stencil S_l and redefine it as
$$S_{l+1}(i) = \{I_{j-1}, \ldots, I_{j+l-1}\} \,, \tag{4.20}$$
else add the cell I_{j+l} to the stencil S_l and redefine it as
$$S_{l+1}(i) = \{I_j, \ldots, I_{j+l}\} \,. \tag{4.21}$$
- For the final stencil $S_k(i) = \{I_{i-r}, \ldots, I_{i+s}\}$, with $r + s + 1 = k$, a Lagrange interpolation polynomial is constructed. After differentiation with respect to x, a polynomial $p(x)$ of at most degree $k-1$ in I_i is obtained
$$p_i(x) = \sum_{m=0}^{k} \sum_{j=0}^{m-1} v_{i-r+j} \Delta x_{i-r+j} \left(\frac{\sum_{l=0, l\neq m}^{k} \Pi_{q=0, q\neq m, l}^{k} (x - x_{i-r+q-\frac{1}{2}})}{\Pi_{l=0, l\neq m}^{k} (x_{i-r+m-\frac{1}{2}} - x_{i-r+l-\frac{1}{2}})} \right) \,. \tag{4.22}$$
Finally, the numerical flux $\hat{y}_{i+\frac{1}{2}}$ reads as
$$\hat{y}^-_{i+\frac{1}{2}} := p_i(x_{i+\frac{1}{2}}) \,, \tag{4.23}$$
$$\hat{y}^+_{i-\frac{1}{2}} := p_i(x_{i-\frac{1}{2}}) \,, \tag{4.24}$$
or
$$\hat{y}^-_{i+\frac{1}{2}} = \sum_{j=0}^{k-1} c_{rj} y_{i-r+j} \,, \tag{4.25}$$
$$\hat{y}^+_{i-\frac{1}{2}} = \sum_{j=0}^{k-1} \tilde{c}_{rj} y_{i-r+j} \,. \tag{4.26}$$

Comparing (4.22) and (4.25)-(4.26), we obtain explicit expressions for the coefficients c_{rj} and $\tilde{c}_{rj}$

$$c_{rj} = \Delta x_{i-r+j} \sum_{m=0}^{k} \left(\frac{\sum_{l=0,l\neq m}^{k} \Pi_{q=0,q\neq m,l}^{k} (x_{i+\frac{1}{2}} - x_{i-r+q-\frac{1}{2}})}{\Pi_{l=0,l\neq m}^{k} (x_{i-r+m-\frac{1}{2}} - x_{i-r+l-\frac{1}{2}})} \right) , \tag{4.27}$$

$$\tilde{c}_{rj} = \Delta x_{i-r+j} \sum_{m=0}^{k} \left(\frac{\sum_{l=0,l\neq m}^{k} \Pi_{q=0,q\neq m,l}^{k} (x_{i-\frac{1}{2}} - x_{i-r+q-\frac{1}{2}})}{\Pi_{l=0,l\neq m}^{k} (x_{i-r+m-\frac{1}{2}} - x_{i-r+l-\frac{1}{2}})} \right) . \tag{4.28}$$

The expressions (4.22), (4.27) and (4.28) are valid for a non-uniform grid, which will be applied in the vicinity of the boundaries with different grid-point densities. The accuracy estimates of interpolation then differ from the uniform-grid case and are, in general, worse.

We now return to the discretisation of the term $\vec{v} \cdot \mathrm{grad}\varphi$ from (4.1). We will consider only the part $v_x \frac{\partial \varphi}{\partial x}$, since the y-counterpart can be discretised in an analogous way. In order to obtain a stable numerical scheme, upwinding is used, that is, using spatial discretisation biased according to the direction of the propagation speed.

- If $v_x(x_i) \geq 0$, we use the ENO reconstruction of fluxes $\hat{\varphi}^-_{i+\frac{1}{2}}$ and $\hat{\varphi}^-_{i-\frac{1}{2}}$ and estimate

$$v_x \frac{\partial \varphi}{\partial x}(x_i) \simeq v_x(x_i) \frac{\hat{\varphi}^-_{i+\frac{1}{2}} - \hat{\varphi}^-_{i-\frac{1}{2}}}{x_{i+\frac{1}{2}} - x_{i-\frac{1}{2}}} , \tag{4.29}$$

where $\hat{\varphi}^-_{i-\frac{1}{2}}$ is defined by

$$\hat{\varphi}^-_{i-\frac{1}{2}} := \hat{\varphi}^-_{(i-1)+\frac{1}{2}} . \tag{4.30}$$

- If $v_x(x_i) < 0$, we use the ENO reconstruction of fluxes $\hat{\varphi}^+_{i+\frac{1}{2}}$ and $\hat{\varphi}^+_{i-\frac{1}{2}}$ and estimate

$$v_x \frac{\partial \varphi}{\partial x}(x_i) \simeq v_x(x_i) \frac{\hat{\varphi}^+_{i+\frac{1}{2}} - \hat{\varphi}^+_{i-\frac{1}{2}}}{x_{i+\frac{1}{2}} - x_{i-\frac{1}{2}}} , \tag{4.31}$$

where $\hat{\varphi}^+_{i+\frac{1}{2}}$ is defined by

$$\hat{\varphi}^+_{i+\frac{1}{2}} := \hat{\varphi}^+_{(i+1)-\frac{1}{2}} . \tag{4.32}$$

With the use of the ENO flux reconstruction and the Runge-Kutta time-explicit discretisation, the problem of the free-surface evolution is resolved, provided that the ice sheet extends over the whole computational domain and the deglaciated regions are represented by a thin layer of ice of a small prescribed thickness. This traditional and useful trick has the great advantage that there is no need not to "switch on and off" the computational nodes when they appear in and out of the glaciated area. An obvious price paid for that is reduced computational effectiveness, since all nodes are active (equations solved in them) all the time.

Nevertheless, the problem of determining and tracking the ice sheet margin may become important in some situations. So far, we have been dealing only with the grounded ice sheets, i.e. glaciers being in contact with the underlying bedrock, but, in nature, ice sheets typically end their journey at ocean shores and as the ice starts floating, the flow regime and boundary conditions dramatically change. Neither the SIA,

nor SIA-I approaches are convenient anymore in these transition regions, and a different type of scaling has to be adopted. This leads typically to some kind of Shallow-Shelf Approximation (SSA), such as in Baral et al. (2001). It is therefore an important, but non-trivial task to track the grounded-floating ice transition line and capture its movement properly. In order to do this, we implement (only in the time explicit formalism) a possible way of tracking the ice sheet extent by the technique of a level-set function, which we now briefly summarize following the paper by Peng et al. (2000).

- **Level set function approach: Tracking the ice sheet extent.**

  The level-set approach is based on the following idea. Our aim is to describe a movement of a closed curve $\Gamma(t)$ in R^2, for instance, where $\Gamma(t)$ is the margin of an ice sheet. Let $\Omega(t)$ be the region enclosed by the curve $\Gamma(t)$. We introduce the so-called level-set function $\Phi(\vec{x},t)$ by the conditions

$$\Phi(\vec{x},t): \begin{cases} > 0 & \text{in } \Omega(t)\ , \\ = 0 & \text{on } \Gamma(t)\ , \\ < 0 & \text{in } R^2 \setminus \bar{\Omega}(t)\ . \end{cases}$$

  Given $\Phi(\vec{x},t)$, the position of the curve $\Gamma(t)$ can be tracked by finding the zero contour of $\Phi(\vec{x},t)$, that is the set of points in R^2 satisfying $\Phi(\vec{x},t) = 0$. The problem of the movement of the curve $\Gamma(t)$ is thus transformed into the problem of the evolution of the level-set function $\Phi(\vec{x},t)$. The corresponding transport equation is obtained by differentiating the relation $\Phi(\vec{x},t) = 0$, holding for all $\vec{x} \in \Gamma(t)$, with respect to time, which gives

$$\frac{\partial \Phi(\vec{x},t)}{\partial t} + \vec{v} \cdot \mathrm{grad}\Phi(\vec{x},t) = 0\ , \qquad \vec{x} \in \Gamma(t)\ , \tag{4.33}$$

  where $\vec{v}$ is the velocity of the material particles on $\Gamma(t)$. This equation can be extended to the whole R^2, provided the velocity field $\vec{v}$ is extended outside the curve. This can be done rather arbitrarily, as the velocity $\vec{v}$ has a specific physical meaning only for the particles on $\Gamma(t)$. If $\Gamma(t)$ is a material curve dragged in a velocity field, it is natural to define the velocity of the level-set $\Phi(\vec{x},t)$ by $\vec{v}$. In the case that $\Gamma(t)$ represents a boundary of a material domain (such as a glacier), the material velocity is well defined only in the domain $\bar{\Omega}(t)$, and it needs to be extended outside this domain. The freedom in the extension allows us to choose the velocity outside $\bar{\Omega}(t)$ such that it yields the best numerical behavior of the function Φ. It is, in particular, convenient that the level-set function resembles a distance function from $\Gamma(t)$ (signed positive in $\Omega(t)$ and negative outside $\bar{\Omega}(t)$), that is when

$$|\mathrm{grad}\Phi| = 1\ , \tag{4.34}$$

  at least, in the vicinity of Γ. The velocity extension can be done such that (4.34) remains approximately satisfied for some period of the evolution of Φ, after which, however, the function Φ has to be reinitialized. The process of reinitialization has to be performed in such way that the zero contour of Φ, that is the position of $\Gamma(t)$, is not affected by the procedure.

  Since the information about the position of $\Gamma(t)$ is maintained only by the zero contour of the function Φ, it is unnecessary to compute the evolution of Φ in R^2, but rather it is sufficient to localize the non-trivial support of Φ in a neighborhood of $\Gamma(t)$ defined by a small prescribed distance from $\Gamma(t)$. This results in the so-called local level-set approach (Peng et al., 2000) which can be characterized by the following five steps:

  - **Initialize**
    Initialize the level-set function $\Phi(\vec{x}, t = 0)$ as the signed distance from the initial position of $\Gamma(t = 0)$ (sign positive inside $\Omega(t)$, negative outside $\bar{\Omega}(t)$).

- **Compute velocity**
  Calculate the material velocity $\vec{v}$ on $\Gamma(t)$ by solving the physical problem associated with the movement of particles on $\Gamma(t)$ (in our case the Stokes problem for ice flow).
- **Extend velocity**
  Provided the material velocity $\vec{v}$ is not well-defined everywhere, extend the velocity field $\vec{v}$ on the neighborhood tube T_γ with a radius γ

$$T_\gamma := \{\vec{x} : |\Phi(\vec{x}, t)| \leq \gamma\} \,. \tag{4.35}$$

- **Advance**
  Solve the transport equation (4.33) to update the level-set function.
- **Reinitialize**
  Apply the reinitialization scheme on the tube N_γ ($T_\gamma \subset N_\gamma$), where N_γ is defined by

$$N_\gamma := \{\vec{x} : |\Phi(\vec{x} + \vec{y})| \leq \gamma \text{ for some } |\vec{y}| < \Delta x\}. \tag{4.36}$$

We must discuss the numerical implementation of these steps. The first one is straightforward to do. The second one has been discussed for the situation of resolving the ice-flow problem by the SIA-I algorithm in Chapter 3. The numerical implementation of the last three steps follow the approach given in Peng et al. (2000).

Velocity extension

For an arbitrary (scalar) quantity q_Γ defined on the curve $\Gamma(t)$, a possible way to extend it outside the curve $\Gamma(t)$ is by solving the following partial differential equation (Peng et al., 2000)

$$\frac{\partial q(\vec{x}, \tau)}{\partial \tau} + S(\Phi)\frac{\text{grad}\Phi}{\|\text{grad}\Phi\|} \cdot \text{grad}\, q(\vec{x}, \tau) = 0 \,, \tag{4.37}$$

$$q(\vec{x}, 0) = \begin{cases} q_\Gamma \text{ at } \Gamma(t) \\ 0 \text{ elsewhere} \end{cases} , \tag{4.38}$$

with

$$S(\Phi) = \begin{cases} -1 & \text{if } \Phi < 0 \\ 0 & \text{if } \Phi = 0 \\ 1 & \text{if } \Phi > 0 \end{cases} .$$

It is a transport (hyperbolic) equation with an artificial "velocity" $S(\Phi)\frac{\text{grad}\Phi}{\|\text{grad}\Phi\|}$ which, if Φ is a signed distance function, is normal to the curve $\Gamma(t)$ and points outwards of Γ on both sides. Note that the equation (4.37) is a special type of transport equation (4.3), for which a robust implementation scheme was introduced above in this section by utilizing the ENO schemes. Because of the freedom in the velocity extension, the numerical accuracy for (4.37) is not crucial and instead of the ENO approach, a simple upwind scheme is applied, giving already a sufficient accuracy. Approximating $S(\Phi)$ by

$$S_\delta(\Phi) := \frac{\Phi}{\sqrt{\Phi^2 + \delta^2}} \tag{4.39}$$

for a small constant δ, and denoting the nodal values of $S_\delta(\Phi)$ by $s_{i,j}$, we compute the normal vector $\vec{n} = \frac{\text{grad}\Phi}{\|\text{grad}\Phi\|}$ by central differencing and denote its nodal values by $\vec{n}_{i,j} = (n^x_{ij}, n^y_{ij})$. Then, we discretise (4.37) as follows

$$\begin{aligned} q^{n+1}_{i,j} = q^n_{i,j} &- \Delta\tau \left\{ (s_{i,j}\, n^x_{i,j})^+ \frac{q_{i,j} - q_{i-1,j}}{\Delta x} + (s_{i,j}\, n^x_{i,j})^- \frac{q_{i+1,j} - q_{i,j}}{\Delta x} \right. \\ &+ \left. (s_{i,j}\, n^y_{i,j})^+ \frac{q_{i,j} - q_{i,j-1}}{\Delta y} + (s_{i,j}\, n^y_{i,j})^- \frac{q_{i,j+1} - q_{i,j}}{\Delta y} \right\} , \end{aligned} \tag{4.40}$$

where

$$(x)^+ := \max(x, 0) \,, \qquad (x)^- := \min(x, 0). \tag{4.41}$$

Advancing the level set

The transport equation for the level-set function $\Phi(\vec{x}, t)$ given in (4.33) is discretised in the same way as the free-surface kinematic equation (4.1) and (4.2). Namely, the time derivative is treated by the Runge-Kutta scheme of the 3rd order according to (4.4), and the spatial discretisation of the term $\vec{v} \cdot \mathrm{grad}\Phi$ is performed by constructing the upwind ENO reconstruction of the numerical fluxes according to (4.29)-(4.32). The velocity field $\vec{v}$ in (4.33) is taken after the extension to be defined at least in the tube T_γ surrounding the zero level-set contour $\Gamma(t)$.

Reinitialization

It is convenient to keep the level-set function Φ close to a signed distance function in the vicinity of $\Gamma(t)$, since then the normal vector to $\Gamma(t)$ is given as a gradient of the level-set function Φ. Since Φ deforms during the time evolution, it is necessary, after a few time steps, to reset Φ to a signed distance function again. A possible way of doing this, without affecting the zero contour of Φ during its resetting, consists of solving an evolutionary partial differential equation for an auxiliary function $d(x, \tau)$ in the form

$$\frac{\partial d}{\partial \tau} + S_\delta(d_0)(\|\mathrm{grad}\, d\| - 1) = 0 \,, \tag{4.42}$$

$$d(x, 0) = d_0(x) = \Phi(x, t) \,, \tag{4.43}$$

where $S_\delta(d)$ approximates the Heaviside step function by

$$S_\delta(d) = \frac{d}{\sqrt{d^2 + \delta^2 |D\, d|^2}} \,, \tag{4.44}$$

where the term $D\, d$ approximates $\mathrm{grad}\, d$ and δ is a small constant. This approximation differs from that given in Peng et al. (2000), but it has better numerical performance for the testing examples.

The steady-state solution $d(x)$ has the desired property, namely $\|\mathrm{grad}\, d\| = 1$, and, at $\Gamma(t)$, $d(x) = \Phi(x, t)$. Thus, the zero contour of d is the same as of $\Phi(x, t)$. We therefore take d for the resetting of Φ. The numerical implementation is done by the following scheme for updating the nodal values of d, which are denoted by d_{ij}:

$$\begin{aligned} d_{ij}^{n+1} = d_{ij} \quad &- \quad \Delta\tau s_{ij}^+ \left(\sqrt{(A^+)^2 + (B^-)^2 + (C^+)^2 + (D^-)^2} - 1 \right) \\ &- \quad \Delta\tau s_{ij}^- \left(\sqrt{(A^-)^2 + (B^+)^2 + (C^-)^2 + (D^+)^2} - 1 \right) \,, \end{aligned} \tag{4.45}$$

where s_{ij} are nodal values of $S_\delta(d)$ defined by (4.44), with $D\, d$ approximated by a central finite-difference approximation of $\mathrm{grad}\, d$, and

$$A := \frac{d_{ij} - d_{i-1\,j}}{x_i - x_{i-1}} \,, \tag{4.46}$$

$$B := \frac{d_{i+1\,j} - d_{ij}}{x_{i+1} - x_i} \,, \tag{4.47}$$

$$C := \frac{d_{ij} - d_{ij-1}}{y_j - y_{j-1}} \,, \tag{4.48}$$

$$D := \frac{d_{ij+1} - d_{ij}}{y_{j+1} - y_j} \,, \tag{4.49}$$

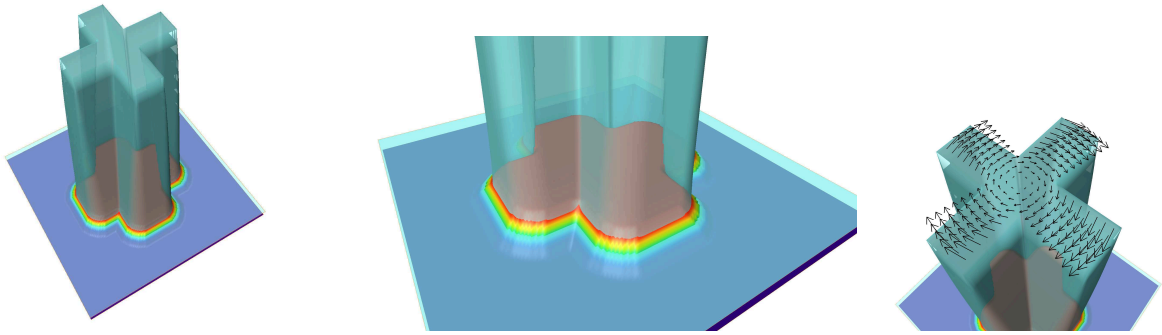

Figure 4.3: The initial shape of the cross with the initial level-set function (left), a detail of the level-set function (middle) and the rigid-body velocity field (right).

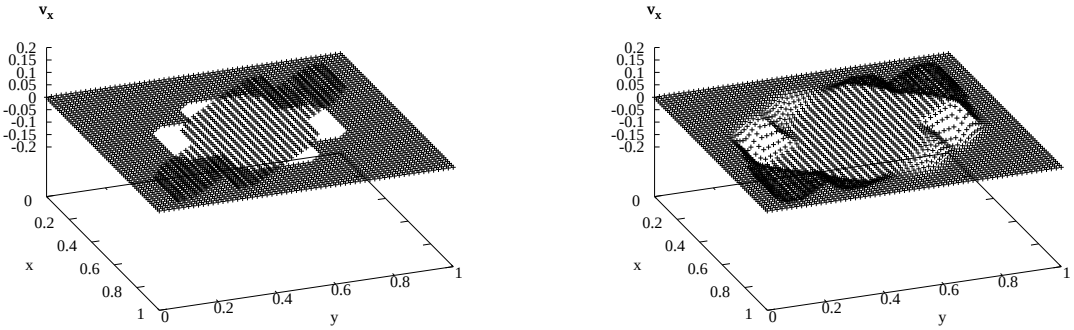

Figure 4.4: A smooth extension of the x component of velocity $\vec{v}$ to the vicinity of the cross margin (right). Compare with v_x before extension (left).

where $(x)^{\pm}$ are given by (4.41). The new local level-set is set as a restriction of the solution d:

$$\Phi = \max(-\gamma, \min(\gamma, d)) \; . \tag{4.50}$$

Finally, the tubes N_γ and T_γ are updated according to their definitions (4.36) and (4.35).

We demonstrate the whole time-explicit kinematic approach by visualizing it for a simple example of a cross that rotates with a rigid-body material velocity and period T. The initial shape, the initial level-set function and the initial velocity field for this example are shown in Fig. 4.3. The extension of the rotational velocity $\vec{v}$, defined originally only for the inner nodes where $\Phi > 0$, is shown for the v_x-component in Fig. 4.4. In Fig. 4.5, we plot the initial shape of the cross, the shape after $\frac{T}{4}$, and after $\frac{T}{2}$. We may observe that the original shape is smoothed during the time evolution, as the corners are affected the most. An important observation is that no oscillations occur as the cross moves, which, as mentioned before, is crucial with respect to the SIA-I approach.

Figures 4.6-4.8 show the results for a similar numerical example as for the cross, but now for a gaussian bell moving with a translational velocity. We can again observe very minor changes in the shape of the bell with again no oscillations in the bell's shape occurring when the bell moves.

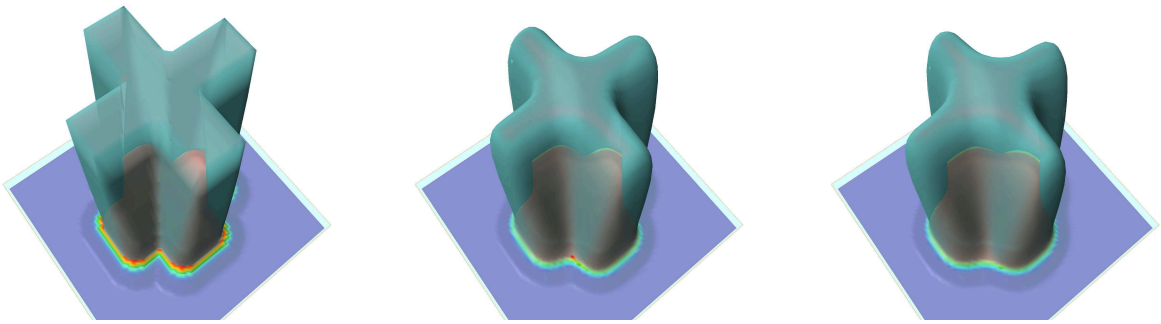

Figure 4.5: The initial shape (left), after $\frac{T}{4}$ (middle) and after $\frac{T}{2}$ (right).

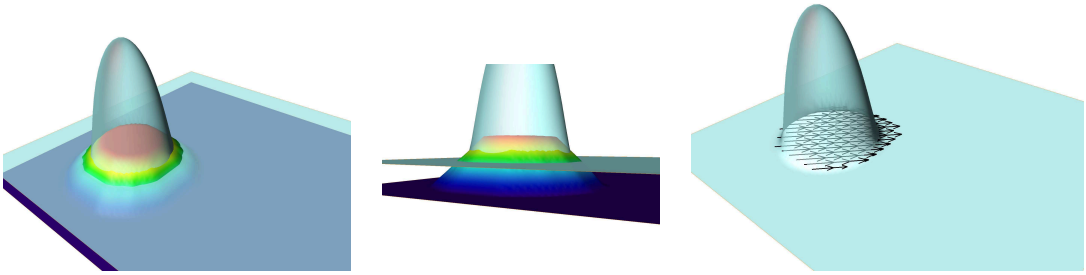

Figure 4.6: The initial shape of the gaussian bell with the initial level-set function (left), a detail of the level-set function (middle) and the rigid-body velocity field (right).

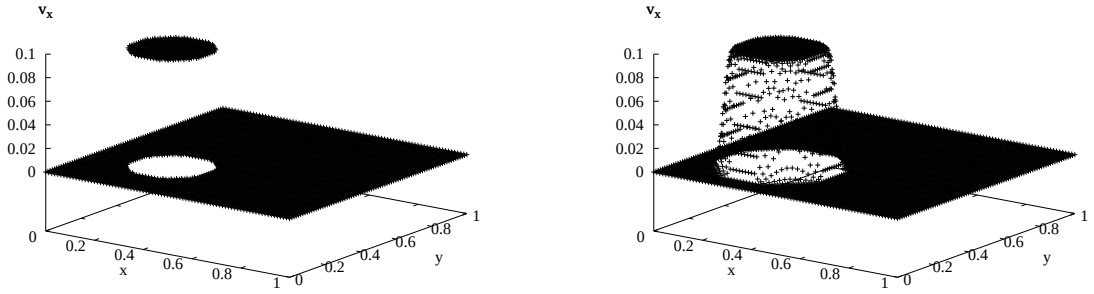

Figure 4.7: A smooth extension of the v_x velocity component to the vicinity of the glacier margin (right) and before extension (left).

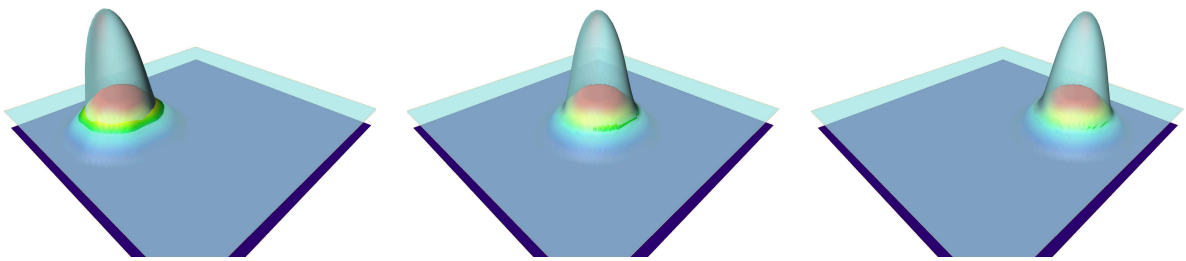

Figure 4.8: The gaussian bell movement from the initial (left) to the final (right) positions.

4.3.2 Time-implicit method.

When we move to a problem where surface accumulation is the dominant forcing for free-surface evolution, the time-explicit approach tends to become unstable and an implicit approach is to be adopted, which can be implemented in the following way.

Let us recall that we are dealing with the free surface evolution equation (1.10), which can be approximated in the sense of SIA by (2.164) (for Cartesian coordinates). For the explicit description of the free surface, $\tilde{F}_s := \tilde{z} - \tilde{f}_s(\tilde{x}, \tilde{y})$, and a purely cold ice ($\tilde{w} = 0$), it takes the following form:

$$\frac{\partial \tilde{f}_s}{\partial \tilde{t}} + \tilde{v}_x(\cdot, \tilde{f}_s(\cdot))\frac{\partial \tilde{f}_s}{\partial \tilde{x}} + \tilde{v}_y(\cdot, \tilde{f}_s(\cdot))\frac{\partial \tilde{f}_s}{\partial \tilde{y}} - \tilde{v}_z(\cdot, \tilde{f}_s(\cdot)) = \tilde{a}^s(\cdot, \tilde{f}_s(\cdot)) \,, \tag{4.51}$$

where $\tilde{\vec{v}}$ is the surface velocity. The SIA is only considered when evaluating the term $\sqrt{1+\epsilon^2()}$, by approximating it by unity. Since this term originally multiplies the accumulation $\tilde{a}^s$, (4.51) can be considered as the exact equation even in "non-shallow" regions, provided that this multiplication factor is included in $\tilde{a}^s$. Assuming that basal melting is not present, ($\tilde{m}_w^b = 0$), and applying the frozen-bed conditions, ($\tilde{\vec{\nu}}_b = \vec{0}$), equation (4.51), with use of (2.60) and (2.176), is traditionally rewritten as

$$\frac{\partial \tilde{f}_s}{\partial \tilde{t}} + \frac{\partial}{\partial \tilde{x}} \int_{\tilde{f}_b}^{\tilde{f}_s} \tilde{v}_x(\cdot, \tilde{z}')\, d\tilde{z}' + \frac{\partial}{\partial \tilde{y}} \int_{\tilde{f}_b}^{\tilde{f}_s} \tilde{v}_y(\cdot, \tilde{z}')\, d\tilde{z}' = \tilde{a}^s \,. \tag{4.52}$$

We must also remember that, for Cartesian coordinates, the SIA provides semi-analytical expressions for the velocity field (e.g. Greve (1997)), which, provided that no-slip basal conditions are applied, read as

$$\tilde{v}_x(\cdot, \tilde{z}) = -2\mathcal{K}\frac{\partial \tilde{f}_s}{\partial \tilde{x}} \left(\left(\frac{\partial \tilde{f}_s}{\partial \tilde{x}}\right)^2 + \left(\frac{\partial \tilde{f}_s}{\partial \tilde{y}}\right)^2 \right) \int_{\tilde{f}_b(\cdot)}^{\tilde{z}} \tilde{\mathcal{A}}(\tilde{T})(\tilde{f}_s - \tilde{z}')^3\, d\tilde{z}' \,, \tag{4.53}$$

$$\tilde{v}_y(\cdot, \tilde{z}) = -2\mathcal{K}\frac{\partial \tilde{f}_s}{\partial \tilde{y}} \left(\left(\frac{\partial \tilde{f}_s}{\partial \tilde{x}}\right)^2 + \left(\frac{\partial \tilde{f}_s}{\partial \tilde{y}}\right)^2 \right) \int_{\tilde{f}_b(\cdot)}^{\tilde{z}} \tilde{\mathcal{A}}(\tilde{T})(\tilde{f}_s - \tilde{z}')^3\, d\tilde{z}' \,. \tag{4.54}$$

These expressions allows us to rewrite equation (4.52) as

$$\frac{\partial \tilde{f}_s}{\partial \tilde{t}} - \frac{\partial}{\partial \tilde{x}} \left(\tilde{D}\frac{\partial \tilde{f}_s}{\partial \tilde{x}} \right) - \frac{\partial}{\partial \tilde{y}} \left(\tilde{D}\frac{\partial \tilde{f}_s}{\partial \tilde{y}} \right) = \tilde{a}^s \,, \tag{4.55}$$

with a diffusivity $\tilde{D}$ defined by

$$\tilde{D}(\cdot) := 2\mathcal{K} \left(\left(\frac{\partial \tilde{f}_s}{\partial \tilde{x}}\right)^2 + \left(\frac{\partial \tilde{f}_s}{\partial \tilde{y}}\right)^2 \right) \int_{\tilde{f}_b}^{\tilde{f}_s} \int_{\tilde{f}_b}^{\tilde{z}'} \tilde{\mathcal{A}}(\tilde{T})(\tilde{f}_s - \tilde{z}'')^3\, d\tilde{z}''\, d\tilde{z}'. \tag{4.56}$$

Provided that, in a numerical scheme, the diffusivity is computed from the previous time-step, (4.55) becomes a parabolic equation for the free-surface function $\tilde{f}_s$, possessing much better numerical properties than the original hyperbolic transport equation (4.51).

Even if the SIA is not applied, the evolution equation (4.51) may still be transformed to (4.55). Following Pattyn (2003), we introduce artificial diffusivities:

$$\tilde{D}_x := \frac{\int_{\tilde{f}_b}^{\tilde{f}_s} \tilde{v}_x\, d\tilde{z}'}{\frac{\partial \tilde{f}_s}{\partial \tilde{x}}} \,, \qquad \tilde{D}_y := \frac{\int_{\tilde{f}_b}^{\tilde{f}_s} \tilde{v}_y\, d\tilde{z}'}{\frac{\partial \tilde{f}_s}{\partial \tilde{y}}}. \tag{4.57}$$

Then, (4.52) reads as

$$\frac{\partial \tilde{f}_s}{\partial \tilde{t}} + \frac{\partial}{\partial \tilde{x}}\left(\tilde{D}_x \frac{\partial \tilde{f}_s}{\partial \tilde{x}}\right) + \frac{\partial}{\partial \tilde{y}}\left(\tilde{D}_y \frac{\partial \tilde{f}_s}{\partial \tilde{y}}\right) = \tilde{a}^s \ . \tag{4.58}$$

We then discretise this equation as follows:

$$\begin{aligned} \frac{\tilde{f}^{n+1}_{s\ i,j} - \tilde{f}^{n}_{s\ i,j}}{\Delta t} \quad &+ \quad \tilde{D}^{n}_{x\ i+\frac{1}{2},j} \frac{\tilde{f}^{n+1}_{s\ i+1,j} - \tilde{f}^{n+1}_{s\ i,j}}{(\Delta x)^2} - \tilde{D}^{n}_{x\ i-\frac{1}{2},j} \frac{\tilde{f}^{n+1}_{s\ i,j} - \tilde{f}^{n+1}_{s\ i-1,j}}{(\Delta x)^2} \\ &+ \quad \tilde{D}^{n}_{y\ i,j+\frac{1}{2}} \frac{\tilde{f}^{n+1}_{s\ i,j+1} - \tilde{f}^{n+1}_{s\ i,j}}{(\Delta y)^2} - \tilde{D}^{n}_{y\ i,j-\frac{1}{2}} \frac{\tilde{f}^{n+1}_{s\ i,j} - \tilde{f}^{n+1}_{s\ i,j-1}}{(\Delta y)^2} \ = (\tilde{a}^s)^n_{i,j}, \end{aligned} \tag{4.59}$$

where the i, j subscripts and superscript ^{n} denote the nodal values and the value at time step n, respectively. We thus see that the linear terms are expressed implicitly in time, whereas the nonlinear diffusivities are expressed explicitly in time. The diffusivities at midpoints are defined by

$$\tilde{D}_{x\ i\pm\frac{1}{2},j} := \frac{\tilde{D}_{x\ i\pm1,j} + \tilde{D}_{x\ i,j}}{2} \ , \qquad \tilde{D}_{y\ i,j\pm\frac{1}{2}} := \frac{\tilde{D}_{y\ i,j\pm1} + \tilde{D}_{y\ i,j}}{2} \ . \tag{4.60}$$

The semi-implicit equation (4.59) results in a band sparse system of equations which we store in a sparse storage mode as described in Press (1992). Its solution is found by an iterative solver taken from Ralph Greve's SICOPOLIS code (http://sicopolis.greveweb.net). This solver updates a solution $\vec{x}$ of the system of equations $\mathrm{A}\vec{x} = \vec{b}$, by a scheme

$$\vec{x}^{n+1} = \vec{x}^n + \omega \mathrm{D}^{-1}(\vec{b} - \mathrm{A}\vec{x}^n) \ , \tag{4.61}$$

where a relaxation parameter ω is typically $\omega \in (0, 1)$, and D the diagonal of matrix A. This easy numerical technique is sufficient, because of a good initial guess of the solution from the previous time-step. There is no necessity to improve it by a more advanced iterative solution technique such as the SOR method or Gauss-Seidel (e.g. Press (1992)).

4.4 Numerical tests

In this section, we present results and performance tests of the evolutionary numerical model described in the previous section. The first is again taken from the ISMIP-HOM intercomparison and concerns finding the steady-state profile of ice flow for ice treated as a Newtonian fluid. We then extend this experiment for ice flow with non-linear rheology and compare the outputs of our model with a finite-element model. The third experiment deals with the flow of an axisymmetric ice sheet under its own weight. The results are again compared with a finite-element simulation. For all three experiments, the time-explicit scheme of the evolution equation is applied. Over the whole computational domain, a minimal nonzero ice thickness is prescribed in order to avoid the necessity of tracking the glacier margin.

4.4.1 ISMIP-HOM experiment F

The setting of the ISMIP-HOM experiment F is as follows (Pattyn, 2008). An ice slab, with an initially flat surface slope of 3°, is flowing over a parallel inclined bed perturbed by a Gaussian bump. The horizontal dimensions of the slab are $\mathrm{L_{sc}} \times \mathrm{L_{sc}}$, with $\mathrm{L_{sc}} = 10^5 \mathrm{m}$, and the mean ice thickness is $\mathrm{H_{sc}} = 10^3 \mathrm{m}$. The coordinate system is chosen such that the $x - y$ plane is parallel with the initial surface f_s, x increases

downslope, and the z-axis is perpendicular to the initial surface, directed upwards. In such a system, we have

$$f_s(x,y,0) = 0\ , \qquad f_b(x,y,t) = -\mathrm{H_{sc}} + \frac{\mathrm{H_{sc}}}{10}\exp\left(-\frac{x^2+y^2}{\sigma^2}\right)\ , \tag{4.62}$$

with $\sigma = 10\,\mathrm{H_{sc}} = 10^4\mathrm{m}$. Periodic boundary conditions on velocity are applied at the sides of the computational domain, i.e.

$$\forall t:\ \forall x \in \langle -\mathrm{L_{sc}}/2, \mathrm{L_{sc}}/2\rangle, \forall z \in \langle f_b(\cdot), f_s(\cdot)\rangle:\ \vec{v}(x,-\mathrm{L_{sc}}/2,z) \ = \ \vec{v}(x,\mathrm{L_{sc}}/2,z)\ , \tag{4.63}$$

$$\forall t:\ \forall y \in \langle -\mathrm{L_{sc}}/2, \mathrm{L_{sc}}/2\rangle, \forall z \in \langle f_b(\cdot), f_s(\cdot)\rangle:\ \vec{v}(-\mathrm{L_{sc}}/2,y,z) \ = \ \vec{v}(\mathrm{L_{sc}}/2,y,z)\ . \tag{4.64}$$

The flow exponent in rheology (1.17) is chosen $n = 1$, which corresponds to Newtonian (linear) rheology. Ice is considered isothermal with the ice-flow parameter $\mathcal{A}(T) = A = 2.140373 \times 10^{-7}\ \mathrm{Pa^{-1}\,a^{-1}}$. The sliding law (1.68) is considered with

$$\beta^2 = \frac{1}{cA\mathrm{H_{sc}}}, \tag{4.65}$$

and two cases are distinguished: $c = 0$ (no-slip conditions) and $c = 1$ (sliding).

- $c = 0$ (**no slip**)
  The results for this case are shown in Fig. 4.9, where the panel in the first row shows the contour of the steady-state surface elevation and surface velocity magnitude. The middle and bottom panels show the SIA-I solution, which is compared with the published results of the ISMIP-HOM experiment F. The full-Stokes solutions and the higher-order models are plotted with lines and points, respectively, at an intersection with plane $y = 0$. Note that the SIA-I solution is closer to the full-Stokes solutions than the higher-order models.

- $c = 1$ (**sliding**)
  The results for this case are shown in Fig. 4.10. We can see the basal velocities are of the same order as the deformational velocities and the SIA-I solution agrees very closely with the full-Stokes solutions, and, it is of a significantly higher accuracy than most of the other higher-order models.

Numerical performance

The computations for both cases, $c = 0$ and $c = 1$, were performed for a model resolution $60 \times 60 \times 40$ and the solution was considered as steady state when the surface profile had not changed within a specified tolerance (maximal relative change of thickness of 5×10^{-5}) for two successive time steps. Approximately 200 time-steps (1 step = 1 year) were needed to reach steady-state. Each step took approximately 3s on an Intel Core i7 Quad-Core 2.6x4GHz. This is considerably faster than the full-Stokes FEM model (oga1 in Fig. 4.9 and 4.10), where time costs per time step vary between 2 and 0.5 CPU hours (see Fig. 11 in Gagliardini, 2008).

4.4.2 Transient simulation with non-linear rheology.

The only reason why the ISMIP-HOM experiment F was set up for linear rheology was to reduce computational demands, as they increase substantially when transient simulations are run instead of steady-state ones. The computational costs of the SIA-I algorithm are, however, by the character of the technique rather independent of the rheology used. This allows us to perform an evolutionary "ISMIP-HOM - like" experiment, in which a steady-state surface elevation is found by running a transient simulation, but with a non-linear rheology, which is more appropriate for the description of ice behavior.

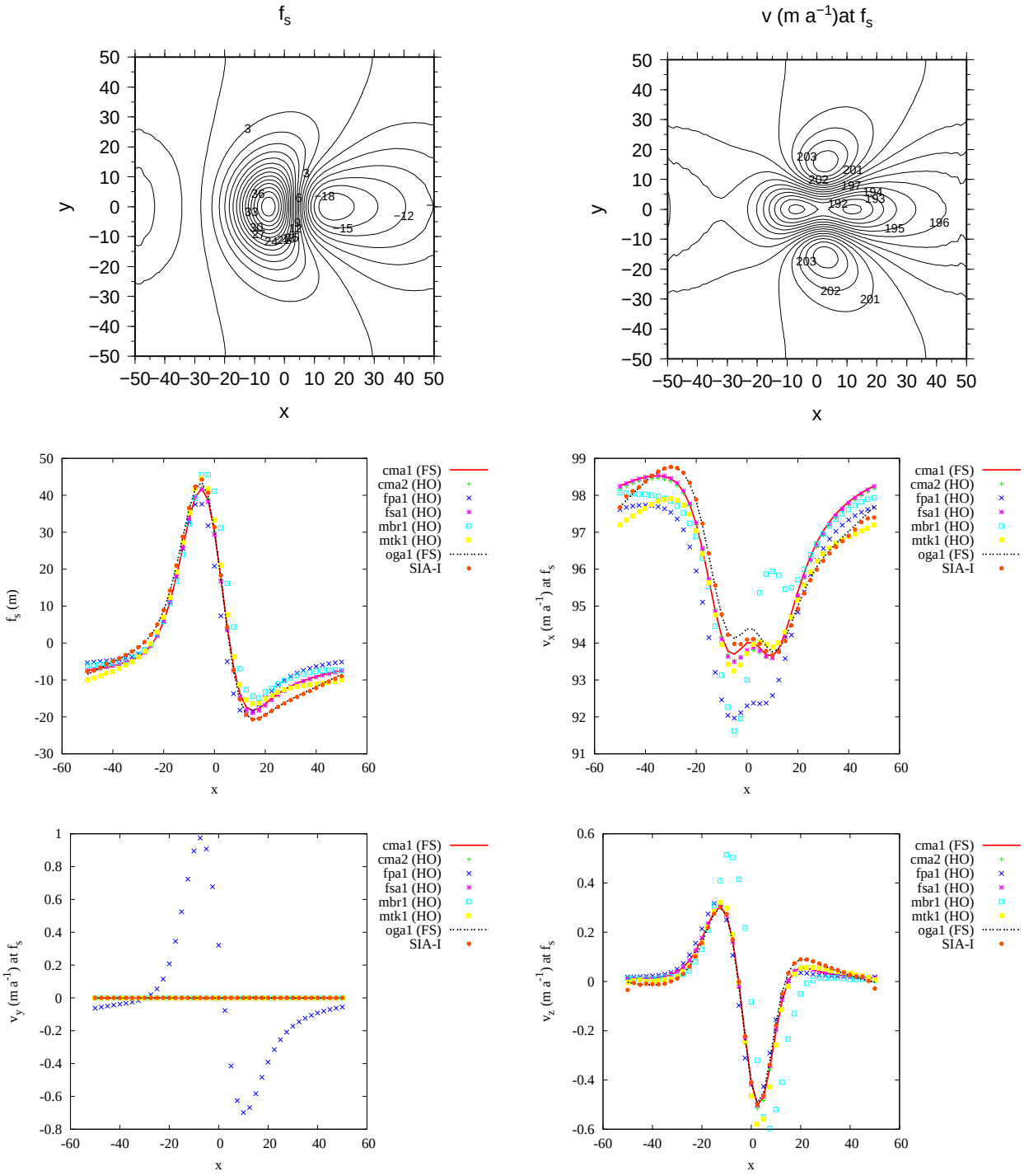

Figure 4.9: The computed steady-state surface elevation profile f_s (m) (top left) and surface-velocity magnitude $|\vec{v}|$ ($\mathrm{m\,a^{-1}}$) (top right). Below we see the steady-state surface elevation f_s in m and the steady-state surface velocity components v_x, v_y and v_z ($\mathrm{m\,a^{-1}}$) obtained by the SIA-I solver (red points), the ISMIP-HOM F solutions for the case $c = 0$ (no-slip at the base) by full-Stokes (red and blue lines) and higher-order approximations (dots). The results are shown at the intersection of the computational domain with the plane $y = 0$. Abbreviations used: FS = full Stokes, HO = higher-order approximation.

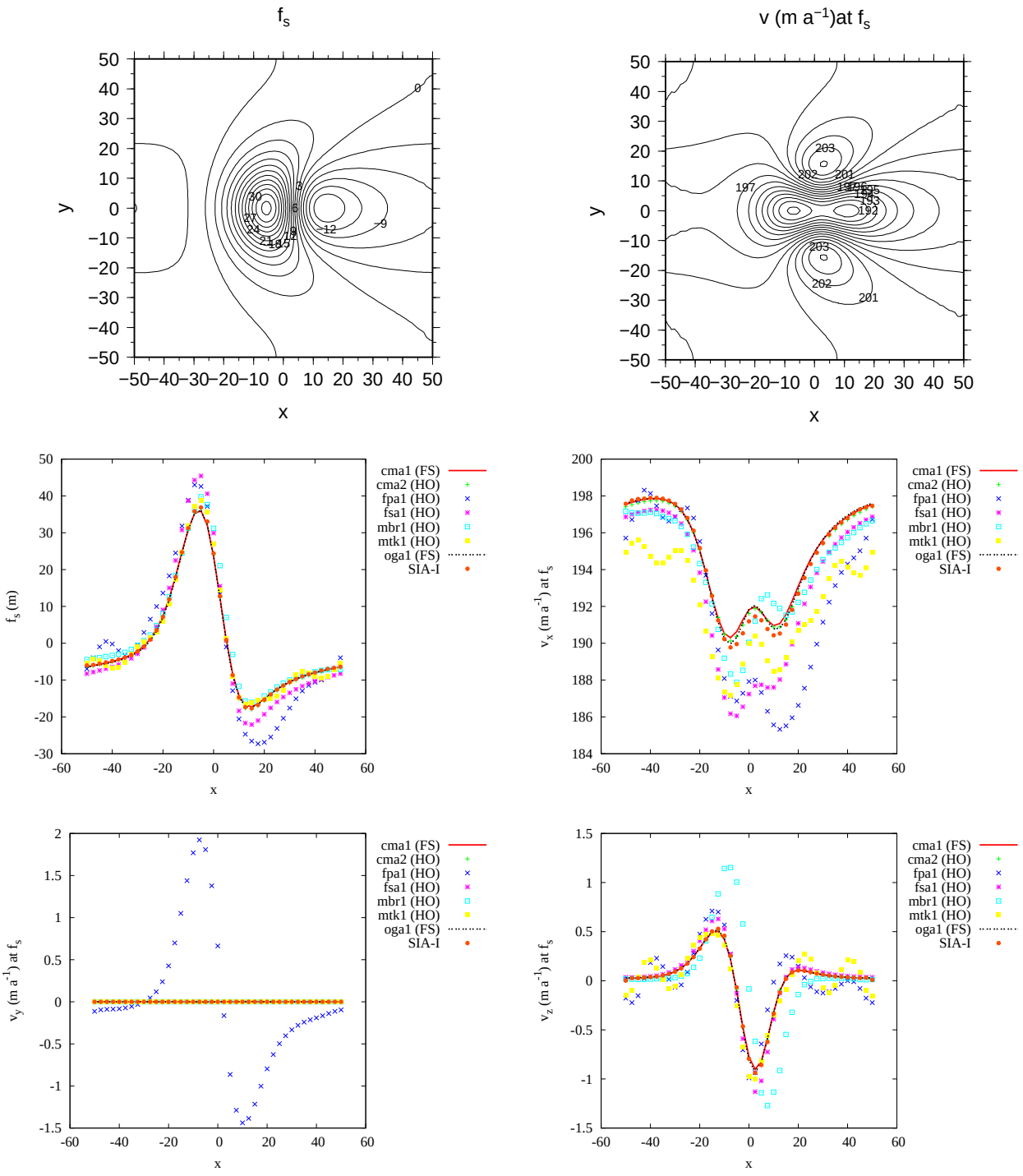

Figure 4.10: As for Fig. 4.9 but for $c = 1$, i.e. basal sliding is included.

The model was set up as follows. We chose a geometry similar to the ISMIP-HOM experiment A-setting, i.e square-base ice slab of size $\mathrm{L_{sc}} \times \mathrm{L_{sc}}$, $\mathrm{L_{sc}} = 80\,\mathrm{km}$, with an initially flat surface flowing over an inclined parallel bed perturbed by sinusoidal bumps. The upper and lower surfaces at the beginning of the simulation are given (in m) by

$$f_s(x,y) = -x\tan\alpha\,, \qquad \alpha = 0.5^\circ, \tag{4.66}$$

$$f_b(x,y) = f_s(x,y) - 1000 + 300\sin(\omega x)\sin(\omega y)\,, \tag{4.67}$$

with

$$\omega = \frac{2\pi}{\mathrm{L_{sc}}}\,.$$

At the sides, the periodic boundary conditions are prescribed:

$$\forall t:\ \forall x \in \langle 0, \mathrm{L_{sc}}\rangle, \forall z \in \langle f_b(\cdot), f_s(\cdot)\rangle:\ \vec{v}(x,0,z) = \vec{v}(x,\mathrm{L_{sc}},z)\,, \tag{4.68}$$

$$\forall t:\ \forall y \in \langle 0, \mathrm{L_{sc}}\rangle, \forall z \in \langle f_b(\cdot), f_s(\cdot)\rangle:\ \vec{v}(0,y,z) = \vec{v}(\mathrm{L_{sc}},y,z)\,. \tag{4.69}$$

In addition, no-slip and no traction were prescribed at the glacier bed and the upper free surface, respectively. The rheology is described by Glen's flow law (1.17). Our model was run until the upper surface was moving not more than a specified tolerance (the same as for the ISMIP-F experiment above). Such a stage, considered as steady state, was reached after approximately 200 time-steps (1 time-step = 1 year).

To check our simulations, we implemented this model setting into the open-source finite-element code Elmer (http://www.csc.fi/english/pages/elmer). Since the time demands for the non-linear rheology given by Glen's flow law (1.17) are too large to run the whole transient simulation, we confined ourselves to compare the SIA-I and full-Stokes FEM solutions only at several time instants. For each of these times we substituted the SIA-I computed geometry into a steady-state finite-element simulation as input data and obtained the corresponding full-Stokes velocity field. This was compared with our SIA-I velocities. In Fig. 4.11, we plot the results for three snapshots $t = 50, 100, 200$ years. The left panels show the surface undulation (in m), the right panels compare the surface velocity magnitude, with the solid line for SIA-I and dotted lines for the full-Stokes by Elmer. We can see a very good agreement between the computed velocity fields, indicating that our SIA-I solution of the steady-state surface profile is close to the full-Stokes solution.

The time costs of the SIA-I solver do not differ from the ISMIP-HOM experiment F, that is they are of the order of seconds per a time-step, depend linearly on the model resolution (number of nodes).

4.4.3 Axisymmetric ice-sheet spreading

In this numerical experiment, we compute the flow of an axisymmetric ice cap under its own weight. We compare the SIA-I solution for several aspect-ratios with a finite-element transient simulation by the Elmer code.

The initial shape of the glacier is a spherical cap with maximum thickness $100\,\mathrm{m}$ lying on a $5\,\mathrm{m}$ thick ice layer. The horizontal dimensions (diameter) of the studied domain are chosen as 1 km, 2 km, 5 km and 10 km, which corresponds to aspect ratios $\epsilon = \frac{1}{10}, \frac{1}{20}, \frac{1}{50}, \frac{1}{100}$. Ice rheology is modelled by Glen's flow law rheology (1.17) for non-linear fluids. At the glacier bed, the sliding law is prescribed by (1.68) with $\beta^2 = 10^6\ \mathrm{Pa\,a\,m^{-1}}$. The upper surface is considered traction-free. The finite-element mesh for the Elmer simulation is depicted in Fig. 4.12. In Fig. 4.13, we plot the surface profiles computed by Elmer for the full-Stokes model and compare them with the SIA-I results for the four aspect ratios. The geometry is scaled to unity and the given times are non-dimensional. The corresponding time steps differ according to

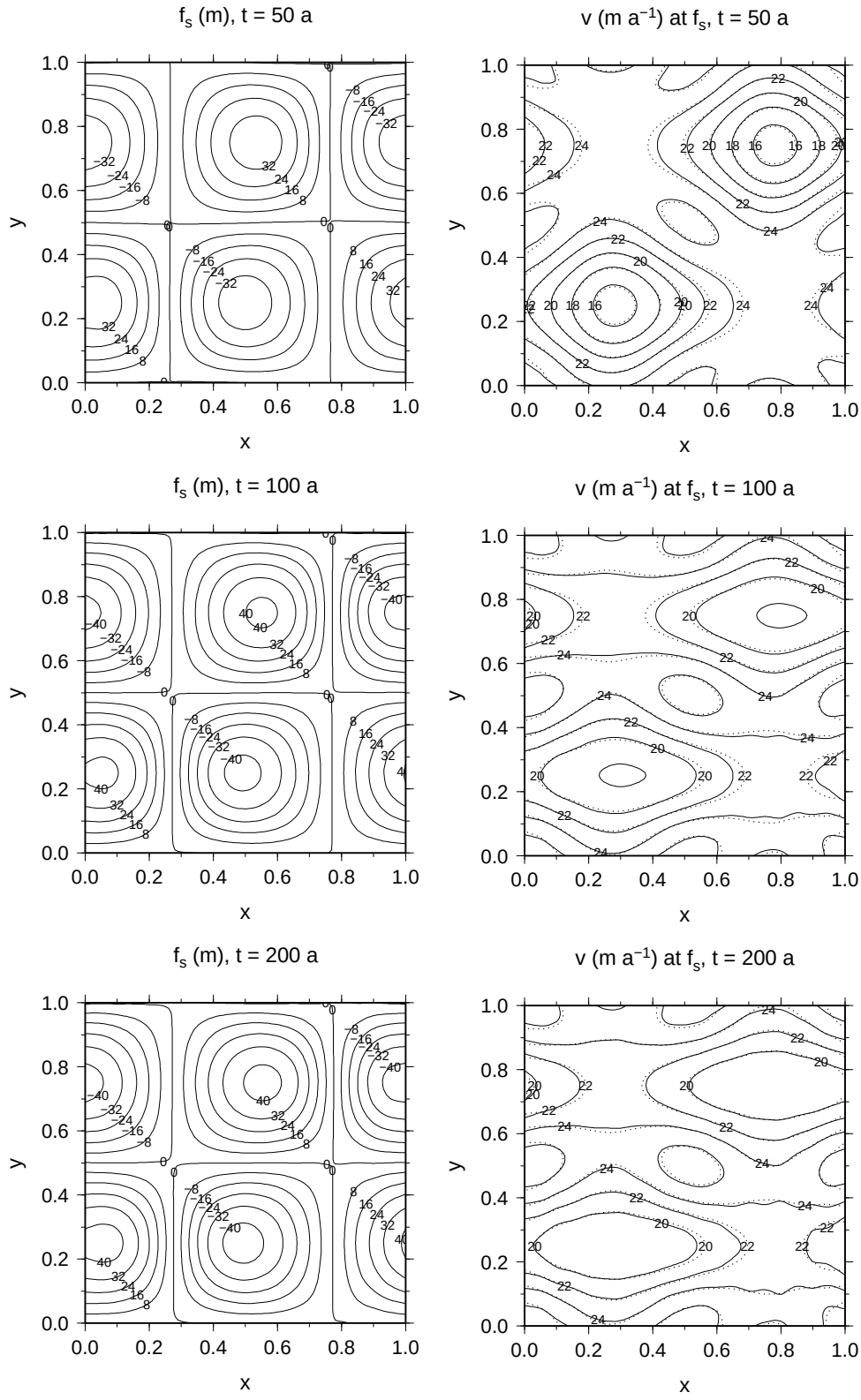

Figure 4.11: The SIA-I computed surface elevation (left panels) and corresponding velocity field (right panels). The full Stokes velocities by FEM (dotted) are compared with the SIA-I velocities (solid line). The last row represents the steady-state solution.

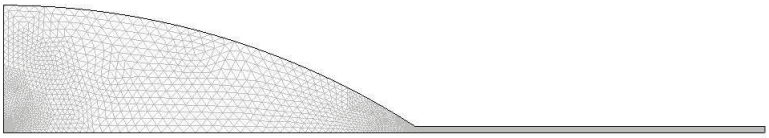

Figure 4.12: The triangular finite-element mesh for the full-Stokes simulation by Elmer.

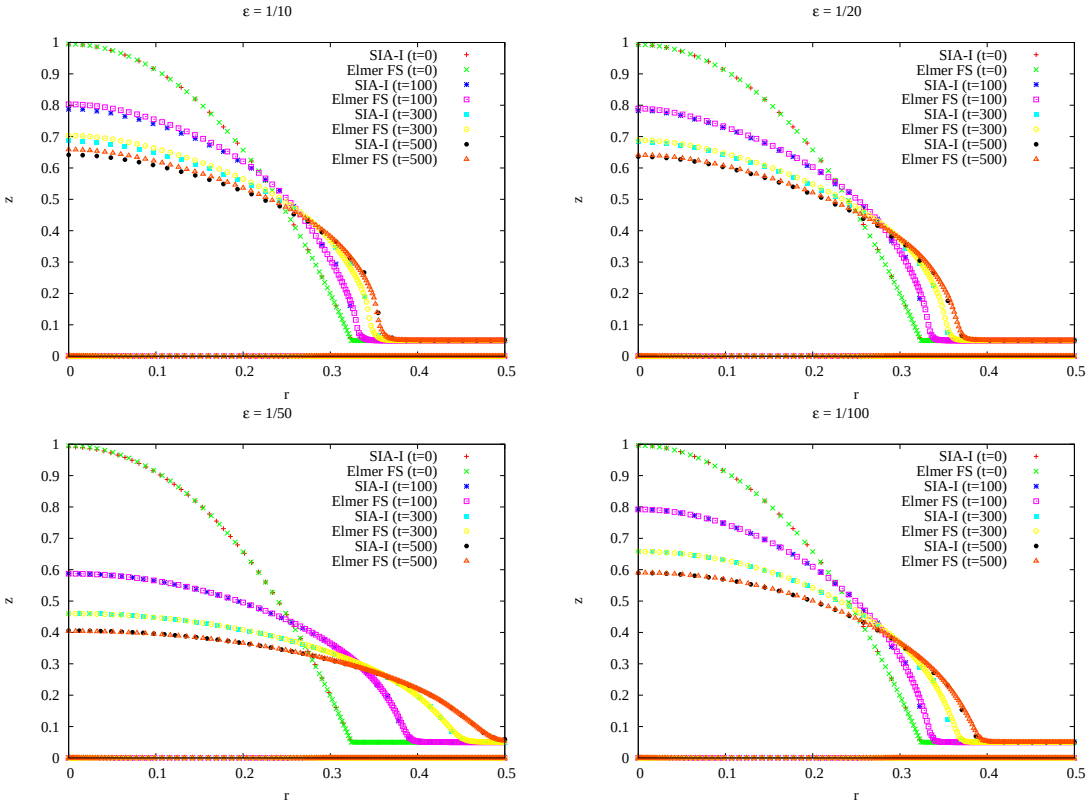

Figure 4.13: A comparison of the free surface profiles obtained by the FEM code Elmer for the full-Stokes model and by our SIA-I-based code, for several time snapshots and four aspect ratios.

the aspect ratios, and are $\Delta t = 0.1$ a, and $\Delta t = 1$ a, for $\epsilon = \frac{1}{10}$, and $\epsilon = \frac{1}{20}$, respectively, and $\Delta t = 100a$, for $\epsilon = \frac{1}{50}$ and $\epsilon = \frac{1}{100}$. A very satisfactory agreement between the finite-element full-Stokes computation and our results is observed even for the large aspect ratio of $\epsilon = \frac{1}{10}$.

4.5 Heat-transport equation

If a more realistic case is to be considered, the effect of thermo-mechanical coupling for ice flow cannot be neglected, because of a strongly temperature-dependent viscosity via the temperature rate-factor $\mathcal{A}(T)$, see (1.21). It is therefore necessary to involve the heat-transport equation (1.28) into our model. For the cold-ice model, we implement the shallow-ice version of the heat-transport equation, which, in Cartesian coordinates, is given by (2.140). Rewriting this equation in stretched coordinates (Appendix C), we arrive

at

$$\hat{c}_v \left(\tilde{\mathcal{H}}^2 \frac{\partial \hat{T}}{\partial \tilde{t}} - \tilde{\mathcal{H}} \frac{\partial \hat{T}}{\partial \xi} \left(\hat{v}_x a_x \tilde{\mathcal{H}} + \hat{v}_y a_y \tilde{\mathcal{H}} - \hat{v}_z + a_t \tilde{\mathcal{H}} \right) + \tilde{\mathcal{H}}^2 \left(\hat{v}_x \frac{\partial \hat{T}}{\partial \tilde{x}} + \hat{v}_y \frac{\partial \hat{T}}{\partial \tilde{y}} \right) \right)$$

$$- \quad \mathcal{D} \frac{\partial}{\partial \xi} \left(\hat{k} \frac{\partial \hat{T}}{\partial \xi} \right) = 2\mathcal{C} \tilde{\mathcal{H}}^2 (\hat{\boldsymbol{\sigma}}_{xz} \hat{\boldsymbol{d}}_{xz} + \hat{\boldsymbol{\sigma}}_{yz} \hat{\boldsymbol{d}}_{yz}) \, . \tag{4.70}$$

This equation is discretised by a semi-implicit way. The implicit scheme is chosen for the vertical derivatives, all the remaining terms are discretised explicitly in time. This approach results in a tri-diagonal system of equations for each (i, j):

$$\hat{T}^{n+1}_{i,j,k+1} \left(\frac{\alpha^n_{i,j,k} \Delta \tilde{t}}{2\Delta\xi} + \frac{\beta^n_{i,j,k} \hat{k}^n_{i,j,k+\frac{1}{2}} \Delta \tilde{t}}{(\Delta\xi)^2} \right) + \hat{T}^{n+1}_{i,j,k} \left((\tilde{\mathcal{H}}^n_{i,j})^2 - \frac{\beta^n_{i,j,k} (\hat{k}^n_{i,j,k+\frac{1}{2}} + \hat{k}^n_{i,j,k-\frac{1}{2}}) \Delta \tilde{t}}{(\Delta\xi)^2} \right)$$

$$+ \quad \hat{T}^{n+1}_{i,j,k-1} \left(-\frac{\alpha^n_{i,j,k} \Delta \tilde{t}}{2\Delta\xi} + \frac{\beta^n_{i,j,k} \hat{k}^n_{i,j,k-\frac{1}{2}} \Delta \tilde{t}}{(\Delta\xi)^2} \right) = (\tilde{\mathcal{H}}^n_{i,j})^2 \hat{T}^n_{i,j,k} + \gamma^n_{i,j,k} \Delta \tilde{t} \, , \tag{4.71}$$

where

$$\alpha^n_{i,j,k} := \tilde{\mathcal{H}}^n_{i,j} \left(-(\hat{v}_x a_x \tilde{\mathcal{H}})^n_{i,j,k} - (\hat{v}_y a_y \tilde{\mathcal{H}})^n_{i,j,k} + \hat{v}^n_{z\ i,j,k} - (a_t \tilde{\mathcal{H}})^n_{i,j,k} \right) \, , \tag{4.72}$$

$$\beta^n_{i,j,k} := -\frac{\mathcal{D}}{\hat{c}^n_{v\ i,j,k}} \, , \tag{4.73}$$

$$\gamma^n_{i,j,k} := -\left(\tilde{\mathcal{H}}^n_{i,j} \right)^2 \left(\hat{v}^n_{x\ i,j,k} \frac{\hat{T}^n_{i+1,j,k} - \hat{T}^n_{i-1,j,k}}{2\Delta\tilde{x}} + \hat{v}^n_{y\ i,j,k} \frac{\hat{T}^n_{i,j+1,k} - \hat{T}^n_{i,j-1,k}}{2\Delta\tilde{y}} \right)$$

$$+ \quad \frac{\mathcal{C} \tilde{\mathcal{H}}^n_{i,j}}{\hat{c}^n_{v\ i,j,k}} \left(\hat{\boldsymbol{\sigma}}^n_{xz\ i,j,k} \frac{\hat{v}^n_{x\ i,j,k+1} - \hat{v}^n_{x\ i,j,k-1}}{2\Delta\xi} + \hat{\boldsymbol{\sigma}}^n_{yz\ i,j,k} \frac{\hat{v}^n_{y\ i,j,k+1} - \hat{v}^n_{y\ i,j,k-1}}{2\Delta\xi} \right) \, , \tag{4.74}$$

and

$$(a_x \tilde{\mathcal{H}})^n_{i,j,k} = \frac{\tilde{f}^n_{b\ i+1,j} - \tilde{f}^n_{b\ i-1,j}}{2\Delta x} + \xi_k \frac{\tilde{\mathcal{H}}^n_{i+1,j} - \tilde{\mathcal{H}}^n_{i-1,j}}{2\Delta x} \, , \tag{4.75}$$

$$(a_y \tilde{\mathcal{H}})^n_{i,j,k} = \frac{\tilde{f}^n_{b\ i,j+1} - \tilde{f}^n_{b\ i,j-1}}{2\Delta y} + \xi_k \frac{\tilde{\mathcal{H}}^n_{i,j+1} - \tilde{\mathcal{H}}^n_{i,j-1}}{2\Delta y} \, , \tag{4.76}$$

$$(a_t \tilde{\mathcal{H}})^n_{i,j,k} = \frac{\tilde{f}^n_{b\ i,j} - \tilde{f}^{n-1}_{b\ i,j}}{\Delta \tilde{t}} + \xi_k \frac{\tilde{\mathcal{H}}^n_{i,j} - \tilde{\mathcal{H}}^{n-1}_{i,j}}{\Delta \tilde{t}} \, . \tag{4.77}$$

At the upper free surface, temperature is prescribed as a boundary condition:

$$\hat{T}^{n+1}_{i,j,N_3} = \hat{T}^{s\ n+1}_{i,j} \, , \tag{4.78}$$

while at the base, the energy condition (2.208) is considered, which, for no basal melting ($\hat{m}^b_w = 0$), is discretised as follows

$$\hat{T}^{n+1}_{i,j,2} - \hat{T}^{n+1}_{i,j,1} = -\frac{\mathcal{H}^n_{i,j} \Delta\xi}{\hat{k}^n_{i,j,1}} \left(\hat{q}^{geo}_{i,j} + \frac{\mathcal{C}}{\mathcal{D}} (\hat{\boldsymbol{\sigma}}_{xz} \hat{v}^{sl}_x + \hat{\boldsymbol{\sigma}}_{yz} \hat{v}^{sl}_y)_{i,j,1} \right) \, . \tag{4.79}$$

The resultant set of tri-diagonal systems is solved by the **tridag** routine from Press (1992).

Table 4.1: Values of physical parameters.

Symbol	Constant	Value	Units
ρ	Ice density	910	$\mathrm{kg\,m^{-3}}$
g	Gravitational acceleration	9.81	$\mathrm{m\,s^{-2}}$
q^{geo}	Geothermal heat flux	4.2×10^{-2}	$\mathrm{W\,m^{-2}}$
C_{Cl}	Pressure dependence of melting temperature	9.7008×10^{-8}	$\mathrm{K\,Pa^{-1}}$
c_v	Specific heat capacity of ice	2009	$\mathrm{J\,kg^{-1}\,K^{-1}}$
k	Thermal conductivity of ice	2.1	$\mathrm{W\,m^{-1}\,K^{-1}}$

4.6 EISMINT benchmarks - effects of thermomechanical coupling

The performance of the heat-equation solver was checked in the comparison with the EISMINT benchmark experiments which contains examples for testing the thermo-mechanical coupling in ice-flow problem. In all numerical experiments, two prognostic equations are solved: (i) The heat-transport equation, and (ii) the free-surface evolution resulting from ice deformation and surface accumulation and ablation. The nonlinear rheology of ice is given by Glen's flow law (1.17) with the rate factor of the dependence (1.22). Ice is assumed to be cold, i.e. its temperature is not allowed to exceed the pressure melting point (1.48). For all numerical experiments, the accumulation-ablation function and the surface temperature are prescribed at the free-surface. At the glacier base, the no-slip boundary condition for velocity is assumed and a constant geothermal heat flux is specified. No melting is taken into account, neither at the base, nor inside the glacier. The constants and parameters used are prescribed in Table 4.1. The surface accumulation–ablation function $\frac{a^s}{\rho}$ is given as a function of position (in $\mathrm{m\ a^{-1}}$) as

$$\frac{a^s}{\rho} := \min[M_{max}, S_b(R_{el} - \sqrt{(x - x_{summit})^2 + (y - y_{summit})^2})] \,, \tag{4.80}$$

where M_{max} is the maximal accumulation rate and S_b is the gradient of the accumulation-ablation function with respect to the distance from the glacier's summit. The accumulation-ablation function is positive in the circle with the origin at (x_{summit}, y_{summit}) and radius R_{el} and it is negative outside this circle.

The surface temperature (in K) is parametrized as

$$T^s := T_{min} + S_T \sqrt{(x - x_{summit})^2 + (y - y_{summit})^2} \,, \tag{4.81}$$

where T_{min} is the minimal surface air temperature and S_T is the gradient of surface air temperature with horizontal distance.

The model domain is a square $1500\mathrm{km} \times 1500\mathrm{km}$ with the summit located at $(x_{summit}, y_{summit}) = (750\ \mathrm{km}, 750\ \mathrm{km})$. The model resolution of $25\,\mathrm{km}$ is prescribed in both horizontal directions, i.e. 61×61 grid points in the horizontal plane and 61 layers in vertical. The bedrock is flat, meaning that the effect of isostasy is not considered. As all the models in the intercomparison are Shallow-Ice models, we perform only the first iteration of the SIA-I algorithm, resulting in the solution in the Shallow-Ice Approximation.

- **EISMINT experiment A.**
  In this experiment, an equilibrium shape is sought, if we start from initially ice-free conditions on a

flat bedrock topography with the climatic forcing described by

$$\begin{aligned} M_{max} &= 0.5\,\mathrm{m\,a^{-1}}\,, \\ S_b &= 10^{-2}\,\mathrm{m\,a^{-1}\,km^{-1}}\,, \\ R_{el} &= 450\,\mathrm{km}\,, \\ T_{min} &= 238.15\,\mathrm{K}\,, \\ S_T &= 1.67\times10^{-2}\,\mathrm{K\,km^{-1}}\,. \end{aligned}$$

The temperature dependence of the rheology (1.22) is specified by

$$A = \begin{cases} 3.61\times10^{-13}\,\mathrm{Pa^{-3}\,s^{-1}} & \text{if } T^\star < 263.15\,\mathrm{K} \\ 1.73\times10^{3}\,\mathrm{Pa^{-3}\,s^{-1}} & \text{if } T^\star \geq 263.15\,\mathrm{K} \end{cases}, \tag{4.82}$$

$$Q = \begin{cases} 6.0\times10^{4}\,\mathrm{J\,mol^{-1}} & \text{if } T^\star < 263.15\,\mathrm{K} \\ 13.9\times10^{4}\,\mathrm{J\,mol^{-1}} & \text{if } T^\star \geq 263.15\,\mathrm{K} \end{cases}, \tag{4.83}$$

where $T^\star$ is the absolute temperature corrected for the pressure melting point: $T^\star := T + C_{Clp}$.

The climatic forcing, that is the surface temperature and accumulation-ablation function, are depicted in Fig. 4.14, where the resultant basal temperature and ice sheet geometry are also displayed. The steady-state temperature and velocity field are visualized in Fig. 4.15.

We compare our model output with the published results of the EISMINT benchmark (Payne et al., 2000). The compared quantities are the final volume of the ice sheet, the glaciated area, the fraction of glaciated area with the basal temperature at the pressure-melting point, the maximal ice thickness (at the ice-divide), and the ice-divide basal temperature. The published 10 numerical models differ quite substantially in several parameters (mainly in the melt-fraction). We therefore show both the mean value and the range of each output parameter. The results are summarized in Table 4.2. We may observe a good agreement in the total volume of the steady-state glacier and the glaciated area, which can be explained by the fact that the glacier is well constrained by the accumulation-ablation function, and also the ice-thickness at the divide. A good agreement is also obtained for the basal temperature at the ice divide. Quite different is, however, our result for the fraction of the glacier bed with the temperature at the pressure-melting point. In fact, our result is just within the edge of the interval of published solutions. Note, however, that there is a large variability in this parameter between all other models, since the range is equal to 40% of the mean value.

- **EISMINT experiment B.**
  This experiment is initiated from the steady-state solution (obtained after 200 ky) of experiment A and applies an altered temperature condition:

$$T_{min} = 243.15\,\mathrm{K}\,, \tag{4.84}$$

  i.e. the surface temperature undergoes a 5 K warming, while all the remaining parameters are kept fixed as in exp A. A new steady-state solution is found, and a change in volume, basal melting fraction, divide thickness and divide basal temperature is evaluated and given in Table 4.3. We see again a satisfactory agreement to a sudden surface warming model response between our and the EISMINT result.

- **EISMINT experiment C.**
  In this experiment, the effect of accumulation and ablation is inspected. Starting from the steady-state

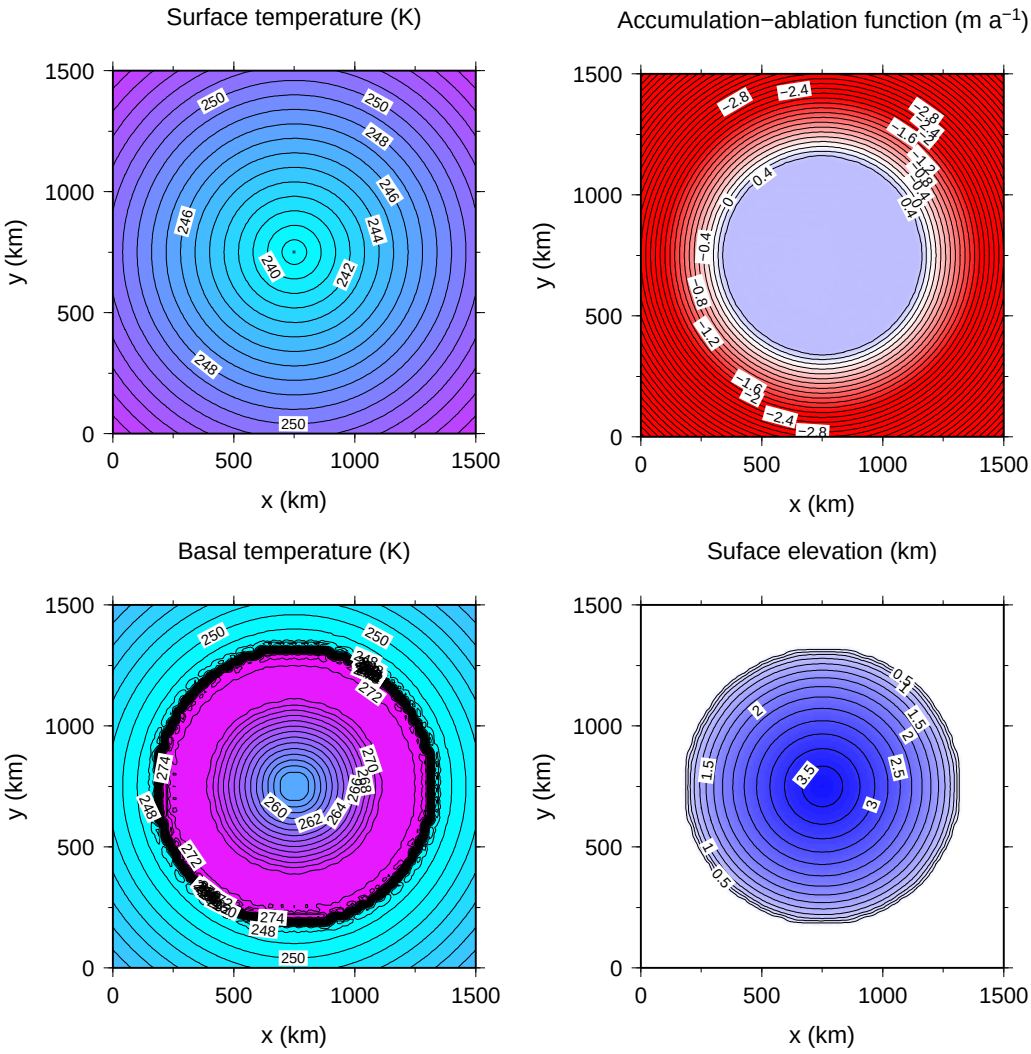

Figure 4.14: Upper row: Surface temperature (left) and accumulation-ablation function (right), Bottom row: Resultant steady-state basal temperature (left) and ice sheet surface elevation (right).

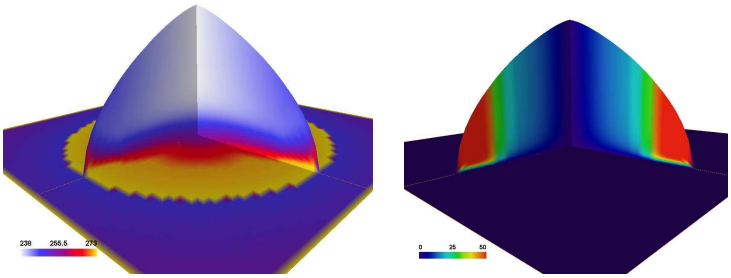

Figure 4.15: Temperature (K) (left) and magnitude of velocity ($\mathrm{m\ a^{-1}}$) (right) in the steady-state solution of EISMINT experiment A.

Table 4.2: EISMINT exp. A results.

Quantity	Our result	EISMINT mean	EISMINT range
Ice volume ($10^6\,\mathrm{km}^3$)	2.074	2.128	0.145
Glaciated area ($10^6\,\mathrm{km}^2$)	1.031	1.034	0.086
Melt fraction	0.582	0.718	0.290
Divide thickness (m)	3710.386	3688.342	96.740
Divide basal temperature (K)	254.538	255.605	2.929

Table 4.3: Differences between exp B and exp A.

Quantity	Our result	EISMINT mean	EISMINT range
Ice volume change (%)	−2.956	−2.589	1.002
Melt fraction change (%)	12.614	11.836	18.669
Divide thickness change (%)	−5.457	−4.927	1.316
Divide basal temperature change (K)	4.587	4.623	0.518

Table 4.4: Differences between exp C and exp A.

Quantity	Our result	EISMINT mean	EISMINT range
Ice volume change (%)	−27.884	−28.505	1.204
Glaciated area change (%)	−20.376	−19.515	3.554
Melt fraction change (%)	−21.964	−27.806	31.371
Divide thickness change (%)	−12.678	−12.928	1.501
Divide basal temperature change (K)	3.680	3.707	0.615

Table 4.5: Differences between exp D and exp A.

Quantity	Our result	EISMINT mean	EISMINT range
Ice volume change (%)	−11.943	−12.085	1.236
Glaciated area change (%)	−10.188	−9.489	3.260
Melt fraction change (%)	−2.309	−1.613	5.745
Divide thickness change (%)	−2.049	−2.181	0.532
Divide basal temperature change (K)	−0.179	−0.188	0.060

solution of experiment A, the boundary conditions are altered as follows:

$$\begin{aligned} M_{max} &= 0.25\ \mathrm{m\ a}^{-1}\ , \\ R_{el} &= 425\ \mathrm{km}\ , \end{aligned}$$

but the other parameters the same as in experiment A. The equilibrium changes of volume, area, melt-fraction, divide thickness and divide basal temperature are given in Table 4.4. A very good agreement can be seen in all the quantities, a difference can be observed for the melt-fraction change, for which, however, the range in EISMINT results is huge.

- **EISMINT experiment D.**
  In the last EISMINT experiment the altered boundary condition

$$R_{el} = 425 \text{ km} ,$$

  is applied to the final steady-state solution of experiment A, while all other parameters are kept unaltered. The changes of steady-state characteristics of the glacier as the reaction to this reduction of accumulation area are summarized in Table 4.4. We may observe that, all parameters agree satisfactorily with the EISMINT mean. The melt-fraction change for the EISMINT solutions shows again a great variability, including the change in sign. Payne et al. (2000) concluded, that there is no clear pattern in change of this parameter.

We may say that our model is able to reproduce the results of the EISMINT benchmarks with a sufficient accuracy, and conclude that the implementation of the heat-transport equation and the thermo-mechanical coupling in our model performs correctly.

4.7 Summary

In this section we have extended our model for a transient case by implementing the evolution equation for the free surface. Two approaches were presented. A time-explicit approach for free-surface evolution equation is based on expressing the spatial gradient of the free-surface function by the ENO schemes. Such an explicit discretization does not, for a sufficiently small time step, suffer from numerical oscillations, which is crucial when either the SIA or the SIA-I technique is employed to compute the velocity field. A level-set function technique was implemented for tracking the ice-sheet margin, being able to capture complex changes in the ice-margin shape and topology.

The second approach was time-implicit. By introducing auxiliary diffusivities, we arrived at the ”SIA-like” discretization of the free-surface evolution equation, possessing for the SIA-I approach much better numerical properties than the original transport equation.

Both approaches were tested in a series of numerical experiments. In particular, we performed the prognostic ISMIP-HOM experiment F with a satisfactory result both in terms of the accuracy and numerical effectiveness. To demonstrate the performance of our model, we also extended the experiment for non-liner rheology following Glen’s flow law, which is in contrast to the original setting, where only a linear, Newtonian, model was used in order to reduce the computational demands. By comparing the SIA-I velocity field with the corresponding FEM full-Stokes velocity solution by Elmer for several time snapshots, we have shown that the SIA-I based model is able to successfully perform the prognostic run even for the non-linear rheology.

The third experiment involved also a FEM simulation by Elmer and compared the SIA-I and full-Stokes solution for an axisymmetric ice-cap spreading under its own weight. A good match in the accuracy of the SIA-I solution was again observed.

Finally, the heat-transport equation was implemented in the stretched coordinates, allowing us to compute also the evolution of temperature field. The effect of thermo-mechanical coupling was evaluated in a series of the EISMINT benchmarks. The results indicate that the implementation of the heat-transport equation into the numerical model for ice flow has been successful.

Chapter 5

Greenland Ice Sheet simulation

In this chapter, we apply our numerical model to a realistic simulation. Inspired by the EISMINT intercomparison, in particular by the EISMINT Greenland models benchmark, we will run three different simulations. First, a steady state of the Greenland Ice Sheet (GIS) is sought if the present-day climatic forcing is kept constant during a transient response of the model. The second simulation aims at reconstructing the Greenland Ice Sheet behavior during last 250 thousand years, i.e. approximately two glacial cycles. The third simulation is a prognostic experiment of modeling a short term (500 years) response of the GIS to a prescribed warming forcing. All experiments will now be described in full detail.

5.1 Steady-state Greenland Ice Sheet simulation

We perform the EISMINT Greenland Ice Sheet steady-state experiment as described by Huybrechts (1998). The summary of this experimental setup is as follows. The bedrock and surface topography of the Greenland region is given by a data set compiled by Anne Letreguilly (Letreguilly, 1991). We choose a variant with a 20 km spatial resolution. The accumulation rates on the same grid are provided for the EISMINT experiment by Huybrechts (1998), who compiled data from Ohmura & Reeh (1991). The employed parametrization is described as follows.

- Mean annual temperature (in $^\circ$ Celsius)

$$T_a = 49.13 - 0.007992 \cdot \mathrm{Z} - 0.7576 \cdot \mathrm{latitude}\ , \tag{5.1}$$

  with

$$Z := \max(\mathrm{surface\ elevation}, 20 \cdot (\mathrm{latitude} - 65)), \tag{5.2}$$

- Summer temperature (in $^\circ$ Celsius)

$$T_s = 30.38 - 0.006277 \cdot \mathrm{surface\ elevation} - 0.3262 \cdot \mathrm{latitude}\ . \tag{5.3}$$

- Standard deviation of the daily temperature $\sigma_T = 5^\circ\mathrm{C}$.

- The ice rheological law is given by Glen's flow law (1.17) with parameters A and Q taken as

$$A = \begin{cases} 10.83 \times 10^{-13}\ \mathrm{Pa}^{-3}\ \mathrm{s}^{-1} & \text{if } T^\star < 263.15\ \mathrm{K} \\ 5.19 \times 10^{3}\ \mathrm{Pa}^{-3}\ \mathrm{s}^{-1} & \text{if } T^\star \geq 263.15\ \mathrm{K} \end{cases}, \tag{5.4}$$

$$Q = \begin{cases} 6.0 \times 10^4 \text{ J mol}^{-1} & \text{if } T^\star < 263.15 \text{ K} \\ 13.9 \times 10^4 \text{ J mol}^{-1} & \text{if } T^\star \geq 263.15 \text{ K} \end{cases} . \tag{5.5}$$

This setting corresponds to the parameters in the EISMINT experiments from the previous chapter (4.82), (4.83), but with the right-hand side of (1.17) multiplied by an enhancement factor $m_{enh} = 3$. Other physical parameters are taken as in Table 4.1, except for the geothermal heat flux, which is now prescribed by a higher value of $q^{geo} = 5 \times 10^{-2} \text{ W m}^{-2}$.

- The ablation is parametrized by the positive degree-day method (van der Veen, 2007), which can be briefly summarized as follows. Given the surface mean annual and summer temperatures T_a and T_s by (5.1) and (5.3), respectively, a cosine annual cycle for surface temperature is assumed, which is, in addition, perturbed by random Gaussian noise ψ with the prescribed standard deviation σ_T, and zero mean

$$T_{surf}(t) = T_a + (T_s - T_a)\cos(2\pi t) \ + \psi \ . \tag{5.6}$$

The ablation during an M-day period $\{t_i\}_{i=1}^M$ is then parametrized by

$$abl = k_{abl} \cdot \sum_{i=1}^{M} \mathrm{H}(T_{surf}(t_i)) T_{surf}(t_i), \tag{5.7}$$

where

$$\mathrm{H}(T) = \begin{cases} 1 & \text{if } T \geq 0^\circ \text{ C} \\ 0 & \text{if } T < 0^\circ \text{ C} \end{cases} , \tag{5.8}$$

and the constant k_{abl} in (5.7) is chosen as

$$k_{abl} = \begin{cases} 8.0 \text{ mm d}^{-1} \, ^\circ\text{C}^{-1} & \text{for ice} \\ 3.0 \text{ mm d}^{-1} \, ^\circ\text{C}^{-1} & \text{for snow} \end{cases} , \tag{5.9}$$

since the albedo is, in general, higher for snow than for ice. The melt-rate is computed according to the snow and ice model of Reeh (1991), where, in the first moment, all accumulation is assumed to be in the form of snowfall. When surface melting occurs, the snow layer is first melted with the meltwater refreezing again to a form of the super-imposed ice, until its amount exceeds 60% of the annual snowpack. From that moment on, all meltwater is assumed to leave the glacier as runoff. The same scenario holds for the meltwater from melted glacier ice.

The initial geometry of the Greenland Ice Sheet and the initial accumulation-ablation function are depicted in Fig. 5.1 (top). Assuming the problem possesses a unique steady-state solution for the given climatic forcing, we have a freedom in the choice of the initial temperature. We chose a simple downward continuation of the surface temperature field. The model was run for 150 thousand years, with a time step of 5 years, which was sufficiently long to reach the steady-state, as seen from Fig. 5.2, where the ice volume and glaciated are shown. In Fig. 5.1, we display the final steady-state geometry of the GIS (bottom left) and the difference between the steady-state and the initial geometry (bottom right).

We see that the effect of present climatic forcing mainly influences the coastal regions, where the extent of the GIS is increased. On the other hand, the topography of the Greenland's interior does not change much and slightly decreases the maximum ice thickness.

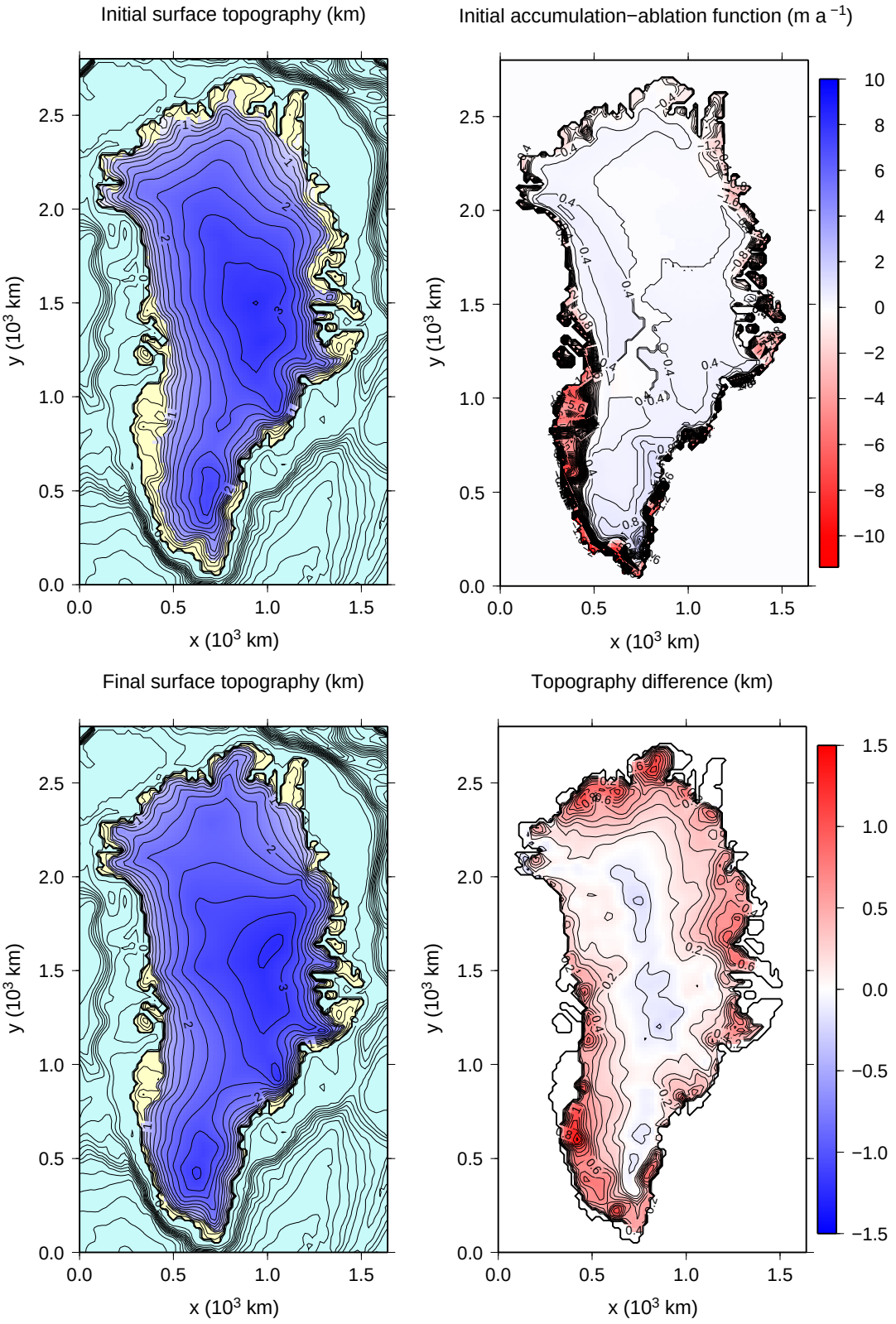

Figure 5.1: The initial (present-day) surface topography of the GIS (top left, dark blue=ice, yellow=ground, light blue = ocean), and the initial accumulation-ablation function (top right). The bottom panel shows the result of the steady-state simulation after 150 thousand years, namely the final topography (bottom left) and the difference between the steady-state and the initial topography (bottom right).

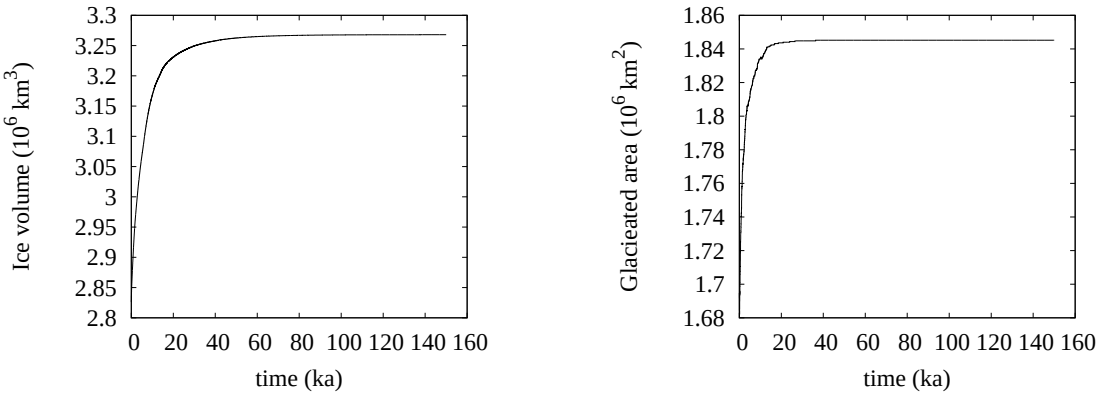

Figure 5.2: The evolution of the GIS volume and glaciated area during the steady-state simulation (see also Fig. 5.1).

5.2 Climatic cycle experiment

This simulation starts from the steady-state obtained by the first experiment. A climatic forcing for a period of approximately 250 thousand years is imposed, consisting of temperature and sea-level contributions. The temperature changes are derived from the $\delta^{18}O$ content of the GRIP ice core (Dansgaard et al., 1993) by the simple conversion

$$\Delta T\ (\mathrm{K}) = 1.5(\delta^{18}O + 35.27)\ . \tag{5.10}$$

Sea-level change constrains the maximal extent of the ice sheet, because immediate calving is assumed whenever the ice sheet reaches the ocean (i.e. no ice-shelf formation is considered). It is again correlated directly to the $\delta^{18}O$ content by the formula (Imbrie et al., 1982)

$$\Delta\mathrm{Sea\ level}\ (\mathrm{m}) = -34.83(\delta^{18}O + 1.93)\ . \tag{5.11}$$

Both the forcing data-sets are shown in the top row of Fig. 5.3, while the bottom panels show the evolution of areal extent and volume of the GIS, computed with the time step of 5 years. Fig. 5.4 reprints the result of the benchmark published in Huybrechts (1998), where, however, the modelers had more freedom in their model setup choice and thus their results are not perfectly comparable. In Fig. 5.5, we display the surface topography for several snapshots during the last glacial cycle, i.e since approximately 150 thousand years ago, to the present, showing the quite substantial reduction in the GIS extent approximately 125 thousand years ago, which is followed by gradual regrowth of the Greenland Ice Sheet towards the present state - see bottom row in Fig.5.5.

The previous glacial cycle, that is period from 250 k – 150 k years ago is excluded from the benchmark because of lower accuracy of the climatical forcing data.

We may state that our results are in satisfactory agreement with other solutions. A similarity among all other model outputs is mainly a consequence of the fact that the surface mass balance, rather than the ice dynamics, plays the major role in controlling large-scale characteristics such as the ice sheet's volume or its extent. Using the same or similar parametrizations of the surface mass balance therefore leads to the same or at least quite similar behavior of the models in terms of these control variables. On the other hand, when the details in topography are compared, significant differences occur between the various models (see Huybrechts, 1998).

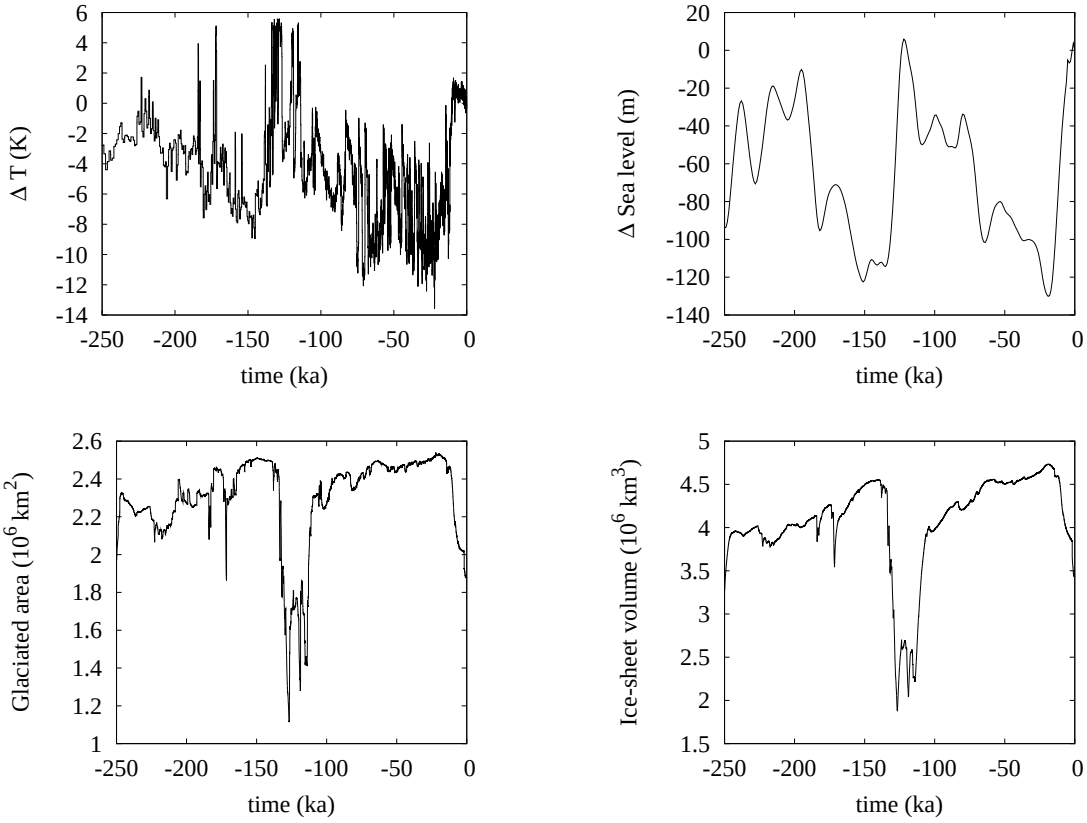

Figure 5.3: Temperature (top left) and sea-level (top right) forcing of the climatic cycle experiment and the evolution of the GIS areal extent (bottom left) and volume (bottom right).

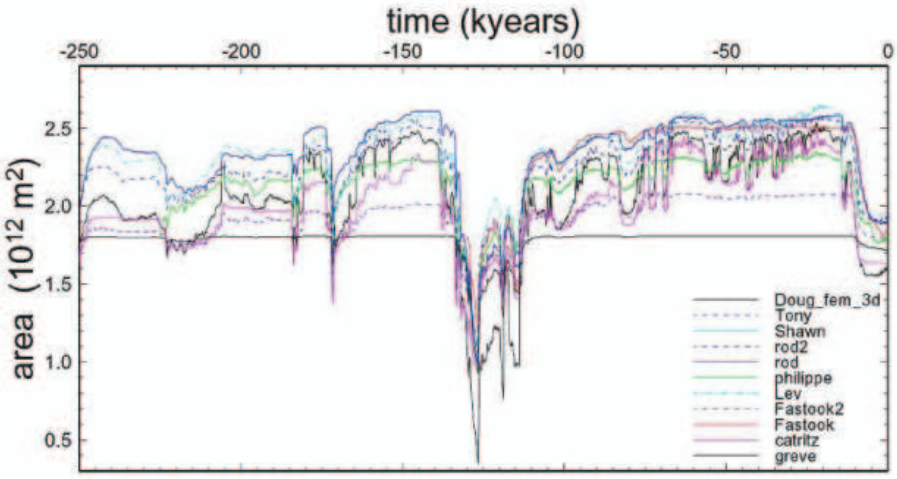

Figure 5.4: The evolution of glaciated area in the climatic experiment, reprinted figure from Huybrechts (1998). The differences in results are partially due to a not-entirely unique set up of the benchmark. Compare with our solution in Fig. 5.3 (bottom left panel).

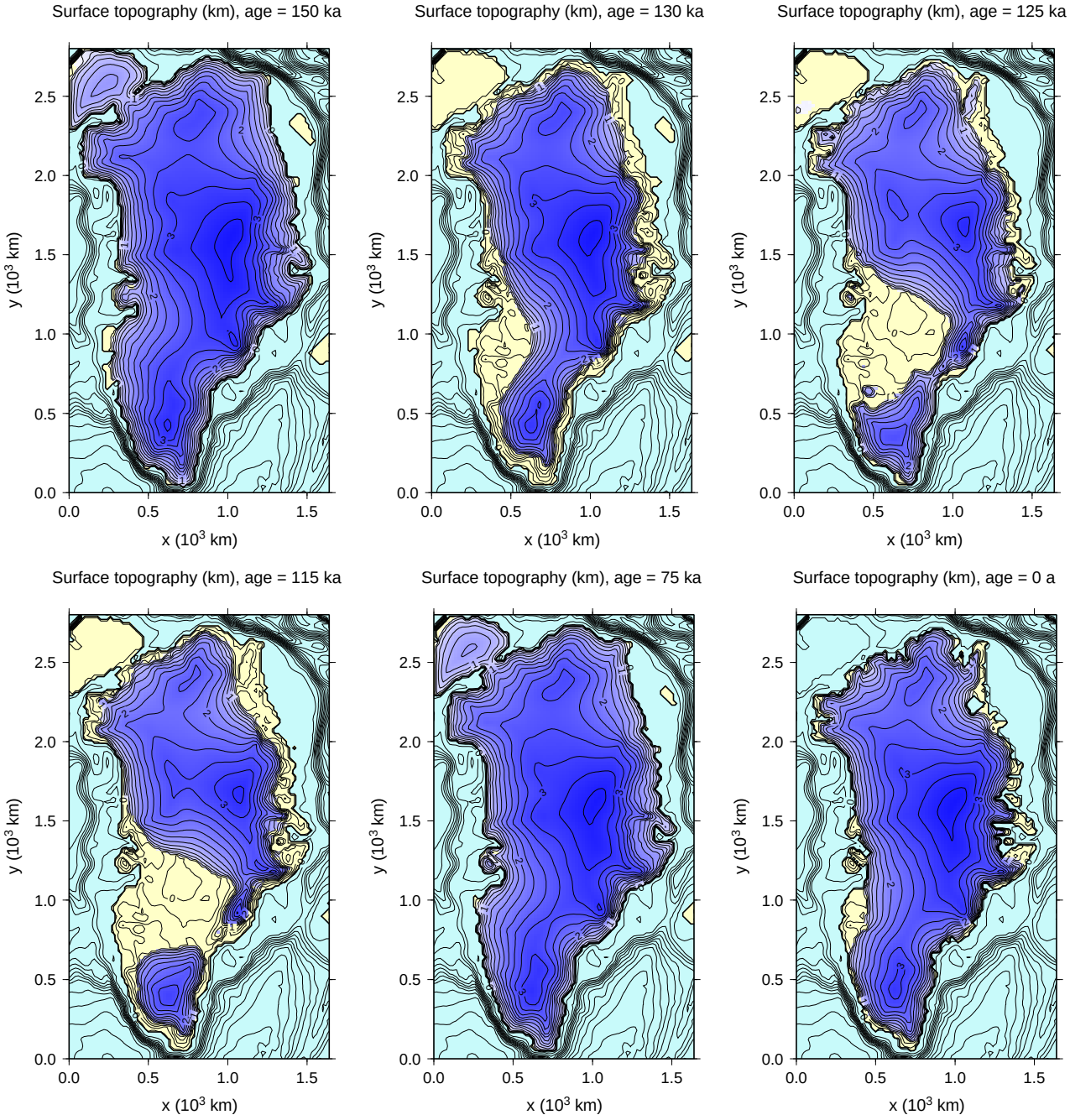

Figure 5.5: Several snapshots of the evolution of our model topography for the climatic cycle experiment, covering approximately the last 150 thousand years.

5.3 Greenhouse warming scenario

This experiment aims at evaluating the effect of one of the possible greenhouse-warming scenarios on the GIS. On the contrary to the EISMINT benchmark setting, where the final state of the climatic simulation is used as input, our simulation is started from the steady-state result of the first simulation (steady-state scenario). We prefer this choice, as the sea-level and topography data are closer to the actual state of the GIS, and thus the outputs are to be of higher relevance.

The model is run for 500 years into the future, with the climatic forcing based solely on surface temperature increase. Hence, no sea-level forcing is considered. The surface temperature is increased annually by 0.035° C for the first 80 years (total 2.8° C increase) and then by 0.0017° C for the remaining 420 years (0.714° C), resulting in a total temperature increase of 3.514° C after 500 years. This model temperature forcing is based on the proposed scenario by Manabe & Stouffer (1994).

The initial and final topography, the topography difference and the evolution of the glaciated area and ice volume are depicted in Fig. 5.6. The reduction of the GIS volume is approximately by 0.135×10^6 km^3.

5.4 Summary

In this chapter, we have presented the output of our numerical model for three runs based on the benchmark setting for European Ice Sheet Model INiTiative (EISMINT) - Greenland Ice Sheet Models. The first one is a steady-state simulation initiated from the present-day topography and climatic conditions for the Greenland Ice-Sheet, and an arbitrarily prescribed initial temperature. A transient simulation was run until a steady-state was reached. The steady-state and present-day topographies differ only slightly in the interior of the ice-sheet, more pronounced differences appear in the vicinity of the ice-sheet margin, where the extent of the steady-state GIS is systematically larger than the extent of the present-day GIS.

In the second simulation, the present-day topography is subject to a climatic and sea-level forcing based on the ice-core reconstruction of the past climate over the last two glacial cycles. The glacial-isostatic adjustment is not taken into account in order to restrict the modelled physical processes only to the response to climatic and sea-level forcing. The reconstructed GIS history shows a clear minimum in the total volume and areal extent approximately 125 thousand years ago, which was then followed by a slow regrowth and finally deglaciation to the present-day state.

The third simulation is prognostic and applies a simply-parametrized global-warming scenario to the steady-state shape of the GIS resulting from the first, steady-state, simulation. We evaluate the changes in the areal extent and volume and observe an enhanced melting confined mostly to the south margin areas of the GIS.

The EISMINT benchmarks have proved a good applicability of our model for long-term large-scale GIS modeling. To make the paleoclimatic simulations however more realistic, it remains to implement the glacio-isostatic adjustment of the Earth, that is, the visco-elastic response of the lithosphere and upper mantle to the glacial surface load. Although the effect of the ice-sheet evolution to the GIA is straightforward, with the ice-sheet evolution being the main driving force for the GIA, the converse is not true. The evaluation of the effect of the GIA on the GIS evolution is a more puzzling question, which remains to be answered by numerical modeling of the two processes, GIA and GIS evolution, simultaneously in a coupled model.

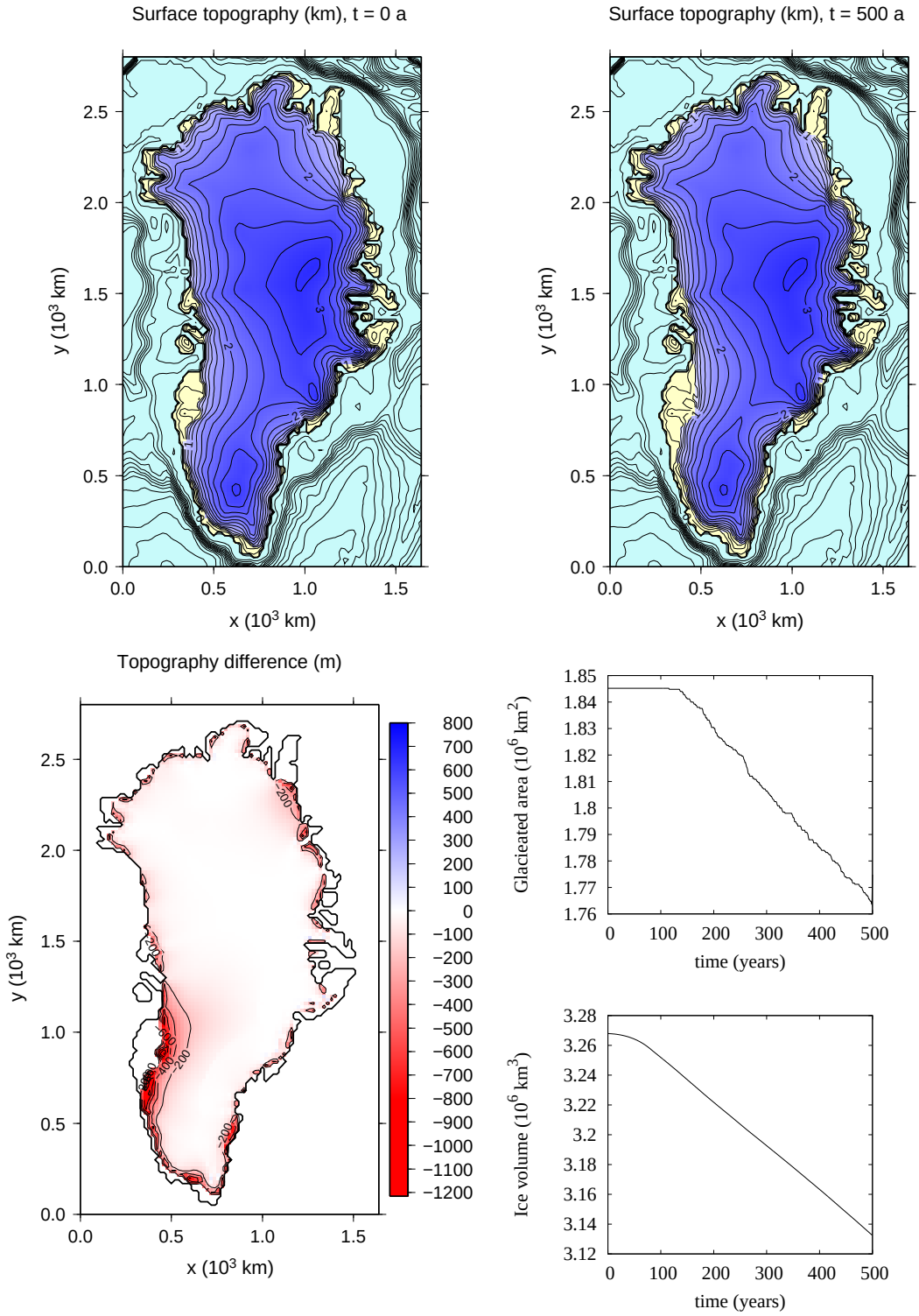

Figure 5.6: The initial surface topography of the GIS (top left), the final surface topography at $t = 500$ a (top right), the topography difference (bottom left) and the evolution of the glaciated area volume (bottom right) in the greenhouse-warming scenario.

Chapter 6

Concluding remarks

In this work, we have been dealing with several aspects of the large-scale numerical modeling of ice sheets, both from the theoretical and numerical perspective.

First in Chapter 1, we have formulated the equations that govern the time evolution of grounded ice sheets in a form that allows us to capture and incorporate liquid water and estimate the effects induced by its presence, such as an enhanced ice deformation, increased basal sliding caused by lubrication of the bedrock till, thermal effects connected with latent heat release, and so on. Based on the principles of rational mixture thermodynamics, in Chapter 2, we rederived the traditional Shallow-Ice Approximation, that is a scaling approximation which makes use of the fact that, in nature, the vertical-to-horizontal aspect ratio is often a small number. This fact allows a perturbation analysis in terms of this ratio. Our main contribution is that we have extended the SIA apparatus by considering general orthogonal curvilinear coordinates and obtained a whole class of shallow-ice approximations whose particular form depends on the chosen coordinate system, and may be easily specified by evaluating associated geometrical quantities.

We then, in Chapter 3, designed a novel computational algorithm denoted as SIA-I, which iteratively improves the ”shallow-ice” solution by including longitudinal stresses in a computationally effective way compared to other approaches. The convergence of the algorithm was investigated numerically but also theoretically, leading to the observation that the iterations converge the faster the ”shallower” the problem, that is the smaller the scaling parameter ϵ. Although we did not provide an exhaustive and rigorous mathematical analysis of the convergence properties of the SIA-I procedure, a number of numerical examples and tests have clearly demonstrated the applicability of the algorithm in practise. We proved, however, that if the procedure converges, the limiting solution satisfies the rheological equation exactly and results in errors in the first two momentum equations, that are of the order of ϵ^2 and can be evaluated explicitly.

We performed comprehensive numerical testing by the verification with other numerical methods such as finite-element, and by computing a number of benchmark examples. We participated in one of the recently designed benchmarks, the Ice-Sheet Model Intercomparison Project - Higher-Order Models (ISMIP-HOM), which was mainly oriented towards non-shallow, higher-order effects in glacier dynamics. This benchmark reported the very good performance of the SIA-I technique, both in accuracy and computational speed.

We also compared our model with a higher-order solution for the region of Dronning Maud Land in Antarctica, by (i) considering realistic topography for both the ice sheet surface and the underlying bedrock surface, (ii) the strongly non-homogeneous basal sliding conditions, and (iii) spatially varying temperature field. The comparison was very satisfactory, as the achieved accuracy was comparable with other higher-order models but the results were obtained with a substantially increased computational speed.

In Chapter 4, we finally developed a finite-difference thermo-mechanical evolutionary ice sheet numerical model based on the SIA-I algorithm, which models the evolution of ice sheet geometry due to the processes of internal deformation, described by a model of viscous non-Newtonian fluid, and due to surface processes such as accumulation, ablation and basal sliding. For most simple setups, with only one iteration of the SIA-I algorithm performed at each time step, this model gave similar results to other existing large-scale SIA models such as e.g. SICOPOLIS (http://sicopolis.greveweb.net/), or GRISLI (Ritz et al., 2001). With more than one iterations of the SIA-I algorithm, our model, however, provides (also locally if necessary) an improved solution to the ice-flow problem by capturing the higher-order dynamics by including the longitudinal stresses, which are neglected in the "shallow" approximation.

The performance of the code was tested in Chapter 5 for four of the European Ice-Sheet Modelling INiTiative (EISMINT) benchmarks that are focused on the effects of thermo-mechanical coupling within an ice sheet while considering the shallow-approximation, with the conclusion that our outputs are in a good agreement with the published results.

In Chapter 6, we finally carried out three benchmarks whose level of complexity fully corresponds to the original purpose of our model, that is, modeling long-term large-scale evolution of large ice sheets. Three EISMINT scenarios of the Greenland Ice Sheet with realistic topographical data, energy and mass fluxes were considered: a steady-state simulation, a paleoclimatic simulation for the period of last two glacial cycles and a 500 year prognostic simulation modeling the possible effects of a prescribed global-warming prognosis.

All numerical results show that we succeeded in developing an applicable numerical tool for simulating large-scale ice sheet evolution. Thanks to the computational effectiveness of the SIA-I approach, the code is capable of capturing also the "non-shallow", i.e. higher-order effects of the ice sheet dynamics.

Finally, we should remind ourselves the original motivation for the development of our code. A numerical model of ice sheet dynamics was meant to be coupled with an existing numerical model for the visco-elastic response of the Earth's lithosphere. By coupling the two models, a more consistent approach was to be achieved for the numerical modeling of glacial-isostatic adjustment, that is response of the Earth's lithosphere to time-dependent surface-load changes caused by the advance and retreat of the ice sheets during glacial cycles. Although this final goal has not yet been achieved, we will concentrate on the completion of such coupled model in the future. We believe that the amount of time and effort spent by testing the model, that is the subject of this work, was necessary and important, since the great complexity of the studied problem allows possible errors to remain unnoticed and contaminate any future outputs. Also, the fact that a novel algorithm for the Stokes problem for ice-flow was proposed, made all the testing inevitable to assess and evaluate its performance and applicability properly.

Appendix A

Convergence proof for the SIA-I algorithm with linear rheology and uniform viscosity

We have undertaken several attempts to provide a deeper mathematical analysis of the SIA-I iterative scheme. The main goal we were trying to reach was to prove a contractivity of the mapping induced by the SIA-I algorithm in some reasonable sense. While we were unsuccessful for the most general situation with non-linear ice rheology, certain basic insights could still be gained for rather simplified conditions, considering only the linear (Newtonian) rheology with uniform viscosity. Despite loosing much of the generality, we still find it interesting to investigate this case as it might provide a good starting point for further analysis.

Let us recall the whole iterative scheme and rewrite it for the purpose of this section in a slightly different manner. First let us observe that pressure $\tilde{p}$ serves in the whole procedure as an independent variable in the sense that it does not appear in formulae for deviatoric stress-tensor updates (3.48), (3.49) as for the first half-step, and nor in the rheology equations (3.22)-(3.29) used in the second half-step. We may therefore exclude it now from our considerations. In the SIA-I algorithm, the velocity components are computed from the deviatoric stress components according to (3.55)-(3.57), or (3.62), (3.63) and (3.59), which enables us to consider only five independent field variables $\tilde{\boldsymbol{\sigma}}_{xx}, \tilde{\boldsymbol{\sigma}}_{xy}, \tilde{\boldsymbol{\sigma}}_{yy}, \tilde{\boldsymbol{\sigma}}_{xz}, \tilde{\boldsymbol{\sigma}}_{yz}$. We arrange these deviatoric-stress components to a vector denoted $\vec{u}$ by

$$\vec{u} := (\tilde{\boldsymbol{\sigma}}_{xx}, \tilde{\boldsymbol{\sigma}}_{xy}, \tilde{\boldsymbol{\sigma}}_{yy}, \tilde{\boldsymbol{\sigma}}_{xz}, \tilde{\boldsymbol{\sigma}}_{yz}) \ . \tag{A.1}$$

One iteration of the SIA-I scheme will be represented by a mapping $\vec{T}$, that is

$$\vec{u}^{k+1} = \vec{T}(\vec{u}^k) \ . \tag{A.2}$$

Recalling (3.64), we may write

$$\vec{T}(\vec{u}^k) = (1-\theta_2)\vec{A}(\vec{u}^k) + \theta_2 \vec{B}(\vec{A}(\vec{u}^k)) \ , \tag{A.3}$$

where we introduced "formal" operators (the appropriate functional spaces will be defined later) $\vec{A}$ and $\vec{B}$ to capture the two half-steps of the iterative procedure. Operator $\vec{A}$ stands for the first half step, that is, according to (3.50),

$$\vec{A}(\vec{u}^k) := \vec{u}^{k+\frac{1}{2}} = \vec{u}^k + \theta_1 \delta \vec{u}^{k+\frac{1}{2}} \ . \tag{A.4}$$

While operator $\vec{B}$ expresses the update of the field according to rheology, that is, in the notation from (3.64),

$$\vec{B}(\vec{A}(\vec{u}^k)) = \vec{u}^{\star k+\frac{1}{2}} \ . \tag{A.5}$$

We confine ourselves to a single step of the SIA-I iteration, and for simplicity omit everywhere the superscripts k, $k+\frac{1}{2}$, $k+1$. Since we aim at demonstrating the contractivity of the mapping $\vec{T}$, we evaluate the difference $\vec{T}(\vec{u}) - \vec{T}(\vec{v})$ for two arbitrarily chosen (stress) vectors $\vec{u}$, $\vec{v}$.

First let us recall the definition of $\vec{A}$. Using (A.4), (3.48) and (3.49), together with (3.51), we can see that

$$
\begin{aligned}
A_1(\vec{u}) &= u_1 \,, && \text{(A.6)}\\
A_2(\vec{u}) &= u_2 \,, && \text{(A.7)}\\
A_3(\vec{u}) &= u_3 \,, && \text{(A.8)}\\
A_4(\vec{u}) &= (1-\theta_1)u_4 - \epsilon\theta_1 \frac{\partial \tilde{f}_s}{\partial \tilde{x}}(\tilde{f}_s - \tilde{z}) \\
&+ \epsilon\theta_1 \left(2\frac{\partial}{\partial \tilde{x}} \int_{\tilde{z}}^{\tilde{f}_s} u_1 \, d\tilde{z}' + \frac{\partial}{\partial \tilde{y}} \int_{\tilde{z}}^{\tilde{f}_s} u_2 \, d\tilde{z}' + \frac{\partial}{\partial \tilde{x}} \int_{\tilde{z}}^{\tilde{f}_s} u_3 \, d\tilde{z}' \right) \,, && \text{(A.9)}\\
A_5(\vec{u}) &= (1-\theta_1)u_5 - \epsilon\theta_1 \frac{\partial \tilde{f}_s}{\partial \tilde{y}}(\tilde{f}_s - \tilde{z}) \\
&+ \epsilon\theta_1 \left(\frac{\partial}{\partial \tilde{y}} \int_{\tilde{z}}^{\tilde{f}_s} u_1 \, d\tilde{z}' + \frac{\partial}{\partial \tilde{x}} \int_{\tilde{z}}^{\tilde{f}_s} u_2 \, d\tilde{z}' + 2\frac{\partial}{\partial \tilde{y}} \int_{\tilde{z}}^{\tilde{f}_s} u_3 \, d\tilde{z}' \right) \,. && \text{(A.10)}
\end{aligned}
$$

If we introduce a vector

$$
\vec{\varphi} := \vec{u} - \vec{v} \,, \qquad \text{(A.11)}
$$

the difference $\vec{A}(\vec{u}) - \vec{A}(\vec{v})$ can be expressed by means of a linear operator $\Delta\vec{A}(\vec{\varphi})$ as follows

$$
\begin{aligned}
\Delta A_1(\vec{\varphi}) &:= A_1(\vec{u}) - A_1(\vec{v}) = \varphi_1 \,, && \text{(A.12)}\\
\Delta A_2(\vec{\varphi}) &:= A_2(\vec{u}) - A_2(\vec{v}) = \varphi_2 \,, && \text{(A.13)}\\
\Delta A_3(\vec{\varphi}) &:= A_3(\vec{u}) - A_3(\vec{v}) = \varphi_3 \,, && \text{(A.14)}\\
\Delta A_4(\vec{\varphi}) &:= A_4(\vec{u}) - A_4(\vec{v}) \\
&= (1-\theta_1)\varphi_4 + \epsilon\theta_1 \left(2\frac{\partial}{\partial \tilde{x}} \int_{\tilde{z}}^{\tilde{f}_s} \varphi_1 \, d\tilde{z}' + \frac{\partial}{\partial \tilde{y}} \int_{\tilde{z}}^{\tilde{f}_s} \varphi_2 \, d\tilde{z}' + \frac{\partial}{\partial \tilde{x}} \int_{\tilde{z}}^{\tilde{f}_s} \varphi_3 \, d\tilde{z}' \right) \\
&=: (1-\theta_1)\varphi_4 + \epsilon\theta_1 \Delta C_4(\vec{\varphi}) \,, && \text{(A.15)}
\end{aligned}
$$

$$
\begin{aligned}
\Delta A_5(\vec{\varphi}) &:= A_5(\vec{u}) - A_5(\vec{v}) \\
&= (1-\theta_1)\varphi_5 + \epsilon\theta_1 \left(\frac{\partial}{\partial \tilde{y}} \int_{\tilde{z}}^{\tilde{f}_s} \varphi_1 \, d\tilde{z}' + \frac{\partial}{\partial \tilde{x}} \int_{\tilde{z}}^{\tilde{f}_s} \varphi_2 \, d\tilde{z}' + 2\frac{\partial}{\partial \tilde{y}} \int_{\tilde{z}}^{\tilde{f}_s} \varphi_3 \, d\tilde{z}' \right) \\
&=: (1-\theta_1)\varphi_5 + \epsilon\theta_1 \Delta C_5(\vec{\varphi}) \,, && \text{(A.16)}
\end{aligned}
$$

where the auxiliary linear operators ΔC_4 and ΔC_5 were introduced.

Let us now focus on the second half-step of the SIA-I, to express the operator $\vec{B}$. First, the stress field, which was already updated in the first half-step, is used to compute the velocity field. Then, this velocity field provides a new stress field by rheological equations. For Newtonian rheology with uniform viscosity, as considered here, we have $\eta = \mathrm{const}$. In this case, the differences between the forward (3.22)-(3.26) and the inverse rheological equations (3.30)-(3.34) vanish, provided that we set $\tilde{\mathcal{A}} = \tilde{\mathcal{S}} = \tilde{\mathcal{V}} = 1$ and replace

(3.27) and (3.28) by

$$\tilde{\eta} = \frac{1}{2\epsilon^{-1}\mathcal{X}}\,, \tag{A.17}$$

$$\mathcal{X} = \frac{[\mathcal{A}]\rho g {\mathrm{H_{sc}}}^3}{[v_h]\mathrm{L_{sc}}}\,. \tag{A.18}$$

Then formulae (3.62), (3.63) and (3.59) can be rewritten as

$$\tilde{v}_x^{k+\frac{1}{2}}(\cdot,\tilde{z}) = \frac{1}{\tilde{\eta}}\left(\int_{\tilde{f}_b(\cdot)}^{\tilde{z}} \tilde{\boldsymbol{\sigma}}_{xz}^{k+\frac{1}{2}}\,d\tilde{z}' + \frac{\epsilon}{2}\int_{\tilde{f}_b(\cdot)}^{\tilde{z}}\frac{\partial}{\partial\tilde{x}}\int_{\tilde{f}_b(\cdot)}^{\tilde{z}'}(\tilde{\boldsymbol{\sigma}}_{xx}^{k}+\tilde{\boldsymbol{\sigma}}_{yy}^{k})d\tilde{z}''\,d\tilde{z}'\right)\,, \tag{A.19}$$

$$\tilde{v}_y^{k+\frac{1}{2}}(\cdot,\tilde{z}) = \frac{1}{\tilde{\eta}}\left(\int_{\tilde{f}_b(\cdot)}^{\tilde{z}} \tilde{\boldsymbol{\sigma}}_{yz}^{k+\frac{1}{2}}\,d\tilde{z}' + \frac{\epsilon}{2}\int_{\tilde{f}_b(\cdot)}^{\tilde{z}}\frac{\partial}{\partial\tilde{y}}\int_{\tilde{f}_b(\cdot)}^{\tilde{z}'}(\tilde{\boldsymbol{\sigma}}_{xx}^{k}+\tilde{\boldsymbol{\sigma}}_{yy}^{k})d\tilde{z}''\,d\tilde{z}'\right)\,, \tag{A.20}$$

$$\tilde{v}_z^{k+\frac{1}{2}}(\cdot,\tilde{z}) = -\frac{1}{2\epsilon\tilde{\eta}}\int_{\tilde{f}_b(\cdot)}^{\tilde{z}}(\tilde{\boldsymbol{\sigma}}_{xx}^{k}+\tilde{\boldsymbol{\sigma}}_{yy}^{k})\,d\tilde{z}'\,. \tag{A.21}$$

Now, by evaluating (3.22)-(3.26) at the $k+\frac{1}{2}$ half-step, with the notation (A.5), we arrive at the following definition of $\vec{B}$

$$B_1(\vec{A}(\vec{u})) = 2\epsilon\frac{\partial}{\partial\tilde{x}}\int_{\tilde{f}_b}^{\tilde{z}}A_4(\vec{u})\,d\tilde{z}' + \epsilon^2\frac{\partial}{\partial\tilde{x}}\int_{\tilde{f}_b}^{\tilde{z}}\frac{\partial}{\partial\tilde{x}}\int_{\tilde{f}_b}^{\tilde{z}'}(A_1(\vec{u})+A_2(\vec{u}))\,d\tilde{z}''\,d\tilde{z}'\,, \tag{A.22}$$

$$\begin{aligned} B_2(\vec{A}(\vec{u})) &= \epsilon\frac{\partial}{\partial\tilde{y}}\int_{\tilde{f}_b}^{\tilde{z}}A_4(\vec{u})\,d\tilde{z}' + \epsilon\frac{\partial}{\partial\tilde{x}}\int_{\tilde{f}_b}^{\tilde{z}}A_5(\vec{u})\,d\tilde{z}' \\ &+ \frac{\epsilon^2}{2}\frac{\partial}{\partial\tilde{y}}\int_{\tilde{f}_b}^{\tilde{z}}\frac{\partial}{\partial\tilde{x}}\int_{\tilde{f}_b}^{\tilde{z}'}(A_1(\vec{u})+A_2(\vec{u}))\,d\tilde{z}''\,d\tilde{z}' \\ &+ \frac{\epsilon^2}{2}\frac{\partial}{\partial\tilde{x}}\int_{\tilde{f}_b}^{\tilde{z}}\frac{\partial}{\partial\tilde{y}}\int_{\tilde{f}_b}^{\tilde{z}'}(A_1(\vec{u})+A_2(\vec{u}))\,d\tilde{z}''\,d\tilde{z}'\,, \end{aligned} \tag{A.23}$$

$$B_3(\vec{A}(\vec{u})) = 2\epsilon\frac{\partial}{\partial\tilde{y}}\int_{\tilde{f}_b}^{\tilde{z}}A_5(\vec{u})\,d\tilde{z}' + \epsilon^2\frac{\partial}{\partial\tilde{y}}\int_{\tilde{f}_b}^{\tilde{z}}\frac{\partial}{\partial\tilde{y}}\int_{\tilde{f}_b}^{\tilde{z}'}(A_1(\vec{u})+A_2(\vec{u}))\,d\tilde{z}''\,d\tilde{z}'\,, \tag{A.24}$$

$$B_4(\vec{A}(\vec{u})) = A_4(\vec{u})\,, \tag{A.25}$$

$$B_5(\vec{A}(\vec{u})) = A_5(\vec{u})\,. \tag{A.26}$$

Let us now define a difference operator $\Delta\vec{B}$ by

$$\begin{aligned} \Delta B_1(\vec{\varphi}) &:= B_1(\vec{A}(\vec{u})) - B_1(\vec{A}(\vec{v})) \\ &= 2\epsilon\frac{\partial}{\partial\tilde{x}}\int_{\tilde{f}_b}^{\tilde{z}}\Delta A_4(\vec{\varphi})\,d\tilde{z}' + \epsilon^2\frac{\partial}{\partial\tilde{x}}\int_{\tilde{f}_b}^{\tilde{z}}\frac{\partial}{\partial\tilde{x}}\int_{\tilde{f}_b}^{\tilde{z}'}(\Delta A_1(\vec{\varphi})+\Delta A_2(\vec{\varphi}))\,d\tilde{z}''\,d\tilde{z}' \\ &=: \epsilon\Delta D_1(\vec{\varphi})\,, \end{aligned} \tag{A.27}$$

$$
\begin{aligned}
\Delta B_2(\vec{\varphi}) &:= B_2(\vec{A}(\vec{u})) - B_2(\vec{A}(\vec{v})) \\
&= \epsilon \frac{\partial}{\partial \tilde{y}} \int_{\tilde{f}_b}^{\tilde{z}} \Delta A_4(\vec{\varphi})\, d\tilde{z}' + \epsilon \frac{\partial}{\partial \tilde{x}} \int_{\tilde{f}_b}^{\tilde{z}} \Delta A_5(\vec{\varphi})\, d\tilde{z}' \\
&+ \frac{\epsilon^2}{2} \frac{\partial}{\partial \tilde{y}} \int_{\tilde{f}_b}^{\tilde{z}} \frac{\partial}{\partial \tilde{x}} \int_{\tilde{f}_b}^{\tilde{z}'} (\Delta A_1(\vec{\varphi}) + \Delta A_2(\vec{\varphi}))\, d\tilde{z}''\, d\tilde{z}' \\
&+ \frac{\epsilon^2}{2} \frac{\partial}{\partial \tilde{x}} \int_{\tilde{f}_b}^{\tilde{z}} \frac{\partial}{\partial \tilde{y}} \int_{\tilde{f}_b}^{\tilde{z}'} (\Delta A_1(\vec{\varphi}) + \Delta A_2(\vec{\varphi}))\, d\tilde{z}''\, d\tilde{z}' \\
&=: \epsilon \Delta D_2(\vec{\varphi})\,, \qquad \text{(A.28)} \\
\Delta B_3(\vec{\varphi}) &:= B_3(\vec{A}(\vec{u})) - B_3(\vec{A}(\vec{v})) \\
&= 2\epsilon \frac{\partial}{\partial \tilde{y}} \int_{\tilde{f}_b}^{\tilde{z}} \Delta A_5(\vec{\varphi})\, d\tilde{z}' + \epsilon^2 \frac{\partial}{\partial \tilde{y}} \int_{\tilde{f}_b}^{\tilde{z}} \frac{\partial}{\partial \tilde{y}} \int_{\tilde{f}_b}^{\tilde{z}'} (\Delta A_1(\vec{\varphi}) + \Delta A_2(\vec{\varphi}))\, d\tilde{z}''\, d\tilde{z}' \\
&=: \epsilon \Delta D_3(\vec{\varphi})\,, \qquad \text{(A.29)} \\
\Delta B_4(\vec{\varphi}) &:= B_4(\vec{A}(\vec{u})) - B_4(\vec{A}(\vec{v})) \\
&= A_4(\vec{u}) - A_4(\vec{v}) = \Delta A_4(\vec{\varphi})\,, \qquad \text{(A.30)} \\
\Delta B_5(\vec{\varphi}) &:= B_5(\vec{A}(\vec{u})) - B_5(\vec{A}(\vec{v})) \\
&= A_5(\vec{u}) - A_5(\vec{v}) = \Delta A_5(\vec{\varphi}). \qquad \text{(A.31)}
\end{aligned}
$$

The differences ΔB_i, together with the auxiliary operators ΔD_i, are again linear in $\vec{\varphi}$.

We now define the functional space for the solution $\vec{u}$. Consider a space of polynomials $P_k^{(3)}$, $k \geq 1$, defined as a set of all polynomials in R^3 of the form

$$
P_k^{(3)} := \left\{ p(\tilde{x}, \tilde{y}, \tilde{z}); p(\tilde{x}, \tilde{y}, \tilde{z}) = \sum_{k_x + k_y + k_z \leq k} a_{k_x, k_y, k_z} \tilde{x}^{k_x} \tilde{y}^{k_y} \tilde{z}^{k_z} \right\},
$$

and introduce a space $X := \left(P_k^{(3)}\right)^5$. For each $\vec{u} \in X$, operators $\vec{A}$ and $\vec{B}$ are well defined, but unfortunately the images $\vec{A}(\vec{u})$ and $\vec{B}(\vec{u})$ do not generally lie in X anymore. The reason is that the terms $\int_{\tilde{z}}^{\tilde{f}_s(\tilde{x},\tilde{y})} u_l(\cdot, \tilde{z}')\, d\tilde{z}'$, in (A.9) and (A.10) which, even for polynomial representation of the free surface $\tilde{f}_s$, are generally not polynomials of the proper degree. In order to overcome this difficulty, we introduce a strong assumption on the representation of the surface functions $\tilde{f}_s$, $\tilde{f}_b$. We will assume that both are represented by piecewise linear functions. This simplification may be to some extent justified concerning the numerical realisation of the algorithm, meaning then that only piecewise linear triangulation is used to capture the surfaces. Moreover, we will assume that the triangulations for both $\tilde{f}_s$ and $\tilde{f}_b$, are defined on the same grid in the horizontal plane. Let us order the faces of the triangulation of $\tilde{f}_s$ by integers and denote the volume beneath the i-th face by Ω_i. The restriction of the space X to Ω_i will be denoted X_i. Analogously, for all introduced operators and functions, let us denote their restriction to X_i and Ω_i, respectively, by a superscript $^{(i)}$. With the assumption of linearity of $\tilde{f}_s$, $\tilde{f}_b$, it holds: $\vec{A}^{(i)} : X_i \to X_i$, $\vec{B}^{(i)} : X_i \to X_i$. Now we define the space where solutions will be looked for as

$$
\hat{X} := \left\{ \vec{u}; \vec{u}^{(i)} \in X_i \right\}\,, \qquad \text{(A.32)}
$$

which is a linear vector space of vectors $\vec{u}$, whose components $u_j,\ j = 1...5$, are piecewise polynomial.

Let us now, for any $\vec{w}^{(i)} \in X_i$, introduce the norms

$$
\|w_j^{(i)}\| := \max_{\vec{x} \in \Omega_i} |w_j^{(i)}(\vec{x})|\,, \qquad j = 1, \ldots, 5\,, \qquad \text{(A.33)}
$$

i.e. the $C^\infty(\Omega_i)$ norm and

$$\|\vec{w}^{(i)}\|_{max} := \max_{j=1,\ldots,5} \|w_j^{(i)}\| \,. \tag{A.34}$$

Before we finally investigate the difference $\vec{T}^{(i)}(\vec{u}) - \vec{T}^{(i)}(\vec{v})$ for some $\vec{u}, \vec{v} \in \hat{X}$, realize that, for arbitrary k in the choice of $P_k^{(3)}$, the space X and, of course also all X_i, are finite dimensional spaces. While we have already shown that ΔA_j, ΔB_j, ΔC_j and ΔD_j, are linear operators, the same holds also for their restrictions to X_i. Using the fact that on finitely-dimensional spaces, all linear operators are bounded (and thus also continuous) (e.g. Lukeš, 2003), we thus have the following estimates

$$\begin{aligned}
\Delta A_j^{(i)}(\vec{\varphi}^{(i)}) &\leq \|\Delta A_j^{(i)}\| \|\vec{\varphi}^{(i)}\|_{max} \,, & \text{(A.35)}\\
\Delta B_j^{(i)}(\vec{\varphi}^{(i)}) &\leq \|\Delta B_j^{(i)}\| \|\vec{\varphi}^{(i)}\|_{max} \,, & \text{(A.36)}\\
\Delta C_j^{(i)}(\vec{\varphi}^{(i)}) &\leq \|\Delta C_j^{(i)}\| \|\vec{\varphi}^{(i)}\|_{max} \,, & \text{(A.37)}\\
\Delta D_j^{(i)}(\vec{\varphi}^{(i)}) &\leq \|\Delta D_j^{(i)}\| \|\vec{\varphi}^{(i)}\|_{max} \,, & \text{(A.38)}
\end{aligned}$$

where operator norms were introduced as usual by

$$\|\Delta A_j^{(i)}\| := \max_{\vec{\varphi}^{(i)} \in X_i, \vec{\varphi}^{(i)} \neq \vec{0}} \frac{\|\Delta A_j^{(i)}(\vec{\varphi}^{(i)})\|}{\|\vec{\varphi}^{(i)}\|_{max}} \,. \tag{A.39}$$

Finally, using (A.3), (A.12)-(A.16) and (A.27)-(A.31), and also recalling that $1 \geq \theta_1 > 0$, $1 \geq \theta_2 > 0$, we obtain the estimates

$$\begin{aligned}
\|T_1^{(i)}(\vec{u}) - T_1^{(i)}(\vec{v})\| &\leq (1-\theta_2)\|\Delta A_1^{(i)}(\vec{\varphi})\| + \theta_2 \|\Delta B_1^{(i)}(\vec{\varphi})\| \\
&\leq (1-\theta_2)\|\varphi_1^{(i)}\| + \epsilon\theta_2 \|\Delta D_1^{(i)}\| \|\vec{\varphi}^{(i)}\|_{max} \\
&\leq (1-\theta_2+\epsilon\theta_2\|\Delta D_1^{(i)}\|)\|\vec{\varphi}^{(i)}\|_{max} \,, \\
\|T_2^{(i)}(\vec{u}) - T_2^{(i)}(\vec{v})\| &\leq (1-\theta_2)\|\Delta A_2^{(i)}(\vec{\varphi})\| + \theta_2 \|\Delta B_2^{(i)}(\vec{\varphi})\| \\
&\leq (1-\theta_2)\|\varphi_2^{(i)}\| + \epsilon\theta_2 \|\Delta D_2^{(i)}\| \|\vec{\varphi}^{(i)}\|_{max} \\
&\leq (1-\theta_2+\epsilon\theta_2\|\Delta D_2^{(i)}\|)\|\vec{\varphi}^{(i)}\|_{max} \,, \\
\|T_3^{(i)}(\vec{u}) - T_3^{(i)}(\vec{v})\| &\leq (1-\theta_2)\|\Delta A_3^{(i)}(\vec{\varphi})\| + \theta_2 \|\Delta B_3^{(i)}(\vec{\varphi})\| \\
&\leq (1-\theta_2)\|\varphi_3^{(i)}\| + \epsilon\theta_2 \|\Delta D_3^{(i)}\| \|\vec{\varphi}^{(i)}\|_{max} \\
&\leq (1-\theta_2+\epsilon\theta_2\|\Delta D_3^{(i)}\|)\|\vec{\varphi}^{(i)}\|_{max} \,, \\
\\
\|T_4^{(i)}(\vec{u}) - T_4^{(i)}(\vec{v})\| &= \|\Delta A_4^{(i)}(\vec{\varphi})\| \\
&\leq (1-\theta_1)\|\varphi_4^{(i)}\| + \epsilon\theta_1 \|\Delta C_4^{(i)}\| \|\vec{\varphi}^{(i)}\|_{max} \\
&\leq (1-\theta_1+\epsilon\theta_1\|\Delta C_4^{(i)}\|)\|\vec{\varphi}^{(i)}\|_{max} \,, \\
\|T_5^{(i)}(\vec{u}) - T_5^{(i)}(\vec{v})\| &= \|\Delta A_5^{(i)}(\vec{\varphi})\| \\
&\leq (1-\theta_1)\|\varphi_5^{(i)}\| + \epsilon\theta_1 \|\Delta C_5^{(i)}\| \|\vec{\varphi}^{(i)}\|_{max} \\
&\leq (1-\theta_1+\epsilon\theta_1\|\Delta C_5^{(i)}\|)\|\vec{\varphi}^{(i)}\|_{max} \,.
\end{aligned}$$

Consider now an arbitrary but fixed small positive constant $\delta > 0$. Then provided $\epsilon < \frac{\epsilon_{\min}}{2}$, with $\epsilon_{\min} := \min_i \left(\frac{1}{\|\Delta D_1^{(i)}\|}, \frac{1}{\|\Delta D_2^{(i)}\|}, \frac{1}{\|\Delta D_3^{(i)}\|}, \frac{1}{\|\Delta C_4^{(i)}\|}, \frac{1}{\|\Delta C_5^{(i)}\|} \right)$ and provided that $1 \geq \theta_1 \geq 2\delta$, $1 \geq \theta_2 \geq 2\delta$, it holds that

$$\forall i : \|\vec{T}^{(i)}(\vec{u}) - \vec{T}^{(i)}(\vec{v})\|_{max} < (1-\delta)\|\vec{u}^{(i)} - \vec{v}^{(i)}\|_{max} \,, \tag{A.40}$$

which is the desired contractivity of the mapping $\vec{T}$. Since δ was an arbitrary (small) positive, the relaxation parameters are actually not constrained for this simple case with uniform constant viscosity and the only restriction is given by a certain "flatness" condition, i.e. by necessity of sufficiently small aspect ratio ϵ.

To finish the procedure, provided the assumptions for contractivity of the mapping $\vec{T}$ are satisfied, we can use the Banach fixed-point theorem (e.g. Lukeš, 2003), as the finite-dimensional spaces X_i are complete. Thus, the operator $\vec{T}$ possesses a unique fixed point, that is, there exists a vector $\vec{u}^F \in \hat{X}$ (composition of appropriate $\vec{u}^{F\,(i)} \in X_i$), such that it holds

$$\forall i : \vec{T}^{(i)}(\vec{u}^F) = \vec{u}^{F\,(i)} \,. \tag{A.41}$$

The relation of the fixed point $\vec{u}^F$ to the exact full-Stokes solution of the considered ice-flow problem is discussed in the following section.

Appendix B

Properties of the fixed point of the SIA-I algorithm

In the previous section, we presented an attempt to demonstrate, at least in some limited sense, the contractivity of the mapping $\vec{T}$, which is induced by each iteration step of the SIA-I algorithm. Let us now investigate the relation of the fixed-point of the mapping $\vec{T}$ and the full-Stokes solution of the original problem. For this purpose, we return to the original general case with ice described by a model of fluid with non-linear rheology given by Glen's flow law (1.17). We will assume that, for certain values of the projection parameters θ_1 and θ_2, the contractivity of the mapping $\vec{T}$ representing the SIA-I algorithm holds in some sense. That is, we assume that the procedure from previous section can be reasonably extended to capture also the non-linear rheology, possibly after reformulation of the mappings $\vec{T}$, $\vec{A}$, $\vec{B}$ in a generalized (e.g. weak) sense for some appropriate complete functional spaces. Under these assumptions, a unique fixed point $\vec{u}^F$ of the mapping $\vec{T}$ exists, and according to (A.3), using the notation from previous section, it holds that

$$\vec{u}^F = \vec{T}(\vec{u}^F) = (1-\theta_2)\vec{A}(\vec{u}^F) + \theta_2\vec{B}(\vec{A}(\vec{u}^F)) \,. \tag{B.1}$$

We intent to show that this implies even a stronger conclusion that $\vec{u}^F = \vec{A}(\vec{u}^F) = \vec{B}(\vec{u}^F)$. Also these relations, as will be revealed in the subsequent text, correspond to both the momentum balance equations and rheology being satisfied. To demonstrate this fact, we first observe, that, by definition,

$$A_1(\vec{u}^F) = u_1^F \,, \tag{B.2}$$
$$A_2(\vec{u}^F) = u_2^F \,, \tag{B.3}$$
$$A_3(\vec{u}^F) = u_3^F \,. \tag{B.4}$$

as only u_4 and u_5 are updated by the operator $\vec{A}$ in the first half-step of the SIA-I (see (3.52)). When the first, second and third components of equation (B.1) are taken, (B.2)-(B.4) give

$$u_1^F = A_1(\vec{u}^F) = B_1(\vec{A}(\vec{u}^F)) \,, \tag{B.5}$$
$$u_2^F = A_2(\vec{u}^F) = B_2(\vec{A}(\vec{u}^F)) \,, \tag{B.6}$$
$$u_3^F = A_3(\vec{u}^F) = B_3(\vec{A}(\vec{u}^F)) \,. \tag{B.7}$$

To interpret these relations, let us recall what operator $\vec{B}$ stands for. Back in the "stress" and "velocity" notation, from the stress field $\vec{u}^F = (\tilde{\boldsymbol{\sigma}}_{xx}^F, \tilde{\boldsymbol{\sigma}}_{xy}^F, \tilde{\boldsymbol{\sigma}}_{yy}^F, \tilde{\boldsymbol{\sigma}}_{xz}^F, \tilde{\boldsymbol{\sigma}}_{yz}^F)$, the first half-step produces $\vec{A}(\vec{u}^F) = \vec{u}^{F+\frac{1}{2}} = (\tilde{\boldsymbol{\sigma}}_{xx}^F, \tilde{\boldsymbol{\sigma}}_{xy}^F, \tilde{\boldsymbol{\sigma}}_{yy}^F, \tilde{\boldsymbol{\sigma}}_{xz}^{F+\frac{1}{2}}, \tilde{\boldsymbol{\sigma}}_{yz}^{F+\frac{1}{2}})$, from which the velocity components $\tilde{v}_x^{F+\frac{1}{2}}$, $\tilde{v}_y^{F+\frac{1}{2}}$ and $\tilde{v}_z^{F+\frac{1}{2}}$ are computed

according to (3.62), (3.63) and (3.59). We remind the reader here of these formulae:

$$\tilde{v}_x^{F+\frac{1}{2}}(\cdot,\tilde{z}) = 2\epsilon^{-1}\mathcal{X}\int_{\tilde{f}_b(\cdot)}^{\tilde{z}} \tilde{\mathcal{A}}\tilde{\mathcal{S}}^{F+\frac{1}{2}}\tilde{\boldsymbol{\sigma}}_{xz}^{F+\frac{1}{2}}d\tilde{z}' + \mathcal{X}\int_{\tilde{f}_b(\cdot)}^{\tilde{z}}\frac{\partial}{\partial\tilde{x}}\int_{\tilde{f}_b(\cdot)}^{\tilde{z}'}\tilde{\mathcal{A}}\tilde{\mathcal{S}}^{F+\frac{1}{2}}(\tilde{\boldsymbol{\sigma}}_{xx}^{F}+\tilde{\boldsymbol{\sigma}}_{yy}^{F})d\tilde{z}''\,d\tilde{z}'\,, \tag{B.8}$$

$$\tilde{v}_y^{F+\frac{1}{2}}(\cdot,\tilde{z}) = 2\epsilon^{-1}\mathcal{X}\int_{\tilde{f}_b(\cdot)}^{\tilde{z}} \tilde{\mathcal{A}}\tilde{\mathcal{S}}^{F+\frac{1}{2}}\tilde{\boldsymbol{\sigma}}_{yz}^{F+\frac{1}{2}}d\tilde{z}' + \mathcal{X}\int_{\tilde{f}_b(\cdot)}^{\tilde{z}}\frac{\partial}{\partial\tilde{y}}\int_{\tilde{f}_b(\cdot)}^{\tilde{z}'}\tilde{\mathcal{A}}\tilde{\mathcal{S}}^{F+\frac{1}{2}}(\tilde{\boldsymbol{\sigma}}_{xx}^{F}+\tilde{\boldsymbol{\sigma}}_{yy}^{F})d\tilde{z}''\,d\tilde{z}'\,, \tag{B.9}$$

$$\tilde{v}_z^{F+\frac{1}{2}}(\cdot,\tilde{z}) = -\epsilon^{-2}\mathcal{X}\int_{\tilde{f}_b(\cdot)}^{\tilde{z}} \tilde{\mathcal{A}}\tilde{\mathcal{S}}^{F+\frac{1}{2}}(\tilde{\boldsymbol{\sigma}}_{xx}^{F}+\tilde{\boldsymbol{\sigma}}_{yy}^{F})\,d\tilde{z}'\,. \tag{B.10}$$

This velocity field is inserted into the rheological equations (3.22)-(3.29), to provide the vector $\vec{B}(\vec{A}(\vec{u}^F)) = \vec{u}^{\star F+\frac{1}{2}} = (\tilde{\boldsymbol{\sigma}}_{xx}^{\star F}, \tilde{\boldsymbol{\sigma}}_{xy}^{\star F}, \tilde{\boldsymbol{\sigma}}_{yy}^{\star F}, \tilde{\boldsymbol{\sigma}}_{xz}^{\star F+\frac{1}{2}}, \tilde{\boldsymbol{\sigma}}_{yz}^{\star F+\frac{1}{2}})$. Also the inverse rheological equations (3.30)-(3.35) are satisfied, in particular (3.30) and (3.31), which read as

$$\frac{\partial\tilde{v}_x^{F+\frac{1}{2}}}{\partial\tilde{x}} = \epsilon^{-2}\mathcal{X}\tilde{\mathcal{A}}\tilde{\mathcal{S}}^{\star F+\frac{1}{2}}\tilde{\boldsymbol{\sigma}}_{xx}^{\star F}\,, \tag{B.11}$$

$$\frac{\partial\tilde{v}_y^{F+\frac{1}{2}}}{\partial\tilde{y}} = \epsilon^{-2}\mathcal{X}\tilde{\mathcal{A}}\tilde{\mathcal{S}}^{\star F+\frac{1}{2}}\tilde{\boldsymbol{\sigma}}_{yy}^{\star F}\,. \tag{B.12}$$

Using the incompressibility condition (3.15), we obtain

$$\frac{\partial\tilde{v}_z^{F+\frac{1}{2}}}{\partial\tilde{z}} = -\epsilon^{-2}\mathcal{X}\tilde{\mathcal{A}}\tilde{\mathcal{S}}^{\star F+\frac{1}{2}}(\tilde{\boldsymbol{\sigma}}_{xx}^{\star F}+\tilde{\boldsymbol{\sigma}}_{yy}^{\star F})\,, \tag{B.13}$$

and by inserting (B.10) into the left-hand side of (B.13), using the fact that according to (B.5) and (B.7) $\tilde{\boldsymbol{\sigma}}_{xx}^{\star F} = \tilde{\boldsymbol{\sigma}}_{xx}^{F}$, and $\tilde{\boldsymbol{\sigma}}_{yy}^{\star F} = \tilde{\boldsymbol{\sigma}}_{yy}^{F}$, we finally obtain

$$\tilde{\mathcal{S}}^{\star F+\frac{1}{2}} = \tilde{\mathcal{S}}^{F+\frac{1}{2}}\,. \tag{B.14}$$

Using this fact we will now prove also that $u_4^F = B_4(\vec{A}(\vec{u}^F))$, $u_5^F = B_4(\vec{A}(\vec{u}^5))$, or $\tilde{\boldsymbol{\sigma}}_{xz}^{F} = \tilde{\boldsymbol{\sigma}}_{xz}^{\star F+\frac{1}{2}}$, $\tilde{\boldsymbol{\sigma}}_{yz}^{F} = \tilde{\boldsymbol{\sigma}}_{yz}^{\star F+\frac{1}{2}}$. To see this, let us recall the rheological equations (3.33) and (3.34), which now read:

$$\frac{\partial\tilde{v}_x^{F+\frac{1}{2}}}{\partial\tilde{z}} + \epsilon^2\frac{\partial\tilde{v}_z^{F+\frac{1}{2}}}{\partial\tilde{x}} = 2\epsilon^{-1}\mathcal{X}\tilde{\mathcal{A}}\tilde{\mathcal{S}}^{\star F+\frac{1}{2}}\tilde{\boldsymbol{\sigma}}_{xz}^{\star F+\frac{1}{2}}\,, \tag{B.15}$$

$$\frac{\partial\tilde{v}_y^{F+\frac{1}{2}}}{\partial\tilde{z}} + \epsilon^2\frac{\partial\tilde{v}_z^{F+\frac{1}{2}}}{\partial\tilde{y}} = 2\epsilon^{-1}\mathcal{X}\tilde{\mathcal{A}}\tilde{\mathcal{S}}^{\star F+\frac{1}{2}}\tilde{\boldsymbol{\sigma}}_{yz}^{\star F+\frac{1}{2}}\,, \tag{B.16}$$

where we insert $\tilde{v}_x^{F+\frac{1}{2}}$, $\tilde{v}_y^{F+\frac{1}{2}}$ and $\tilde{v}_z^{F+\frac{1}{2}}$ from (B.8)-(B.10), using (B.14), which gives

$$A_4(\vec{u}^F) = u_4^{F+\frac{1}{2}} = \tilde{\boldsymbol{\sigma}}_{xz}^{F+\frac{1}{2}} = \tilde{\boldsymbol{\sigma}}_{xz}^{\star F+\frac{1}{2}} = B_4(\vec{A}(\vec{u}^F))\,, \tag{B.17}$$

$$A_5(\vec{u}^F) = u_5^{F+\frac{1}{2}} = \tilde{\boldsymbol{\sigma}}_{yz}^{F+\frac{1}{2}} = \tilde{\boldsymbol{\sigma}}_{yz}^{\star F+\frac{1}{2}} = B_5(\vec{A}(\vec{u}^F))\,. \tag{B.18}$$

Together with (B.5)-(B.7), we thus obtained

$$\vec{A}(\vec{u}^F) = \vec{B}(\vec{A}(\vec{u}^F))\,, \tag{B.19}$$

and from (B.1) also immediately

$$\vec{u}^F = \vec{A}(\vec{u}^F)\,, \tag{B.20}$$
$$\vec{u}^F = \vec{B}(\vec{u}^F)\,. \tag{B.21}$$

The second of these relations states that the fixed point stress solution is consistent with the rheological equations, because it confirms that, if the stress field $\vec{u}^F$ is first used to compute the velocities according to (B.8)-(B.10) (with $\tilde{\mathcal{S}}^{F+\frac{1}{2}} = \tilde{\mathcal{S}}^F$, $\tilde{\boldsymbol{\sigma}}_{xz}^{F+\frac{1}{2}} = \tilde{\boldsymbol{\sigma}}_{xz}^F$, $\tilde{\boldsymbol{\sigma}}_{yz}^{F+\frac{1}{2}} = \tilde{\boldsymbol{\sigma}}_{yz}^F$ by (B.20)), by inserting this velocity field into the rheology equations (3.22)-(3.29), we obtain the same stress field.

The first condition (B.20) implies according to (A.4) that $\delta\vec{u}^{F+\frac{1}{2}} = \vec{0}$. In view of (3.48) and (3.49), we thus obtain

$$\begin{aligned} 0 &= -\tilde{\boldsymbol{\sigma}}_{xz}^F - \epsilon\frac{\partial\tilde{f}_s}{\partial\tilde{x}}(\tilde{f}_s-\tilde{z}) + 2\epsilon\frac{\partial}{\partial\tilde{x}}\int_{\tilde{z}}^{\tilde{f}_s}\tilde{\boldsymbol{\sigma}}_{xx}^F(\cdot,\tilde{z}')d\tilde{z}' \\ &+ \epsilon\frac{\partial}{\partial\tilde{y}}\int_{\tilde{z}}^{\tilde{f}_s}\tilde{\boldsymbol{\sigma}}_{xy}^F(\cdot,\tilde{z}')d\tilde{z}' + \epsilon\frac{\partial}{\partial\tilde{x}}\int_{\tilde{z}}^{\tilde{f}_s}\tilde{\boldsymbol{\sigma}}_{yy}^F(\cdot,\tilde{z}')d\tilde{z}'\,, \end{aligned} \tag{B.22}$$

$$\begin{aligned} 0 &= -\tilde{\boldsymbol{\sigma}}_{yz}^F - \epsilon\frac{\partial\tilde{f}_s}{\partial\tilde{y}}(\tilde{f}_s-\tilde{z}) + \epsilon\frac{\partial}{\partial\tilde{y}}\int_{\tilde{z}}^{\tilde{f}_s}\tilde{\boldsymbol{\sigma}}_{xx}^F(\cdot,\tilde{z}')d\tilde{z}' \\ &+ \epsilon\frac{\partial}{\partial\tilde{x}}\int_{\tilde{z}}^{\tilde{f}_s}\tilde{\boldsymbol{\sigma}}_{xy}^F(\cdot,\tilde{z}')d\tilde{z}' + 2\epsilon\frac{\partial}{\partial\tilde{y}}\int_{\tilde{z}}^{\tilde{f}_s}\tilde{\boldsymbol{\sigma}}_{yy}^F(\cdot,\tilde{z}')d\tilde{z}'\,. \end{aligned} \tag{B.23}$$

If we take an arbitrary initial pressure field $\tilde{p}^0$ and compute the increment $\delta\tilde{p}$ for $\vec{u}^F$ according to (3.47) and denote the sum as $\tilde{p}^F := \tilde{p}^0 + \delta\tilde{p}^F$, from (3.47) we obtain

$$0 = -\tilde{p}^F - \tilde{\boldsymbol{\sigma}}_{xx}^F - \tilde{\boldsymbol{\sigma}}_{yy}^F + (\tilde{f}_s-\tilde{z}) - \epsilon\int_{\tilde{z}}^{\tilde{f}_s}\frac{\partial\tilde{\boldsymbol{\sigma}}_{xz}^F}{\partial\tilde{x}}\,d\tilde{z}' - \epsilon\int_{\tilde{z}}^{\tilde{f}_s}\frac{\partial\tilde{\boldsymbol{\sigma}}_{yz}^F}{\partial\tilde{y}}\,d\tilde{z}'\,. \tag{B.24}$$

Taking the $\tilde{z}$-derivative of (B.22) and (B.23) gives

$$0 = -\frac{\partial\tilde{\boldsymbol{\sigma}}_{xz}^F}{\partial\tilde{z}} + \epsilon\frac{\partial\tilde{f}_s}{\partial\tilde{x}} - 2\epsilon\frac{\partial\tilde{\boldsymbol{\sigma}}_{xx}^F}{\partial\tilde{x}} - \epsilon\frac{\partial\tilde{\boldsymbol{\sigma}}_{xy}^F}{\partial\tilde{y}} - \epsilon\frac{\partial\tilde{\boldsymbol{\sigma}}_{yy}^F}{\partial\tilde{x}}\,, \tag{B.25}$$

$$0 = -\frac{\partial\tilde{\boldsymbol{\sigma}}_{yz}^F}{\partial\tilde{z}} + \epsilon\frac{\partial\tilde{f}_s}{\partial\tilde{y}} - \epsilon\frac{\partial\tilde{\boldsymbol{\sigma}}_{xx}^F}{\partial\tilde{y}} - \epsilon\frac{\partial\tilde{\boldsymbol{\sigma}}_{xy}^F}{\partial\tilde{x}} - 2\epsilon\frac{\partial\tilde{\boldsymbol{\sigma}}_{yy}^F}{\partial\tilde{y}}\,. \tag{B.26}$$

Now, evaluating the $\tilde{x}$, $\tilde{y}$ and $\tilde{z}$-derivative of (B.24) with the use of (B.25) and (B.26) gives

$$\epsilon^2\frac{\partial}{\partial\tilde{x}}\int_{\tilde{z}}^{\tilde{f}_s}\left(\frac{\partial\tilde{\boldsymbol{\sigma}}_{xz}^F}{\partial\tilde{x}} + \frac{\partial\tilde{\boldsymbol{\sigma}}_{yz}^F}{\partial\tilde{y}}\right)d\tilde{z}' = -\epsilon\frac{\partial\tilde{p}^F}{\partial\tilde{x}} + \epsilon\frac{\partial\tilde{\boldsymbol{\sigma}}_{xx}^F}{\partial\tilde{x}} + \epsilon\frac{\partial\tilde{\boldsymbol{\sigma}}_{xy}^F}{\partial\tilde{y}} + \frac{\partial\tilde{\boldsymbol{\sigma}}_{xz}^F}{\partial\tilde{z}}\,, \tag{B.27}$$

$$\epsilon^2\frac{\partial}{\partial\tilde{y}}\int_{\tilde{z}}^{\tilde{f}_s}\left(\frac{\partial\tilde{\boldsymbol{\sigma}}_{xz}^F}{\partial\tilde{x}} + \frac{\partial\tilde{\boldsymbol{\sigma}}_{yz}^F}{\partial\tilde{y}}\right)d\tilde{z}' = -\epsilon\frac{\partial\tilde{p}^F}{\partial\tilde{y}} + \epsilon\frac{\partial\tilde{\boldsymbol{\sigma}}_{xy}^F}{\partial\tilde{x}} + \epsilon\frac{\partial\tilde{\boldsymbol{\sigma}}_{yy}^F}{\partial\tilde{y}} + \frac{\partial\tilde{\boldsymbol{\sigma}}_{yz}^F}{\partial\tilde{z}}\,, \tag{B.28}$$

$$1 = -\frac{\partial\tilde{p}^F}{\partial\tilde{z}} + \epsilon\frac{\partial\tilde{\boldsymbol{\sigma}}_{xz}^F}{\partial\tilde{x}} + \epsilon\frac{\partial\tilde{\boldsymbol{\sigma}}_{yz}^F}{\partial\tilde{y}} - \frac{\partial(\tilde{\boldsymbol{\sigma}}_{xx}^F + \tilde{\boldsymbol{\sigma}}_{yy}^F)}{\partial\tilde{z}}\,, \tag{B.29}$$

which would be, when compared with (3.12)-(3.14), the linear-momentum balance equations if the left-hand side "ϵ^2" terms in (B.27) and (B.28) vanished.

It remains to show how the fixed-point solution meets the boundary conditions. The no-slip condition at the base ($\vec{v}^{F+\frac{1}{2}} = \vec{0}$), which has been assumed throughout this paragraph, is automatically satisfied by (B.8)-(B.10). To check the stress-free conditions at the upper surface, let us first evaluate the stress conditions there according to (B.22)-(B.24), where we obtain

$$0 = -\tilde{\boldsymbol{\sigma}}^F_{xz} + 2\epsilon\frac{\partial\tilde{f}_s}{\partial\tilde{x}}\tilde{\boldsymbol{\sigma}}^F_{xx} + \epsilon\frac{\partial\tilde{f}_s}{\partial\tilde{y}}\tilde{\boldsymbol{\sigma}}^F_{xy} + \epsilon\frac{\partial\tilde{f}_s}{\partial\tilde{x}}\tilde{\boldsymbol{\sigma}}^F_{yy} , \tag{B.30}$$

$$0 = -\tilde{\boldsymbol{\sigma}}^F_{yz} + \epsilon\frac{\partial\tilde{f}_s}{\partial\tilde{y}}\tilde{\boldsymbol{\sigma}}^F_{xx} + \epsilon\frac{\partial\tilde{f}_s}{\partial\tilde{x}}\tilde{\boldsymbol{\sigma}}^F_{xy} + 2\epsilon\frac{\partial\tilde{f}_s}{\partial\tilde{y}}\tilde{\boldsymbol{\sigma}}^F_{yy} , \tag{B.31}$$

$$0 = -\tilde{p}^F - \tilde{\boldsymbol{\sigma}}^F_{xx} - \tilde{\boldsymbol{\sigma}}^F_{yy} , \tag{B.32}$$

at $\tilde{z} = \tilde{f}_s(\tilde{x},\tilde{y})$. Equations (B.30) and (B.31) can be rewritten with the use of (B.32) and we can write the stress conditions at the upper surface as follows

$$0 = \epsilon\frac{\partial\tilde{f}_s}{\partial\tilde{x}}\tilde{p}^F - \epsilon\frac{\partial\tilde{f}_s}{\partial\tilde{x}}\tilde{\boldsymbol{\sigma}}^F_{xx} - \epsilon\frac{\partial\tilde{f}_s}{\partial\tilde{y}}\tilde{\boldsymbol{\sigma}}^F_{xy} + \tilde{\boldsymbol{\sigma}}^F_{xz} , \tag{B.33}$$

$$0 = \epsilon\frac{\partial\tilde{f}_s}{\partial\tilde{y}}\tilde{p}^F - \epsilon\frac{\partial\tilde{f}_s}{\partial\tilde{x}}\tilde{\boldsymbol{\sigma}}^F_{xy} - \epsilon\frac{\partial\tilde{f}_s}{\partial\tilde{y}}\tilde{\boldsymbol{\sigma}}^F_{yy} + \tilde{\boldsymbol{\sigma}}^F_{yz} , \tag{B.34}$$

$$0 = \tilde{p}^F + \tilde{\boldsymbol{\sigma}}^F_{xx} + \tilde{\boldsymbol{\sigma}}^F_{yy} , \tag{B.35}$$

at $\tilde{z} = \tilde{f}_s(\tilde{x},\tilde{y})$. We may now compare these equations with the stress-free conditions (3.17)-(3.19) and observe that (B.33) and (B.34) coincide with (3.17) and (3.18), while (B.35) differs from (3.19). The difference can be evaluated if we add the missing terms to both sides of (B.35) and evaluate them on the left-hand side with the use of (B.33) and (B.34). We then obtain

$$\epsilon^2 E = \tilde{p}^F + \tilde{\boldsymbol{\sigma}}^F_{xx} + \tilde{\boldsymbol{\sigma}}^F_{yy} + \epsilon\frac{\partial\tilde{f}_s}{\partial\tilde{x}}\tilde{\boldsymbol{\sigma}}^F_{xz} + \epsilon\frac{\partial\tilde{f}_s}{\partial\tilde{y}}\tilde{\boldsymbol{\sigma}}^F_{yz} , \tag{B.36}$$

where

$$E = \frac{\partial\tilde{f}_s}{\partial\tilde{x}}\left(-\frac{\partial\tilde{f}_s}{\partial\tilde{x}}\tilde{p}^F + \frac{\partial\tilde{f}_s}{\partial\tilde{x}}\tilde{\boldsymbol{\sigma}}^F_{xx} + \frac{\partial\tilde{f}_s}{\partial\tilde{y}}\tilde{\boldsymbol{\sigma}}^F_{xy}\right) + \frac{\partial\tilde{f}_s}{\partial\tilde{y}}\left(-\frac{\partial\tilde{f}_s}{\partial\tilde{y}}\tilde{p}^F + \frac{\partial\tilde{f}_s}{\partial\tilde{x}}\tilde{\boldsymbol{\sigma}}^F_{xy} + \frac{\partial\tilde{f}_s}{\partial\tilde{y}}\tilde{\boldsymbol{\sigma}}^F_{yy}\right) . \tag{B.37}$$

To sum up, the relation of the fixed-point of the SIA-I algorithm and the exact full-Stokes solution is as follows. We have shown that the fixed-point solution satisfies the rheological equation and the z-component of momentum equation exactly, the horizontal components of the momentum equation, that is (3.12) and (3.13), are satisfied only approximately where the errors can be expressed by the left-hand sides of (B.27) and (B.28) and are of the order of ϵ^2. The free-surface boundary condition (3.17) and (3.18) are satisfied exactly, the third equation (3.19) is only approximated, with the error expressed by the left-hand side of (B.36) and is also of the order of ϵ^2.

Appendix C

Stretched coordinates

It is very common in glacier-flow modeling (see e.g. Pattyn, 2003) to transform the computational domain to a new one with uniform height by a generally non-orthogonal mapping. In order to do this also for the SIA-I algorithm, all the formulae have to be transformed. We will substitute the spatial coordinates $(\tilde{x}, \tilde{y}, \xi)$ for $(\tilde{x}, \tilde{y}, \tilde{z})$ by a mapping

$$\tilde{z} = \tilde{f}_b(\tilde{x}, \tilde{y}) + \xi(\tilde{f}_s(\tilde{x}, \tilde{y}) - \tilde{f}_b(\tilde{x}, \tilde{y})) \; . \tag{C.1}$$

All physical fields considered in the stretched coordinates will be marked by a "hat", that is

$$\tilde{f}(\tilde{x}, \tilde{y}, \tilde{z}) \quad \rightarrow \quad \hat{f}(\tilde{x}, \tilde{y}, \xi) \; , \tag{C.2}$$

or, in the abbreviated form,

$$\tilde{f}(\cdot, \tilde{z}) \quad \rightarrow \quad \hat{f}(\cdot, \xi) \; . \tag{C.3}$$

The partial derivatives transform as follows

$$\left.\frac{\partial}{\partial \tilde{x}}\right|_{\tilde{y},\tilde{z}} \quad \rightarrow \quad \left.\frac{\partial}{\partial \tilde{x}}\right|_{\tilde{y},\xi} - a_x(\cdot, \xi) \left.\frac{\partial}{\partial \xi}\right|_{\tilde{x},\tilde{y}} \; , \tag{C.4}$$

$$\left.\frac{\partial}{\partial \tilde{y}}\right|_{\tilde{x},\tilde{z}} \quad \rightarrow \quad \left.\frac{\partial}{\partial \tilde{y}}\right|_{\tilde{x},\xi} - a_y(\cdot, \xi) \left.\frac{\partial}{\partial \xi}\right|_{\tilde{x},\tilde{y}} \; , \tag{C.5}$$

$$\left.\frac{\partial}{\partial \tilde{z}}\right|_{\tilde{x},\tilde{y}} \quad \rightarrow \quad \frac{1}{\tilde{\mathcal{H}}(\cdot)} \left.\frac{\partial}{\partial \xi}\right|_{\tilde{x},\tilde{y}} \; , \tag{C.6}$$

where

$$a_x(\cdot, \xi) \quad := \quad \frac{1}{\tilde{\mathcal{H}}(\cdot)} \left(\frac{\partial \tilde{f}_b(\cdot)}{\partial \tilde{x}} + \xi \frac{\partial \tilde{\mathcal{H}}(\cdot)}{\partial \tilde{x}} \right) \; , \tag{C.7}$$

$$a_y(\cdot, \xi) \quad := \quad \frac{1}{\tilde{\mathcal{H}}(\cdot)} \left(\frac{\partial \tilde{f}_b(\cdot)}{\partial \tilde{y}} + \xi \frac{\partial \tilde{\mathcal{H}}(\cdot)}{\partial \tilde{y}} \right) \; , \tag{C.8}$$

$$\tilde{\mathcal{H}}(\cdot) \quad := \quad \tilde{f}_s(\cdot) - \tilde{f}_b(\cdot) \; . \tag{C.9}$$

We rewrite the individual steps of the SIA-I algorithm in the stretched coordinates, such that the formulae

(3.47)-(3.49) for stress increments transform as

$$\begin{aligned}
\delta\hat{p}^{k+\frac{1}{2}}(\cdot,\xi) &= \tilde{\mathcal{H}}(\cdot)(1-\xi) - \hat{p}^{k}(\cdot,\xi) - \hat{\boldsymbol{\sigma}}^{k}_{xx}(\cdot,\xi) - \hat{\boldsymbol{\sigma}}^{k}_{yy}(\cdot,\xi) \\
&- \epsilon\left(\frac{\partial}{\partial\tilde{x}} - a_x(\cdot,\xi)\frac{\partial}{\partial\xi}\right)\left(\tilde{\mathcal{H}}(\cdot)\int_{\xi}^{1}\hat{\boldsymbol{\sigma}}^{k}_{xz}(\cdot,\xi')d\xi'\right) \\
&- \epsilon\left(\frac{\partial}{\partial\tilde{y}} - a_y(\cdot,\xi)\frac{\partial}{\partial\xi}\right)\left(\tilde{\mathcal{H}}(\cdot)\int_{\xi}^{1}\hat{\boldsymbol{\sigma}}^{k}_{yz}(\cdot,\xi')d\xi'\right) \\
&+ \epsilon\frac{\partial\tilde{f}_s(\cdot)}{\partial\tilde{x}}\hat{\boldsymbol{\sigma}}^{k}_{xz}(\cdot,1) + \epsilon\frac{\partial\tilde{f}_s(\cdot)}{\partial\tilde{y}}\hat{\boldsymbol{\sigma}}^{k}_{yz}(\cdot,1)\,, \qquad \text{(C.10)}
\end{aligned}$$

$$\begin{aligned}
\delta\hat{\boldsymbol{\sigma}}^{k+\frac{1}{2}}_{xz}(\cdot,\xi) &= -\epsilon\frac{\partial\tilde{f}_s(\cdot)}{\partial\tilde{x}}\tilde{\mathcal{H}}(\cdot)(1-\xi) - \hat{\boldsymbol{\sigma}}^{k}_{xz}(\cdot,\xi) \\
&+ 2\epsilon\left(\frac{\partial}{\partial\tilde{x}} - a_x(\cdot,\xi)\frac{\partial}{\partial\xi}\right)\left(\tilde{\mathcal{H}}(\cdot)\int_{\xi}^{1}\hat{\boldsymbol{\sigma}}^{k}_{xx}(\cdot,\xi')d\xi'\right) \\
&+ \epsilon\left(\frac{\partial}{\partial\tilde{x}} - a_x(\cdot,\xi)\frac{\partial}{\partial\xi}\right)\left(\tilde{\mathcal{H}}(\cdot)\int_{\xi}^{1}\hat{\boldsymbol{\sigma}}^{k}_{yy}(\cdot,\xi')d\xi'\right) \\
&+ \epsilon\left(\frac{\partial}{\partial\tilde{y}} - a_y(\cdot,\xi)\frac{\partial}{\partial\xi}\right)\left(\tilde{\mathcal{H}}(\cdot)\int_{\xi}^{1}\hat{\boldsymbol{\sigma}}^{k}_{xy}(\cdot,\xi')d\xi'\right)\,, \qquad \text{(C.11)}
\end{aligned}$$

$$\begin{aligned}
\delta\hat{\boldsymbol{\sigma}}^{k+\frac{1}{2}}_{yz}(\cdot,\xi) &= -\epsilon\frac{\partial\tilde{f}_s(\cdot)}{\partial\tilde{y}}\tilde{\mathcal{H}}(\cdot)(1-\xi) - \hat{\boldsymbol{\sigma}}^{k}_{yz}(\cdot,\xi) \\
&+ \epsilon\left(\frac{\partial}{\partial\tilde{y}} - a_y(\cdot,\xi)\frac{\partial}{\partial\xi}\right)\left(\tilde{\mathcal{H}}(\cdot)\int_{\xi}^{1}\hat{\boldsymbol{\sigma}}^{k}_{xx}(\cdot,\xi')d\xi'\right) \\
&+ 2\epsilon\left(\frac{\partial}{\partial\tilde{y}} - a_y(\cdot,\xi)\frac{\partial}{\partial\xi}\right)\left(\tilde{\mathcal{H}}(\cdot)\int_{\xi}^{1}\hat{\boldsymbol{\sigma}}^{k}_{yy}(\cdot,\xi')d\xi'\right) \\
&+ \epsilon\left(\frac{\partial}{\partial\tilde{x}} - a_x(\cdot,\xi)\frac{\partial}{\partial\xi}\right)\left(\tilde{\mathcal{H}}(\cdot)\int_{\xi}^{1}\hat{\boldsymbol{\sigma}}^{k}_{xy}(\cdot,\xi')d\xi'\right)\,, \qquad \text{(C.12)}
\end{aligned}$$

and (3.52) remain unaltered.

Formulae (3.55)-(3.57) for velocity increments transform as

$$\begin{aligned}
\hat{v}_x^{k+\frac{1}{2}}(\cdot,\xi) &= 2\epsilon^{-1}\mathcal{X}\tilde{\mathcal{H}}(\cdot)\int_0^{\xi}\hat{\mathcal{A}}\hat{\mathcal{S}}^{k+\frac{1}{2}}(\cdot,\xi')\hat{\boldsymbol{\sigma}}^{k+\frac{1}{2}}_{xz}(\cdot,\xi')d\xi' \\
&- \epsilon^2\tilde{\mathcal{H}}(\cdot)\int_0^{\xi}\left(\frac{\partial}{\partial\tilde{x}} - a_x(\cdot,\xi')\frac{\partial}{\partial\xi'}\right)\tilde{v}_z^{k-\frac{1}{2}}(\cdot,\xi')\,d\xi', \qquad \text{(C.13)} \\
\hat{v}_y^{k+\frac{1}{2}}(\cdot,\xi) &= 2\epsilon^{-1}\mathcal{X}\tilde{\mathcal{H}}(\cdot)\int_0^{\xi}\hat{\mathcal{A}}\hat{\mathcal{S}}^{k+\frac{1}{2}}(\cdot,\xi')\hat{\boldsymbol{\sigma}}^{k+\frac{1}{2}}_{yz}(\cdot,\xi')d\xi' \\
&- \epsilon^2\tilde{\mathcal{H}}(\cdot)\int_0^{\xi}\left(\frac{\partial}{\partial\tilde{y}} - a_y(\cdot,\xi')\frac{\partial}{\partial\xi'}\right)\tilde{v}_z^{k-\frac{1}{2}}(\cdot,\xi')\,d\xi'\,, \qquad \text{(C.14)} \\
\hat{v}_z^{k+\frac{1}{2}}(\cdot,\xi) &= -\tilde{\mathcal{H}}(\cdot)\int_0^{\xi}\left(\frac{\partial}{\partial\tilde{x}} - a_x(\cdot,\xi')\frac{\partial}{\partial\xi'}\right)\hat{v}_x^{k+\frac{1}{2}}(\cdot,\xi')d\xi' \\
&- \tilde{\mathcal{H}}(\cdot)\int_0^{\xi}\left(\frac{\partial}{\partial\tilde{y}} - a_y(\cdot,\xi')\frac{\partial}{\partial\xi'}\right)\hat{v}_y^{k+\frac{1}{2}}(\cdot,\xi')d\xi'\,, \qquad \text{(C.15)}
\end{aligned}$$

with

$$\hat{\mathcal{S}} = \hat{\boldsymbol{\sigma}}_{xx}^2 + \hat{\boldsymbol{\sigma}}_{yy}^2 + \hat{\boldsymbol{\sigma}}_{xx}\hat{\boldsymbol{\sigma}}_{yy} + \hat{\boldsymbol{\sigma}}_{xy}^2 + \hat{\boldsymbol{\sigma}}_{xz}^2 + \hat{\boldsymbol{\sigma}}_{yz}^2 \,, \tag{C.16}$$

or alternatively, when (3.62), (3.63) and (3.59) are used, are written as

$$\begin{aligned} \hat{v}_x^{k+\frac{1}{2}}(\cdot,\xi) &= 2\epsilon^{-1}\mathcal{X}\tilde{\mathcal{H}}(\cdot)\int_0^{\xi}\hat{\mathcal{A}}\hat{\mathcal{S}}^{k+\frac{1}{2}}(\cdot,\xi')\hat{\boldsymbol{\sigma}}_{xz}^{k+\frac{1}{2}}(\cdot,\xi')d\xi' \\ &+ \mathcal{X}\tilde{\mathcal{H}}(\cdot)\int_0^{\xi}\left(\frac{\partial}{\partial\tilde{x}} - a_x(\cdot,\xi')\frac{\partial}{\partial\xi'}\right)\left(\tilde{\mathcal{H}}(\cdot)\int_0^{\xi'}\hat{\mathcal{A}}\hat{\mathcal{S}}^{k+\frac{1}{2}}(\hat{\boldsymbol{\sigma}}_{xx}^k + \hat{\boldsymbol{\sigma}}_{yy}^k)(\cdot,\xi'')\,d\xi''\right)d\xi' \,, \end{aligned} \tag{C.17}$$

$$\begin{aligned} \hat{v}_y^{k+\frac{1}{2}}(\cdot,\xi) &= 2\epsilon^{-1}\mathcal{X}\tilde{\mathcal{H}}(\cdot)\int_0^{\xi}\hat{\mathcal{A}}\hat{\mathcal{S}}^{k+\frac{1}{2}}(\cdot,\xi')\hat{\boldsymbol{\sigma}}_{yz}^{k+\frac{1}{2}}(\cdot,\xi')d\xi' \\ &+ \mathcal{X}\tilde{\mathcal{H}}(\cdot)\int_0^{\xi}\left(\frac{\partial}{\partial\tilde{y}} - a_y(\cdot,\xi')\frac{\partial}{\partial\xi'}\right)\left(\tilde{\mathcal{H}}(\cdot)\int_0^{\xi'}\hat{\mathcal{A}}\hat{\mathcal{S}}^{k+\frac{1}{2}}(\hat{\boldsymbol{\sigma}}_{xx}^k + \hat{\boldsymbol{\sigma}}_{yy}^k)(\cdot,\xi'')\,d\xi''\right)d\xi' \,, \end{aligned} \tag{C.18}$$

$$\hat{v}_z^{k+\frac{1}{2}}(\cdot,\xi) = -\epsilon^{-2}\mathcal{X}\tilde{\mathcal{H}}(\cdot)\int_0^{\xi}\hat{\mathcal{A}}\hat{\mathcal{S}}^{k+\frac{1}{2}}(\hat{\boldsymbol{\sigma}}_{xx}^k + \hat{\boldsymbol{\sigma}}_{yy}^k)(\cdot,\xi')\,d\xi' \,. \tag{C.19}$$

Finally, formulae (3.22)-(3.29) for the rheological equations transform as

$$\hat{\boldsymbol{\sigma}}_{xz}(\cdot,\xi) = \hat{\eta}(\cdot,\xi)\left(\frac{\partial\hat{v}_x(\cdot,\xi)}{\partial\xi} + \epsilon^2\left(\tilde{\mathcal{H}}(\cdot)\frac{\partial}{\partial\tilde{x}} - a_x\tilde{\mathcal{H}}(\cdot,\xi)\frac{\partial}{\partial\xi}\right)\tilde{v}_z(\cdot,\xi)\right) \,, \tag{C.20}$$

$$\hat{\boldsymbol{\sigma}}_{yz}(\cdot,\xi) = \hat{\eta}(\cdot,\xi)\left(\frac{\partial\hat{v}_y(\cdot,\xi)}{\partial\xi} + \epsilon^2\left(\tilde{\mathcal{H}}(\cdot)\frac{\partial}{\partial\tilde{y}} - a_y\tilde{\mathcal{H}}(\cdot,\xi)\frac{\partial}{\partial\xi}\right)\tilde{v}_z(\cdot,\xi)\right) \,, \tag{C.21}$$

$$\begin{aligned} \hat{\boldsymbol{\sigma}}_{xy}(\cdot,\xi) &= \hat{\eta}(\cdot,\xi)\left(\left(\tilde{\mathcal{H}}(\cdot)\frac{\partial}{\partial\tilde{y}} - a_y\tilde{\mathcal{H}}(\cdot,\xi)\frac{\partial}{\partial\xi}\right)\hat{v}_x(\cdot,\xi)\right. \\ &+ \left.\left(\tilde{\mathcal{H}}(\cdot)\frac{\partial}{\partial\tilde{x}} - a_x\tilde{\mathcal{H}}(\cdot,\xi)\frac{\partial}{\partial\xi}\right)\hat{v}_y(\cdot,\xi)\right) \,, \end{aligned} \tag{C.22}$$

$$\hat{\boldsymbol{\sigma}}_{xx}(\cdot,\xi) = 2\hat{\eta}(\cdot,\xi)\left(\tilde{\mathcal{H}}(\cdot)\frac{\partial}{\partial\tilde{x}} - a_x\tilde{\mathcal{H}}(\cdot,\xi)\frac{\partial}{\partial\xi}\right)\hat{v}_x(\cdot,\xi) \,, \tag{C.23}$$

$$\hat{\boldsymbol{\sigma}}_{yy}(\cdot,\xi) = 2\hat{\eta}(\cdot,\xi)\left(\tilde{\mathcal{H}}(\cdot)\frac{\partial}{\partial\tilde{y}} - a_y\tilde{\mathcal{H}}(\cdot,\xi)\frac{\partial}{\partial\xi}\right)\hat{v}_y(\cdot,\xi) \,, \tag{C.24}$$

$$\hat{\eta}(\cdot,\xi) = \left(2\tilde{\mathcal{H}}(\cdot)\epsilon^{-1}\mathcal{A}\mathcal{X}\mathcal{H}^2\hat{\mathcal{V}}(\cdot,\xi)\right)^{-\frac{1}{3}} \,, \tag{C.25}$$

where

$$\begin{aligned}
\mathcal{H}^2\hat{\mathcal{V}}(\cdot,\xi) &= 4\epsilon^2\left\{\left(\tilde{\mathcal{H}}(\cdot)\frac{\partial}{\partial\tilde{x}} - a_x\tilde{\mathcal{H}}(\cdot,\xi)\frac{\partial}{\partial\xi}\right)\hat{v}_x(\cdot,\xi)\right\}^2 \\
&+ 4\epsilon^2\left\{\left(\tilde{\mathcal{H}}(\cdot)\frac{\partial}{\partial\tilde{y}} - a_y\tilde{\mathcal{H}}(\cdot,\xi)\frac{\partial}{\partial\xi}\right)\hat{v}_y(\cdot,\xi)\right\}^2 \\
&+ 4\epsilon^2\left\{\left(\tilde{\mathcal{H}}(\cdot)\frac{\partial}{\partial\tilde{x}} - a_x\tilde{\mathcal{H}}(\cdot,\xi)\frac{\partial}{\partial\xi}\right)\hat{v}_x(\cdot,\xi)\right\} \\
&\qquad \left\{\left(\tilde{\mathcal{H}}(\cdot)\frac{\partial}{\partial\tilde{y}} - a_y\tilde{\mathcal{H}}(\cdot,\xi)\frac{\partial}{\partial\xi}\right)\hat{v}_y(\cdot,\xi)\right\} \\
&+ \epsilon^2\left\{\left(\tilde{\mathcal{H}}(\cdot)\frac{\partial}{\partial\tilde{y}} - a_y\tilde{\mathcal{H}}(\cdot,\xi)\frac{\partial}{\partial\xi}\right)\hat{v}_x(\cdot,\xi)\right. \\
&\qquad \left.+\left(\tilde{\mathcal{H}}(\cdot)\frac{\partial}{\partial\tilde{x}} - a_x\tilde{\mathcal{H}}(\cdot,\xi)\frac{\partial}{\partial\xi}\right)\hat{v}_y(\cdot,\xi)\right\}^2 \\
&+ \left\{\frac{\partial\tilde{v}_y(\cdot,\xi)}{\partial\xi} + \epsilon^2\left(\tilde{\mathcal{H}}(\cdot)\frac{\partial}{\partial\tilde{y}} - a_y\tilde{\mathcal{H}}(\cdot,\xi)\frac{\partial}{\partial\xi}\right)\hat{v}_z(\cdot,\xi)\right\}^2 \\
&+ \left\{\frac{\partial\tilde{v}_x(\cdot,\xi)}{\partial\xi} + \epsilon^2\left(\tilde{\mathcal{H}}(\cdot)\frac{\partial}{\partial\tilde{x}} - a_x\tilde{\mathcal{H}}(\cdot,\xi)\frac{\partial}{\partial\xi}\right)\hat{v}_z(\cdot,\xi)\right\}^2 . \qquad \text{(C.26)}
\end{aligned}$$

When time is also taken into account, the mapping actually reads as

$$\tilde{f}(\tilde{x},\tilde{y},\tilde{z},\tilde{t}) \quad\rightarrow\quad \hat{f}(\tilde{x},\tilde{y},\xi,\tilde{t})\,, \qquad \text{(C.27)}$$

and the partial time derivative has to be transformed as

$$\left.\frac{\partial}{\partial\tilde{t}}\right|_{\tilde{x},\tilde{y},\tilde{z}} \rightarrow \left.\frac{\partial}{\partial\tilde{t}}\right|_{\tilde{x},\tilde{y},\xi} - a_t(\cdot,\xi,\tilde{t})\frac{\partial}{\partial\xi}\,, \qquad \text{(C.28)}$$

with

$$a_t(\cdot,\xi,\tilde{t}) := \frac{1}{\tilde{\mathcal{H}}(\cdot,\tilde{t})}\left(\frac{\partial\tilde{f}_b(\cdot,\tilde{t})}{\partial\tilde{t}} + \xi\frac{\partial\tilde{\mathcal{H}}(\cdot,\tilde{t})}{\partial\tilde{t}}\right)\,. \qquad \text{(C.29)}$$

Appendix D

Basic spatial differential operators in general orthogonal curvilinear coordinates

Bellow we summarize the most important formulae for basic differential operators expressed in the general orthogonal curvilinear coordinates. We will follow the lecture notes by Martinec (http://geo.mff.cuni.cz/vyuka) and also Brdička et al. (2000). Given the Cartesian coordinates of a point in the 3D space (y_1, y_2, y_3) and given a coordinate transformation, i.e. a mapping

$$x_k = x_k(y_1, y_2, y_3), \qquad k = 1, 2, 3, \tag{D.1}$$

which is C^1 (continuous partial derivatives) with a non-vanishing Jacobian

$$j = \det\left(\frac{\partial x_k}{\partial y_l}\right) \neq 0 \qquad \text{almost everywhere}\,, \tag{D.2}$$

we define the unit base vectors of a new coordinate system by

$$\vec{e}_k := \frac{1}{h_k}\frac{\partial \vec{p}}{\partial x_k}\,, \tag{D.3}$$

where $\vec{p}$ is the position vector and h_k is a scale factor (Lame coefficient)

$$h_k := \sqrt{\sum_{l=1}^{3}\left(\frac{\partial y_l}{\partial x_k}\right)^2} = \sqrt{\frac{\partial \vec{p}}{\partial x_k}\cdot\frac{\partial \vec{p}}{\partial x_k}}\,, \tag{D.4}$$

with no summation over index k. We will assume that the new curvilinear coordinates x_k are orthogonal and form a right-hand system, i.e. the new basis vectors satisfy

$$\vec{e}_k \cdot \vec{e}_l = \delta_{kl}\,, \qquad \vec{e}_k \times \vec{e}_l = \epsilon_{klm}\vec{e}_m\,, \tag{D.5}$$

where ϵ_{klm} is the Levi-Civita permutation symbol. The basis vectors $\vec{e}_k$ are now generally varying in space and we define the Christoffel symbols Γ^m_{kl} by

$$\frac{\partial \vec{e}_k}{\partial x_l} = \sum_{m=1}^{3}\Gamma^m_{kl}\vec{e}_m\,, \tag{D.6}$$

thus

$$\Gamma_{kl}^{m} = \frac{\partial \vec{e}_k}{\partial x_l} \cdot \vec{e}_m \, . \tag{D.7}$$

The Christoffel symbols can be expressed by means of the Lame coefficients by

$$\Gamma_{kl}^{m} = \frac{1}{h_k} \frac{\partial h_l}{\partial x_k} \delta_{lm} - \frac{1}{h_m} \frac{\partial h_k}{\partial x_m} \delta_{kl} \, , \tag{D.8}$$

from which it follows that for $k \neq l \neq m$

$$\Gamma_{kl}^{m} = \Gamma_{kk}^{k} = \Gamma_{kl}^{k} = 0 \, , \tag{D.9}$$

and also

$$\Gamma_{kl}^{l} = -\Gamma_{ll}^{k} \, , \tag{D.10}$$

as a result of which only six Christoffel symbols are independent. With the use of Christoffel symbols, we may now rewrite the basic invariant differential operators in the general curvilinear orthogonal coordinates.

Gradient of a scalar

$$\mathrm{grad}\phi = \sum_k \frac{1}{h_k} \frac{\partial \phi}{\partial x_k} \vec{e}_k \tag{D.11}$$

Divergence of a vector

$$\begin{aligned} \mathrm{div}\vec{v} &= \sum_k \frac{1}{h_k} \left[\frac{\partial v_k}{\partial x_k} + \sum_m \Gamma_{mk}^{k} v_m \right] \\ &= \sum_k \frac{1}{h_k} \left(\frac{\partial v_k}{\partial x_k} + \sum_{m,m\neq k} \frac{1}{h_m} \frac{\partial h_k}{\partial x_m} v_m \right) \end{aligned} \tag{D.12}$$

Gradient of a vector

$$\begin{aligned} \mathrm{grad}\vec{v} &= \sum_{k\,l} \frac{1}{h_k} \left(\frac{\partial v_l}{\partial x_k} + \sum_m \Gamma_{mk}^{l} v_m \right) \vec{e}_k \otimes \vec{e}_l \\ &= \sum_k \frac{1}{h_k} \left(\frac{\partial v_k}{\partial x_k} + \sum_{m,m\neq k} \frac{1}{h_m} \frac{\partial h_k}{\partial x_m} v_m \right) \vec{e}_k \otimes \vec{e}_k + \sum_k \sum_{l,l\neq k} \frac{1}{h_k} \left(\frac{\partial v_l}{\partial x_k} - \frac{1}{h_l} \frac{\partial h_k}{\partial x_l} v_k \right) \vec{e}_k \otimes \vec{e}_l \end{aligned} \tag{D.13}$$

Divergence of a tensor

$$\begin{aligned} \mathrm{div}\mathbf{T} &= \sum_{kl} \frac{1}{h_k} \left(\frac{\partial T_{kl}}{\partial x_k} + \sum_m \Gamma_{mk}^{k} T_{ml} + \sum_m \Gamma_{mk}^{l} T_{km} \right) \vec{e}_l \\ &= \sum_l \left\{ \frac{1}{h_1 h_2 h_3} \left[\frac{\partial}{\partial \tilde{x}_1} \left(h_2 h_3 \mathbf{T}_{1l} \right) + \frac{\partial}{\partial \tilde{x}_2} \left(h_1 h_3 \mathbf{T}_{2l} \right) + \frac{\partial}{\partial \tilde{x}_3} \left(h_1 h_2 \mathbf{T}_{3l} \right) \right] \right. \\ &+ \left. \sum_k \frac{1}{h_k h_l} \left(\frac{\partial h_l}{\partial x_k} \mathbf{T}_{lk} - \frac{\partial h_k}{\partial x_l} \mathbf{T}_{kk} \right) \right\} \vec{e}_l \end{aligned} \tag{D.14}$$

Bibliography

Baral, D.R., K. Hutter, R. Greve, 2001. Asymptotic theories of large-scale motion, temperature and moisture distribution in land-based polythermal ice sheets. A critical review and new developments, *Appl. Mech. Rev*, **54** (3), 215-256.

Blatter, H., G. Clarke, and J. Colinge. 1998. Stress and velocity fields in glaciers: Part II. sliding and basal stress distribution. *J. Glaciol.*, **44** (148), 457-466.

Brdička, M., L. Samek, and B. Sopko. 2000. Mechanika kontinua. Academia, Praha.

Dansgaard, W., S.J. Johnsen, H.B. Clausenm, D. Dahl-Jensen, N.S. Gunderstrup, C.U. Hammer, C.S. Hvidberg, J.P. Steffensen, A.E. Sveinbjrnsdottir, J. Jouzel, and G. Bond, 1993. Evidence for general instability of past climate from a 250-kyr ice-core record. *Nature*, **364**, 218-220.

Gagliardini, O., T. Zwinger, 2008. The ISMIP-HOM benchmark experiments performed using the Finite-Element code Elmer. *The Cryosphere Discuss.*, **2**, 75-109.

Granas, A., J. Dugundji, 2003. Fixed Point Theory, Springer-Verlag, New York.

Greve, R., 1997. A continuum-mechanical formulation for shallow polythermal ice sheets, *Phil. Trans. R. Soc. Lond. A*, **355** (1726), 921-974.

Hindmarsh, R.C.A., 2004. A numerical comparision of approximations to the Stokes equations used in ice-sheet and glacier modeling. J. *Geophys. Res.*, **109**, F01012.

Hutter, K., 1983. Theoretical Glaciology; material science of ice and the mechanics of glaciers and ice sheets. Reidel, Dordrecht, Netherlands, 510 pp.

Hutter, K., K. Jöhnk, 2004. Continuum Methods of Physical Modeling Continuum Mechanics, Dimensional Analysis, Turbulence. Springer, Berlin, 635 pp.

Huybrechts, P., 1992. The Antarctic ice sheet and environmental change: a three-dimensional modelling study. *Berichte zur Polarforschung*, **99**, 241 p.

Huybrechts, P., 1998. Report of the Third EISMINT Workshop on Model Intercomparison. European Science Foundation (Strasbourg), 120 p.

Huybrechts, P., O. Rybak, F. Pattyn, U. Ruth, and D. Steinhage, 2007. Ice thinning, upstream advection, and non-climatic biases for the upper 89% of the EDML ice core from a nested model of the Antarctic ice sheet. *Climate of the Past*, **3**, 577-589.

Imbrie, J., J.D. Hays, D.G. Martinson, A. McIntyre, A.C. Mix, J.J. Morley, N.G. Pisias, W.L. Prell, and N.J. Shackleton, 1982. The orbital theory of Pleistocene climate: Support from a revised chronology of the

marine δ^{18}O record. in Berger, A.L. et al. (eds) : Milankovitch and climate, part I, NATO ASI series, p 269-305.

Kamb, B., K.A. Echelmeyer, 1986. Stress-gradient coupling in glacier flow: I. Longitudinal averaging of the influence of ice thickness and surface slope. *J. Glaciol.*, **32**, 267-279.

Le Meur, E., O. Gagliardini, T. Zwinger, and J. Ruokolainen, 2004. Glacier flow modelling: a comparison of the Shallow Ice Approximation and the full-Stokes solution. *C.R. physique*, **5**, p. 709-722.

Letreguilly, A., P. Huybrechts, N. Reeh, 1991. Steady state characteristics of the Greenland ice sheet under different climates. *J. Glaciol.*, **37** (125), pp 149-157.

Lukeš, J., 2003. Zápisky z funkcionální analýzy. Univerzita Karlova v Praze, Karolinum, Praha.

Manabe, S., R.J. Stouffer, 1994. Multiple century response of a coupled oceanatmosphere model to an increase of atmospheric carbon dioxide. *J. Climate*, **7**, 5-23.

Marshall, S.J., H. Bjrnsson, G.E. Flowers, G.K.C. Clarke, 2005. Simulation of Vatnajkull ice cap dynamics. *J. Geophys. Res.*, **110** F3, F03009.

Ohmura, A., N. Reeh, 1991. New precipitation and accumulation maps for Greenland. *J. Glaciol.*, **37**, pp 140-148.

Paterson, W. S. B., 1981. The Physics of Glaciers. Pergamon Press, Oxford.

Pattyn, F., L. Perichon, A. Aschwanden, B. Breuer, B. de Smedt, O. Gagliardini, G. H. Gudmundsson, R. Hindmarsh, A. Hubbard, J. V. Johnson, T. Kleiner, Y. Konovalov, C. Martin, A. J. Payne, D. Pollard, S. Price, M. Rckamp, F. Saito, O. Souček, S. Sugiyama, and T. Zwinger, T., 2008. Benchmark experiments for higher-order and full Stokes ice sheet models (ISMIP-HOM), *The Cryosphere Discuss.*, **2**, 111-151.

Pattyn, F., 2003. A new three-dimensional higher-order thermomechanical ice-sheet model: basic sensitivity, ice-stream development and ice flow across subglacial lakes. *J. Geophys. Res.*, **108**-B8 2382.

Pattyn, F., 2002. Transient glacier response with a higher-order numerical ice-flow model, *J. Glaciol.*, **48**, 467-477.

Payne, A.J. , Ph. Huybrechts, A. Abe-Ouchi, R. Calov, J.L. Fastook, R. Greve, S.J. Marshall, I. Marsiat, C. Ritz, L. Tarasov, and M.P.A. Thomassen, 2000. Results from the EISMINT model intercomparison: the effects of thermomechanical coupling. *J. Glaciol.*, **46** (153), 227-238.

Peng, D., B. Merriman, S. Osher, H.K. Zhao, and M. Kang, 1999. A PDE based fast local level set method, *J. Comp. Phys.*, **155**, 410-438.

Press W.H. et al., 1992. Numerical Recepies in FORTRAN: The Art of Scientific Computing, Second edition, Cambridge University Press.

Price, S. F., E. D. Waddington, and H. Conway, 2007. A full-stress, thermomechanical flow band model using the finite volume method, *J. Geophys. Res.*, **112**, F03020.

Quarteroni, A., A. Valli, 1994. Numerical Approximation Of Partial Differential Equations (Springer Series In Computational Mathematics), Springer-Verlag Berlin Heidelberg.

Reeh, N. 1991. Parameterization of melt rate and surface temperature on theGreenland ice sheet. *Polarforschung*, **59** (3), 113-128.

Ritz, C., V. Rommelaere and C. Dumas, 2001. Modelling the evolution of the Antarctic ice sheet over the last 420 000 years: implications for altitude changes in the Vostok region, *J. Geophys. Res.*, **109**, 31943-31964.

Saito, F., A. Abe-Ouchi, H. Blatter, 2003. Effects of first-order stress gradients in an ice sheet evaluated by a three-dimensional thermomechanical coupled model. *Ann. Glaciol.* **37**, 166-172.

Shu, C.-W., 1998. Essentially non-oscillatory and weighted essentially non-oscillatory schemes for hyperbolic conservation laws, in Advanced Numerical Approximation of Nonlinear Hyperbolic Equations, edited by A. Quarteroni, Lecture Notes in Mathematics, Springer-Verlag, Berlin/New York, Vol. **1697**, p. 325.

Souček, O., Z. Martinec, 2005. Thermomechanical polythermal ice-sheet model. Scientific Technical Report, STR 06/13, GeoForschungsZentrum, Potsdam, 106 pp.

Souček O., Z. Martinec, 2008. Iterative improvement of the shallow-ice approximation. *J. Glaciol.*, **54**, 188, 812-822.

van der Veen, C.J., 1999. Fundamentals of Glacier Dynamics, A.A. Balkema, Rotterdam, Netherlands, 462 pp.

Zwinger, T., R. Greve, O. Gagliardini, T. Shiraiwa, M. Lyly, 2007. A Full Stokes-flow Thermo-mechanical Model for Firn and Ice applied to the Gorshkov Crater Glacier, Kamchatka. *Ann. Glaciol.*, **45**, 29-37.